Influence of Tissue Conductivity Inhomogeneity and Anisotropy on EEG/MEG based Source Localization in the Human Brain

Influence of Tissue Conductivity Inhomogeneity and Anisotropy on EEG/MEG based Source Localization in the Human Brain

von Dipl.-Math. Carsten Hermann Wolters

geboren am 10. Juni 1967 in Emsdetten

Bibliographical data

Abstract

The inverse problem in Electro- and Magneto-EncephaloGraphy (EEG/MEG) aims at reconstructing the underlying current distribution in the human brain using potential differences and/or magnetic fluxes that are measured non-invasively directly, or at a close distance, from the head surface. The solution requires repeated computation of the forward problem, i.e., the simulation of EEG and MEG fields for a given dipolar source in the brain using a volume-conduction model of the head. The associated differential equations are derived from the Maxwell equations. Not only do various head tissues exhibit different conductivities, some of them are also anisotropic conductors as, e.g., skull and brain white matter. To our knowledge, previous work has not extensively investigated the impact of modeling tissue anisotropy on source reconstruction. Currently, there are no readily available methods that allow direct conductivity measurements. Furthermore, there is still a lack of sufficiently powerful software packages that would yield significant reduction of the computation time involved in such complex models hence satisfying the time-restrictions for the solution of the inverse problem. In this dissertation, techniques of multimodal Magnetic Resonance Imaging (MRI) are presented in order to generate high-resolution realistically shaped anisotropic volume conductor models. One focus is the presentation of an improved segmentation of the skull by means of a bimodal T1/PD-MRI approach. The eigenvectors of the conductivity tensors in anisotropic white matter are determined using whole head Diffusion-Tensor-MRI. The Finite Element (FE) method in combination with a parallel algebraic multigrid solver yields a highly efficient solution of the forward problem. After giving an overview of state-of-the-art inverse methods, new regularization concepts are presented. Next, the sensitivity of inverse methods to tissue anisotropy is tested. The results show that skull anisotropy affects significantly EEG source reconstruction whereas white matter anisotropy affects both EEG and MEG source reconstructions. Therefore, high-resolution FE forward modeling is crucial for an accurate solution of the inverse problem in EEG and MEG.

Contents

Notations

$\mathbb{R}$ ($\mathbb{R}^+$), $\mathbb{R}^s$	–	Set of real (pos. real) numbers and set of s-dim. vectors.
$\mathbb{N}$, $\mathbb{N}_0$	–	Set of positive integers without and with zero.
$\mathbf{x}, \vec{\mu}$	–	3-dim. vector (latin,greek): $\mathbf{x} = (x_1, x_2, x_3)^{tr}$.
$\mathbf{v}_i, \Delta_i$	–	i^{th} vertex (primitive) of a mesh.
$\mathbf{e}_i, \mathbf{e}_z$	–	i^{th} unit basis vector (3-dim.), $\mathbf{e}_z = \mathbf{e}_3$.
u, $\mathbf{B}$	–	Scalar valued function, vector valued function.
$B_z, (\vec{\mu} \times \mathbf{B})_z$	–	z-component of a vector valued function.
$u_h, \underline{u}_h$	–	Finite element function and its vector representation.
ψ_i	–	Finite element Ansatz-function.
N_h	–	Order of the FE equation system.
$\underline{u}_h^{[i]}$	–	i^{th} entry of the vector $\underline{u}_h \in \mathbb{R}^{N_h}$.
K_h	–	FE system matrix $\mathsf{K}_h \in \mathbb{R}^{N_h \times N_h}$.
$\mathsf{K}_h^{[ij]}$	–	entry in i^{th} row and j^{th} column of matrix K_h.
X, X^{tr}, X^{-tr}	–	a matrix, its transpose and the transpose of the inverse.
$\text{trace}(X)$	–	For $X \in \mathbb{R}^{n \times n}$, it is $\text{trace}(X) := X^{[11]} + \ldots + X^{[nn]}$.
$\mathsf{W} := \text{DIAG}(w_1, \ldots, w_n)$	–	$\mathsf{W}^{[ii]} = w_i, \ \forall i = 1, \ldots, n$ and $\mathsf{W}^{[ij]} = 0, \ \forall i \neq j$.
$\mathbf{S} := \mathbf{diag}(s_1, s_2, s_3)$	–	$\mathbf{S}^{[ii]} = s_i, \ i = 1, 2, 3$ and $\mathbf{S}^{[ij]} = 0, \ \forall i \neq j$.
δ_{ij}	–	Kronecker delta, $\delta_{ij} = 1$ for $i = j$, $\delta_{ij} = 0$ for $i \neq j$.
$\mathbf{D}, \underline{\sigma}, D^{[ij]}, \sigma^{[ij]}$	–	tensors of order two (latin, greek) and their entries.
$\underline{x}_i$	–	i^{th} column vector of an arbitrary matrix X.
$\underline{\mathbf{x}}$	–	For matrix $X \in \mathbb{R}^{m \times T}$, it is $\underline{\mathbf{x}} := (\underline{x}_1^{tr}, \ldots, \underline{x}_T^{tr})^{tr} \in \mathbb{R}^{mT}$.
$\underline{x}^i, \mathbf{x}^i$	–	i^{th} iterate for the vectors $\underline{x}$ and $\mathbf{x}$.
$\otimes$	–	Kronecker product for matrices, see Definition 6.5.1.
$\text{Id}^s, \mathbf{Id}$	–	Identity matrix, rang s and rang 3.
$0^s, \underline{0}^s$	–	Zero matrix and zero vector of order s.
$\underline{e}_i$	–	i^{th} unit vector.
$(.,.)$	–	Euclidean inner product.

$\langle .,. \rangle$	–	Duality product.
$\Omega \, (\bar{\Omega}), \, \Gamma = \partial \Omega$	–	Open (closed) bounded domain and its boundary.
$\mathbf{n}$	–	3D normal unit vector to a boundary.
grad	–	Gradient, $\operatorname{grad} u(\mathbf{x}) := \left(\frac{\partial u(\mathbf{x})}{\partial x_1}, \frac{\partial u(\mathbf{x})}{\partial x_2}, \frac{\partial u(\mathbf{x})}{\partial x_3} \right)^T$ for $\mathbf{u} : \mathbb{R}^3 \to \mathbb{R}$.
Δ	–	Laplace operator, $\Delta u(\mathbf{x}) = \sum_{i=1}^{3} \frac{\partial^2 u(\mathbf{x})}{\partial x_i^2}$ for $\mathbf{u} : \mathbb{R}^3 \to \mathbb{R}$.
curl	–	curl–operator (also: rot),
		$\operatorname{curl} \mathbf{u} = \left(\frac{\partial u_3}{\partial x_2} - \frac{\partial u_2}{\partial x_3}, \frac{\partial u_1}{\partial x_3} - \frac{\partial u_3}{\partial x_1}, \frac{\partial u_2}{\partial x_1} - \frac{\partial u_1}{\partial x_2} \right)^T$, for $\mathbf{u} : \mathbb{R}^3 \to \mathbb{R}^3$.
div	–	Divergence operator, $\operatorname{div} \mathbf{u} = \sum_{i=1}^{3} \frac{\partial u_i}{\partial x_i}$ for $\mathbf{u} : \mathbb{R}^3 \to \mathbb{R}$.
$L^2(\Omega)$	–	Space of scalar square-integrable (Lebesgue) functions on Ω.
$H^1(\Omega)$	–	Sobolev space:
		$H^1(\Omega) = \{ v \in L^2(\Omega) : \; \nabla v \in (L^2(\Omega))^3 \}$ (weak sense).
P	–	The number of processors.
n_{inf}	–	The number of influence nodes for discrete source space.
p	–	Focal source model: The number of sources.
m	–	The number of sensors.
T	–	The number of timepoints.
$\mathbf{E}, \mathbf{H}$	–	Electric and magnetic field.
$\mathbf{D}, \mathbf{B}$	–	Electric displacement and magnetic induction.
$\mathbf{j}, \mathbf{j}^p$	–	Electric current density, impressed or primary current.
$\underline{\underline{\sigma}}$	–	Conductivity tensor.
ρ, ε, μ	–	Electric free charge density, electric and magnetic permeability.
u, $\mathbf{A}$	–	Scalar electric potential, magnetic vector potential.
Ψ	–	Magnetic flux.

Abbreviations

AFCM	Adaptive Fuzzy-C-Means		MPI	Message Passing Interface
AMG	Algebraic Multi-Grid		MR	Magnetic Resonance
BE	Boundary Element		MRI	Magnetic Resonance Imaging
CDS	Continuous Downhill Simplex method		OSC	Outer Skull Compacta
			OSS	Outer Skull Surface
CG	Conjugate Gradient		PCG	Preconditioned Conjugate Gradient
COF	Complete Orthogonal Factorization		PET	Positron Emission Tomography
CSF	Cerebrospinal Fluid		PDE	Partial Differential Equation
CT	Computed Tomography		PD-MRI	Proton-Density-weighted MRI
DT	Diffusion Tensor		RDM	Relative Difference Measure
dyn-EIT	dynamical Electrical Impedance Tomography		RS	Remaining Skull (spongiosa and inner compacta)
EEG	ElectroEncephaloGraphy		SA	Simulated Annealing
EISS	Estimated Inner Skull Surface		SEP	Somatosensory Evoked Potential
ELAN	Early Left Anterior Negativity			
EMA	Effective Medium Approach		SNR	Signal-to-Noise Ratio
ERG	Extended Region Growing		SOR	Successive OverRelaxation
ERP	Event Related Potential		SPD	Symmetric Positive Definite
FE	Finite Element		SPECT	Single Photon Emission Tomography
fMRI	functional MRI			
GM	Grey Matter		SQUID	Superconducting QUantum Interference Device
GMG	Geometric Multi-Grid			
IC0	Incomplete Cholesky without fill-in		SSSM	Smooth Surface Spongiosa Model
ILDLT	Incomplete LDL^{tr}		SVD	Singular Value Decomposition
ISS	Inner Skull Surface		TSVD	Truncated SVD
MAG	MAGnification factor		T1-MRI	T1-weighted MRI
MEG	MagnetoEncephaloGraphy		U-FLARE	Ultra-Fast Low Angle RARE
MG	Multi-Grid.		WM	White Matter
MI	Mutual Information			

Chapter 1

Introduction

Everything should be made as simple as possible, but not simpler.

The main concern in all scientific work must be the human being himself.
This, one should never forget among all those diagrams and equations.

Albert Einstein

Nowadays devices and tools are available for analyzing and monitoring the human brain at a high level of detail. These details are necessary, e.g., for successful surgery or, more generally, for basic brain research. Rapid advances were achieved in the fields of functional imaging modalities such as Positron Emission Tomography (PET), Single Photon Emission Tomography (SPECT), functional Magnetic Resonance Imaging (fMRI), ElectroEncephaloGraphy (EEG) and MagnetoEncephaloGraphy (MEG). Since PET, SPECT, fMRI, EEG and MEG each have their strengths and weaknesses, the modalities complement each other and synergetic effects are expected from their integration. Computational methods are often used in the diagnostic and pre-surgical phase. The field of EEG/MEG source reconstruction is a representative of such methods. Non-invasive tools are of course preferable to invasive methods which may be of high risk to patients. In fundamental brain research, most often there is no other choice besides computational methods. However, the acceptance of tools depends very much on their reliability and robustness and on their speed.

1.1   EEG/MEG source reconstruction

It is common practice in cognitive research and in clinical routine and research to reconstruct current sources in the human brain by means of their electric poten-

tials, measured with electrodes which are fixed on the scalp (EEG) and/or their magnetic flux, measured in a distance of a few centimeters from the head surface (MEG). The first human EEG was recorded in 1924 by Hans Berger, who published his results in 1929 [20]. Cohen measured the first MEG, alpha-rhythms of the brain, in 1968 [38]. The magnetic signal related to alpha-activity is about 10^7 times weaker than the earth's magnetic field and its measurement only became possible with the development of Superconducting QUantum Interference Devices (SQUIDS). The activity that is measured in EEG and MEG is the result of movements of ions, the so-called *impressed currents*, within activated regions in the cortex sheet of the human brain. Brazier [27] first had the idea to model an impressed current mathematically by means of a *current dipole*. The current dipole causes ohmic *return currents* to flow through the surrounding medium. The EEG measures the potential differences from the return currents at the scalp surface, whereas the MEG measures the magnetic flux of both impressed and return currents. The reconstruction of the dipole sources is called the *inverse problem* of EEG/MEG. Its solution requires the repeated simulation of the field distribution in the head for a given dipole in the brain, the so-called *forward problem*. One of the major advantages of EEG and MEG source reconstruction over the other brain imaging techniques is its high temporal resolution.

For the forward problem, the volume conductor head has to be modeled. An overview of the head tissues with different conductivities can be found in Haueisen [77; 103]. It is known that the five head tissue compartments scalp, skull, cerebro-spinal fluid, brain gray matter and white matter have different conductivities. If even a finer discrimination is needed, the scalp layer, e.g., may also be divided into the fat and the muscle compartments [103]. The human skull consists of a soft bone layer (spongiosa) enclosed by two hard bone layers (compacta). Since the spongiosa have a much higher conductivity than the compacta [3], the skull shows a direction-dependent (*anisotropic*) conductivity. A ratio of 1 to 10 has been measured radially to tangentially to the skull surface [197]. It is also known that brain white matter has an anisotropic conductivity with a ratio of about 1:9 (normal:parallel to fibers) [165; 77], but still, no direct technique exists for its robust and non-invasive measurement. However, recently, formalisms have been described for relating the effective electrical conductivity tensor of brain tissue to the effective water diffusion tensor as measured by Diffusion Tensor Magnetic Resonance Imaging (DT-MRI) [16; 223; 224].

Different numerical approaches for the forward problem have been used and the complexity of the corresponding field computations increases with the accuracy of the volume conductor description. Simple models (and still the most commonly used) describe the head by three spherical layers, representing scalp, skull and brain. In each of these layers, the conductivity is assumed to be isotropic

and homogeneous. Some spherical models can also take into account anisotropy by assigning a constant radial and tangential conductivity value to a layer, e.g., to better model the skull. Series expansion formulas can then be used to analytically compute the potential distribution in the multilayer sphere model [49; 52]. In order to better take into account the realistic shape of the scalp, the inner and the outer skull surface, Boundary Element (BE) head models were developed (see, e.g., [97; 156; 50; 269; 254; 70]), being adequate for piecewise homogeneous isotropic compartments. Finite Element (FE) head models, developed by various research groups (see, e.g., [21; 103; 228; 30; 10; 152]), are able to treat both realistic geometries and inhomogeneous and anisotropic material parameters.

A relevant question is if it is really necessary to model inhomogeneities and anisotropies and in which cases less-computationally expensive forward models give sufficient results. The influence of volume conductor inhomogeneities on EEG and MEG have been studied by various authors. It was shown that, in certain cases, holes in the skull [105; 103; 228] (e.g., patients with trepanned skull, the openings, where the optic nerve enters or the occipital hole, where the brain stem passes) and skull inhomogeneities [135; 185; 174] (e.g., the accreted sutures in adults [185]) have a non-negligible effect on EEG and MEG. Another interesting field are newborns with open sutures [83; 82]. It was also shown that it can be important to model inhomogeneities of the brain compartment such as lesions [228], since simulated fields are especially sensitive to local conductivity changes around the source [104]. With regard to skull anisotropy, van den Broek et al. [227; 228] reported a smearing effect on the EEG forward problem and Marin et al. [151; 152] showed a non-negligible impact on the EEG inverse problem for certain inverse methods of the distributed source model class. Sensitivity studies of various other inverse methods or source models towards skull anisotropy, e.g., the continuous single dipole fit, frequently used in many applications such as epilepsy and brain tumors [81; 195; 110; 237; 111; 48], have not yet been carried out, mainly because of the high computation amount. White matter conductivity anisotropy was shown to have an influence on the EEG and MEG forward problem [106], but no study exists for the sensitivity of the inverse problem towards white matter anisotropy.

An important question is thus how to handle the high computation amount of FE-modeling with regard to the inverse problem. Waberski et al. [237], e.g., conclude that for the achievement of the final goal in epilepsy source localization, i.e., the general clinical use, realistically shaped high resolution head models are necessary and parallel computing has to speed up the computation. For FE modeling, in general, iterative solvers like the Preconditioned Conjugate Gradient (PCG) method with conventional preconditioners on single processor machines have been used for solving the large linear FE equation system. The hundred or

even thousand times repeated solution of such a system with a constant geometry or stiffness matrix and varying right hand sides (the sources) is the major time consuming part within the inverse localization process. These calculation times limited the resolution of the models or, even worse, the broader application of anisotropic FE based head modeling to practical source localization problems got stuck. Geometric MultiGrid (GMG) methods have proved to be of optimal order with respect to arithmetic costs and memory requirement [91; 93], but they suffer from their need of a grid hierarchy, which is difficult to generate in our case. In contrast, Algebraic MultiGrid (AMG) methods use only single grid information (see, e.g., [196; 26; 120; 189] and for parallel implementations, [57; 128; 238; 88]) while mostly preserving the properties of the geometric version.

The solution of the inverse problem is generally not unique. Many dipole source configurations can result in the same EEG and MEG. Additional assumptions about the sources thus have to be made. As already mentioned, simple one dipole models and thus quite elementary optimization procedures for the inverse problem are often sufficient. It is therefore interesting how sensitive single dipole fit methods react to model inaccuracies. If multiple dipoles (see, e.g., [200; 161; 260; 259]) or a whole current distribution (see, e.g., [95; 191; 11; 72]) are assumed to underly the measured fields, the inverse problem remains ill-posed. The sources, underlying the Early Left Anterior Negativity component (ELAN), which is interpreted as a phase of language comprehension where the input is parsed into an initial syntactic structure [66; 65; 67], is an example of such a complicated source configuration. Small perturbations such as data noise or errors in the forward model may result in a completely different reconstruction. Regularization of multiple dipole [73; 260; 259] or current distribution modeling [95; 191; 11; 72] then gets an important tool, but how sensitive is it towards anisotropy? A further important question is if an exploitation of the high temporal resolution of EEG/MEG through a further temporal constraint for current distribution modeling [202; 203] can help in stabilizing the result.

In their review article about the future of EEG and MEG, Wikswo et al. [252] specify important future issues for EEG/MEG source reconstruction: One of them is how to gauge "the role of anisotropies in the electrical conductivity of brain tissues", a second is "how to incorporate physiological and anatomical constraints to inverse calculations", and a third is "how to treat multiple and extensive sources". As described in the following, this thesis tries to give answers to the above-posed questions.

1.2 Scope of this thesis

In this thesis, four major topics are investigated. In chapters 2 and 3, the generation of realistically shaped head models with anisotropic conducting compartments skull and brain white matter and the incorporation of physiological and anatomical constraints to the inverse problem are described, using multimodal MRI. The fast solution of the EEG/MEG forward problem using high resolution FE models of the head is considered in chapters 4 and 5. An overview of different techniques for solving the inverse problem and new algorithmic developments for multiple and extensive sources are presented in Chapter 6. Finally, the influence of tissue anisotropy is explored in the last chapter.

Chapter 2 describes image registration and segmentation methods for the generation of a multi tissue head model. The chapter focuses on an improved segmentation of human skull surfaces from bimodal MRI volumes.

Chapter 3 is dedicated to strategies for a realistic modeling of tissue conductivity anisotropy of the skull and the white matter compartment. White matter anisotropy is derived from whole-head DT-MRI.

Chapter 4 contains the description of the forward problem. The chapter begins with the physical modeling, it proceeds with FE meshing and discretization aspects for EEG and MEG, presents the various volume conductor models which are used in the following chapters and terminates with simulations on forward modeling accuracy aspects.

Chapter 5 presents efficient parallel AMG solution strategies for the large linear equation systems, arising from the FE approach. Fast solver methods are especially needed with regard to the inverse solution.

Chapter 6 gives an overview of the various inverse EEG/MEG source reconstruction methods, most of which are used in the last chapter for sensitivity considerations. A new algorithm for a regularized multi-dipole fit approach will be described and the application of efficient algorithms for the regularization of spatio-temporal current density reconstructions to source localization and dynamical electrical impedance tomography is discussed.

Chapter 7 reports on the influence of realistic tissue conductivity anisotropy on EEG/MEG source localization. The first part describes the influence on the forward problem. The second part focuses on error estimations for single dipole fits and for the reconstruction of the ELAN sources. For the latter, regularized and non-regularized dipole fit methods and various instantaneous current density reconstruction methods are used.
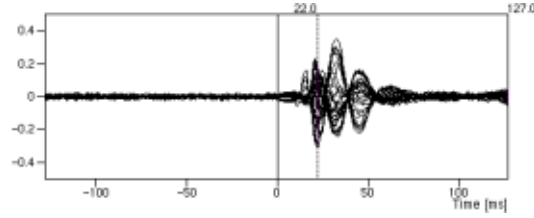
Figure 1.1: *SEP example dataset: Butterfly plot of averaged EEG data from* -0.4 *to* $0.4\,\mu V$. *The P22 signal component is marked.*

1.3   Overview of applications of source reconstruction

A short overview of well-established application fields of EEG/MEG source reconstruction is given now in order to motivate especially readers, who are not from the bioelectromagmetism area. For further applications refer to Andrä and Nowak [6].

A first example is the study of functional cortical organization by means of Event Related Potentials (ERPs) of the somatosensory system. In the following, the Somatosensory Evoked Potential (SEP) experiment of Fuchs et al. [73] is described. In this study, 31 electrodes were distributed (unevenly in order to optimize EEG sampling properties) over the right somato-sensory areas (see Fig. 1.2). Stimulation of the left medianus nerve was done by means of an electric wrist stimulator with an intensity of twice the motor threshold. The different evoked signal components of interest in such studies appear during the first 100 ms poststimulus. EEG signals were therefore sampled over periods of 128 ms pre- and 128 ms post-stimulus with a sampling rate of 1 kHz. Since the components are well time-locked and not dependent on the attention of the subjects, the signal can be averaged over a large number of trials so that the signal components of interest are obtained with a relatively good Signal-to-Noise Ratio (SNR). In the study of Fuchs et al. [73], four replications of 1000 epochs each were averaged for SNR improvement. Figure 1.1 shows the resulting averaged EEG measurements for the SEP in 31 channel butterfly plot from this study, included as an example dataset in the software package CURRY (see Appendix D). As an example for a medically interesting source reconstruction result, the continuous dipole fit method, introduced by Scherg and von Cramon [200], with two dipoles at the peak of the SEP-P22 signal component ("P" stands for Positivity and "22" for an average peak latency of 22 ms after stimulus) is shown in Fig. 1.2. The result has been calculated using the example dataset and methods within CURRY.

The non-invasive EEG/MEG-source reconstruction diagnosis method is suc-
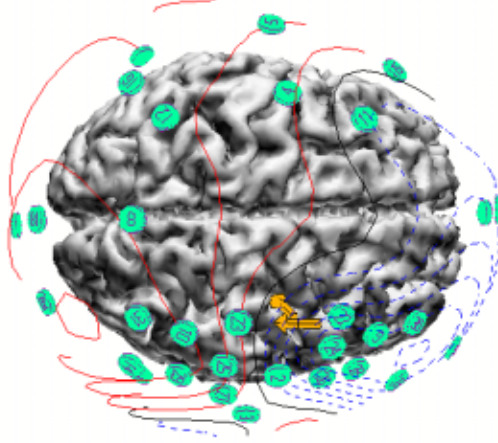
Figure 1.2: *SEP source reconstruction example: Results of the continuous dipole fit method with two dipoles at the peak of the P22 signal component.*

cessfully used in clinical research and application. For instance tumors may distort brain anatomy so that the presurgical localization of sensory or motor areas on the basis of anatomical landmarks is impossible. In Sutherling et al. [221], the agreement between invasive and non-invasive methods was evaluated and an "excellent precision of the source reconstruction results" was found. About 0.25 % of the world population suffers from drug-resistant epilepsy and about 10 to 15 % would profit from a surgical removal of the epileptogenic tissue [6]. As opposed to alternative invasive diagnostic procedures, i.e., opening the skull and implanting electrodes near the assumed focus (ECoG surface electrodes or depth electrodes) which put the patient under a considerable risk and is cost intensive, source localization procedures are non-invasive and can give a more "global" overview since the sensors can be placed around the whole head. Waberski et al. [237], e.g., found a high congruence of source reconstruction and invasive determination of the focus of epileptiform activity using realistically shaped head models.

Source reconstruction methods have also been introduced to characterize the generators of signals related to higher cognitive function. An example is a recent study of Maess et al. [149] showing equivalences between speech and music processing in the brain. Further examples are the studies of Knösche et al. [124] and Friederici et al. [68] for the reconstruction of the ELAN sources.

Chapter 2

Registration and segmentation of MRI

2.1 Introduction

A prerequisite for a realistic representation of the volume conductor is the segmentation of head tissues with different conductivity properties.

The exact modeling of the low conducting human skull is of special importance for EEG/MEG source reconstruction. The skull can be seen as an isolating layer which leads to a strong decrease and a blurring of the potential distribution towards the measurement EEG electrodes [42; 43]. For MEG, the modeling of the small currents in the skull layer (and also skin layer) are often considered to be negligible in a non-pathological case, i.e. no surgery hole in the skull. However, a correct segmentation of the boundary between intracranial tissues and skull (inner skull surface) is still important, since superficial sources imply strong return currents close to that border which contribute to MEG [96]. Strong localization improvements were reported when using realistically shaped head models compared with spherical analytical approximations [43; 194]. An average error of about 2cm and a maximal error of up to 4cm appeared in frontal and temporal areas, where the skull is least spherical.

MRI is known as a safe and non-invasive method for imaging the human head. Because of high contrasts, T1-weighted MRI (T1-MRI) is well suited for the segmentation of tissue boundaries like white and gray matter, outer skull and skin. In contrast, the identification of the inner skull surface is problematic. Realistic head models, which exploit exclusively a T1-MRI, use a segmentation estimation procedure for this surface where mainly the T1 segmented brain is closed and inflated [243; 107; 239]. It is assumed for the convex parts of the brain, that this estimation is close to the inner skull, but it is also known, that the deviations in

9

the skull base areas are larger. Nevertheless, the estimation procedure based on an exclusive use of a T1-MRI modality can be seen as the current standard for modeling the inner skull surface in the field of EEG/MEG source localization. Another interesting estimation approach was presented by Rifai et al. [193]. A deformable model, propagating by means of a level set method and thus allowing topology changes, was used in order to estimate the interface between the cerebro-spinal fluid and the skull in a T1-MRI, taking the partial volume effect into account.

Accurate EEG based localization of especially basal frontal and mesial temporal current sources in the human brain are of high importance in epilepsy surgery. Huiskamp et al. [111] reported EEG localization errors of about 1cm for those areas. The errors were due to the limited modeling accuracy of the inner skull by means of the T1-MRI based closing and inflation procedure when compared to skull models from matched sets of Computed Tomography (CT) and T1-MRI. It was concluded that this imprecision may be detrimental in clinical applications. Furthermore, for pathological cases causing brain atrophy, the estimation of the cerebro-spinal fluid layer thickness by means of a global inflation parameter in the estimation procedure can locally be far from realistic, so that the need for a second image modality arises.

CT is of course best suited for imaging bone tissues as the human skull. A registration of a CT and a T1-MRI [220] enables an exact modeling of the skull. Nevertheless, in neurological or neuro-psychological brain research, large numbers of healthy subjects often take part in statistical experiments and their exposure to ionized radiation is not appropriate. Furthermore, most often a T1-MRI has to be measured additionally to a CT (e.g., for the segmentation of the brain surface), an amount of work, which should not be underestimated, so that the choice of a CT/T1-MRI multimodal approach has to be ruled out for many applications.

Within this chapter, algorithms for the registration and the segmentation of bimodal MR data sets will be presented in order to generate a multi-compartment model of the head. In order to simplify denotation, we will now introduce the abbreviations ISS (Inner Skull Surface), EISS (Estimated Inner Skull Surface from T1-MRI closing and inflation of the brain), OSS (Outer Skull Surface), Cerebro-Spinal Fluid (CSF), WM (White Matter) and GM (Gray Matter). Since the difference in the quantity of water protons between intracranial and bone-tissues is large, a Proton Density MRI (PD-MRI) sequence is well suited as a second modality for the ISS segmentation. The PD modality can be measured in the same session as the T1 image, only the protocol has to be adapted, so that the additional amount of work is in reasonable limits. After the basic definitions and operations on images and meshes and the acquisition of the T1- and the PD-MRI,

described in Sections 2.2 and 2.3, resp., the PD-MRI is registered onto the corresponding T1 image in Section 2.4 in order to correct for movement of the subject and geometrical distortions. The registered PD image enables the segmentation of the ISS. The methodological segmentation part in Section 2.5 is divided into the description of the main segmentation components, whose algorithms are shortly presented as pseudo-codes. A fuzzy segmentation algorithm which compensates for image intensity inhomogeneities, and an extended region growing approach are the main components for the generation of an initial guess for a surface which has to be segmented, followed by an algorithm for segmentation improvement by means of a deformable model. The segmentation scripts will then be presented in Section 2.6, i.e., processing chains which consist of a concatenation of the segmentation components in order to achieve the final segmentation results for the multiple head compartment surfaces. In Section 2.6.2, the accuracy improvement for the segmentation of the cortex compartment and in Section 2.6.3, the ISS segmentation and its comparison with the EISS are presented, two central results of this chapter.

2.2 Basic definitions and operations

This section briefly introduces the basic definitions and operations on images and meshes. Refer, e.g., to the book of Lohmann [140] for a more detailed description.

2.2.1 Definitions of images and meshes

A three dimensional image is composed of a stack of two-dimensional *slices*, which are indexed from top (slice 0) to bottom (the orientations are already given with respect to the measured object, i.e., the human head). Each two dimensional slice is discretized into *rows* (front to back) and *columns* (left to right), resulting in the *image lattice*

$$L = \{(s,r,c) \in \mathbb{N}_0^3 | (0 \le s < nslices), (0 \le r < nrows), (0 \le c < ncolumns)\} \,.$$

A *feature space G* represents the set of values of an *image intensity function* $I : L \to G$. The feature space is restricted here to the one-dimensional case, so that each *image lattice address* (s,r,c) is assigned a one-dimensional intensity $I(s,r,c)$. Cartesian coordinates $\mathbf{x}_{(s,r,c)} \in \mathbb{R}^3$ of the lattice address (s,r,c) are calculated by multiplying each component with its discretization size, denoted by *ssize* $\in \mathbb{R}$, *rsize* $\in \mathbb{R}$ and *csize* $\in \mathbb{R}$. A cubic volume element with barycentre $\mathbf{x}_{(s,r,c)}$, cubic edge lengths *ssize*, *rsize* and *csize* and the constant intensity $I(s,r,c)$

throughout its volume will be called a *voxel*. We denote the number of voxels with N_x, i.e., $N_x = nslices \cdot nrows \cdot ncolumns$. In order to simplify indices, a voxel is identified with its image lattice address, so that denotations like $\mathbf{x} \in L$, $\mathbf{x} = (s, r, c)$ and $I(\mathbf{x}) := I(s, r, c)$ are used.

Together with the above explanations, the following definition will now be made:

Definition 2.2.1. *A "general 3D image" $GI = (L, G, I)$ consists of the image lattice $L \subseteq \mathbb{N}_0^3$, a feature space $G \subseteq \mathbb{R}$, also called "gray code" and an intensity function $I : L \rightarrow G$. The set of all 3D images GI will be denoted by $\mathcal{GI}$.*

An image, resulting from a restriction to the set of integer gray codes $G = G_{MRI} = \{i | i = 0, \ldots, 255\}$ will be denoted by MRI with the corresponding class $\mathcal{MRI}$. "Black" and "white" are used for the gray codes 0 and 255, respectively, while the intermediate values represent various shades of gray. An image, resulting from a restriction to the triplet $(L, G_{0,1}, I)$ with the set of boolean gray codes $G_{0,1} = \{i | i = 0, 1\}$ will be called a "binary image" or a "binary mask" and will be denoted by BI with the corresponding class $\mathcal{BI}$. A voxel $\mathbf{x}$ with intensity $I(\mathbf{x}) = 0$ will be called a "background" or "black" voxel and with intensity $I(\mathbf{x}) = 1$ a "foreground" or "white" voxel. An image, resulting from a restriction to the triplet $(L, G_{\mathbb{N}_0}, I)$ with $G_{\mathbb{N}_0} = \{i | i \in \mathbb{N}_0\}$ will be called a "positive integer image" PI with the corresponding class $\mathcal{PI}$. An image, resulting from a restriction to the triplet (L, G_C, I) with $G_C = \{i | i = 0, \ldots, C-1\}$ will be called a "C-class positive integer image" CPI with the corresponding class $\mathcal{CPI}$.

Definition 2.2.2. *The* image histogram $h_{MRI} : G_{MRI} \rightarrow G_{N_x^0}$ *with* $G_{N_x^0} = \{i | i = 0, \ldots, N_x\}$ *counts the occurrence of each gray code in* $MRI \in \mathcal{MRI}$, *i.e.,* $h_{MRI}(g) = | \{\mathbf{x} | \mathbf{x} \in L \wedge I(\mathbf{x}) = g\} |$. *A* 2D histogram $h_{MRI_1, MRI_2} : G_{MRI} \times G_{MRI} \rightarrow G_{N_x^0}$ *for* $MRI_1, MRI_2 \in \mathcal{MRI}$ *with intensity functions* I_1 *and* I_2, *resp., is defined through*

$$h_{MRI_1, MRI_2}(g_1, g_2) = | \{\mathbf{x} \mid \mathbf{x} \in L \wedge I_1(\mathbf{x}) = g_1 \wedge I_2(\mathbf{x}) = g_2\} | .$$

In the following, cuts through a 3D image with fixed value for *s* will be called *axial*, cuts with fixed value for *r coronal* and with fixed value for *c sagittal*. Some basic definitions about neighborhood, adjacency and connectivity in an image lattice *L* have to be made, formulated in

Definition 2.2.3. *The set of the 6 neighbors of a voxel $\mathbf{x}$ in the 3D image lattice L, differing (by one) in at most one coordinate is called the* 6-neighborhood, *the set of those, differing in at most two coordinates is called the* 18-neighborhood *and the set of voxels with at most three different coordinates is called the* 26-neighborhood.

Two voxels are said to be n-adjacent, *iff both are n-neighbors of one another.*

6-neighborhood	18-neighborhood	26-neighborhood
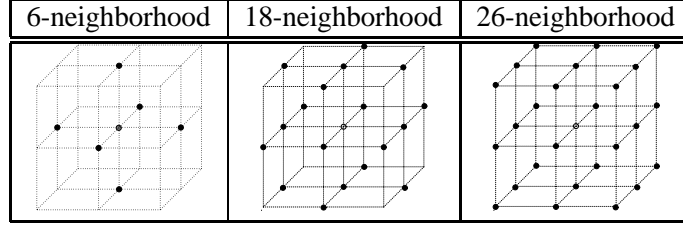
Figure 2.1: *Neighborhoods in 3D from Lohmann [140].*

A set of voxels is called n-connected *if for any two of them, a sequence of voxels* $(\mathbf{x}_{i_1}, \ldots, \mathbf{x}_{i_k})$ *can be found that are pairwise (i.e.,* $(\mathbf{x}_{i_j}, \mathbf{x}_{i_{j+1}})$, $\forall j = \{1, \ldots, k\}$) *n-adjacent.*

Figure 2.1 shows the three different neighborhoods in a 3D image lattice.

The gray code of a voxel did not play a role in the above definition. In order to make sure for $BI \in BI$, that a closed m-connected surface of foreground voxels completely encloses a k-connected background component and thus divides the background into two k-connected components (the one interior to the closed foreground surface and the one exterior to it, see Figure 2.2, middle, as an illustration in 2D), the restriction to the (m,k) pairs $(26,6)$, $(6,26)$, $(18,6)$ and $(6,18)$ has to be made [140].

In the following, $(m,k) = (26,6)$ will be used for all $BI \in BI$:

Definition 2.2.4. *For $BI \in BI$, two foreground voxels are called* adjacent *if they are 26-adjacent and two background voxels are called* adjacent *if they are 6-adjacent. A set of foreground voxels is called* connected *if it is 26-connected and a set of background voxels is called* connected *if it is 6-connected.*

Definition 2.2.5. *For $BI \in BI$, a foreground voxel is called* border voxel*, iff at least one of its 6-neighbors is a background voxel.*

The Euler number is an important measure for several topological characteristics [140], so that it will be defined in

Definition 2.2.6. *The Euler number of a binary object $IN \in BI$ is defined as the number of connected components plus the number of cavities, i.e., totally enclosed components of the background, minus the number of handles (imagine a handle of a tea-cub).*

A binary object is *topologically equivalent to a sphere*, if it has the Euler number 1. The following definition completes the basic nomenclature for 3D images, defined on a regular lattice:

Definition 2.2.7. *Two markers, STOP and PASS, for an MRI $\in MRI$ are introduced, offering a possibility to influence image segmentation independently of the image intensity. Each marker can be seen as a binary image, defined on the image lattice of its corresponding MRI, so that each lattice point $\mathbf{x}$ of the "extended"image MRI_{ext} has three attributes, a gray value $I(\mathbf{x})$ and a binary value (0 for "not set"or deleted and 1 for "set") for each of its two markers $STOP(\mathbf{x})$ and $PASS(\mathbf{x})$. For each $\mathbf{x}$, the setting of one of the markers is automatically followed by the deletion of the other, i.e., the combination $STOP(\mathbf{x}) = PASS(\mathbf{x}) = 1$ is impossible. The class of extended images MRI_{ext} will be denoted by MRI_{ext}*

The rest of this subsection is concerned with structures for geometrical models on irregular grids. A geometrical model is composed of a tuple $(\mathbf{v}, \Delta)$ of *vertices* $\mathbf{v}$ and *primitives* Δ. To make an example, such a model could be a triangulated surface in 3D, i.e. a 2D manifold with $\mathbf{v}_i$ the 3D Cartesian coordinates of the triangle node i and Δ_i the description of the ith triangle by means of its three node points $\mathbf{v}_{i_1}$, $\mathbf{v}_{i_2}$ and $\mathbf{v}_{i_3}$.

Definition 2.2.8. *A mesh $= \{(\mathbf{v}_i, \Delta_j), i = 1, \ldots, N_v, j = 1, \ldots, N_p\}$ consists of a list of N_v vertices $\mathbf{v}_i \in \mathbb{R}^3$ and a list of N_p primitives $\Delta_j \in \Delta$, where each primitive consists of a subset of vertices of the mesh, i.e., $\Delta = \{\mathbf{v}_{i_k} | k = 1, \ldots \Delta_v\}$. The number of vertices Δ_v, a primitive is consisting of, depends on its type. A triangle comprises $\Delta_v = 3$, a tetrahedron $\Delta_v = 4$ and a cube $\Delta_v = 8$ vertices. The class of all meshes will be denoted by $MESH$.*

Definition 2.2.9. *The Euler characteristic of a triang. mesh is defined as the number of vertices N_v plus the number of faces N_p minus the number of edges N_e.*

A triangulated mesh is *topologically equivalent to a sphere*, if it has the Euler number 2 [2].

2.2.2   Operations on images and meshes

Operations on 3D images

Within this subsection, those basic operations on 3D images will be presented by definitions and short explanations which are frequently used later in this chapter. Refer to [140] for a more detailed description. The first simple operation is

Operation 2.2.10. *By means of*

$$OUT = AND(IN1, IN2),$$

each voxel of $IN1 \in GI$ will be taken over to $OUT \in GI$, if it is a foreground voxel in $IN2 \in BI$. By means of

$$OUT = OR(IN1, IN2),$$

each voxel of IN1 ∈ GI will be taken over to OUT ∈ GI, if its intensity is not equal to 0 or if it is a foreground voxel in IN2 ∈ BI.

If *IN*1 is restricted to a binary mask, the operation *AND* (*OR*) leads to a binary mask *OUT* which is the minimum (maximum) of both input masks.
Remember Definition 2.2.5 for the following operation:

Operation 2.2.11. *By means of*

$$OUT = BORDER(IN),$$

border voxels of IN ∈ BI are detected and written out as the new foreground of OUT ∈ BI.

Within the algorithm, which realizes the above operation, background voxels will be searched in the 6-neighborhood of each foreground voxel of *IN*. As soon as at least one is found, the examined foreground voxel is successfully detected as a border voxel.

Operation 2.2.12. *By means of*

$$OUT = LABEL(IN),$$

connected foreground components of IN ∈ BI are detected and labeled in order. The result is written to OUT ∈ PI. The operation

$$OUT = SELBIG(IN)$$

selects the connected component with the most frequent label value of IN ∈ PI. All voxels of that component become foreground voxels in OUT ∈ BI. The combination

$$OUT = BIGGESTCOMP(IN) := SELBIG(LABEL(IN))$$

finds a biggest connected component in IN ∈ BI.

The labeling algorithm begins by selecting an arbitrary foreground voxel and assigns the label "1"to it. It then propagates this label recursively to all adjacent foreground voxels, until no more foreground voxel connected to any already labeled one can be found. The algorithm then tries to find a further foreground voxel, which has still not been labeled and starts a second round with label "2". The procedure is stopped when all foreground voxels have been labeled [140].
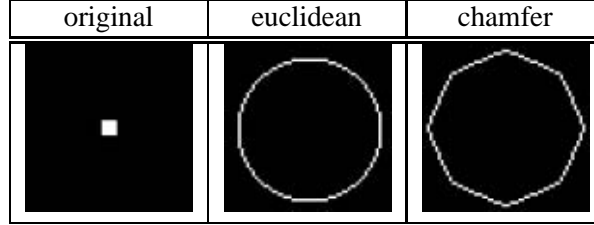
Figure 2.2: *Original binary mask (left), iso-euclidian distance points (middle) and iso-chamfer distance points (right).*

Operation 2.2.13. *The distance transform $OUT = DIST(IN)$ on $IN \in BI$ with $OUT \in FI$ attaches a label to each background voxel which encodes the shortest distance towards the closest foreground voxel. The distance within DIST is measured by an euclidian metric, whereas the distance transform DIST_CHAM uses a chamfer metric.*

The operation *DIST_CHAM* can be seen as a fast method to approximate *DIST*. To illustrate the difference: If a binary mask with only one foreground voxel in the middle of the mask will be transformed, iso-euclidian distance points are arranged as a circle and iso-chamfer distance points as a hexagon around this foreground voxel, see Figure 2.2 [140].

Operation 2.2.14. *The operation $OUT = BINARIZE(IN, min, max)$ thresholds $IN \in GI$ to produce $OUT \in BI$. The parameter min specifies the minimal and the parameter max the maximal foreground value.*

In Figure 2.2, all foreground voxels in the middle and the right figure have a distance of 25 to the original foreground voxel, realized by choosing minimal and maximal foreground value as 25.

Operation 2.2.15. *The operation $OUT = INVERT(IN)$ inverts $IN \in BI$ so that foreground voxels in IN become background voxels in $OUT \in BI$ and vice versa.*

Based on the last three basic operations, the following morphological basis operations can be derived:

Operation 2.2.16. *The operation $OUT = DILATION(IN, rad)$ with $IN, OUT \in BI$ will be defined by thresholding a distance transform, i.e.*

$$DILATION(IN, rad) := BINARIZE(DIST(IN), 0, rad).$$

The operation $OUT = EROSION(IN, rad)$ with $IN, OUT \in BI$ will be defined by

$$EROSION(IN, rad) := BINARIZE(DIST(INVERT(IN)), rad, \infty)).$$

original surface	surface after opening	surface after closing
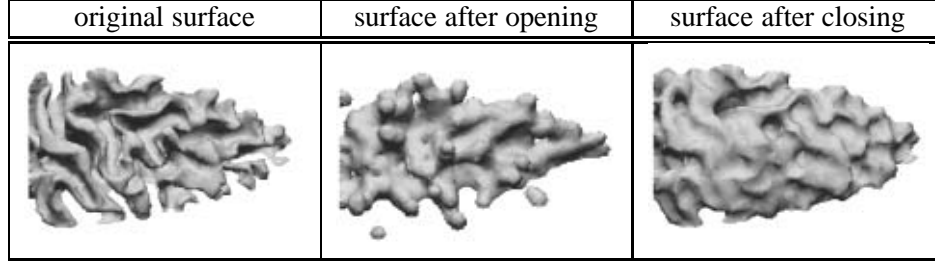
Figure 2.3: *Visualization of two morphological operations from Lohmann [140].*

It should be mentioned that the operations *DILATION* and *EROSION* are basically defined in mathematical morphology and that, in fact, they are only simulated by the above operations. Nevertheless, if a distance transform with an euclidian metric is used, the result of the above procedures will be the same as a morphological filtering with a sphere-shaped structuring element of radius *rad* [140].

By means of these two morphological basis operations, we can further define

Operation 2.2.17. *The operation $OUT = OPENING(IN, rad)$ with $IN, OUT \in BI$ will be defined by*

$$OPENING(IN, rad) := DILATION(EROSION(IN, rad), rad).$$

The operation $OUT = CLOSING(IN, rad)$ with $IN, OUT \in BI$ will be defined by

$$CLOSING(IN, rad) := EROSION(DILATION(IN, rad), rad).$$

The operation $OUT = SMOOTHING(IN, rad)$ with $IN, OUT \in BI$ will be defined by

$$SMOOTHING(IN, rad) := OPENING(CLOSING(IN, rad), rad).$$

Figure 2.3 illustrates the effect of opening and closing on a brain WM surface. Thin gyri disappear during opening. The closing operator fills the sulci but does not cause the gyri to rise.

Two image filters will now be introduced. The first is the well-known operation, which convolves an image with a Gauss filter with standard deviation σ [113]:

Operation 2.2.18. *The operation $OUT = GAUSS(IN, \sigma)$ applies a Gauss-filter with standard deviation σ to the image $IN \in MRI$ in order to produce a smoothed and noise-reduced $OUT \in MRI$.*

The Gauss-filter also smoothes the edges of an image, which is not wanted for certain applications. Lee filters, also called sigma filters [138], replace each voxel with the mean value of its surrounding window, where the mean is taken only from the neighboring voxels whose intensities do not differ by more than a σ threshold from the value of the current voxel.

Operation 2.2.19. *The operation $OUT = LEE(IN, \sigma)$ applies a sigma filter with a σ threshold to the image $IN \in \mathcal{MRI}$ and produces an edge-preserved smoothed and noise-reduced $OUT \in \mathcal{MRI}$.*

In Chapter 3, the following operation is needed for modifying the intensity values of an MRI:

Operation 2.2.20. *The operation*

$$MRI_{mod} = MODINT(MRI, BI, I^{new})$$

sets the intensity values of all those lattice points of the image $MRI \in \mathcal{MRI}$ to the new intensity value $I^{new} \in G_{MRI}$, which are foreground in the binary mask $BI \in \mathcal{BI}$.

The last two operations are concerned with the image markers.

Operation 2.2.21. *The operation*

$$MRI_{ext} = INTRODUCE\_MARKERS(MRI)$$

extends MRI, i.e., copies the intensity for each lattice point and defines its markers as "not set".

Operation 2.2.22. *By means of the operation*

$$MRI_{ext} = MARK(MRI_{ext}, BI, marker),$$

the marker $= STOP, PASS$ of all those lattice points of the extended image $MRI_{ext} \in \mathcal{MRI}_{ext}$ will be set, which are foreground in the binary mask $BI \in \mathcal{BI}$.

Mesh operations

The later introduced deformable models use mesh representations of surfaces which are defined as iso-surfaces in digitized volumetric data. It will be focussed here on the extraction of a border of a binary mask in form of a mesh consisting of triangle elements (see Def.2.2.8). The *marching tetrahedra algorithm* [179] is
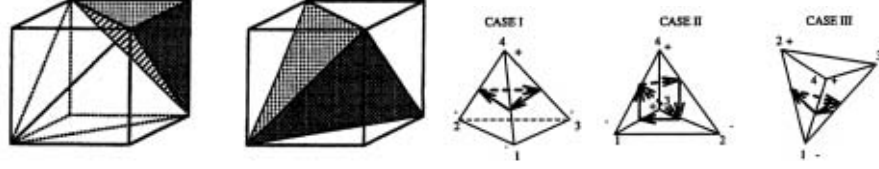
Figure 2.4: *The two cases for a decomposition of an 8-cell into 5 tetrahedra (two figures left) and the three cases for the intersection scenarios (three figures right)*

now presented as such an extraction method resulting in a closed and oriented triangular surface mesh, i.e., the vertices of each triangle are ordered so that, viewed from the outside, the vertex-cycle is traversed in counterclockwise ordering.

The starting point within the algorithm is a decomposition of each so-called 8-cell (or cube) into 5 tetrahedra, where the vertices of the cube are the addresses of 8 neighbored voxels in the image lattice. Two such decompositions are possible and it must be alternated in a 3D checkerboard fashion between both of them so that faces and edges of 8-cell tetrahedra match those of neighboring ones (see Figure 2.4). The second step in the algorithm is an identification of those tetrahedra with vertices $\mathbf{v}_{i_1}, \mathbf{v}_{i_2}, \mathbf{v}_{i_3}, \mathbf{v}_{i_4}$, intersecting with the iso-surface of the binary mask. This is controlled by means of a sign-change of $I(\mathbf{v}_{i_k}) - I_0$ with $I_0 \in]0, 1[$. The intersection points along the edges of a tetrahedron and thus the vertices of the resulting triangle mesh, are dependent on the used interpolation basis function. Gueziec and Hummel [85] proposed a bilinear basis function on an 8-cell, since a linear led to an excessive spikeness of the resulting triangle surface mesh. The bilinear basis function reduces to a linear along the edges of an 8-cell and to a quadratic along 8-cell diagonals. Triangle vertices are calculated as the zero-crossings of the interpolation function within a tetrahedron. Three different intersection scenarios have to be distinguished, one of them results in two triangles for the surface mesh, the other two in one (see Figure 2.4). During the above process, the first surface triangle will be assigned a correct orientation by appropriately ordering its vertices. Since any given edge of the mesh has to be traversed in opposite directions by the vertex-cycles from the two neighboring triangles, the correct orientation of the surface mesh can then be ensured by a recursive procedure. The above explanations led to

Operation 2.2.23. *The operation $OUT = EXTRACT(IN)$ extracts the border of $IN \in BI$ as a closed and well-oriented triangulated surface mesh $OUT \in MESH$ by means of the marching tetrahedra method.*

The extracted mesh generally consists of a large number of triangles. In order

$N_v = 50,000$	$N_v = 15,000$	$N_v = 5,000$
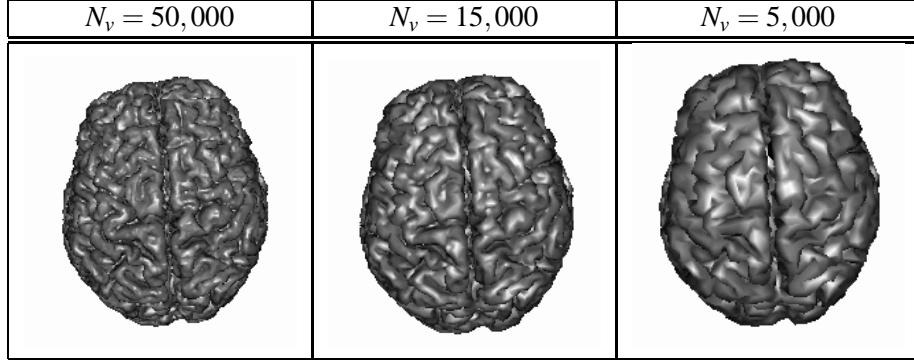
Figure 2.5: *Result of Operation 2.2.24 on a mesh, extracted from a brain mask for different settings of N_v.*

to remove badly shaped ones and to coarsen the mesh in regions of small curvature, a mesh simplification follows the extraction. In Gueziec and Hummel [85], each edge $(\mathbf{v}_{i_1}, \mathbf{v}_{i_2})$ goes through a deletion test and if the tests are positive, it will be replaced by $\mathbf{v} = (\mathbf{v}_{i_1} + \mathbf{v}_{i_2})/2$, i.e., former edges to $\mathbf{v}_{i_1}$ and $\mathbf{v}_{i_2}$ will be replaced by edges to $\mathbf{v}$ and two triangles are removed. If $\mathbf{v}_{i_3}$ and $\mathbf{v}_{i_4}$ denote the remaining vertices of the two triangles which contain the edge $(\mathbf{v}_{i_1}, \mathbf{v}_{i_2})$, the first demand is, that the distance between $\mathbf{v}_{i_1}$ and $\mathbf{v}_{i_2}$ is smaller than the distance between $\mathbf{v}_{i_3}$ and $\mathbf{v}_{i_4}$. A second prerequisite is a limit for the projection distance of $\mathbf{v}_{i_1}$ and $\mathbf{v}_{i_2}$ on the resulting surface after the deletion.

Operation 2.2.24. *The operation $OUT = SIMPLIFY(IN, N_v)$ with $IN, OUT \in MESH$ simplifies an extracted mesh to N_v vertices by a coarsening in regions of small curvature and by removing badly shaped triangles.*

Figure 2.5 shows the result of Operation 2.2.24 on a mesh with $750,000$ vertices, extracted from a brain mask for different settings of N_v. It can be seen, that 5.000 vertices are no longer sufficient to correctly represent the neocortical surface.

Later in this chapter, the transformation of a triangle mesh into a binary image is needed. The following operation deals with this problem:

Operation 2.2.25. *By means of $mask = VOXELIZE(mesh)$ with $mesh \in MESH$ consisting of triangle primitives ($\Delta_v = 3$), a triangle mesh is transformed into a binary image $mask \in BI$. Therefore, each voxel of mask becomes a foreground voxel, if the distance of its lattice point projection onto the closest triangle primitive is smaller than $\sqrt{3}/2$.*

Operation 2.2.25 yields a mask, which has to be filled in certain situations. The filling process is described in Script 2.2.26 and illustrated in Figure 2.6. In the

cont	*dilated_cont_to_bg*	*eroded_bg*	*mask*
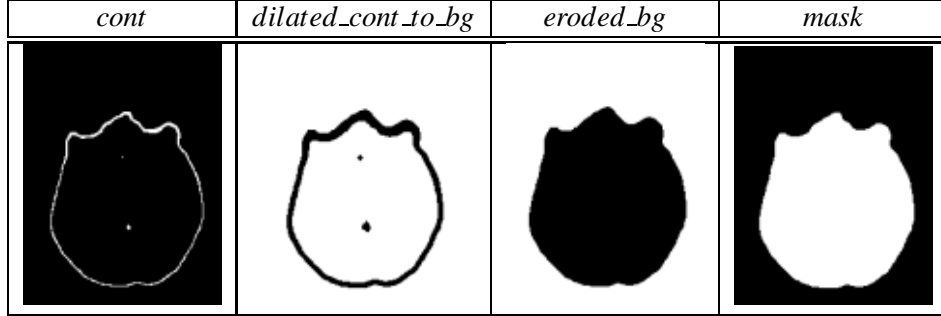
Figure 2.6: *Example for Script 2.2.26: Filling the ISS mesh.*

second step of the script, the contour of the transformed mesh is dilated as the background component with the parameter *d*, so that the biggest connected component of the resulting mask is the *d* eroded image background. The dilation is then canceled by a *d* erosion and the filled *mask* is achieved.

2.3 Data acquisition

MR imaging of a healthy 32 year old male subject was performed on a 3 Tesla whole-body scanner (Medspec 30/100, Bruker, Ettlingen/Germany). The 3D PD-MRI was acquired using a 3D FLASH protocol with *TE*=6ms (see Appendix A.4), a flip angle of $25°$ and *TR*=11.7ms (A.7). For the T1-MRI, measured in another session about a week before, an inversion recovery MDEFT sequence [137] was employed (flip angle of $25°$, *TR*=11.7ms, *TE*=6ms, $T_{MD} = 1.3$s). The readout gradient was parallel to the z-axis (superior to inferior) and had a strength of 4.3 mT/m. The resolution was $1 \times 1 \times 1.5$ mm^3 in both acquisitions. Both images were linearly interpolated to image cubes with *nslices* = 249, *nrows* = 249

Script 2.2.26. **FILL** : $(mesh \in MESH, d \in \mathbb{R}) \rightarrow (mask \in BI)$:

1. $cont = VOXELIZE(mesh)$

2. $dilated\_cond\_to\_bg = BINARIZE(DIST(cont), d, \infty)$

3. $eroded\_bg = BIGGESTCOMP(dilated\_cond\_to\_bg)$

4. $mask = INVERT(BINARIZE(DIST(eroded\_bg), 0, d)))$

T1-MRI	PD-MRI
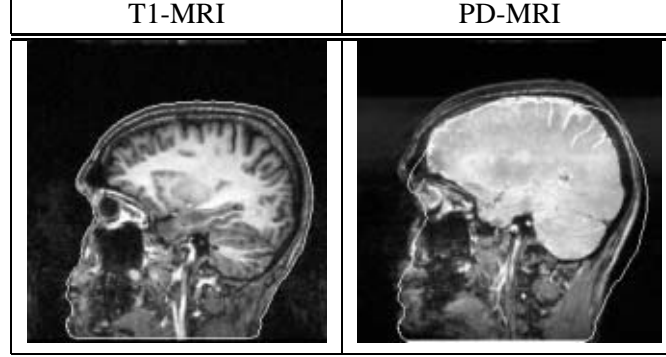
Figure 2.7: *T1-weighted MRI (left) and non-registered PD-weighted MRI (right). The outer surface of the head was extracted from the T1 image and visualized on both data sets.*

and *ncolumns* = 192. A voxel is described by *ssize = rsize = csize* = 1. Figures 2.7 (sagittal slice) and 2.8 (axial slice) show the resulting bimodal MR data set. The spatial deformation between both image acquisition sessions is visualized by means of the head mask, extracted from the T1-MRI and visualized on both T1- and PD-MRI. In order to exploit both image modalities, it is thus necessary to register the images.

2.4   Registration

The registration of a bimodal data set is a fundamental step in order to exploit the information in both images in the segmentation process (see Figures 2.7 and 2.8). Three different classes of registration algorithms are distinguished in the literature, the *point landmark based*, the *surface based* and the *voxel based* methods (see e.g., [75; 214; 148]). The result of point landmark based methods [75] depends strongly on the spatial accuracy of the marker fixation in both modalities and its accuracy is thus quite limited. Algorithms from the second class register by means of corresponding surfaces [214], which first have to be extracted from both image modalities. Surface segmentation is known to be highly dependent on the quality of the data and often are hard to achieve. Therefore, we focus our interest on a voxel-similarity based linear registration algorithm without pre-segmentation, which will be presented within this section. The approach is inspired by [40; 148; 249], using mutual information as a voxel-based similarity criterion between the T1 and the PD image.

T1-MRI	T1 histogram	PD-MRI	PD histogram
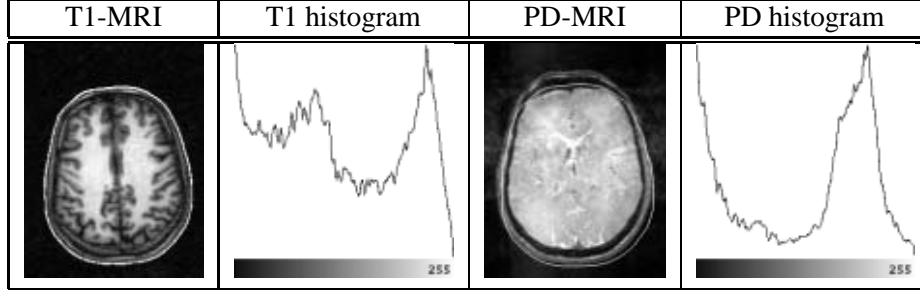
Figure 2.8: *T1-weighted MRI (left), its histogram h_{T1} (left, middle) and non-registered PD-weighted MRI (right, middle) and its histogram h_{PD} (right). The outer surface of the head was extracted from the T1 image and visualized on both data sets.*

2.4.1 Transformation

For our purposes, the human head may be assumed as a rigid body, so that the mapping is described by a concatenation of a 3D rotation matrix

$$\mathbf{R}(\phi_x, \phi_y, \phi_z) = \mathbf{R}_z(\phi_z) \cdot \mathbf{R}_y(\phi_y) \cdot \mathbf{R}_x(\phi_x) \in \mathbb{R}^{3 \times 3}$$

with $\mathbf{R}_x \in \mathbb{R}^{3 \times 3}$, $\mathbf{R}_y \in \mathbb{R}^{3 \times 3}$ and $\mathbf{R}_z \in \mathbb{R}^{3 \times 3}$ the rotations around x-, y- and z- axis and a 3D rotation vector $\mathbf{r} := (\phi_x, \phi_y, \phi_z) \in \mathbb{R}^3$ with rotation angles ϕ_x, ϕ_y and ϕ_z (in degrees) and a 3D translation vector $\mathbf{t} := (t_x, t_y, t_z) \in \mathbb{R}^3$ with distances t_x, t_y and t_z (in millimeters). Such a rigid-body transformation is able to correct for movement of the subject between the image acquisition sessions. Nevertheless, static field inhomogeneity in MRI produces geometrical distortions, which restrict the applicability of a rigid transformation. De Munck et al. [51] presented a method to compute the distortions, caused by the difference in magnetic susceptibility between the head and the surrounding air. Using the presented method, the displacement vector field of the head surface was computed. It was demonstrated that the MRI distortions can be as large as 3 mm for points just outside the head and, more important for our following assumption, it was observed that within the head, the distortion can be described accurately by means of a linear scaling. We thus include three scaling parameters s_x, s_y and s_z for a modeling of a linear distortion between T1 and PD image, so that the transformation is uniquely characterized by means of the parameter vector

$$\underline{P} = (t_x, t_y, t_z, \phi_x, \phi_y, \phi_z, s_x, s_y, s_z) \in \mathbb{R}^9.$$

The transformation of a floating image lattice point $\mathbf{x}_{\text{float}}$ is thus given by

$$T_{\underline{P}}(\mathbf{x}_{\text{float}}) = \mathbf{R} \cdot \mathbf{diag}(s_x, s_y, s_z) \cdot (\mathbf{x}_{\text{float}} - \mathbf{c}_{\text{float}}) + \mathbf{t} + \mathbf{c}_{\text{dest}} \qquad (2.1)$$

with $\mathbf{c}_{\text{float}}$ and $\mathbf{c}_{\text{dest}}$ the image coordinates of the centers of the floating and destination image, resp., and $\mathbf{diag}(s_x, s_y, s_z)$ the diagonal matrix with scaling factors. The PD image is mostly registered onto the T1-MRI, because often, the former has a coarser resolution and the latter features more detail and is already prealigned with some reference system, such as the stereotactical coordinate system [129]. The PD- is thus the floating and the T1- the destination image during the determination phase of the transformation parameters $\underline{P}$.

2.4.2   The Mutual Information

The basic theory of mutual information will now be summarized, which is used to measure the adaption of the T1- and the transformed PD-MRI. The description closely follows [40; 148; 249].

Let h_{T1} and h_{PD} be the histograms of the T1- and the PD-MRI, resp. (see Definition 2.2.2 and Figure 2.8 as an example), $h_{T1,PD}$ their two-dimensional joint histogram and let g be a specific intensity value. Please refer to the end of this subsection for more informations about the calculation of the joint histogram. With X_{T1} and X_{PD}, random variables are denoted which are associated to the intensity values in the images. The marginal probability distributions of these random variables are then given by

$$P(X_{MRI} = g_{MRI}) = \frac{h_{MRI}(g_{MRI})}{\sum_j h_{MRI}(j)} \quad , MRI = T1, PD \in MRI$$

and the joint probability distribution by

$$P(X_{T1} = g_{T1}, X_{PD} = g_{PD}) = \frac{h_{T1,PD}(g_{T1}, g_{PD})}{\sum_{i,j} h_{T1,PD}(i,j)}.$$

The two random variables are statistically independent if

$$P(X_{T1} = g_{T1}, X_{PD} = g_{PD}) = P(X_{T1} = g_{T1}) \cdot P(X_{PD} = g_{PD})$$

and they are maximally dependent if a one-to-one mapping $f : G_{MRI} \rightarrow G_{MRI}$ exists, so that equation

$$P(X_{T1} = g_{T1}, X_{PD} = f(g_{T1})) = P(X_{T1} = g_{T1})$$

holds.

The mutual information *MI* measures the distance between the joint distribution and the distribution associated to complete independence by means of the Kullback-Leibler measure

$$MI(X_{T1}, X_{PD}) := \sum_{g_{T1}} \sum_{g_{PD}} P(X_{T1} = g_{T1}, X_{PD} = g_{PD}) \log \frac{P(X_{T1} = g_{T1}, X_{PD} = g_{PD})}{P(X_{T1} = g_{T1}) P(X_{PD} = g_{PD})}.$$

It can be shown, that *MI* is related to the entropy $H(X_{MRI})$, i.e., the well-known measure for the amount of uncertainty about the random variable X_{MRI} (see [187] for a brief introduction), by

$$MI(X_{T1}, X_{PD}) = H(X_{T1}) - H(X_{T1}|X_{PD})$$

with $H(X_{T1}|X_{PD})$ the conditional entropy of X_{T1} given X_{PD} [148]. It is thus the goal of the registration of the PD- onto the T1-MRI to find transformation parameters $\underline{P}$, which maximize the mutual information between both images, i.e.,

$$\underline{P}^* := \arg\max_{\underline{P} \in \mathbb{R}^9} C_{X_{T1}, X_{PD}}(\underline{P}) \tag{2.2}$$

with

$$C_{X_{T1}, X_{PD}}(\underline{P}) := MI\left(X_{T1}, X_{T_{\underline{P}}(PD)}\right)$$

(see Equation (2.1) for the definition of $T_{\underline{P}}$). This is equivalent to searching for parameters $\underline{P}$, so that the random variable $X_{T_{\underline{P}}(PD)}$ of the transformed PD image contains maximal information about X_{T1}, i.e., minimizes $H(X_{T1}|X_{T_{\underline{P}}(PD)})$, the uncertainty in X_{T1} given $X_{T_{\underline{P}}(PD)}$. $T_{\underline{P}}(\mathbf{x}_{PD})$, a transformed image lattice point $\mathbf{x}_{PD}$ of the floating PD image, with gray code $g_{PD}(\mathbf{x}_{PD})$ will generally not coincide with an image lattice point of the reference T1-MRI, so that the question arises to which gray code(s) g_{T1} in the joint histogram $h_{T1, T_{\underline{P}}(PD)}$ it has a contribution to. Maes et al. [148] discussed three different techniques. The recommended so-called *trilinear Partial Volume distribution Interpolation* (PVI) was used here. PVI distributes the contribution of $g_{PD}(\mathbf{x}_{PD})$ to the joint histogram over the intensity values of all nearest neighbors of $T_{\underline{P}}(\mathbf{x}_{PD})$ in the T1 image lattice, using the same weights as for trilinear interpolation. As a consequence, with a varying parameter vector $\underline{P}$, the joint histogram and thus the *MI* trace change smoothly and optimization robustness is given [148].

2.4.3 Optimization

As described in the previous subsection (see Equation (2.2)), the optimal transformation parameters are considered to maximize the function $C_{X_{T1}, X_{PD}} : \mathbb{R}^N \to \mathbb{R}$ with, in our case, $N = 9$. Nelder-Mead's simplex method is an algorithm, which tries to determine a local extremum in multidimensional space [162]. The concept of the algorithm (see, e.g., [187]) was based on a Freudenthal triangulation, described by Allgower and Georg [5]

$$
\begin{aligned}
\underline{a}_1 &:= \underline{0}^N \in \mathbb{R}^N \\
\underline{a}_{i+1} &:= \underline{a}_i + \underline{e}_i, \ \forall i = 1, \dots, N,
\end{aligned}
$$

Algorithm 1 SIMP:$(T1, PD \in MRI, \underline{P}_{\text{start}}, \underline{l} \in \mathbb{R}^9, d_{\text{start}}, d_{\text{stop}} \in \mathbb{R}) \rightarrow (\underline{P}^* \in \mathbb{R}^9)$

Initialize: $\underline{P} = \underline{P}_{\text{start}}$, $d = d_{\text{start}}$

while $d \geq d_{\text{stop}}$ **do**

   $\underline{s}_1 = \underline{P}$ /* starting simplex */

   $\underline{s}_{i+1} = d \cdot l_i \cdot \underline{e}_i + \underline{s}_i$ $\forall i = 1, \ldots, N$

   repeat

      Determine $\pi \in S_{N+1}$ with: /* ordering and uphill pivoting */

         $C_{X_{T1}, X_{PD}}(\underline{s}_{\pi(i)}) \leq C_{X_{T1}, X_{PD}}(\underline{s}_{\pi(i+1)}) \; \forall i = 1, \ldots, N$

      for i=1,…,N+1 **do**

         if $C_{X_{T1}, X_{PD}}(\text{refl}(\underline{s}_{\pi(i)})) > C_{X_{T1}, X_{PD}}(\underline{s}_{\pi(i)})$ **then**

            $\underline{s}_{\pi(i)} = \text{refl}(\underline{s}_{\pi(i)})$

            Leave the for-loop

         end if

      end for

   until No more replacement of any $\underline{s}_i$

   $\underline{P} = \underline{s}_{\pi(N+1)}$, $d = d/2$ /* translate and contract */

end while

$\underline{P}^* = \underline{P}$

---

with $\underline{e}_i$ the ith unit basis vector of $\mathbb{R}^N$, in order to avoid degenerate simplices and to be successful for the considered application. The resulting method, presented in Algorithm 1, starts with a simplex with vertices $\underline{s}_1, \ldots, \underline{s}_{N+1} \in \mathbb{R}^N$, being images of Freudenthal's triangulation under an affine map, i.e.,

$$\underline{s}_i = d \cdot \text{DIAG}(l_1, \ldots, l_N) \cdot \underline{a}_i + \underline{P}_{\text{start}}, \; \forall i = 1, \ldots, N+1$$

with the user-given $N \times N$ diagonal matrix of scaling factors l_i, the resolution parameter d and the starting transformation vector $\underline{P}_{\text{start}}$. In the next step, a permutation π from the set of all permutations of the integers 1 to $N + 1$, S_{N+1}, is determined, arranging the vertices with respect to the corresponding value of mutual information. The simplex is then pivoted by reflection away from the minimal vertex value of $C_{X_{T1}, X_{PD}}$ with the reflection function

$$\text{refl}(\underline{s}_i) := \text{pre}(\underline{s}_i) - \underline{s}_i + \text{suc}(\underline{s}_i)$$

based on the cyclic left/right shift order-relation

$$\text{pre}(\underline{s}_i) \quad := \quad \begin{cases} \underline{s}_{i-1} & \text{if} \quad i = 2, \ldots, N+1 \\ \underline{s}_{N+1} & \text{if} \quad i = 1 \end{cases}$$

$$\text{suc}(\underline{s}_i) \quad := \quad \begin{cases} \underline{s}_{i+1} & \text{if} \quad i = 1, \ldots, N \\ \underline{s}_1 & \text{if} \quad i = N+1 \end{cases}$$

Algorithm 2 MR_REG:$(T1, PD \in MRI, \underline{P}_{\text{start}}, \underline{l} \in \mathbb{R}^9, M \in \mathbb{N}, d_{\text{start}}, d_{\text{stop}} \in \mathbb{R}) \rightarrow (\underline{P}^* \in \mathbb{R}^9, PD^{\text{reg}} \in MRI)$

$T1^0 = T1$, $PD^0 = PD$, $\underline{P}_0^0 = \underline{P}_{\text{start}}$
for i=1,...,M-1 **do**
   $\underline{P}_0^i = REDUCE(\underline{P}_0^{i-1})$
   $T1^i = COARSEN(T1^{i-1})$, $PD^i = COARSEN(PD^{i-1})$
end for
for i=M-1,...,0 **do**
   $\underline{P}_*^i = \textbf{SIMP}(T1^i, PD^i, \underline{P}_0^i, \underline{l}, d_{\text{start}}, d_{\text{stop}})$
   if $i > 0$ **then**
      $\underline{P}_0^{i-1} = EXPAND(\underline{P}_*^i)$
   end if
end for
Set $\underline{P}^* = \underline{P}_*^0$ and determine PD^{reg}

---

for the simplex vertices with $\text{suc}(\underline{s}_i)$ the successor and $\text{pre}(\underline{s}_i)$ the predecessor of $\underline{s}_i$ [5]. After pivoting, the algorithm restarts with a new shrunk version of a simplex at the actual maximum. It terminates, when the resolution parameter d falls under the predefined resolution bound d_{stop}. The registration process is embedded into a hierarchical framework, shown in Algorithm 2. The general idea is, that rough estimates of the desired transformation parameters can be calculated at coarser resolutions using subsampled images. By means of the operation *COARSEN*, an image is first Gauss-filtered and then downscaled to half its resolution. The downscaling is realized by simply an equidistant sampling of the original image, i.e., taking over every second voxel. After the calculation of the transformation parameters $\underline{P}_*^i$ on a coarser level i, scaling parameters $\mathbf{s}_*^i$ and rotation parameters $\mathbf{r}_*^i$ can be taken over, but the translation parameters $\mathbf{t}_*^i$ have to be doubled in order to find an appropriate starting vector $\underline{P}_0^{i-1}$ for the finer resolution $i-1$. This is denoted with the operation *EXPAND*. The inverse of this operation, *REDUCE*, is needed in order to downscale the starting vector $\underline{P}_{\text{start}}$. The registered PD image PD^{reg} is then determined in a last step by transforming each point of its image lattice $\mathbf{x}_{PD^{\text{reg}}}$ with the inverse transformation $T_{\underline{P}^*}^{-1}$ and interpolating its intensity by trilinear interpolation in the starting PD image.

2.4.4 Registration results

In order to test the accuracy of the registration and to determine appropriate values for the free parameters, Algorithm 2 was first applied to five T1/T1 data sets, where the second T1-modality was subject to a known affine transforma-

Reference transformation parameters $\underline{P}^{\text{ref}}$									
Translation in voxels			Rot. angles in degree			Scaling			Error
t_x	t_y	t_z	ϕ_x	ϕ_y	ϕ_z	s_x	s_y	s_z	Δreg
1,59	-17,0	-37,7	-5,62	1,90	-6,02	1,01	0,99	1,02	
3,04	0,10	24,14	6,23	-18,5	3,96	0,96	0,95	0,99	
-7,14	-4,13	-18,0	-14,2	4,38	7,71	1,03	1,00	1,02	
21,94	-7,28	10,30	9,34	-1,29	-10,9	0,99	0,97	1,03	
-17,8	19,13	28,45	1,20	-7,30	12,45	1,04	1,02	0,97	
Calculated transformation parameters $\underline{P}^*$									
1,6	-17,0	-37,7	-5,59	1,84	-5,96	1,01	0,99	1,02	0,3
3,1	0,2	24,2	6,27	-18,6	3,96	0,96	0,95	0,99	0,26
-7,2	-4,2	-18,0	-14,2	4,42	7,73	1,03	1,00	1,02	0,08
21,9	-7,3	10,3	9,28	-1,31	-10,9	0,99	0,97	1,03	0,11
-17,8	19,1	28,4	1,15	-7,35	12,44	1,04	1,02	0,97	0,08

Table 2.1: *Accuracy test for Algorithm 2: Reference transformation parameters $\underline{P}^{ref}$ and calculated transformation parameters $\underline{P}^*$ for the five T1/T1 test pairs.*

tion of the first. No image noise was added. The chosen parameters $\underline{P}^{\text{ref}}$ for the reference transformations are shown in Table 2.1. In a second step, the five transformed (under $T_{\underline{P}^{\text{ref}}}^{-1}$) T1 images were registered onto the reference T1 image, yielding an optimization result $\underline{P}^*$ for each transformed image. With $\|T_{\underline{P}^{\text{ref}}}^{-1}(\mathbf{x}_{\text{ref}}) - T_{\underline{P}^*}^{-1}(\mathbf{x}_{\text{ref}})\|_2$ (measured in voxel) as a difference measure for an image lattice point $\mathbf{x}_{\text{ref}}$ of the reference T1 image, the registration error Δreg is defined as the maximal difference over eight lattice points with coordinates $(\pm 100, \pm 100, \pm 100)^T$ relative to the center of the reference image. Since the considered points were chosen to be located outside the head, the registration error can be interpreted as a maximal upper error bound for all points lying inside the imaged object.

Table 2.1 shows the calculated transformation parameters $\underline{P}^*$ and the corresponding registration errors of Algorithm 2 for the five T1/T1 test data sets. Errors between 0.08 and 0.30 (in voxels) were measured, demonstrating a subvoxel precision of the presented method. The execution times were less than 40 minutes [1]. The choice of the free parameters in Algorithm 2 will now be discussed. The initial mesh size of the triangulation, d_{start}, and the scaling, $\underline{l}$, are important for finding the global extremum, they should not be chosen too small. d_{stop} controls the final resolution of the solution. The smaller d_{stop} was chosen, the more accurate, but also the more computationally expensive. The setting of $d_{\text{start}} = 1$

---

[1]Linux-based, Intel Pentium III, 1Ghz.

	t_x	t_y	t_z	ϕ_x	ϕ_y	ϕ_z	s_x	s_y	s_z	C
$\underline{l}$	0.5	0.5	0.5	2.5	2.5	2.5	.03	.03	.03	
$\underline{P}_{start}$	0.0	-6	-15	0.0	0.0	0.0	1.0	1.0	1.0	
$\underline{P}^2_{start}$	0.0	-1.5	-3.8	0.0	0.0	0.0	1.0	1.0	1.0	.62
$\underline{P}^2_*$	-0.5	-1.9	-3.6	-4.4	-0.66	2.9	1.0	1.0	1.0	.72
$\underline{P}^1_{start}$	-1.0	-3.7	-7.1	-4.4	-0.66	2.9	1.0	1.0	1.0	.62
$\underline{P}^1_*$	-0.9	-3.9	-7.0	-4.5	-0.74	2.8	1.0	1.0	1.0	.63
$\underline{P}^0_{start}$	-1.8	-7.7	-14	-4.5	-0.74	2.8	1.0	1.0	1.0	.52
$\underline{P}^0_*$	-1.67	-8.44	-14.2	-4.57	-0.74	2.66	1.01	1.0	1.01	.53

Table 2.2: *Registration result of Algorithm 2: Choice of $\underline{l}$ and $\underline{P}_{start}$ with exploitation of information from visual inspection.*

(in mm), a choice of 5.0 (in mm) for all translation, 2.5 (in degrees) for the rotation and 0.03 for the scaling parameters in $\underline{l}$ and $d_{stop} = 0.01$ (in mm) was shown to yield high accuracy (see Table 2.1) in feasible calculation time. A choice of the identity transformation for $\underline{P}_{start}$ was sufficient for all tested data sets. $M = 3$ levels for the multiresolution approach enabled high accuracy in short calculation time. Notice, that each function evaluation on $i - 1$ level is 2^3 times as expensive as for the ith level. Burkhardt [31] compared the multiresolution simplex optimization with a genetic optimization, used e.g. in [214], and Powells-Algorithm, used e.g. in [148]. It was found to be most accurate and efficient.

The registration Algorithm 2 was applied to the measured bimodal MR data set presented in Section 2.3. Results for two different scenarios of start vectors $\underline{P}_{start}$ and corresponding scalings $\underline{l}$ will now be presented, the first exploiting information from visual inspection of the images to yield a good starting vector and the second appropriate as an automatic choice for the case where no user-intervention is possible.

Since only a moderate rotation between both image modalities was present, a translation of about -6 voxels in y- and of about -15 voxels in z-direction could be easily estimated by visual inspection of sagittal (see Figure 2.7) and axial (see Figure 2.8) slices. This led to a choice of $\underline{P}_{start}$, which is shown in Table 2.2. The chosen $\underline{l}$ was considered to be an appropriate guess for the problem's characteristic length scale. For each level i, the starting vector $\underline{P}^i_{start}$ and the determined transformation parameters $\underline{P}^i_*$ and the value of mutual information C are shown in the table. It can be observed, that due to the starting vector, already on the coarsest level a quite good estimate for the transformation is achieved. It seems that the simplex method already found the global maximum, so that the increase in mutual information through further optimization on level 1 and 0 is thus minimal.

	t_x	t_y	t_z	ϕ_x	ϕ_y	ϕ_z	s_x	s_y	s_z	C
$\underline{l}$	5.0	5.0	5.0	2.5	2.5	2.5	.03	.03	.03	
$\underline{P}_{start}$	0.0	0.0	0.0	0.0	0.0	0.0	1.0	1.0	1.0	
$\underline{P}^2_{start}$	0.0	0.0	0.0	0.0	0.0	0.0	1.0	1.0	1.0	.44
$\underline{P}^2_*$	-0.8	-1.3	-3.8	-1.0	-0.74	0.0	1.0	1.0	1.0	.66
$\underline{P}^1_{start}$	-1.6	-2.6	-7.6	-1.0	-0.74	0.0	1.0	1.0	1.0	.55
$\underline{P}^1_*$	-0.9	-3.4	-7.0	-3.2	-0.62	2.3	1.0	1.0	1.0	.61
$\underline{P}^0_{start}$	-1.9	-6.9	-14	-3.2	-0.62	2.3	1.0	1.0	1.0	.51
$\underline{P}^0_*$	-1.64	-8.44	-14.3	-4.53	-0.74	2.62	1.01	1.0	1.01	.53

Table 2.3: *Registration result of Algorithm 2: Automatic choice of $\underline{l}$ and $\underline{P}_{start}$.*

An automatic choice of $\underline{P}_{start}$ and $\underline{l}$ under the assumption of a moderate mis-registration is shown in Table 2.3. On the coarsest level 2, the global maximum of C could not yet be found. The translation parameters were well approximated, but the rotation parameter error was still significant. Therefore, compared to Tab.2.2, much more computational work was carried out on level 1. The fine-tuning on level 0 then resulted in parameters with only a small difference to the parameters in Table 2.2. The computation time was less than 1 hour when setting up the 2D-histogram in parallel, using 8 processors on an SGI ORIGIN 2000 [2]. When comparing the transformed PD image with the image, resulting from Table 2.2, no difference could be observed. Figure 2.9 presents the configuration of Figure 2.8 with now the registered PD image, using the transformation parameters of Table 2.2. In order to show the high accuracy of the approach, the outer surface of the brain (top, see Script 2.6.3) and of the head (bottom, see Script 2.6.1) were extracted from the T1 image and visualized on the registered PD modality. No noticeable registration error could be observed.

2.5 Segmentation of MR-images

In the following, the segmentation components are described, which, together with the basic components of Section 2.2, are later used as the ingredients for the segmentation scripts in Sections 2.6. It will be focused on three central methods, two of them emerged as important voxel-based classification tools, the Adaptive Fuzzy C-Means (AFCM) algorithm and the Extended Region Growing (ERG) concept. The third method, a deformable model, is then described as a tool for segmentation improvement.

---

[2]See the description of the SGI ORIGIN 2000 in Chapter 5.
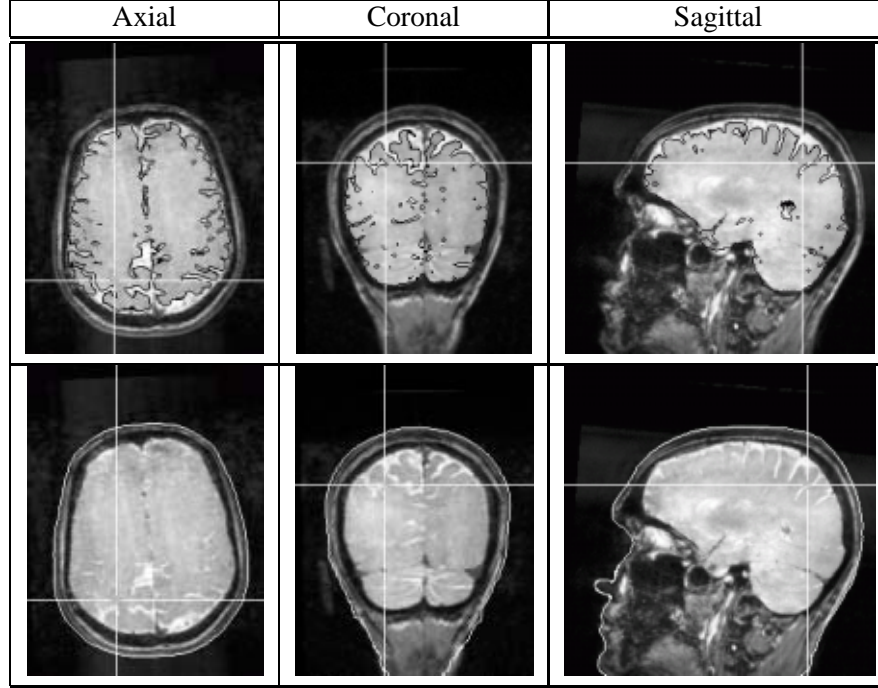
Figure 2.9: *Registration result: The outer surfaces of the brain (top) and of the head (bottom), extracted from the T1-, are mapped on the registered PD-MRI.*

2.5.1 Unsupervised clustering

Clustering methods classify voxels by feature space partitioning, i.e. voxels within a certain intensity range are sorted into a common cluster. A clustering method is called unsupervised, if it automatically determines the intensity ranges for a user-given number C of clusters $\text{Clust}_j, j = 1, \ldots, C$. ISODATA, a representant of such a method (see, e.g., Lohmann [140]), is shown in Algorithm 3. After an initialization of the cluster centres c_j, e.g., an arbitrary distribution over the set of gray codes G_{MRI}, new cluster mean values are iteratively computed trying to minimize the distance towards its cluster members. The algorithm realizes a minimization of the objective function

$$J_{ISODATA}(c_j) = \sum_{j=0}^{C-1} \sum_{\mathbf{x} \in \text{Clust}_j} |I(\mathbf{x}) - c_j|.$$

The output is a C-class positive integer image, where its class index is assigned to each voxel. The class with the darkest input voxels receives gray code 0 and the brightest the gray code $C - 1$.

Algorithm 3 ISODATA : $(IN \in MRI, C \in \mathbb{N}) \rightarrow (OUT \in CPI, c_1^{\text{iso}}, \ldots, c_{C-1}^{\text{iso}} \in G_{MRI})$

$l = 0$, Initialize $c_j^{(0)}$, $\forall j = 0, \ldots, C-1$
repeat
  $l = l + 1$
  for all voxels **x** of *IN* **do**
    $min = BIGNUM$
    for $j = 0, \ldots, C-1$ **do**
      if $|I(\mathbf{x}) - c_j| < min$ **then**
        $k = j, min = |I(\mathbf{x}) - c_j|$
      end if
    end for
    Put **x** into Clust$_k$
  end for
  for $j = 0, \ldots, C-1$ **do**
    $c_j^l = \frac{1}{|\text{Clust}_j|} \sum_{\mathbf{x} \in \text{Clust}_j} I(\mathbf{x})$
  end for
until $\sum_{j=0}^{C-1} |c_j^{(l)} - c_j^{(l-1)}| < \varepsilon$
$c_j^{\text{iso}} = c_j^{(l)}$, $\forall j = 0, \ldots, C-1$

2.5.2   Fuzzy segmentation in the presence of intensity inhomogeneities

The FCM algorithm

Unlike hard classification methods such as the presented ISODATA clustering, the *Fuzzy C-Means* (FCM) algorithm [225] does not force a voxel **x** to belong to exclusively one class, but assigns a membership value $u_j(\mathbf{x})$ for each class with $\sum_{j=0}^{C-1} u_j(\mathbf{x}) = 1$. FCM minimizes the objective function

$$J_{FCM}(u_j, c_j) = \sum_{\mathbf{x}} \sum_{j=0}^{C-1} u_j^2(\mathbf{x}) |I(\mathbf{x}) - c_j|^2,$$

so that, in contrast to ISODATA, more than one tissue class may be present in a single voxel. Imaging very fine structures results in partial volume averaging, which is taken into account by means of fuzzy segmentation. Likewise, a noisy voxel only changes the classification by a fractional amount and does not influence the entire segmentation process.

The AFCM algorithm

Intensity inhomogeneities, i.e., slow gray value variations of voxels of the same tissue class over the whole image domain can be often observed in T1 and PD MRI. This phenomenon may be caused by such factors as radio frequency (RF) excitation field inhomogeneity [155], non-uniform reception coil sensitivity, eddy currents driven by field gradients [208] as well as RF penetration and standing wave effects [24]. It is assumed that the inhomogeneities are well modeled by the product of the original image with a smoothly varying multiplier field $m(\mathbf{x})$ [47; 248]. A theoretical analysis of the intensity non-uniformity by means of an analytical approach for an elliptically shaped geometry using circularly polarized RF coils was presented by Sled and Pike [209]. The multiplicative and smooth form of m was proved and a high dependency of the pattern of intensity variation on the shape of the object was shown for PD images.

The *Adaptive Fuzzy-C-Means* (AFCM) algorithm, introduced for 2D images in [181], seeks to compensate the described inhomogeneities while performing a fuzzy segmentation of the image. AFCM minimizes the objective function

$$
\begin{aligned}
J_{AFCM}(u_j, c_j, m) \;=\; & \sum_{\mathbf{x}} \sum_{j=1}^{C} u_j^2(\mathbf{x}) |I(\mathbf{x}) - m(\mathbf{x}) c_j|^2 \\
& + \lambda_1 \sum_{\mathbf{x}} \left(((D_x * m)(\mathbf{x}))^2 + ((D_y * m)(\mathbf{x}))^2 + ((D_z * m)(\mathbf{x}))^2 \right) \\
& + \lambda_2 \sum_{\mathbf{x}} \left(((D_{xx} * m)(\mathbf{x}))^2 + ((D_{yy} * m)(\mathbf{x}))^2 + ((D_{zz} * m)(\mathbf{x}))^2 \right. \\
& \qquad + 2((D_{xy} * m)(\mathbf{x}))^2 + 2((D_{xz} * m)(\mathbf{x}))^2 \\
& \qquad \left. + 2((D_{xz} * m)(\mathbf{x}))^2 \right) ,
\end{aligned}
\tag{2.3}
$$

where D_i is the first order finite difference along the ith axis of the image volume, $D_{ij} = D_i * D_j$ is a second-order finite difference and $*$ denotes the discrete convolution operator. The λ-terms are regularizing the multiplier field m. Their parameters λ_i should be set according to magnitude and smoothness of the inhomogeneities. The first necessary condition for J_{AFCM} in equation (2.3) to be at a minimum, i.e., step 1 in Algorithm 4, can be derived using the method of Lagrange multipliers for the minimization of J_{AFCM} towards u_j to the constraint that the sum of membership values is equal to 1. Taking the first derivative of J_{AFCM} with respect to c_j and setting it equal to zero results in step 2 of the algorithm.

Algorithm 4 AFCM : $(MRI \in \mathcal{MRI}, C \in \mathbb{N}, \lambda_1, \lambda_2, \varepsilon, \delta \in \mathbb{R}) \rightarrow (MRI^{\mathrm{corr}} \in \mathcal{MRI}, MRI^{\mathrm{afcm}} \in \mathcal{CPI}, c_1^{\mathrm{afcm}}, \ldots, c_{C-1}^{\mathrm{afcm}} \in \mathbb{N})$

Initialize: $l = 0, \forall \mathbf{x} : m^{(0)}(\mathbf{x}) = 1, \forall j = 0, \ldots, C-1 : c_j^{(0)} = c_j^{iso}$

repeat

   1. Compute new memberships, $\forall j = 0, \ldots, C-1, \forall \mathbf{x}$:

$$u_j^{(l+1)}(\mathbf{x}) = |I(\mathbf{x}) - m^{(l)}(\mathbf{x})c_j^{(l)}|^{-2} \left/ \sum_{k=0}^{C-1} |I(\mathbf{x}) - m^{(l)}(\mathbf{x})c_k^{(l)}|^{-2} \right.$$

   2. Compute new centroids, $\forall j = 0, \ldots, C-1$:

$$c_j^{(l+1)} = \sum_{\mathbf{x}} u_j^{(l+1)}(\mathbf{x})^2 \, m^{(l)}(\mathbf{x}) I(\mathbf{x}) \left/ \sum_{\mathbf{x}} u_j^{(l+1)}(\mathbf{x})^2 \, m^{(l)}(\mathbf{x})^2 \right.$$

   3. Comp. new mult. field (solve up to relative accuracy δ):

$$f(\mathbf{x}) = w(\mathbf{x})m^{(l+1)}(\mathbf{x}) + \lambda_1 \left(H_1 * m^{(l+1)}\right)(\mathbf{x}) + \lambda_2 \left(H_2 * m^{(l+1)}\right)(\mathbf{x})$$

   4. $l = l + 1$

until $\max_{\mathbf{x}} \left\{ \max_{j=0,\ldots,C-1} |u_j^{(l)}(\mathbf{x}) - u_j^{(l-1)}(\mathbf{x})| \right\} < \varepsilon$

Save $\lfloor I(\mathbf{x})/m^{(l)}(\mathbf{x}) \rfloor$ to $MRI^{\mathrm{corr}}(\mathbf{x})$

Save $\{k | u_k^{(l)}(\mathbf{x}) = \max_{j=0,\ldots,C-1} u_j^{(l)}(\mathbf{x})\}$ to $MRI^{\mathrm{afcm}}(\mathbf{x})$

Finally, minimization of J_{AFCM} towards m proceeds in algorithm step 3, where

$$
\begin{aligned}
f(\mathbf{x}) &= I(\mathbf{x}) \sum_{j=0}^{C-1} \left(u_j^{(l+1)}(\mathbf{x})\right)^2 c_j^{(l+1)}, \\
w(\mathbf{x}) &= \sum_{j=0}^{C-1} \left(u_j^{(l+1)}(\mathbf{x})\right)^2 \left(c_j^{(l+1)}\right)^2, \\
H_1 &= \sum_i D_i * \check{D}_i, \\
H_2 &= \sum_i \left(D_{ii} * \check{D}_{ii}\right) + 2(D_{xy} * D_{xy}) + 2(D_{yz} * D_{yz}),
\end{aligned}
$$

$$(2.4)$$

using the notation $\check{D}(i) = D(-i)$ [265]. More detailed informations about the derivation of the 3D AFCM version can be found in Burkhardt [31].

    Input parameters for Algorithm 4 are the MR image *MRI*, the number of classes *C*, which is estimated from the image histogram and the regularization

parameters λ_1 and λ_2. Furthermore, the AFCM iteration (top index, l) is denoted by *outer iteration* and is terminated when the maximal difference between the membership values of two successive outer iterations is less than ε (the *outer convergence* criterion of Algorithm 4). Another input parameter is the bound for inner AFCM convergence, δ, discussed below. The algorithm determines the centroids c_j and solves the equation system for m in step 3 up to a relative residual of δ and extracts the multiplier field from *MRI*, resulting in the corrected image *MRI*$^{\text{corr}}$. A vector of fuzzy membership values $\underline{u} \in \mathbb{R}^C$ is calculated for each lattice point up to an outer accuracy of ε, from which the hard segmentation *MRI*$^{\text{afcm}}$ is determined by labeling each lattice point with the index of the class with maximal membership value. Within our implementation, the centroids are initialized by means of the ISODATA algorithm. The multipliers $m(\mathbf{x})$ for border-points with a maximal distance of 2 to the image-border are fixed to 1.0 in order to define boundary conditions.

Solver for the multiplier field

We will now focus on the solution process of the large sparse linear equation system $Am = b$ in step 3 of Algorithm 4. Because of its size, A cannot explicitly be stored as a band matrix and direct solvers cannot be considered for the solution process. Instead, A is described by means of its star notation (see, e.g., [93, §2.1.3]) and iterative solvers have to be used. The following two theorems can be shown for the Successive OverRelaxation method (SOR) for iteratively solving the equation system:

Theorem 2.5.1. *If A is SPD, then SOR will converge monotonically with respect to the energy norm for any $\omega \in]0,2[$ and for any initial guess $m^{(0)}$.*

Proof: Hackbusch [93, Theorem 4.4.21].

Theorem 2.5.2. *If A is symmetric and strictly diagonally dominant with positive diagonal elements, then A is SPD.*

Proof: Hackbusch [93, Lemma 6.4.12].

It is easy to show, that for non-border indices i, A is only diagonally dominant if $w_i > 60\lambda_2$, since $|a_{ii}| = w_i + 6\lambda_1 + 42\lambda_2$ and $\sum_{j \neq i}|a_{ij}| = 6\lambda_1 + 102\lambda_2$.

Saad [198] pointed out that, in fact, the reverse of the theorem is also true:

Theorem 2.5.3. *If A is symmetric with positive diagonal elements and for $0 < \omega < 2$, SOR converges for any $m^{(0)}$ if and only if A is positive definite.*

Let χ be the order of the Jacobi-iteration. Then, when choosing the optimal relaxation parameter, it can be shown for SPD matrices A (fulfilling one further condition), that the SOR method leads to an order improvement of $\chi/2$ [93, Remark 4.4.26].

Large condition numbers of A have to be expected, which can lead to a spoiled convergence behavior of iterative solvers. A first substantial improvement can be often achieved by a simple scaling of A in combination with a Conjugate Gradient (CG) solver method [206, pp.257f]. For the algorithm and its convergence properties see Section 5.2 and especially Theorem 5.2.1. It can be shown, that the scaling does not influence the convergence of the SOR method [206, p.258]. Therefore, a parallel scaled CG method was implemented for AFCM and tested against SOR. Let us denote the solver iteration (bottom index, j) by *inner iteration* and let us define the *inner convergence* in step 3 by means of

$$d_{(j)}^{(l)} := \frac{\|Am_{(j)}^{(l)} - b\|}{\|Am_{(0)}^{(1)} - b\|} < \delta, \tag{2.5}$$

i.e., as the residual (rescaled in order to allow the comparison to the SOR solver) of the actual j^{th} inner iteration, divided by the (rescaled) residual, calculated for the identity starting vector (i.e., $j = 0$) within the first outer iteration (i.e., $l = 1$), parameterized with δ. Since in our implementation, the multiplier field $m^{(l)}$ is exploited as a starting vector for the iterative calculation of $m^{(l+1)}$, the number of inner iterations decreases with increasing number of outer iterations. In case of only a small change of membership values and centroids in the first two AFCM steps, it is thus possible that inner convergence is achieved without any inner iteration, leading to outer convergence of the AFCM.

2.5.3   Contextual segmentation

Clustering techniques like ISODATA and AFCM do not use adjacency relations for the classification (see Definition 2.2.4). Contextual segmentation algorithms bring together adjacency and classification by feature space partitioning. The latter means that a voxel **x** becomes foreground voxel if its gray value is in a given range, i.e. $I_{min} \leq I(\mathbf{x}) \leq I_{max}$. The region growing algorithm [12], a simple method of contextual segmentation, starts at a seedpoint, whose intensity value is in the given range, and inspects its neighborhood. Voxels, "similar"enough, are recursively added to the region. Here, the "similarity"criterion for a voxel **x** of

the 6-neighborhood is concretized by the boolean function

$$
\text{Inside}(\mathbf{x}) = \begin{cases} true & : & \begin{cases} & PASS(\mathbf{x}) = 1 \\ \vee & [PASS(\mathbf{x}) = STOP(\mathbf{x}) = 0 \\ \wedge & (I_{min} \leq I(\mathbf{x}) \leq I_{max})] \end{cases} \\ false & : & otherwise \end{cases} ,
$$

using the markers *PASS* and *STOP* from Definition 2.2.7. In order to segment a three dimensional connected component *V* and simultaneously identify the corresponding two dimensional surface *S*, the region growing concept has to be extended so that not only the region, but also the corresponding one voxel thick region surface is growing (*extended region growing* (ERG), see [239; 241]). When looking back to Figure 2.2 (middle), *S* can be seen as the 26-connected foreground circle, where a foreground voxel is now a voxel, which fulfills the similarity criterion. *V* can be seen as the 6-connected background which is interior to the circle in the figure. The surface voxels are thus 26-connected within *S* and 6-connected to at least one element of *V*. The above is formalized by introducing the pair of binary arrays (S, V) with $S, V : L \rightarrow G_{0,1}$. Each voxel $\mathbf{x}$ is either a surface- $(S(\mathbf{x}) = 1)$ or (exclusive) a volume- $V(\mathbf{x}) = 1$ or (exclusive) a background-voxel $V(\mathbf{x}) = S(\mathbf{x}) = 0$.

A pseudocode for the resulting ERG concept is shown in Algorithm 5. The abort criterion is tuned with the parameter elastic, whose default is elastic $= 0$. Increasing this parameter results in a higher elasticity so that the algorithm is able to grow into thin regions. This can be important, e.g., for the segmentation of the outer skull surface, if a very thin low-contrast compacta skull layer is lying between high-contrast spongiosa and skin, see Figure 2.19.

2.5.4 Refinement by means of a deformable model

Much research has been done in the field of deformable (or active contour) models [119; 222; 39; 139; 154; 7]. Unlike voxel-based segmentation methods, a deformable contour model moves an extracted mesh of an initial surface continuously through the spatial domain of a 3D image with the goal of improving the initial segmentation by means of a minimization of a suitable energy functional. The success of this method is strongly dependent on the quality of the mask, from which the initial mesh is extracted. Active contour models take the partial volume effect into account and they are insensitive w.r.t. image noise to some degree. Generally, the energy functional consists of two forces, the internal smoothing force $\mathbf{F}_{int}$ and the external repulsive or attractive force $\mathbf{F}_{ext}$, acting perpendicular to the surface mesh and seeking to constrain the final surface to fit the given data. An overview of various definitions of forces in deformable models was given by McInerney and Terzopoulos [154]. Many successful applications are reported for

---

Algorithm 5 ERG : $(IN \in MRI_{\text{ext}}, \text{elastic} \in G_{0,1}, I_{min}, I_{max} \in G_{MRI}) \rightarrow OUT \in BI$

$\forall \mathbf{x} : V(\mathbf{x}) = S(\mathbf{x}) = OUT(\mathbf{x}) = 0$, Put seedpoint to empty *queue*

while *queue* $\neq \emptyset$ **do**

    Set counter $= 0$ and take $\mathbf{x}_{akt}$ out of *queue*

    for each 6-neighbor $\mathbf{x}_i$ of $\mathbf{x}_{akt}$ **do**

      if $(\text{Inside}(\mathbf{x}_i) = false)$ **then**

        counter $=$ counter $+ 1$

      end if

    end for

    if $(\text{counter} > \text{elastic})$ **then**

      $S(\mathbf{x}_{akt}) = 1$

    else

      $V(\mathbf{x}_{akt}) = 1$

      for each 6-neighbor $\mathbf{x}_i$ of $\mathbf{x}_{akt}$ **do**

        if $V(\mathbf{x}_i) = S(\mathbf{x}_i) = 0$ **then**

          Put $\mathbf{x}_i$ to *queue*

        end if

      end for

    end if

end while

$\forall \mathbf{x}$ with $((V(\mathbf{x}) = 1) \vee (S(\mathbf{x}) = 1))$: $OUT(\mathbf{x}) = 1$

---

the segmentation of the human cortex [44; 46; 265; 130], whereas only one study for the skull was found [193]. Davatzikos and Bryan [46] reported the importance of the quality of the initial guess for the cortex application. It was shown, that deformable models may have difficulties in progressing into the sulci, when simply initialized from an elliptically shaped surface outside the cortex.

Algorithm 6 shows a pseudo-code of the active contour model, that is used in the following for the skull segmentation improvement. The model closely follows the descriptions of Kruggel and von Cramon [130], based on ideas of Dale and Sereno [44] and Xu et al. [265]. In a first step, *EXTRACT* (see Operation 2.2.23) extracts a triangle mesh from a given binary *initial_mask*. The operation *SIMPLIFY* (see Operation 2.2.24) is then applied to achieve a reduction in the vertex count to N_v vertices, while retaining the shape of the surface. Output are the mesh vertices $\mathbf{v}^0$, its normal vectors $\mathbf{n}^0$ and the triangle elements Δ, where the normal vector for each vertex was calculated as the arithmetic mean of the neighboring triangle normals. The internal force $\mathbf{F}_{\text{int}}(\mathbf{v}^i)$ for a vertex in the ith iteration, $\mathbf{v}^i$, generally an expression of the surface curvature at $\mathbf{v}^i$ [265; 193], is

---

Algorithm 6 DEFORM : $(MRI \in MRI, INI \in BI, N_v \in \mathbb{N}, I_{\lim}, \omega_{int}, \omega_{ext}, \tau \in \mathbb{R}) \rightarrow (mesh \in MESH)$

$(\mathbf{v}^0, \mathbf{n}^0, \Delta) = SIMPLIFY(EXTRACT(INI), N_v)$, $i = 0$, $\kappa = 1/3$
repeat
    for each of the N_v vertices $\mathbf{v}^i$ **do**
        $\mathbf{F}_{int}(\mathbf{v}^i) = 0$ /* calculate smoothing force */
        for each of the N edge-connected neighbors $\mathbf{v}^i_j$ of $\mathbf{v}^i$ **do**

$$\mathbf{F}_{int}(\mathbf{v}^i) = \mathbf{F}_{int}(\mathbf{v}^i) + \frac{1}{N}\left(\mathbf{v}^i_j - \mathbf{v}^i\right)$$

        end for
        $F_{ext,1}(\mathbf{v}^i) = \langle -\nabla I_g(\mathbf{v}^i), \mathbf{n}^i \rangle$ /* magnitude of gradient force */
        $F_{ext,2}(\mathbf{v}^i) = \tanh\left(\kappa(I(\mathbf{v}^i) - I_{\lim})\right)$ /* magn. of capturing force */
        $\mathbf{v}^{i+1} = \mathbf{v}^i + \omega_{int}\mathbf{F}_{int}(\mathbf{v}^i) + \omega_{ext}\left(F_{ext,1}(\mathbf{v}^i)F_{ext,2}(\mathbf{v}^i) + F_{ext,2}(\mathbf{v}^i)\right)\mathbf{n}^i$
    end for
    $i = i + 1$
until $\frac{1}{N_v}\sum_{\mathbf{v}^i}\|\mathbf{v}^i - \mathbf{v}^{i-1}\| < \tau$
$mesh = (\mathbf{v}^i, \mathbf{n}^i, \Delta)$

---

chosen as a force, which pulls the vertex to the centroid of its N edge-connected neighbor vertices [44; 130]. The magnitude of the external force, acting along the vertex normal $\mathbf{n}^i$, is divided into two parts [265; 130]. The first, $F_{ext,1}$, is attached to the local intensity value gradient of the Gauss smoothed input MR image (see Operation 2.2.18), ∇I_g, while the second term, $F_{ext,2}$, captures the surface within a narrow range around an image intensity $I_{\lim}$. The parameter $\kappa \in \mathbb{R}$ defines the capturing range, which is related to the amount of noise in the MR data. It was fixed to $\kappa = 1/3$, following [130]. With τ we denote the bound for the convergence of the deformable model.

2.5.5 Segmentation results

The performance of ISODATA and AFCM will now be compared within a model study and for the bimodal data set from Section 2.3. The contextual segmentation and the deformable model are applied in the next section.

Studies in a three layer sphere model

In order to test the implemented AFCM code and the defined convergence criteria from Section 2.5.2, a three layer sphere model was generated with gray code 50 for background and middle layer and 150 for inner and outer layer. Sinusoidal inhomogeneities were overlayed onto this reference image. The resulting model
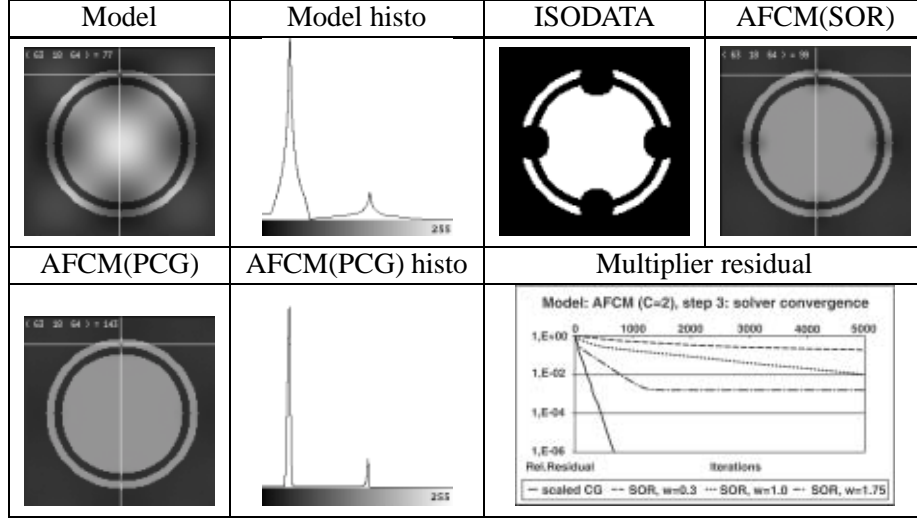
Figure 2.10: *Comparison of segmentation results of Algorithms 3 and 4 for a sphere model with sinusoidal intensity inhomogeneities. Top row: The model (left), its histogram (middle, left), the classification result of ISODATA (middle, right) and the AFCM (SOR) intensity corrected model (right). Bottom row: AFCM (PCG) intensity corrected model (left), its histogram (middle) and the relative residuals $d_{(j)}^{(1)}$ (see (2.5)) for the first 5000 inner iterations of the PCG and the SOR (for various ω) solver.*

is shown in Figure 2.10 (top, left). Voxel $\mathbf{x} = (63, 18, 64)$ with a strong intensity inhomogeneity of $m(\mathbf{x}) = 0.513$, leading to a gray code of $I(\mathbf{x}) = 77$ is marked in the model. The number of classes $C = 2$ was estimated by means of the number of maxima in the image histogram (top, middle left). ISODATA unsupervised clustering determined the class centers $c_0^{\text{iso}} = 50$, $c_1^{\text{iso}} = 149$ in good agreement with the histogram, but the sinusoidal inhomogeneities led to large misclassifications (top, middle right). AFCM showed a fairly robustness towards the regularization parameters and the choice of $\lambda_1 = 20,000$ and $\lambda_2 = 200,000$ gave good results for all tested applications, in agreement with [181] for 2D images.

Let us first look at the results of AFCM, based on the scaled CG solver. The convergence bounds were chosen as $\varepsilon = 0.01$ and $\delta = 0.1$. Three outer iterations were necessary for outer convergence and the scaled CG solver needed 193 inner iterations within the first, 99 within the second and 57 within the last outer iteration, then achieving the ε bound. The result is visualized by means of the corrected image (bottom, left) and its histogram (bottom, middle). When taking into account, that the multiplier field was only roughly approximated with

ISODATA	AFCM (PCG)	AFCM (SOR)	Multiplier residuals
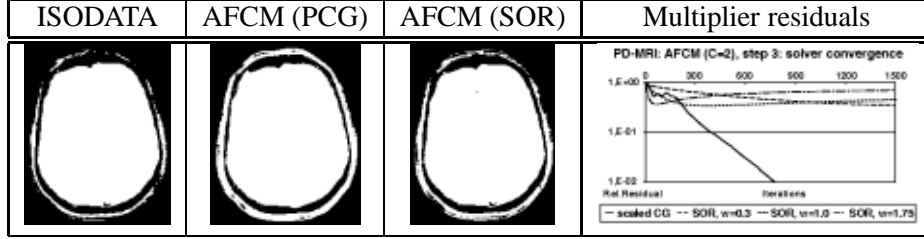
Figure 2.11: *PD-MRI: Comparison of segmentation results of Algorithms 3 (left) and 4 with scaled CG solver (left middle) and with SOR solver (right middle) and the relative residuals $d_{(j)}^{(1)}$ (see (2.5)) for the first 1500 inner iterations of PCG and SOR (for various ω) solver (right).*

$\delta = 0.1$, the inhomogeneities were already well extracted, shown by means of the sharp peaks at the class centers in the histogram. For $\mathbf{x} = (63, 18, 64)$, $m(\mathbf{x})$ was determined as 0.538, leading to the corrected intensity $I(\mathbf{x}) = 143$ (bottom, left). Certainly, the choice $\delta = 0.001$ led to the better result $I(\mathbf{x}) = 145$ and to even a bit sharper peaks in the histogram, but the sum of inner iterations increased by more than a factor 3 (not shown). The scaled CG method was able to reduce the relative residual (2.5) to any tested inner convergence bound, e.g., 683 inner iterations were needed for $\delta = 10^{-6}$, shown in Figure 2.10 (bottom, right).

The SOR residuals in the first outer iteration for $\omega = 0.3$ (underrelaxation), $\omega = 1.0$ (Gauss-Seidel) and $\omega = 1.75$ (overrelaxation) are shown in the same figure. Within 5000 iterations, SOR was not able to reduce residual (2.5) below $\delta \approx 10^{-3}$, even if the necessary condition, that $\|m_{j+1}^{(l)} - m_j^{(l)}\|$ is a sequence in j, tending to zero for all l, was fulfilled. The result of the AFCM corrected image with $\varepsilon = 0.01$ and an upper bound of 5000 SOR iterations with $\omega = 0.3$ is shown in Figure 2.10 (top, right). A relative residual of $d_{(5000)}^{(l)} \approx 0.2$ was not sufficient to correctly extract the inhomogeneities, for $\mathbf{x} = (63, 18, 64)$, $m(\mathbf{x}) = 0.777$ only led to $I(\mathbf{x}) = 99$.

Segmenting the PD-MRI

The comparison of Algorithms 3 and 4, applied to the PD-MRI is shown in Figure 2.11. Motivated by the histogram in Figure 2.8, the number of classes was chosen as $C = 2$. As a goal, skull (compacta and spongiosa) voxels should belong to class 0 and scalp, skin fat and intracranial tissue voxels to class 1. ISODATA found the centers $c_0^{\text{iso}} = 16$ and $c_1^{\text{iso}} = 167$ in good agreement with the histogram, so that class 0 consists of voxels with intensities up to 91. Because large parts of scalp and skin fat voxels, especially in the frontal area, have lower intensities than

voxels from the same tissues in more occipital parts, the ISODATA algorithm misclassified them to the skull class, resulting in large holes in the segmented scalp and even skin fat layer (Figure 2.11, left). As Figure 2.11, middle left, shows, the AFCM (PCG) method interprets the intensity variations as scanner inhomogeneities, which may be compensated. Thus, most of the remaining holes were small. The break-off criteria were set to $\varepsilon = 0.01$ and $\delta = 0.1$. The number of inner iterations and the starting residual was continuously decreased from 428 and $d_{(0)}^{(1)} = 1.0$ up to 64 and $d_{(0)}^{(5)} = 0.12$, resp., in the 5th outer iteration. Because of $d_{(0)}^{(6)} < \delta$, the 6th iteration led to outer convergence. A moderate continuous down shift of the centroid with highest intensity from $c_1^{(2)} = 164.7$ to $c_1^{(5)} = 162$ prevented the AFCM to naturally converge with the ε bound. The scaled CG method was again able to reduce the relative residual (2.5) to any tested inner convergence bound, e.g., 2283 inner iterations for $\delta = 10^{-6}$. The SOR solver for AFCM was, with no tested ω, able to reduce $d_{(j)}^{(l)}$ below 0.34 ($\omega = 0.3$, 2093 iterations). It was observed, that SOR converged up to a certain iteration bound, depending on ω. During the subsequent iterations, the relative residual (2.5) was continuously increased up to a plateau. For $\omega = 1.75$, this plateau at about 0.75 was reached after about 3000 iterations (Figure 2.11, right). The AFCM (SOR) classification result with break-off after 4 outer and 1000 SOR inner iterations is shown in Figure 2.11, middle right.

Segmenting the T1-MRI

For the T1-image, the number of classes was chosen as $C = 3$ according to its histogram in Figure 2.8. It is assumed, that skull compacta and CSF voxels should belong to the class with lowest intensity, scalp and gray matter voxels to the middle and white matter and skin fat voxels to the highest intensity class. ISODATA determined the centroids $c_0^{\text{iso}} = 13$, $c_1^{\text{iso}} = 93$ and $c_2^{\text{iso}} = 191$ in good agreement with the maxima of the histogram. Nevertheless, parts of scalp and even skin fat voxels were misclassified to class 0, leading again to holes in those layers, whereas the AFCM (PCG) segmented scalp and skin fat layer was mostly closed (see especially Figure 2.12, top row, middle and right). Furthermore, ISODATA misclassified certain WM voxels to class 1 (Figure 2.12, middle). The thickness of the cortical layer would thus measure about 8 mm at the presented location, being far from realistic (see Section 2.6.2 for more information). Concerning scaled CG and SOR solver for AFCM, comparable results were observed as for the PD-MRI, so that the discussion will be limited to the remarks, that the scaled CG method was again able to reduce $d_{(j)}^{(l)}$ to any tested inner convergence bound (e.g., 2117 inner iterations for $\delta = 10^{-6}$) and that the SOR solver was, with no

T1-MRI	ISODATA	AFCM (PCG)
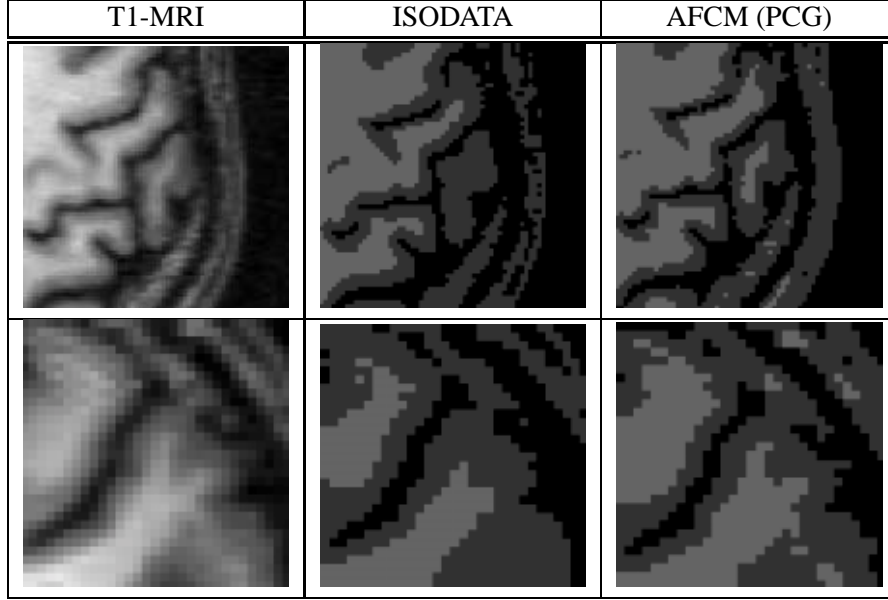
Figure 2.12: *T1-MRI (left): Comparison of segmentation results of Algorithms 3 (middle) and 4 with scaled CG solver (right). Magnification of axial (top) and coronal (bottom) cut through an area with larger segmentation differences.*

tested ω, able to reduce residual (2.5) below 0.27 ($\omega = 0.3$, 1355 iters). The following discussion will thus only concern the AFCM on the basis of the scaled CG. As Figure 2.12, right, shows, the AFCM interprets the intensity variation as scanner inhomogeneities and extracts them during the segmentation. The skin layer is closed and the WM seems to be well segmented, especially when compared with the original T1 image in the coronal cut (bottom row). This results in a cortex layer with a thickness of 4 mm at the presented location. Refer to Figure 2.15 in Section 2.6.2 for a visualization of the overall cortical layer difference between AFCM and ISODATA results. With break-off criteria of $\varepsilon = 0.01$ and $\delta = 0.1$, the number of inner iterations and the starting residual was continuously decreased from 472 and $d_{(0)}^{(1)} = 1.0$ up to 35 and $d_{(0)}^{(14)} = 0.101$, resp., in the 14th outer iteration. Because of $d_{(0)}^{15} < \delta$, the 15th iteration led to outer convergence. Again, a moderate continuous down shift of the centroid with highest intensity from $c_2^{(8)} = 169$ to $c_2^{(14)} = 161$ prevented the AFCM to naturally converge with the ε bound, whereas the centroids c_0 and c_1 were stable. This led to the observation, that with increased number of outer iterations, the skin layer gets more and more accurate, but on the other hand, more and more gray matter voxels are mis-

classified to the WM class. Since the same effect was observed for $\delta = 10^{-2}$, the problem can only be attributed to model limitations when applying the AFCM to the measured data set from Section 2.3. The best results were achieved with the limitation to 4 outer iterations, presented in Figure 2.12 (right). On one processor of the SGI ORIGIN 2000, this calculation took 2 : 18 hours, a period of time, which can be linearly reduced through parallel computing.

Discussion and conclusion for AFCM

With the presented studies, the AFCM was shown to considerably improve the segmentation of MR images in the presence of intensity inhomogeneities when compared to unsupervised clustering methods like the ISODATA algorithm. Concerning the solver method for step 3 of the AFCM, it was observed that SOR was not converging, but that a scaled CG solver reduced the residual to any tested bound. An explanation could be that, since the diagonal entries in A are clustered with the size of the centroids (see definition of w in (2.4)), the scaling decreases the difference of corresponding eigenvalue clusters and already leads to an acceptable improvement of the condition number (see also Section 5.2.1). Since it was observed that moderate solution accuracies are sufficient, a simple scaled CG solver already led to satisfying results. It should be mentioned with a reference to Chapter 5 that solvers, based on multigrid approaches[181] or the embedding of a simple preconditioned solver like the scaled CG into a multiresolution approach as presented for the registration in Section 2.4.3, would still considerably speed up the computation time. Nevertheless, with the newest 2 GB processor generation, the current implementation is satisfactory also for an application with a larger number of data sets.

2.6   Scripts for multicompartment head modeling

2.6.1   Extraction of the head surface

As presented in Section 2.5.5, a basis for the generation of the head mask is the compensation of intensity inhomogeneities while classifying the MR image. It was shown for both image modalities, that unsupervised clustering of such noise-flawed images can lead to large holes in scalp and skin fat layers, so that AFCM is an important ingredient within the head mask generation process. The extraction is described by Script 2.6.1. In the first step, AFCM is applied to the input MR image. The number of classes is fixed dependent on the modality, $C = 2$ for a PD- and $C = 3$ for a T1-MRI. With $g_1(2) = g_2(2) = 1$ or $g_1(3) = 1$ and $g_2(3) = 2$, the classification result MRI^{afcm} is first binarized into *segm_bin*. Parameter d_1 closes remaining holes or hollows in the segmented scalp and skin fat layers with

Script 2.6.1. HEAD : $(MRI \in MRI, C \in \mathbb{N}, \lambda_1, \lambda_2, \varepsilon, \delta \in \mathbb{R}, d_1, d_2, d_3 \in \mathbb{N}_0, OSS \in BI) \rightarrow (HEAD, SCALP \in BI)$

1. $(MRI^{corr}, MRI^{afcm}, c_j^{afcm}) = \mathbf{AFCM}(MRI, C, \lambda_1, \lambda_2, \varepsilon, \delta)$ /* class. */

2. $segm\_bin = BINARIZE(MRI^{afcm}, g_1(C), g_2(C))$ /* fusion */

3. $borders = BORDER(BIGGESTCOMP(segm\_bin))$ /* closing holes */

4. $eroded\_bg = BIGGESTCOMP(BINARIZE(DIST(borders), d_1, \infty))$

5. $back\_dilated = BINARIZE(DIST(eroded\_bg), d_1, \infty)$

6. $HEAD = SMOOTHING(back\_dilated, d_2)$ /* smoothing */

7. $SCALP = AND(HEAD, DILATE(OSS, d_3))$ /* for multi-tissue model */

a maximal size of $2d_1$ within the next block of the script (steps 3-5), before a smoothing for the case of stronger background noise terminates the generation of the head mask.

In EEG/MEG-source reconstruction, it is assumed that the weak volume currents outside the skull and far away from EEG and MEG sensors have a negligible influence on the measurements. Therefore, it is generally accepted that the parts of the head mask, lying outside the d_3 dilated outer skull surface mask, *OSS*, can be cut away when generating a volume conductor model (see, e.g., [239]). This concerns especially large parts of the face. Truncation of the head mask strongly reduces the computation amount when solving the inverse problem. The generation of the *SCALP*, i.e. the outer mask for a multi-tissue model, is thus the last step of Script 2.6.1. Please refer to Section 2.6.4 for *OSS* generation.

Results

Since the basic AFCM classification and its parameter tuning was already presented in Section 2.5.5, only the discussion of d_1, d_2 and d_3 remains. Burkhardt [31] tested different settings and found $d_1 = 4$ to be well suited for filling remaining hollows/holes in the segmented scalp and skin fat layers in a study with 5 different data sets. It was observed that a subsequent smoothing with $d_2 = 5$ could generally improve the head mask, especially for images with stronger background noise. The truncation of the head mask for the multi-compartment model was carried out by means of a parameter choice $d_3 = 10$. Intermediate results of Script 2.6.1 for the T1-MRI are shown in Figure 2.13.
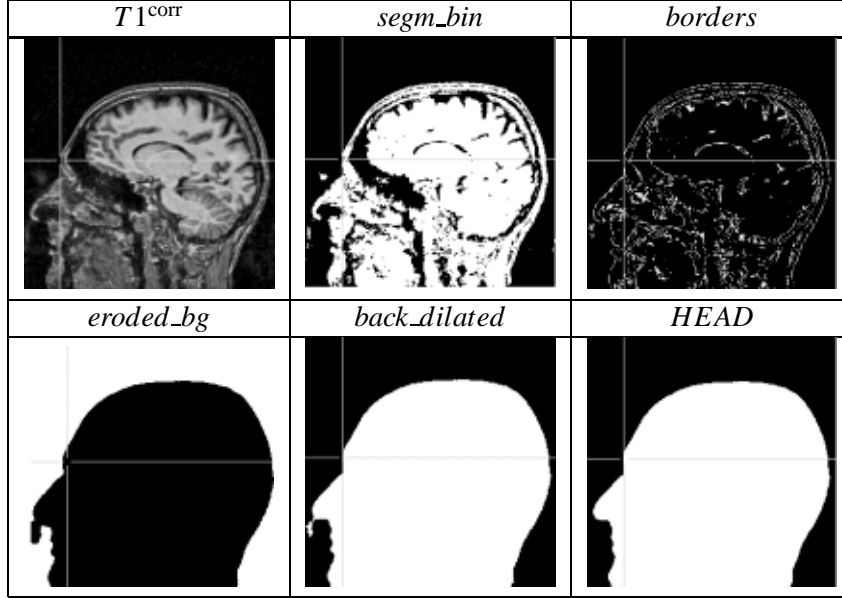
Figure 2.13: *Intermediate results for the generation of the head mask.*

2.6.2   Generation of brain and white matter masks

Peeling the brain

A first step in the generation process of the GM- and the WM- mask is the separation of the brain from its outer hulls, the so-called *brain peeling*. The border of the GM- and WM-mask models the boundary between CSF/GM and GM/WM, resp.. Peeling the brain is an important problem in the analysis of medical images and a large number of articles was published so far. It will not be discussed in full detail, only the key ingredients are presented here. Refer to [29; 129] for further informations. Script 2.6.2 describes the peeling process. After preprocessing the T1 image by means of a Lee-filter (Operation 2.2.19), a fast segmentation into two classes is carried out. The key ingredients of the peeling are the application-specific morphological erosion and dilation operations. Generally, they are implemented like the Operations 2.2.16, but it has to be taken special care of the anatomical connections between the brain and its outer hulls, i.e., the optic nerves and the brainstem. After pre-segmentation of eyes and brainstem, Operation 2.2.16 is adapted by locally increasing parameter d_1 around those critical points in order to successfully remove the outer hulls from the eroded brain in steps 4 and 5. A closing with large radius terminates the peeling, so that cavities and handles are filled and the surface of the mask is smoothed (see Figure 2.3).

Script 2.6.2. PEELING : $(T1 \in MRI, d_1, d_2 \in \mathbb{R}) \to (PEEL \in BI)$

1. $t1\_filt = LEE(t1)$ */* binarize filtered T1 */*

2. $bin = BINARIZE(ISODATA(t1\_filt, 2), 1, 1)$

3. $and1 = AND(bin, EROSION\_SPEC(BORDER(bin), d_1))$ */* erode */*

4. $big = BIGGESTCOMP(OPENING(and1, 3))$ */* extract */*

5. $and2 = AND(bin, DILATION\_SPEC(big, d_2))$ */* inflate */*

6. $PEEL = CLOSING(and2, 12)$

Results

The peeled brain with a parameter setting $d_1 = 2$ and $d_2 = 4$ is shown in Figures 2.14 (left) and 2.16. Using an algorithm described by Lohmann [140], the Euler number (Definition 2.2.6) of the peeling mask *PEEL* was controlled to be 1, i.e., equivalent to the topology of a sphere.

The brain mask

When the peeling mask is successfully determined, the brain mask, whose border models the GM/CSF boundary, can be generated quite easily. This process is described in Script 2.6.3. In the first step, the AFCM segmented brain is peeled from its outer hulls and binarized so that gray and WM classes are assembled as the image foreground in the intermediate binary mask *bin*. Image degradations at the border of the peeled brain are extracted in a second step. The binary mask *bin* is eroded using a parameter d, so that the brain is separated from the degradations, and the biggest component is then dilated with the same parameter.

Script 2.6.3. GEN_BRAIN : $(PEEL \in BI, d \in \mathbb{N}) \to (BRAIN \in BI)$:

1. $bin = BINARIZE(AND(T1^{afcm}, PEEL), 1, 2)$

2. $BRAIN = DILATION(BIGGESTCOMP(EROSION(bin, d)), d)$

$AND(T1^{\text{afcm}}, PEEL)$	*bin*	*BRAIN*
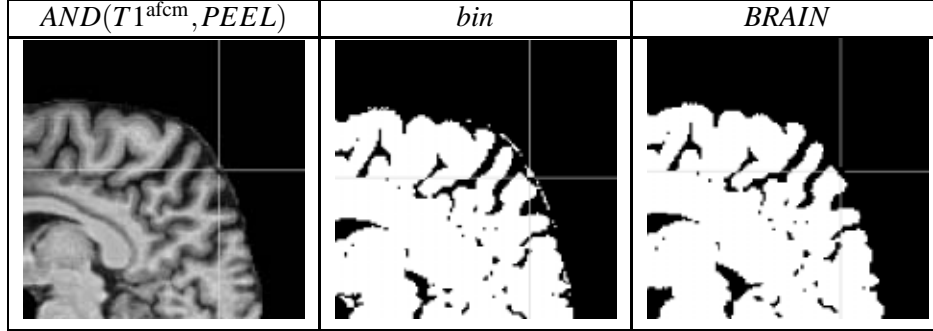
Figure 2.14: *Intermediate results of Script 2.6.3.*

Results

The free parameter was fixed to $d_1 = 2$ and the Script 2.6.3 was executed. Intermediate results are shown in Figure 2.14. Figure 2.16 shows the border of the resulting mask on the peeled brain. It was also already presented on the underlying registered PD image in Figure 2.9, indicating the accuracy of both the registration and the above segmentation. Note, that the resulting brain mask does no longer have the topology of a sphere, since a larger number of cavities and handles was introduced (Euler number 98). Furthermore, a 3D rendering of the brain surface after extraction of a mesh and its optimization to 100,000 nodes is shown in Figure 2.20.

The white matter mask

The problem of segmenting the human cortex (GM) will be addressed now. The neocortex, a 1.5 up to 4.5mm thick layer at the outer surface of both brain hemispheres, contains about 80% of the neurons of the central nervous system [22], whereas the rest of GM can be found in deeper structures such as basal ganglia or the thalamus. The extraction of the GM from the brain leads to the WM mask for the multicompartment model.

When evaluating the T1 image segmentation results of the ISODATA clustering (Figure 2.12), unrealistic thicknesses of the GM were observed, whereas the compensation of intensity inhomogeneities by means of the AFCM yielded a more realistic cortical layer. Thus, one idea for the generation of the WM mask would be simply the extraction of all voxels with centroid c_2^{afcm} of the peeled and segmented brain, $T1^{\text{afcm}}$, i.e.,

$$WM^{\text{afcm}} := VBINARIZE(AND(T1^{\text{afcm}}, PEEL), 2, 2).$$

Axial	Coronal	Sagittal
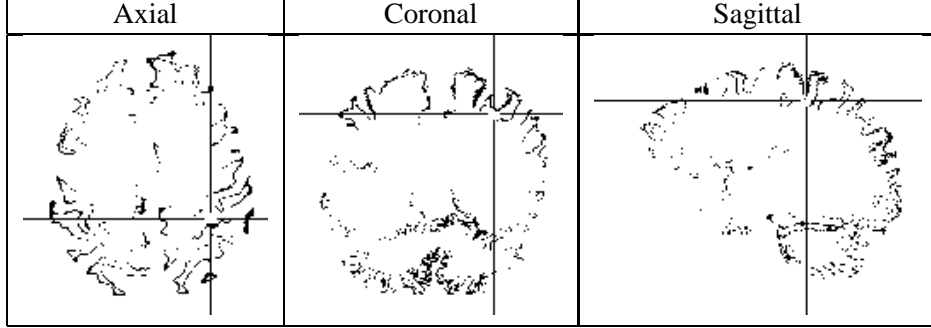
Figure 2.15: *Difference between the cortical layer thicknesses of the ISODATA and the AFCM segmentation results.*

If we denote

$$WM^{\text{iso}} := VBINARIZE(AND(T1^{\text{iso}}, PEEL), 2, 2),$$

the result of the operation $AND(VINVERT(WM^{\text{iso}}), WM^{\text{afcm}})$, shown in Figure 2.15, underlines again the difference between the cortical layer thicknesses of the AFCM and the ISODATA segmentation results. Since the inverse procedure, inverting WM^{afcm} and masking it with WM^{iso}, was observed to be empty (not shown), it can be concluded that ISODATA leads to a much thicker cortical layer.

Stimulated by the results of Lohmann et al. [141], a second way of generating a WM mask will be presented now, which better exploits anatomical knowledge about the cortex and which is not sensitive to remaining intensity differences between distant cortical areas in the corrected image $T1^{\text{corr}}$. The WM mask is generated through the call

$$WM = \textbf{GEN\_WHITE}(AND(T1^{\text{corr}}, PEEL), BRAIN, min, \alpha),$$

and Algorithm 7 presents the procedure as pseudocode. In the preprocessing steps, the voxels of the binary mask *BRAIN* (being assigned to the "update" version of the WM mask, WM^{upd}) are labeled (from outside to inside) and sorted by depth. Maximal global background and minimal global WM intensities and the parameter for statistics, I_{low}, I_{up} and α, resp., are determined from the image histogram of the peeled intensity corrected MRI of the brain, $BRAIN^{\text{corr}}$. Under the assumption of a minimal cortical thickness *min* and in order to build a sufficient local statistic,

$$I_{\text{loc}}(\mathbf{x}, \alpha) := I_\mu(\mathbf{x}) + \alpha I_\sigma(\mathbf{x})$$

Algorithm 7 GEN_WHITE($BRAIN^{\mathrm{corr}} \in MRI, WM^{\mathrm{upd}} \in BI, min \in \mathbb{N}, \alpha \in \mathbb{R}) \to (WM \in BI)$

$label = DIST(INVERT(WM^{\mathrm{upd}}))$

Sort *label* by depth, Determine I_{low} and I_{up} from $h_{MRI}(BRAIN^{\mathrm{corr}})$

for depth $d = 1$ to MAXDEPTH **do**

   ndelete $= 1$

   while *ndelete* ≥ 0 **do**

     ndelete $= 0$

     for all $\mathbf{x}$ of *label* at depth d **do**

       if $(label(\mathbf{x}) \leq min \ \vee \ I(\mathbf{x}) \leq I_{\mathrm{loc}}(\mathbf{x}, \alpha) \vee \ I(\mathbf{x}) \leq I_{low} \ \vee \ I_{up} \leq I(\mathbf{x}))$ **then**

         Delete $\mathbf{x}$ from WM^{upd} and from *label*

         ndelete $= ndelete + 1$

       end if

     end for

   end while

end for

$WM = BIGGESTCOMP(WM^{\mathrm{upd}})$

---

with I_μ the mean intensity and I_σ its standard deviation over all already deleted voxels in a local neighborhood of $\mathbf{x}$, the algorithm starts by removing the outer-most *min* layers of voxels. A voxel $\mathbf{x}$ within subsequent layers is only removed, if its intensity is not brighter than $I_{\mathrm{loc}}(\mathbf{x}, \alpha)$, otherwise it is assumed to be a WM voxel.

Results

The generation of the WM mask was carried out with the choice for the minimal cortical thickness of $min = 1$ and with the parameter setting $\alpha = 1.0$. Figure 2.16 shows the inner border of the resulting mask on the underlying peeled brain of the T1-MRI. Accurate segmentation of the WM/GM boundary was observed. A 3D rendering of the WM surface after extraction of a mesh and its optimization to 100,000 nodes is shown in Figure 2.20.

Discussion for the generation approach of the WM mask

Since the statistics for I_{loc} are based on local gray codes, Algorithm 7 can be seen as a segmentation strategy for the WM surface dealing with the problem of intensity inhomogeneities in the image and, in fact, this was one reason to develop it [141]. A comparison to the result of **GEN_WHITE** with the peeled brain from the uncorrected T1 image, $AND(T1, PEEL)$, was thus carried out,

Axial	Coronal	Sagittal
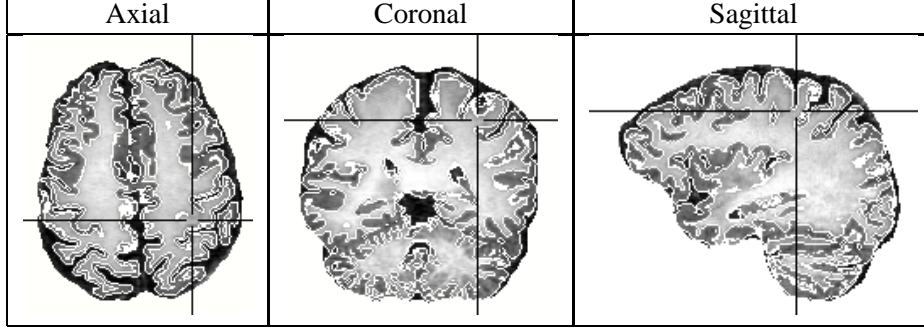
Figure 2.16: *Results for inner and outer cortical surface on underlying peeled brain.*

leading to slightly thicker gyral crowns and slightly thinner sulcal basins. Nevertheless, since the AFCM takes into account the problem of partial volume effect while dealing with intensity inhomogeneities, *WM* was found to have a slightly superior quality, but more data sets need to be analyzed to confirm this suggestion. Many other interesting approaches for the segmentation of the cortex can be found in the literature. In [44; 265; 130], a mesh was extracted from a presegmented GM/WM boundary, yielding a good initial surface, which is then refined using a deformable model, similar to the descriptions in Section 2.5.4. Such energy-minimizing deformable models generally preserve the topology of the initial surface. If it has the topology of a sphere (Euler number 2, see Definition 2.2.9), the deformation result has the same topology. This feature was used by Dale and Sereno [44] to computationally flatten the cortex after deformation in order to ease interpretations of source reconstruction results. In contrast to such classical "snake" models obtained via energy minimization, intrinsic ones derived from curvature based flows and implementing the surface propagation by level set approaches automatically handle topology changes if, e.g., pieces of the boundary merge or break. A theoretical link between such approaches and the classical models was developed by Caselles et al. [36]. High elasticity of the intrinsic models, being able to grow into sharp corners or cusps, and a lower sensitivity to the choice of the initial surface were reported by Malladi et al. [150]. Zeng et al. [272] applied a level set approach to the problem of cortex segmentation, yielding promising results.

2.6.3 Improved segmentation of the inner skull surface

As explained in the introduction to this chapter, the accurate segmentation of the boundary between the skull and the intracranial tissues is considered to be of

---

Script 2.6.4. ISS : $(T1, PD^{reg} \in MRI, \lambda_1, \lambda_2, N_v \in \mathbb{N}, \varepsilon, \delta, \omega_{int}, \omega_{ext}, \tau, d \in \mathbb{R}) \rightarrow (ISS \in BI)$

1. $(PD^{corr}, PD^{afcm}, c_0^{PD}, c_1^{PD}) = \mathbf{AFCM}(PD^{reg}, 2, \lambda_1, \lambda_2, \varepsilon, \delta)$ /* class. */

2. $segm\_bin = BIGGESTCOMP(BINARIZE(PD^{afcm}, 1, 1))$ /* peeling */

3. $small\_inner = BIGGESTCOMP(EROSION(segm\_bin, 6))$

4. $too\_large\_inner = DILATION(small\_inner, 8)$

5. $peeled\_inner = AND(segm\_bin, too\_large\_inner)$

6. $del\_iso\_points = BIGGESTCOMP(peeled\_inner)$ /* cleaning */

7. $IN = INVERT(BIGGESTCOMP(INVERT(del\_iso\_points)))$

8. $IS = (\mathbf{DEFORM}(PD^{corr}, IN, N_v, \frac{c_0^{PD}+c_1^{PD}}{2}, \omega_{int}, \omega_{ext}, \tau))$ /* Improve */

9. $ISS = \mathbf{FILL}(IS, d)$ /* fill */

---

special importance for both EEG [194; 42; 43; 111; 185] and MEG [96] source reconstruction. Since therefore, the additional information in the registered PD modality is exploited, the generation of the ISS can be seen as the central result of this chapter. Within the following, the scripts for the generation of ISS and EISS are presented and a segmentation accuracy comparison is carried out.

Exploiting the registered PD-MRI

Script 2.6.4 describes the process of exploiting PD^{reg}, the result of the PD image registration onto the corresponding T1 modality (see Algorithm 2), for an accurate segmentation of the inner skull surface. The script begins in step 1 with a basic classification of the voxels. The fixed number of classes $C = 2$ is motivated by the two clear maxima in the PD image histograms, the first for skull voxels and the second for the proton-rich other tissues (see histogram h_{PD} in Figure 2.8). Within the next block of the script (steps 2-5), the *peeled_inner* mask (intracranial tissues) is peeled from its outer hulls, i.e., from water proton rich extracranial tissues, a process, which is comparable to the brain peeling in Script 2.6.2. Two parameters were fixed within this processing chain, the first one to 6 and the second to 8. This choice led to a satisfactory peeling for all tested data sets. After deletion of isolated points in step 6 and filling of cavities in step 7, a deformable

Script 2.6.5. EISS : $(T1 \in MRI, BRAIN \in BI, \lambda_1, \lambda_2 \in \mathbb{N}, \varepsilon, \delta, d_1, d_2 \in \mathbb{R}, I_{min}, I_{max} \in G_{MRI}) \rightarrow (EISS \in BI)$

1. $(T1^{corr}, T1^{afcm}, c_0^{T1}, c_1^{T1}, c_2^{T1}) = AFCM(T1, 3, \lambda_1, \lambda_2, \varepsilon, \delta)$ /* class. */

2. $close = \textbf{CLOSING}(BRAIN, d_1)$ /* Generate minimal inner mask */

3. $min\_inner = \textbf{DILATION}(close, d_2)$

4. $max\_inner = DILATION(min\_inner, 2)$ /* Gen. maximal inner mask */

5. $T1_{ext}^{corr} = INTRODUCE\_MARKERS(T1^{corr})$ /* extend MRI */

6. $T1_{ext}^{corr} = MARK(T1_{ext}^{corr}, min\_inner, PASS)$ /* Meninges/skull segm. */

7. $T1_{ext}^{corr} = MARK(T1_{ext}^{corr}, INVERT(max\_inner), STOP)$

8. $meninges = \textbf{ERG}(T1_{ext}^{corr}, 0, I_{min}, I_{max})$

9. $EISS = OR(SMOOTHING(meninges, 20), min\_inner)$ /* Smoothing */

model is applied in the last step, which extracts a mesh from the initial inner skull mask *IN*, simplifies it to N_v vertices and refines this surface by means of the registered intensity corrected image PD^{corr}. I_{lim} is chosen as the arithmetic mean of the centroids c_0^{PD} and c_1^{PD}. In a last step, the mesh *IS* is filled using Script 2.2.26, resulting in the final binary mask for the inner skull surface, *ISS*.

Estimation procedure based on an exclusive use of a T1-MRI

In Wagner et al. [243; 239], a procedure was presented for estimating the inner skull by means of closing and inflating the brain surface, using only a T1-MRI. It can be seen as the standard for inner skull modeling in EEG/MEG source reconstruction. Script 2.6.5 describes the estimation process. A basic classification of the T1 image into three tissue classes is carried out in the first step, where $C = 3$ is motivated by the three maxima in the T1 image histogram (see histogram h_{T1} in Figure 2.8). The generation of the minimal inner skull mask in steps 2 and 3, i.e., the d_1 closing of the brain mask and the subsequent inflation under the assumption of a CSF minimal thickness of d_2 are the main ingredients. Therefore, these operations were highlighted in the script. Since in T1-MRI, thick meninges can form a contrast to the skull tissues, the rest of the script (steps 4-9) is devoted to the segmentation of the meninges/skull boundary, making use of the extended region growing segmentation, presented in Algorithm 5. The minimal and maxi-

mal intensities of the meninges, I_{min} and I_{max}, resp., are estimated from the image histogram between *min_inner* and *max_inner*.

Results and comparison

Script 2.6.4 was applied to various dual echo data sets (see also [31]). The parameter tuning and the results for the first step were described in detail in Section 2.5.5. Here, the choice of parameters for the active contour model and the filling process are discussed. The number of vertices is reduced to $N_v = 30,000$, since the inner skull surface is only moderately curved. For the test sets, it was found that the weights $\omega_{int} = 0.06$ for the smoothing internal force and $\omega_{ext} = 0.01$ for the external force led to the best results and should thus be recommended. Nevertheless, for the presented data set, the binary mask *IN* was quite strongly flawed by imaging noise in the areas of the venae diploicae and granulationes arachnoideales (Pacchioni), so that better results of the deformable model were achieved by means of a stronger smoothing with $\omega_{int} = 0.09$ while choosing a moderate $\omega_{ext} = 0.002$. For $\tau = 10^{-2}$, the deformable model converged within 118 iterations. The choice of $d = 2$ was sufficient to get an Euler number of 1 for *ISS*. A 3D rendering of the resulting mesh *IS* is shown in Figure 2.20. Figure 2.6 shows the filling process within the last step of the script and Figure 2.21 visualizes the final result for the multicompartment head model.

Script 2.6.5 was then used for the generation of the EISS. The global parameters were set to $d_1 = 18$ and $d_2 = 0$, leading to the best "overall" results for the *EISS*.

Figure 2.17 presents the borders of *ISS* and *EISS* for the example data set. The *ISS* models well the boundary between intracranial and skull tissues, only a small inaccuracy at the cerebrum/skull boundary due to smoothing in the deformation algorithm remained. Because of the strong d_1 closing, the *EISS* is lying outside the *ISS* in especially the concave parts, i.e., the areas of temporal, sphenoidal and occipital skull base, as it can be seen in the saggital slice in Fig.2.17. Moreover, due to the meninges/skull-segmentation block in Script 2.6.5 (steps 5-9), misinterpreting skull spongiosa as meninges voxels, the *EISS* is lying outside the *ISS* in a small frontal area of the neurocranial roof. A more moderate choice of the closing parameter d_1 improves the result at the skull base, but causes an even worse closing of the cortex layer at the neurocranial roof, discussed in the following. The estimated surface is lying inside the ISS in parietal and large parts of the frontal areas of the neurocranial roof, partly caused by an underestimation of the CSF layer by means of the parameter choice $d_2 = 0$.

In Fig.2.18, the parietal area in the neurocranial roof with the largest error in the coronal slice of Fig. 2.17 was magnified. Notice the high registration accu-

Axial	Coronal	Sagittal
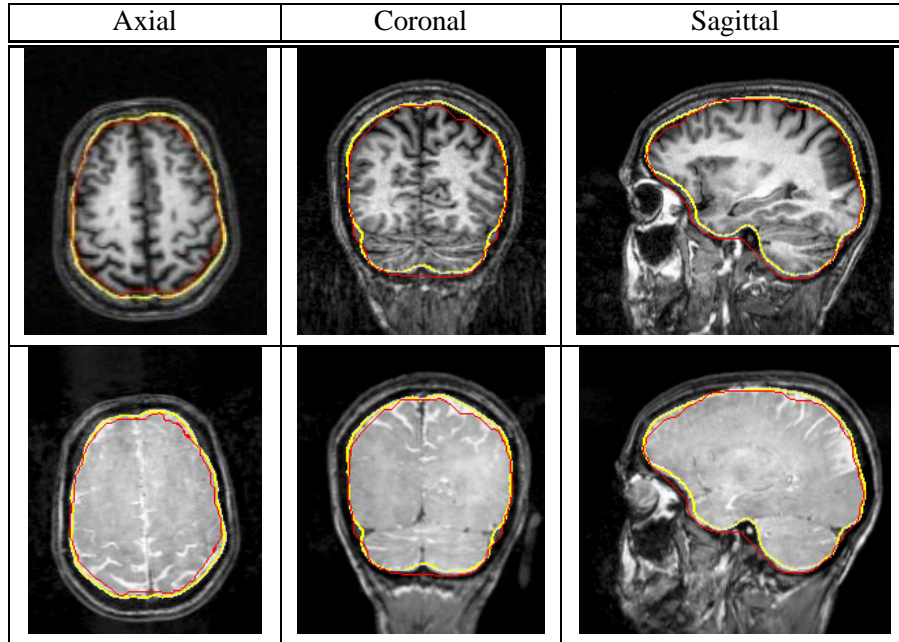
Figure 2.17: *Comparison of the inner skull segmentation results, using the bimodal data set and Script 2.6.4 (border of ISS, yellow) or exclusively the T1 image and Script 2.6.5 (border of EISS, red).*

racy, which can be made out again. In this area, the CSF layer was much thicker than estimated using the T1 MRI and $d_2 = 0$. It can be seen that the EISS is 6 voxels in diagonal direction, i.e., 8.49mm, away from the realistic inner skull boundary. The choice $d_2 = 2$ improved the *EISS* in parietal and large parts of the frontal roof and led to a reduction of the maximal error to 5.6mm in the magnified area in Fig. 2.17, but pushed the boundary so far outside a realistic one at especially the skull base, that a subsequent accurate OSS determination (see next subsection) is difficult. Comparable results were found for the other data sets.

With regard to EEG/MEG source localization, $d_2 = 2$ is considered to be the better choice, if sources in the upper frontal, parietal or occipital areas should be localized, whereas $d_2 = 0$ is better suited for mesial-temporal and basal frontal sources. The presented results are in agreement with those, reported by Huiskamp et al. [111], where a matched set of CT and MR were compared with the estimation procedure.

EISS on T1	*EISS* on PD	*ISS* on T1	*ISS* on PD
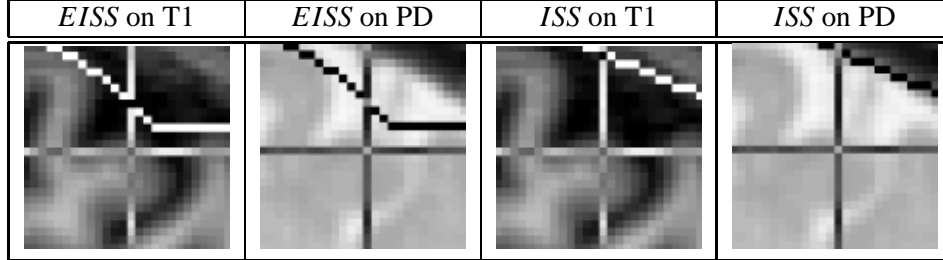
Figure 2.18: *Magnification of the parietal area of the neurocranial roof where the CSF layer is thicker than being estimated by means of the T1-MRI based EISS, as the PD image and the border of the ISS show.*

2.6.4 Modeling the outer skull surface

With regard to EEG source reconstruction, an exact modeling of skull shape and thickness and thus an accurate segmentation of the OSS is important. This was reported in [58; 135; 185; 228; 174]. In contrast, an exact OSS modeling is not necessary, if exclusively MEG data is used and the skull layer is closed (no surgery hole). In that case, the volume currents outside the ISS boundary are so weak, that they are assumed to be negligible for magnetic field simulations [97; 103].

As seen in Section 2.5.5, the compensation for scanner inhomogeneities led to strong segmentation improvements for especially the skull/skin boundary, whereas large holes in the skin layer resulted from the use of simple clustering methods like ISODATA. Therefore, the intensity corrected images are used here for a contrast enhancement. The corrected PD image can not only be used for the ISS segmentation, but also for the outer skull surface. Nevertheless, the *OSS* segmentation on the basis of the PD image can be seen as being a subset of the script for the segmentation of the T1 image, since the skull spongiosa do not complicate the process as much as for the T1 image.

The processing chain for the *OSS* generation from the T1 image is presented in Script 2.6.6. One ingredient for this script is the mask of the head surface, *HEAD*, which was already generated in Section 2.6.1. The script begins with the extension of the intensity corrected T1 image using Operation 2.2.21. In step 2, a minimal mask *min* for the outer skull is generated under the assumption of a minimal skull thickness of 3 voxels. Notice, that generally, parts of the border of *min* will still be inside the spongiosa, whereas other parts will be already well-located in the outer compacta layer of the 3-layered (compacta/spongiosa/compacta) skull. In step 3, a maximal outer mask *max* is determined, so that *min* and *max* enclose the boundary that has to be segmented. Image markers are set in steps 4 and

Script 2.6.6. OSS : $(T1^{corr} \in MRI, ISS, HEAD \in BI, elastic \in G_{0,1}, I_{min}, I_{max}, N_v, c_0^{afcm}, c_1^{afcm} \in \mathbb{N}, \omega_{int}, \omega_{ext}, \tau \in \mathbb{R}) \rightarrow (OSS \in BI)$

1. $T1_{ext}^{corr} = INTRODUCE\_MARKERS(T1^{corr})$ /* extend MRI */

2. $min = DILATION(ISS, 3)$ /* minimal outer mask */

3. $max = AND(DILATION(min, 6), HEAD)$ /* maximal outer mask */

4. $T1_{ext}^{corr} = MARK(T1_{ext}^{corr}, min, PASS)$ /* segm. initial mask */

5. $T1_{ext}^{corr} = MARK(T1_{ext}^{corr}, INVERT(max), STOP)$

6. $OSS\_in = OR(SMOOTHING(\mathbf{ERG}(T1_{ext}^{corr}, elastic, I_{min}, I_{max}), 6), min)$

7. $OS = \mathbf{DEFORM}(T1^{corr}, OSS\_in, N_v, \frac{c_0^{afcm} + c_1^{afcm}}{2}, \omega_{int}, \omega_{ext}, \tau)$ /* Improve */

8. $OSS = FILL(OS, 1)$

5 (Operation 2.2.22). In step 6, beginning from a seedpoint inside *min* and using Algorithm 5, the region grows towards the skull/skin-boundary. Subsequent smoothing of the resulting mask while respecting the assumption of a minimal skull thickness yields the initial outer skull mask *OSS_in*. Minimal and maximal intensities for the skull compacta, I_{min} and I_{max}, resp., are estimated from the image histogram between the masks *min* and *max*. An active contour model is then applied, which extracts a mesh from *OSS_in*, simplifies it to N_v vertices and refines this surface by means of the intensity corrected image $T1^{corr}$. I_{lim} is chosen as the arithmetic mean of the centroids c_0^{afcm} and c_1^{afcm} of the T1 image classification. In a last step, the mesh *OS* is filled using Script 2.2.26, resulting in the final binary mask, *OSS*.

Results and discussion

Intermediate results and parameter choices of Script 2.6.6 are now discussed. Figure 2.19 (middle left) shows the resulting surface *S* of Algorithm 5 for high elasticity (*elastic* = 1). The subsequent smoothing yielded the initial outer skull mask *OSS_in*, which is located outside the skull spongiosa, as Figure 2.19 (middle right) shows. Most spongiosa voxels have a higher gray value than estimated for I_{max}, the maximal intensity of the skull compacta. Therefore, *elastic* = 1 is needed in order to enable a surface-growing into the thin cleft between the spongiosa and the skin. Low elasticity (*elastic* = 0) is not sufficient in order to

elastic = 0	elastic = 1	*OSS_in*	*OSS*
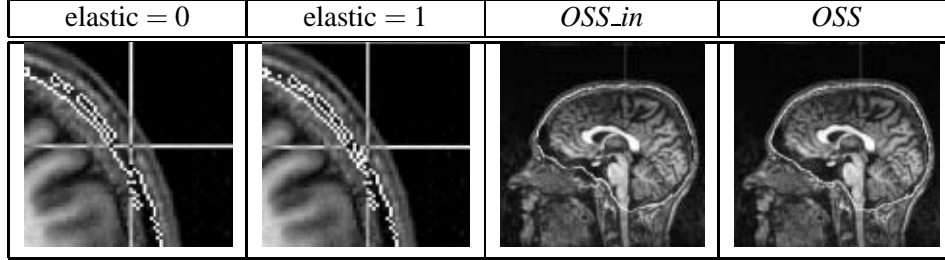
Figure 2.19: *Results of script 2.6.6: ERG surface results for low (left) and higher (left middle) elasticity, border of OSS_in (right middle) and of OSS (right) on underlying T1 image for high elasticity.*

generate a mask *OSS_in* as a suitable initialization of the deformable model from outside the spongiosa. This is shown with the resulting surface *S* of Algorithm 5 for *elastic* = 0 (Fig.2.19, left). In order to refine the initial mesh, a deformable model is applied. The choice of $\omega_{int} = 0.05$ and $\omega_{ext} = 0.01$ was appropriate for the presented data set and with $\tau = 10^{-2}$, convergence was achieved within 99 iterations. The active contour model compensated especially for a remaining outer skull surface error in the area of the sinus sphenoidales (see Fig.2.19, right). The mesh *OS* is shown in Figure 2.20 and Figure 2.21 shows the final result in the multicompartment head model. The Euler number of *OSS* was controlled to be 1.

However, one problem has to be discussed for the used MR data sets with regard to the OSS segmentation. Since fat hydrogen protons have a different magnetic resonance than those of water, they could be shifted relative to water in the readout gradient direction, i.,e., for the presented data set, in the superior to inferior direction. For a 1.5 Tesla scanner, this could mean a fat shift of up to 1mm, while for the used 3 Tesla scanner, the shift could amount up to 2mm in superior to inferior direction. A possibility to avoid such errors may be the use of separate fat/water MR sequences.

2.6.5   Generation of multi compartment head models

In Figure 2.20, 3D renderings of the multicompartment model tissue boundaries are shown. The mesh for the scalp was extracted from the corresponding mask *SCALP* and appropriately simplified for visualization. The rendering for the ventricles was produced by means of an extended region growing and a subsequent extraction of the surface mesh.

The generation of the multicompartment model of the class CPI is now straight-

ventricles	white matter	brain
inner skull	outer skull	scalp
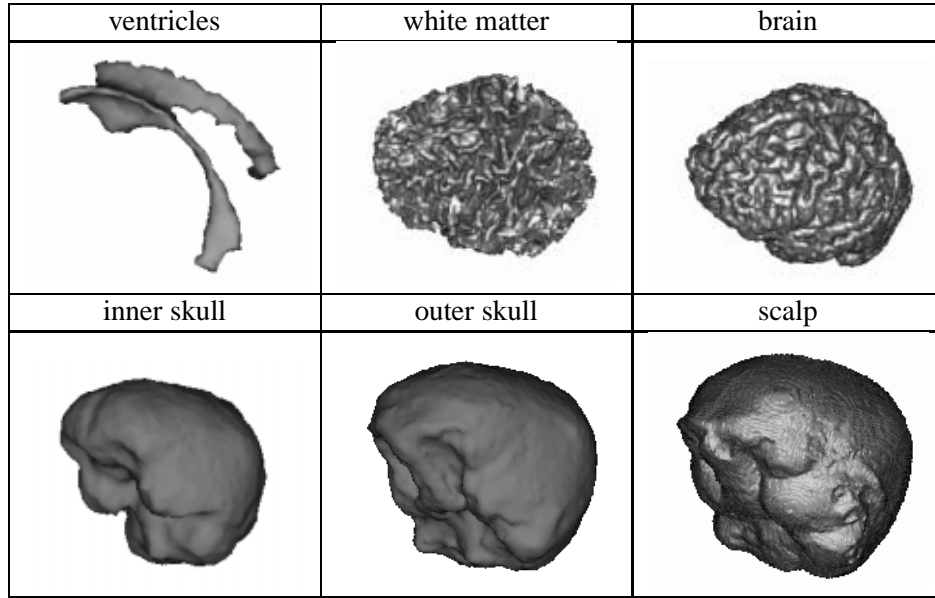
Figure 2.20: *3D rendering of tissue boundaries in multicompartment head model.*

forward. Each voxel is labeled with regard to its membership as a skin, skull, CSF, GM or WM voxel. This yields the *5 tissue head model*, which is shown in Figure 2.21.

Following recent conductivity measurements of Akhtari et al. [3], the skull has to be seen as a three-layer model with strongly differing conductivities for the compartments Outer Skull Compacta (OSC), skull spongiosa and inner skull compacta. This is visualized in Figure 2.22 [182]. The OSC compartment was observed to have a relatively constant thickness of about 2mm and the lowest measured conductivity of all three layers, while the relative thicknesses of the two layers of the Remaining part of the Skull (RS), i.e., spongiosa to inner compacta, are location dependent (see [3; 240] and Section 4.8.4). Together with the fact, that the MRI contrast is insufficient, a further decomposition of the RS compartment into its two layers is not possible here. The skull was thus further decomposed by means of eroding the OSS with a distance of 2mm, resulting into the mask for the remaining skull,

$$RS = EROSION(OSS, 2). \tag{2.6}$$

On this way, the *6 tissue head model* is obtained.

Axial	Coronal	Sagittal
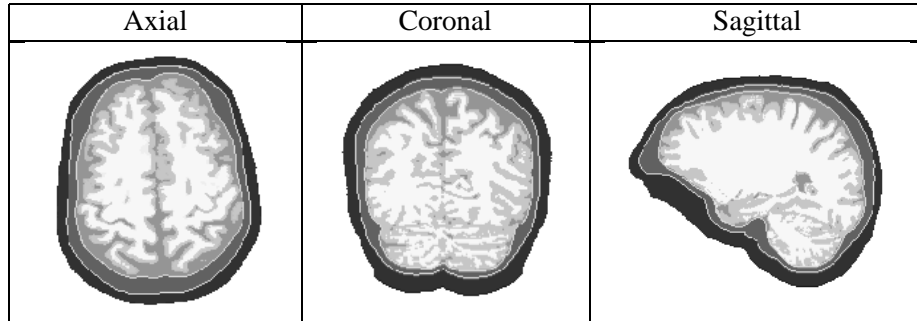
Figure 2.21: *The 5 tissue head model.*

2.7   Summary and Conclusions

Within this chapter, methods were presented for the generation of a realistic 5 or 6 compartment model of the human head, based on bimodal T1/PD MR data sets. It was focused on an improved segmentation of the inner skull surface. Scripts were presented for the segmentation of scalp, outer and inner skull and brain and white matter surfaces.

Many studies can be found in the literature, reporting large errors of EEG-based [42; 43; 110; 111] or MEG-based [96; 97] source reconstruction procedures due to misspecifications of skull shape or incorrect modeling of the inner skull surface, resp.. When a CT image cannot be attained because the necessary radiation cannot be justified, then the current standard approach for skull surface modeling is based only on a T1-MRI. A T1 MR image is well suited for the segmentation of surfaces like white and gray matter and scalp, as shown in this chapter, but poses problems in the identification of the inner skull surface. In order to overcome this problem, estimation procedures were presented in [243; 107; 239; 193] for a T1-MRI based approximation. In [243; 107; 239], the T1 segmented brain surface was closed and inflated in order to approximate the inner skull surface. Nevertheless, errors in the EEG-based localization of current sources in the human brain of up to 1cm were reported [111]. The errors were arising from skull models with estimated inner surface when compared with models from a matched set of CT/T1-MRI and appeared in mesial-temporal and basal frontal areas, especially important in the area of epilepsy surgery. Furthermore, in pathological cases with brain atrophy, the local estimation of the CSF layer thickness by means of the global inflation parameter in the estimation procedure is far from realistic. With modifications, the T1-MRI based inner skull estimation procedure of Wagner el al. [243; 239] was used in order to compare segmentation results for the inner skull surface.

Figure 2.22: *The human skull: Suture lines and the tri-layeredness [182].*

With the presented approach, the PD image, measured together with the T1 image in a single session, fills the information gap for accurate inner skull surface segmentation. As a first step of the script, a voxel-similarity based affine registration of the PD onto the corresponding T1 image is carried out, correcting for movement of the subject and geometrical distortions. The presented implementation showed subvoxel accuracies in the registration results. An initial mask, whose surface is a good guess for the boundary between intracranial and bone tissues, is then generated using a 3D implementation of an AFCM algorithm, and a combination of basic image operations. In a last step, a mesh is extracted from the initial mask, simplified to a coarser vertex count and refined by means of a deformable model, yielding a smooth and accurate, memory efficient representation of the inner skull surface.

When comparing the result of the presented approach with the result of the T1-MRI based estimation procedure, strong segmentation improvements were found at the skull base in especially frontal and temporal areas. The results are in agreement with [111]. A more moderate choice of the global closing parameter in the estimation procedure improved its segmentation result at the skull base, but led to larger errors at the neurocranial roof. Additionally, we found segmentation discrepancies in those upper parietal and frontal areas, where the thickness of the CSF layer was underestimated. If the closed brain surface is not globally inflated, an error of the estimation procedure of up to 8.5mm was found for the presented data set in a parietal area of the neurocranial roof. The assumption of

a global minimal CSF layer thickness of 2 voxels reduced the error in this area to 5.6mm, whereas an even increased error in the skull base had to be accepted. This shows, that an optimal tuning of the global closing and inflation parameters of the estimation procedure to all local needs is difficult, whereas such problems do not exist for the presented approach.

Under the assumption of a minimal skull thickness, the presented outer skull segmentation script uses the dilated inner skull surface as a starting point for a high elastic extended region growing algorithm. A high elasticity is needed to enable the growing into the thin skull compacta cleft between spongiosa and skin. An initial guess outside the skull spongiosa resulted, an important prerequisite. A subsequent application of the active contour model refined to the outer skull surface, improving the initial guess especially in the skull base area around the sinus sphenoidales. Nevertheless, the possibility of using separate fat/water sequences should be discussed to avoid the chemical fat shift, which may spoil the representation accuracy of the outer skull surface modeling, especially on a 3 Tesla scanner.

The presented segmentation scripts provide a nearly automatic, individual and improved modeling of the various head compartments, using the information of non-invasive MR protocols. Only the weighting for inner and outer forces of the deformable model for the inner skull surface had to be adapted for one of the five tested data sets, since its PD image was locally noise-flawed. Nevertheless, both MR protocols do not give a contrast between bone tissues and air, so that the presented approach is unable to delineate the frontal sinuses or the sinus sphenoidales, which are erroneously addressed as bone. Moreover, the assumption of a minimal skull thickness in the segmentation script for the outer skull surface is incorrect at the foramen magnum, the foramen jugulare and the optic nerve and sphenoidal tract, where the skull has openings.

However, in EEG/MEG the sensors are far from the above mentioned areas, so that an exact modeling of those parts of the skull is not necessary for source localization and the openings are generally filled [73; 111; 237].

The 3D AFCM implementation was shown to improve the segmentation of MR images in the presence of intensity inhomogeneities when compared to unsupervised clustering methods like the ISODATA algorithm. Preconditioning solver techniques yielded the necessary accuracy in extracting the multiplier field from the noise-flawed images. The AFCM led to an improved segmentation of the cortex layer and to a closed skin surface and the intensity corrected images build an important basis for the generation of the initial outer skull surface guess. For images, flawed with stronger intensity inhomogeneities, presented e.g. in [181], one could imagine an ERG growing into the skin layer or even into the background, if the nonuniformities were not taken into account. Strong inhomogeneities could

also spoil an initial guess for the inner skull surface. This underlines the importance of the chosen AFCM classification as a basic segmentation component for multicompartment modeling. The improved cortex segmentation through AFCM can be exploited for an incorporation of physiological and anatomical constraints to inverse source reconstruction, i.e., a better representation of the influence space (see Section 6.2).

The new results of this chapter have been published in Wolters et al. [261; 255] and Burkhardt et al. [31; 32]. A further manuscript is in the review process [33].

Chapter 3

Modeling tissue conductivity anisotropy

3.1   Introduction

The particular importance of an exact modeling of the skull shape for EEG- and of the inner skull surface for MEG-source reconstruction was pointed out in the last chapter. From a macroscopic point of view, the head compartment skull has to be regarded as one unit consisting of a soft bone layer (the well-conducting spongiosa, visualized as the layer with small liquid-filled holes in Fig. 2.22) enclosed by two hard bone layers (the low-conducting outer and inner compacta). Its conductivity then shows an anisotropy with a ratio of about 1 to 10 (radially to tangentially to the skull surface) [197; 49; 52; 228; 152]. This is due to the fact, that in the radial direction the three layers are connected in series whereas they are connected parallel in both tangential directions. First results show that neglecting this anisotropy in the forward problem can lead to spurious errors in the inverse current reconstruction result [227; 151; 228; 152].

Conductivity anisotropy with a ratio of about 1 to 9 (normal to parallel to fibers) has also been measured for brain WM by Nicholson [165], but still, its robust and non-invasive direct measurement seems to be impossible. Nevertheless, a formalism has been described recently for relating the effective electrical conductivity tensor to the effective water diffusion tensor in brain WM (Tuch et al. [223; 224]). Water diffusion can be measured non-invasively by DT-MRI. Fig. 3.1 shows a WM fiber orientation map from a DT-MRI experiment [261]. The mutual restriction of both the ionic and the water mobility by the geometry of the porous medium (the WM fibers) builds the basis for the described relationship. The assumption is not, of course, that a fundamental relation exists between the free mobility of ionic and water particles. The claim is rather that
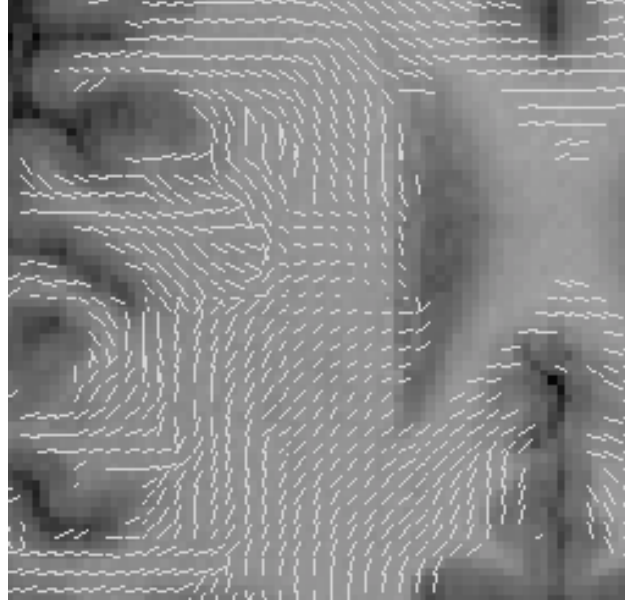
Figure 3.1: *Fiber orientation map from a DT-MRI experiment. Eigenvector orientations corresponding to the largest eigenvalue are projected onto the imaging plane, and overlaid on a T1 weighted MRI. Eigenvector directions were suppressed in voxels with FA < 0.2 (see Definition for FA in Equation (3.16))*

the restricted mobilities are related through the geometry. Basser et al. [16] introduced the assumption that the conductivity tensor shares the eigenvectors with the water diffusion tensor.

This chapter describes the modeling of realistic skull and WM conductivity anisotropy, exploited in the next chapter for the generation of realistic anisotropic high-resolution volume conductor models of the head.

3.2 Notion of a tensor

We will now closely follow Danielson [45] for the notion of a tensor.
Tensors defined: We begin with a *tensor of order zero*, which is defined as being simply another name for a scalar [45].

A given vector $\mathbf{a}$ may be dotted into any vector $\mathbf{v}$ to produce a scalar $\mathbf{a} \cdot \mathbf{v}$. The combination $\mathbf{a} \cdot$ is a linear function, since it is

$$\mathbf{a} \cdot (c\mathbf{u} + \mathbf{v}) = c\mathbf{a} \cdot \mathbf{u} + \mathbf{a} \cdot \mathbf{v}$$

for all scalars c and vectors $\mathbf{u}$ and $\mathbf{v}$. A *tensor of order one* is a linear function that maps every vector into a scalar [45]. Any combination $\mathbf{a}\cdot$ is thus a tensor of order one.

A pair of vectors $\mathbf{ab}$ is called a *dyad*. A dyad is defined through the mapping rules

$$\mathbf{ab}\cdot\mathbf{v} := \mathbf{a}(\mathbf{b}\cdot\mathbf{v}) \qquad \mathbf{u}\cdot\mathbf{ab} := (\mathbf{u}\cdot\mathbf{a})\mathbf{b}.$$

Dyads have linear properties. A *tensor of order two* is a linear function that maps every vector into a vector [45]. Any combination $\mathbf{ab}\cdot$ is thus a tensor of order two.

Some properties: Every second order tensor $\mathbf{S}$ has a unique transpose $\mathbf{S}^{tr}$, obeying $\mathbf{v}\cdot\mathbf{S}^{tr} = \mathbf{S}\cdot\mathbf{v}$ for all vectors $\mathbf{v}$ ($(\mathbf{ab})^{tr} = \mathbf{ba}$). A tensor is called symmetric if $\mathbf{S}^{tr}\cdot\mathbf{v} = \mathbf{S}\cdot\mathbf{v}$ for all $\mathbf{v}$. In a 3-dimensional space every second order tensor $\mathbf{S}$ maps certain vectors into scalar multiples of themselves, i.e., $\mathbf{S}\cdot\mathbf{v} = \lambda\mathbf{v}$. λ is called an eigenvalue and $\mathbf{v}$ is called an eigenvector corresponding to λ.

Tensor components: Any tensor can be expressed in terms of components along an orthonormal basis. The components of a tensor are completely determined by its action on the base vectors. If a tensor of order one is considered, denoted by $\mathbf{f}$, and the Cartesian components of $\mathbf{f}$ are defined by $a_i := \mathbf{f}(\mathbf{e}_i)$, then it is

$$\mathbf{f}(\mathbf{v}) = \sum_{i=1}^{3} \mathbf{f}(v_i\mathbf{e}_i) = \sum_{i=1}^{3} v_i\mathbf{f}(\mathbf{e}_i) = \mathbf{a}\cdot\mathbf{v} \qquad \forall\mathbf{v},$$

since it is a linear function. Therefore, any tensor $\mathbf{f}$ of order one can be represented by a vector $\mathbf{a}$. Consider now a tensor of order two, $\mathbf{S}$. Define the nine Cartesian components of $\mathbf{S}$ by $S^{[ij]} := \mathbf{e}_i\cdot\mathbf{S}\cdot\mathbf{e}_j$. We then find

$$\mathbf{u}\cdot\mathbf{S}\cdot\mathbf{v} = \sum_{i,j=1}^{3} u_i S^{[ij]} v_i = \sum_{i,j=1}^{3} \mathbf{u}\cdot(S^{[ij]}\mathbf{e}_i\mathbf{e}_j)\cdot\mathbf{v} \qquad \forall\mathbf{u},\mathbf{v},$$

so that it follows $\mathbf{S} = \sum_{i,j=1}^{3} S^{[ij]}\mathbf{e}_i\mathbf{e}_j$, i.e., any second order tensor can be decomposed into a linear combination of the dyads (called *dyadic*) formed from the base vectors. Therefore, a 3×3 matrix can be formed from the Cartesian components of the tensor of order two, the so-called *matrix of the tensor* (relative to the given basis), and all the components can then be manipulated with standard techniques of matrix algebra. It follows, that $\mathbf{S}$ is a symmetric tensor if and only if $S^{[ij]} = S^{[ji]}$, i.e., its matrix is symmetric.

Eigenvector representation: A symmetric tensor $\mathbf{S}$ has three real eigenvalues, $s_1, s_2, s_3 \in \mathbb{R}$, which can be determined by means of the characteristic polynomial of the tensor [45] (the determination procedure is well-known for the matrix of the tensor). The corresponding eigenvectors, $\hat{\mathbf{e}}_1, \hat{\mathbf{e}}_2, \hat{\mathbf{e}}_3$, are mutually orthogonal. The *principal axis* of $\mathbf{S}$ are the Cartesian axes in the direction of its eigenvectors. Since

it is $\mathbf{S} \cdot \hat{\mathbf{e}}_i = s_i \hat{\mathbf{e}}_i$, and when dotting this relation from the left with the eigenvectors and exploiting the symmetry relation $\mathbf{S} = \mathbf{S}^{tr}$, then the following equations can be derived [45]

$$(s_1 - s_2)\hat{\mathbf{e}}_1 \cdot \hat{\mathbf{e}}_2 = 0 \qquad (s_1 - s_3)\hat{\mathbf{e}}_1 \cdot \hat{\mathbf{e}}_3 = 0 \qquad (s_2 - s_3)\hat{\mathbf{e}}_2 \cdot \hat{\mathbf{e}}_3 = 0.$$

With regard to skull and WM tensors, two different cases are important:

- If $s_1 \neq s_2 \neq s_3$, then $\hat{\mathbf{e}}_1 \cdot \hat{\mathbf{e}}_2 = \hat{\mathbf{e}}_1 \cdot \hat{\mathbf{e}}_3 = \hat{\mathbf{e}}_2 \cdot \hat{\mathbf{e}}_3 = 0$, so the eigenvectors are orthogonal.

- If $s_1 = s_2 \neq s_3$, then $\hat{\mathbf{e}}_1 \cdot \hat{\mathbf{e}}_3 = \hat{\mathbf{e}}_2 \cdot \hat{\mathbf{e}}_3 = 0$, so $\hat{\mathbf{e}}_1$ and $\hat{\mathbf{e}}_2$ may be chosen mutually orthogonal with any orientation in a plane normal to $\hat{\mathbf{e}}_3$.

A symmetric tensor $\mathbf{S}$ can be represented by the dyadic $\mathbf{S} = \sum_{i=1}^{3} s_i \hat{\mathbf{e}}_i \hat{\mathbf{e}}_i$ [45], called the *spectral representation* of $\mathbf{S}$. When the principle axes of $\mathbf{S}$ are chosen for the coordinates $(\hat{v}_1, \hat{v}_2, \hat{v}_3)$ of a vector $\hat{\mathbf{v}}$ (i.e., $\hat{\mathbf{v}} = \sum_{i=1}^{3} \hat{v}_i \hat{\mathbf{e}}_i$), the spectral representation of $\mathbf{S}$ produces a diagonal quadratic form

$$\hat{\mathbf{v}} \cdot \mathbf{S} \cdot \hat{\mathbf{v}} = \sum_{i=1}^{3} s_i \hat{v}_i^2.$$

The equation $\hat{\mathbf{v}} \cdot \mathbf{S} \cdot \hat{\mathbf{v}} = 1$ defines a quadric surface, whose equation in the principle axis of $\mathbf{S}$ is

$$s_1 \hat{v}_1^2 + s_2 \hat{v}_2^2 + s_3 \hat{v}_3^2 = 1.$$

The signs of the eigenvalues of $\mathbf{S}$ determine the type of surface, given by this equation. If $\mathbf{S}$ is positive definite, i.e., its eigenvalues are all positive, then the quadric surface is an *ellipsoid*.

The later considered self-diffusion and conductivity tensors are Symmetric Positive Definite (SPD). For the diffusion tensor, e.g., symmetry follows from the microscopic reversibility of the particle trajectories [15] and positivity of the eigenvalues from the second law of thermodynamics [126].

In our case, it was sufficient to define tensors along dyads of base vectors that are orthonormal. Note as a final remark for the notion of tensors that the more general definition of the so-called *covariant* and *contravariant tensors* [271; 45] does not necessarily assume an orthonormal system.

3.3   Modeling the skull conductivity anisotropy

As mentioned in the introduction, the human skull shows a conductivity anisotropy with high resistance in the radial direction (series connection of a high, a low and a high resistor) and with much lower resistance in both tangential directions

---

Script 3.3.1. ANI : $(T1^{corr} \in MRI, ISS, OSS, RS \in BI, N_v \in \mathbb{N}, I_{lim}, \omega_{int}, \omega_{ext}, \tau \in \mathbb{R}) \rightarrow (SSSM \in MESH)$

   1. $T1^{corr}_{mod} = MODINT(T1^{corr}, ISS, 255)$ */* force SSSM to skull */*

   2. $T1^{corr}_{mod} = MODINT(T1^{corr}_{mod}, INVERT(OSS), 255)$

   3. $SSSM = \textbf{DEFORM}(T1^{corr}_{mod}, RS, N_v, I_{lim}, \omega_{int}, \omega_{ext}, \tau)$ */* smooth */*

(parallel connection of the three resistors). Our first assumption is that the skull tensor eigenvalues in both tangential directions are identical. As a consequence it is sufficient to determine the eigenvector in radial direction and exploit the vector product for both tangential ones.

The determination of the radial skull eigenvector is described in the first part of this section. The second part then focuses on modeling the eigenvalues.

3.3.1 Determination of the tensor eigenvectors

Marin et al.[151; 152] pointed out the importance of well-defined skull conductivity tensor eigenvectors and reported larger errors for the EEG potential in the case of an erroneous modeling. We therefore base our determination on the resulting mesh of a discrete deformable surface model, whose pseudo-code was presented in Section 2.5.4. The deformable model is applied here in order to generate a Smooth Surface Spongiosa Model (SSSM), i.e., a strongly smoothed triangular mesh, which is shrunken from the RS mask (see (2.6)) onto the outer spongiosa surface. In order to extract the radial direction of the skull by means of the surface normals of this mesh, the following requirements are made for the SSSM:

- The mesh has to be located inside the skull compartment.

- The mesh has to approximate the outer surface of the skull spongiosa.

- The mesh has to be smooth, so that radial directions are not changing too strongly for neighbored points in the skull.

Script 3.3.1 is considered to be appropriate for fulfilling the above requirements. In the first two steps, in order to force the SSSM to remain inside the segmented skull compartment, the gray values of all voxels of the intensity corrected T1 image inside the inner skull mask, *ISS*, and outside the outer skull surface are set to the highest MRI gray value (see Operation 2.2.20), resulting
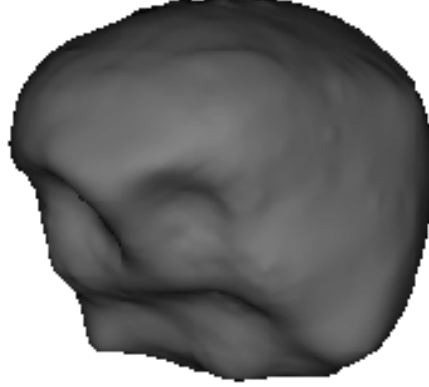
Figure 3.2: *3D rendering of the resulting SSSM for the determination of radial skull anisotropy directions.*

in the modified intensity corrected T1 image, $T1_{\text{mod}}^{\text{corr}}$. An active contour model is applied in the last step, which extracts a mesh from the *RS* mask, simplifies it to N_v vertices and smoothes this surface and refines it onto the outer spongiosa exploiting the modified intensity corrected T1 image. For each point in the skull layer, the radial skull direction is then modeled by means of the normal vector $\mathbf{n}_k$ of the SSSM vertex with minimal distance, $\mathbf{v}_k$. The two tangential directions are chosen mutually orthogonal in the plane normal to $\mathbf{n}_k$ using the vector product.

Result

Script 3.3.1 was applied with $N_v = 30,000$, a good choice for only moderately curved surfaces. For the presented data set, it was chosen a strong weighting of the smoothing force, $\omega_{int} = 0.07$, a moderate weighting for the external force, $\omega_{ext} = 0.002$, and with $\tau = 10^{-2}$, convergence was achieved within less than 100 iterations. Figure 3.2 shows a 3D rendering of the *SSSM*. The border of the mask, resulting from the application of Operation 2.2.25 to the *SSSM* is shown on the underlying T1 image in Fig. 3.3.

3.3.2 Determination of the tensor eigenvalues

Later in this thesis, SPD conductivity tensors in the barycenters of each skull finite element, in diagonalized form $\underline{\underline{\sigma}} = \mathbf{S}\,\mathbf{diag}(\sigma^{\text{tang}}, \sigma^{\text{tang}}, \sigma^{\text{rad}})\,\mathbf{S}^T$, are used when defining the FE volume conductor models. $\mathbf{S}$ denotes the orthogonal eigen-

Axial	Coronal	Saggital
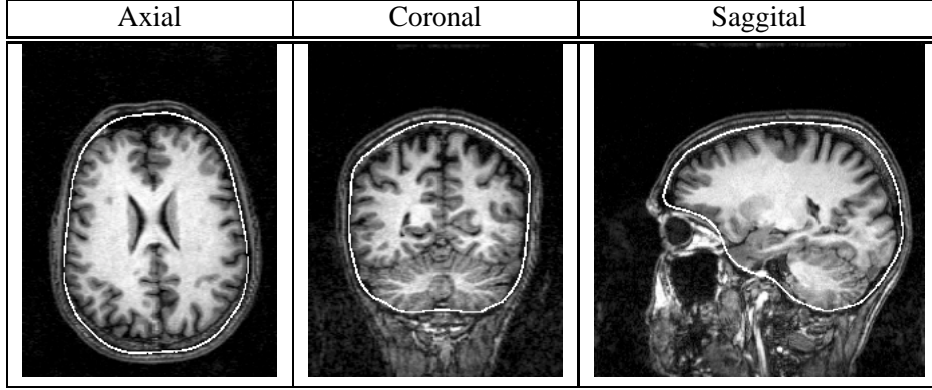
Figure 3.3: *Visualization of the SSSM for the determination of radial skull anisotropy directions onto the underlying T1-MRI.*

vector matrix, build of the two tangential and the radial skull tensor eigenvectors as described above, and $\sigma^{\text{tang}} \in \mathbb{R}^+$ and $\sigma^{\text{rad}} \in \mathbb{R}^+$ are the corresponding tangential and radial eigenvalues.

Simulated eigenvalues using the volume and Wang's constraint

Realistic modeling of the eigenvalues is a difficult task, not only because the thicknesses of spongiosa and inner compacta layers are varying and their inner boundary is difficult to segment, but especially because of skull resistivity inhomogeneities [135; 185; 174]. Therefore, while exploiting measured anisotropy ratios from the literature [197], the eigenvalues will be simulated within this thesis. For a given anisotropy ratio, $\sigma^{\text{rad}} : \sigma^{\text{tang}}$, radial and tangential eigenvalues are calculated, obeying two different constraints: A first constraint,

$$\sigma^{\text{rad}} \cdot \sigma^{\text{tang}} \stackrel{!}{=} \sigma_{\text{skull}}^2, \tag{3.1}$$

with $\sigma_{\text{skull}} \in \mathbb{R}^+$ the skull's isotropic bulk conductivity value (see Table 4.2) is denoted by *Wang's constraint* [245; 227]. The second, the *volume constraint*, retains the geometric mean of the eigenvalues and thus the volume of the conductivity tensor, i.e.,

$$\frac{4}{3}\pi\sigma^{\text{rad}}(\sigma^{\text{tang}})^2 \stackrel{!}{=} \frac{4}{3}\pi\sigma_{\text{skull}}^3. \tag{3.2}$$

The eigenvalues in a simplified 3-layer skull model

The following subsection should be considered as an additional remark concerning the determination of the skull's conductivity eigenvalues in the case of a sim-

o	o	o
s	s	s
i	i	i

Figure 3.4: *Two-dimensional variant of a simple 3x3 model of the three-layer skull with "o", "s" and "i" denoting "hexahedral elements" of outer compacta, spongiosa and inner compacta layers, resp. (Wagner et al. [240]).*

plified skull model (see Wagner et al. [240]). Figure 3.4 shows a two-dimensional variant of a simple 3x3 model of a three-layer skull. Let us now assume that the assumptions inherent in this model, i.e., modeling the skull by means of an extracted piece and thus the assumption of constant thickness of each layer over the whole skull, are not too restrictive. In this case, radial and tangential conductivity eigenvalues σ^{rad} and σ^{tang} can be computed from measured conductivities σ_i and thicknesses l_i^{rad} (see Akhtari et al. [3]) of each individual layer, as will be described in the following. The three equations

$$R^{\text{rad}} = R_1 + R_2 + R_3 \qquad \frac{1}{R^{\text{tang}}} = \frac{1}{R_1}\frac{1}{R_2}\frac{1}{R_3} \qquad R_i = \frac{l_i}{\sigma_i A_i}.$$

describe the basic relations for resistors in series and resistors in parallel and the relationship between conductivity σ_i and resistance R_i of the ith layer with thickness l_i and surface A_i [127, p.17,p.69]. When making use of the relation $A^{\text{rad}} = A_i^{\text{rad}}$ (see Fig. 3.4), the equation

$$\frac{l^{\text{rad}}}{\sigma^{\text{rad}}} = \sum_{i=1}^{3} \frac{l_i}{\sigma_i} \text{ with } l^{\text{rad}} = \sum_{i=1}^{3} l_i \qquad (3.3)$$

can be derived for the radial conductivity eigenvalue σ^{rad}, whereas the use of $l^{\text{tang}} = l_i^{\text{tang}}$ (see Fig. 3.4) yields the equation for the tangential conductivity eigenvalue σ^{tang},

$$A^{\text{tang}}\sigma^{\text{tang}} = \sum_{i=1}^{3} A_i^{\text{tang}}\sigma_i \text{ with } A^{\text{tang}} = \sum_{i=1}^{3} A_i^{\text{tang}}. \qquad (3.4)$$

3.4 Modeling white matter conductivity anisotropy

The relationship between the effective electrical conductivity tensor and the effective water diffusion tensor will now be worked out. Water diffusion in the

brain is non-invasively measured by DT-MRI, as described in Appendix A.9. The Section begins with the definition and the properties of the self-diffusion tensor. Based on a self-consistent differential effective medium approach in the porous brain medium, presented in Section 3.4.2, a linear relationship between the eigenvalues of both tensors for small intracellular diffusion and high resistivity of the cell membrane will be derived in Section 3.4.3. The last section is then concerned with the generation of a realistic anisotropic WM compartment, using whole-head DT-MRI measurements.

3.4.1 Definition of the self-diffusion tensor

All molecules and ions in the body fluids, including both water molecules and dissolved substances, are in constant random molecular motion due to thermal energy, the so-called Brownian motion. *Diffusion*, a result of this motion, is the process by which matter is transported from one part of the system to another [41]. In a fluid system with two types of non-uniformly distributed molecules, the molecule concentrations change with time until the equilibrium, i.e, both concentrations have the same value throughout the system, is reached. This process is also called transport diffusion. If the fluid consists of only one type of molecules, a part of them considered as being labeled, the process of translational motion is generally called *self-diffusion*. We will deal with self-diffusion throughout the rest of this thesis. In a paper of Einstein [56], the path of a diffusing molecule was modeled as a "random walk" and a proportionality relation, referred to as Einstein's equation, was derived between the mean square displacement of a particle, $< \mathbf{s}^2(t) >$, and the diffusion coefficient D and diffusion time t for free diffusion,

$$< \mathbf{s}^2(t) > = 6Dt. \tag{3.5}$$

In bounded systems, e.g., in biological systems, where cell membranes limit the free motion of the particles, the mean-squared displacement is usually reduced from that predicted by the Einstein relation and thus equation (3.5) does not strictly apply [108]. The effect experienced by diffusing water molecules will depend upon the diffusion time, i.e., as the molecules diffuse for a longer period of time, more restricting barriers will generally be encountered. An effective diffusion coefficient is commonly defined dependent on the observation time t as [126]

$$D^{\text{eff}}(t) = \frac{< \mathbf{s}^2(t) >}{6t}.$$

For small t, it is $D^{\text{eff}} = D$ and for long observation times, the mean displacement is bounded by the cell size so that D^{eff} goes to 0. In brain WM, diffusion is heterogeneous (i.e., depends upon position) at a microscopic length scale but is

homogeneous and anisotropic at a macroscopic length scale [16]. Therefore, an SPD (see Section 3.2) effective diffusion tensor, $\mathbf{D}^{\text{eff}}$, has to be used [15].

3.4.2 The differential effective medium approach

In the following, the differential Effective Medium Approach (EMA) will be presented which relates both the conductivity tensor eigenvalues and the diffusion tensor eigenvalues to the geometry of the medium. Following Stratton [217], the dielectric constant $\varepsilon_{CE}^*(\eta)$ of a coated ellipsoid (in the presented application a cylindrical WM fiber surrounded by extracellular medium) with volume fraction η can be computed as

$$\varepsilon_{CE}^*(\eta) = \varepsilon_e^* \left[\frac{\varepsilon_e^* + (\varepsilon_i^* - \varepsilon_e^*)(\eta + (1-\eta)L_v)}{\varepsilon_e^* + L_v(1-\eta)(\varepsilon_i^* - \varepsilon_e^*)} \right], \qquad \forall v = 1, 2, 3, \qquad (3.6)$$

with ε_e^* and ε_i^* the dielectric constants of the extra- and the intracellular medium, resp., and L_v the electromagnetic depolarization factor, which captures the contribution of the cell geometry to the bulk conductivity. The depolarization factors for a conducting ellipsoid have been derived by Landau and Lifshitz [131, p.19–25]. For a medium, made up of coated ellipsoids (in the presented application the WM compartment), Sen et al. [207] computed the dielectric constant ε^* from the dielectric constant of the assumed homogeneous medium, ε_0^*, plus the fluctuations through the jth coated ellipsoid, $\varepsilon_{CE}^{*(j)}(\eta_j) - \varepsilon_0^*$, using a multiple scattering formalism from solid state physics for disordered systems,

$$\varepsilon^* = \varepsilon_0^* \left(1 + 2 \sum_j f_j \frac{\varepsilon_{CE}^{*(j)}(\eta_j) - \varepsilon_0^*}{\varepsilon_{CE}^{*(j)}(\eta_j) + 2\varepsilon_0^*} \right) \left(1 - \sum_j f_j \frac{\varepsilon_{CE}^{*(j)}(\eta_j) - \varepsilon_0^*}{\varepsilon_{CE}^{*(j)}(\eta_j) + 2\varepsilon_0^*} \right)^{-1}. \qquad (3.7)$$

f_j is the volume fraction of the jth coated ellipsoid to the whole medium. In a next step, the *self-consistent approximation* $\varepsilon^* = \varepsilon_0^*$ was made, so that (3.7) transformed to

$$\sum_j f_j \frac{\varepsilon_{CE}^{*(j)}(\eta_j) - \varepsilon^*}{\varepsilon_{CE}^{*(j)}(\eta_j) + 2\varepsilon^*} = 0. \qquad (3.8)$$

In general, f_j and η_j are unrelated. The simplest case arises under the assumption that the volume fraction is the same for all coated ellipsoids, $\eta_j = 1 - \phi$ with ϕ the porosity of the medium. In this case, Equation (3.8) simply collapses to the simple case $\varepsilon^* = \varepsilon_{CE}^*$, so that the following result was achieved [207]

$$\frac{\varepsilon^* - \varepsilon_e^*}{L_v\varepsilon^* + (1-L_v)\varepsilon_e^*} = (1-\phi) \frac{\varepsilon_i^* - \varepsilon_e^*}{L_v\varepsilon_i^* + (1-L_v)\varepsilon_e^*} \qquad (3.9)$$

The above equation only holds for a dilute suspension of cells. In order to take into account an increasing concentration, Sen et al. [207] used a differential effective medium approximation of this equation. Their approach starts from a dilute suspension and in each step a small amount of cells is added and the dielectric constant is determined self-consistently, using (3.9). If ε_k^* is the dielectric constant of the mixture at step k and an additional amount ΔI_k of cells is added to the suspension, the self-consistent dielectric constant ε_{k+1}^* is then determined by

$$\frac{\varepsilon_{k+1}^* - \varepsilon_k^*}{L_v \varepsilon_{k+1}^* + (1 - L_v)\varepsilon_k^*} = \left(\frac{\Delta I_k}{E + I}\right)\left(\frac{\varepsilon_i^* - \varepsilon_k^*}{L_v \varepsilon_i^* + (1 - L_v)\varepsilon_k^*}\right) \qquad (3.10)$$

with E and I the total amount of the extracellular and the cell volume, resp.. If we define $\Psi := I/(E + I)$ with the derivative $d\Psi/dI = (1 - \Psi)/(E + I)$ and we consider the limit $k \to \infty$, Equation (3.10) transforms to

$$\frac{d\varepsilon^*}{\varepsilon^*} \frac{L_v \varepsilon_i^* + (1 - L_v)\varepsilon^*}{\varepsilon_i^* - \varepsilon^*} = \frac{d\Psi}{1 - \Psi}.$$

When integrating this equation from 0 up to $1 - \phi$ and when respecting the boundary conditions $\varepsilon^*(0) = \varepsilon_e^*$ and $\varepsilon^*(1 - \phi) = \varepsilon^*$, we get

$$\begin{aligned}
\ln(\phi^{-1}) &= \int_0^{1-\phi} \frac{d\Psi}{1 - \Psi} = L_v \varepsilon_i^* \int_0^{1-\phi} \frac{1}{(\varepsilon_i^* - \varepsilon^*)\varepsilon^*} d\varepsilon^* + (1 - L_v) \int_0^{1-\phi} \frac{1}{\varepsilon_i^* - \varepsilon^*} d\varepsilon^* \\
&= \ln\left\{\left(\frac{\varepsilon^*}{\varepsilon_e^*}\right)^{L_v} \left(\frac{\varepsilon_i^* - \varepsilon_e^*}{\varepsilon_i^* - \varepsilon^*}\right)\right\},
\end{aligned}$$

so that, for the considered low-frequency range, where only the real part of ε^*, the conductivity σ, is considered, the tensor eigenvalues, σ_v ($\forall v = 1, 2, 3$), are related to the geometry of the medium by means of the final differential EMA

$$\left(\frac{\sigma_i - \sigma_v}{\sigma_i - \sigma_e}\right)\left(\frac{\sigma_e}{\sigma_v}\right)^{L_v} = \phi \qquad \forall v = 1, 2, 3, \qquad (3.11)$$

where σ_e and σ_i denote the conductivities of the extra- and the intracellular medium, resp..

Latour et al. [133] derived a similar differential EMA formula, which relates the effective water diffusion tensor eigenvalues, d_v, to the geometry of the medium,

$$\left(\frac{d_i - d_v}{d_i - d_e}\right)\left(\frac{d_e}{d_v}\right)^{L_v} = \phi \qquad \forall v = 1, 2, 3, \qquad (3.12)$$

with d_e and d_i the diffusion of the extra- and the intracellular medium, resp..

3.4.3   Relating conductivity and diffusion tensor eigenvalues

Tuch et al. [223] coupled both EMA-formulae (3.11) and (3.12) through the unknown porosity variable. Together with the assumption that the intracellular phase is electrically shielded by the high resistivity of the cell membrane so that $\sigma_i = 0$ and the assumption that the cell membrane water permeability is negligible, they derived the following formula for the conductivity tensor eigenvalues:

$$\sigma_v = \sigma_e \left[\frac{d_v - d_i}{d_e - d_i} \left(\frac{d_e}{d_v} \right)^{L_v} \right]^{1/(1-L_v)} \qquad \forall v = 1, 2, 3 \qquad (3.13)$$

In order to determine the depolarization factors L_v, the normalization condition $\sum_{v=1}^{3} L_v = 1$ [131, p.24] was exploited. If we define

$$f_v(L_v) := \ln \left(\frac{d_v - d_i}{d_e - d_i} \right) + L_v \ln \left(\frac{d_e}{d_v} \right),$$

a formula of the depolarization factor, e.g., $L_2(d_1, d_2, d_3, d_i, d_e)$, can be derived on the following way: First, a formula of $L_3(L_2)$ is derived exploiting the relation $f_3(L_3) = \ln(\phi) = f_2(L_2)$. In a second step, $L_3(L_2)$ is substituted into the relation $f_1(1 - L_2 - L_3) = f_1(L_1) = \ln(\phi) = f_2(L_2)$. The second relation thus exploits the normalization condition. Refer to [223] for the resulting formulas for the depolarization factors L_v.

In order to validate the approach, Tuch et al. [223] carried out DT-MRI measurements and compared the results of the effective medium approximation (3.13) to electrical conductivity measurements collated from the literature. Good agreements were found.

Under the further assumption of small intracellular diffusion, Tuch et al. [224] later worked out the simple linear relationship

$$\sigma_v = \frac{\sigma_e}{d_e} (d_v - d_i) \qquad \forall v = 1, 2, 3. \qquad (3.14)$$

3.4.4   Generation of realistic white matter conductor models

Whole head DT-MRI measurements

Whole-head-DT-MRI was performed using a 4-slice displaced Ultra-Fast Low Angle RARE (U-FLARE) protocol with centric phase-encoding [168]. Refer to Appendix A.9 for the basics of the DT-MRI technique. Diffusion weighting was implemented as a Stejskal-Tanner type spin-echo preparation [126]. Although Echo Planar Imaging (EPI) is being widely applied for DT-MRI purposes, U-FLARE was preferred to EPI in order to avoid spatial misregistration between
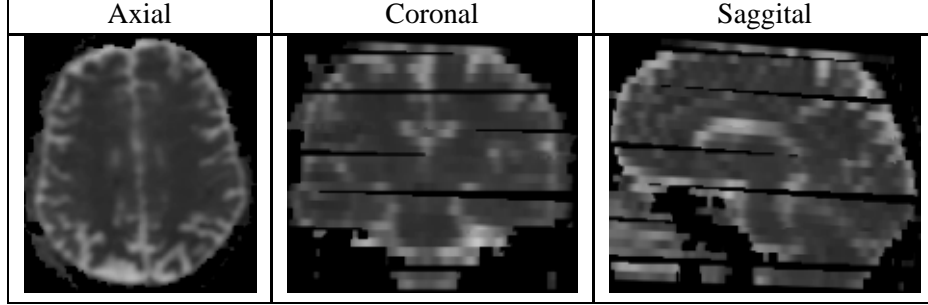
Figure 3.5: trace($\mathbf{D}$) *of the 8 registered DT-MRI sessions. Water diffusion coefficients in CSF (white) are much larger than in the brain, allowing a quality check of the registration.*

the DT-MRI data and the 3D data sets due to magnetic field inhomogeneities. The effective echo time was $TE = 120$ms, and $TR = 11$s. The diffusion weighting gradient pulses had a duration of δ=22ms, and their onset was separated by Δ=40ms (see Fig. A.3). Four different $\mathbf{b}$ (see Chapter A.9) with evenly spaced trace $\mathbf{b}$ between 50 and 800 s/mm^2 were applied through variation of the gradient strength [126]. The slices were axially oriented and 5mm thick. In-plane resolution was 2×2 mm^2. In order to increase the signal-to-noise ratio, 5 to 16 images (depending on $\mathbf{b}$) with identical diffusion weighting were averaged. Due to the long measurement time (50 min for 4 slices) data acquisition was split into 8 sessions. Diffusion tensor calculation [14] was based on a multivariate regression algorithm in IDL (Interactive Data Language, Research Scientific, Bolder, Colorado/USA). Figure 3.1 shows a detail of an axial slice of the measured DT-MRI data with 2×2 mm^2 resolution on an underlying coregistered T1-MRI. The coregistered T1 images of the same slices allowed the registration of the DT-MRI data on the 3D T1 data set. The registered DT data were then resampled to $1 \times 1 \times 1$ mm^3. In order to handle the orientation information in the registered DT images appropriately, the matrix of each diffusion tensor, $\mathbf{D}^{\text{eff}} \in \mathbb{R}^{3 \times 3}$, was rotated with the rotation matrix $\mathbf{R} \in \mathbb{R}^{3 \times 3}$ of the respective registration process via the similarity transform $\mathbf{D} = \mathbf{R}\mathbf{D}^{\text{eff}}\mathbf{R}^T \in \mathbb{R}^{3 \times 3}$ [4].

Figure 3.5 shows trace($\mathbf{D}$), i.e., the sum of the diagonal tensor elements, of the 8 registered DT-MRI sessions. Since water diffusion coefficients in CSF are much larger than in the brain, a large contrast is achieved at the brain surface, which allows a quality check of the registration. As the figure shows, the registered DT-MRI slices are not exactly parallel. Later in this thesis, with regard to the generation of FE volume conductor models, the gaps were filled with isotropic WM conductivity tensors.

Axial	Coronal	Saggital
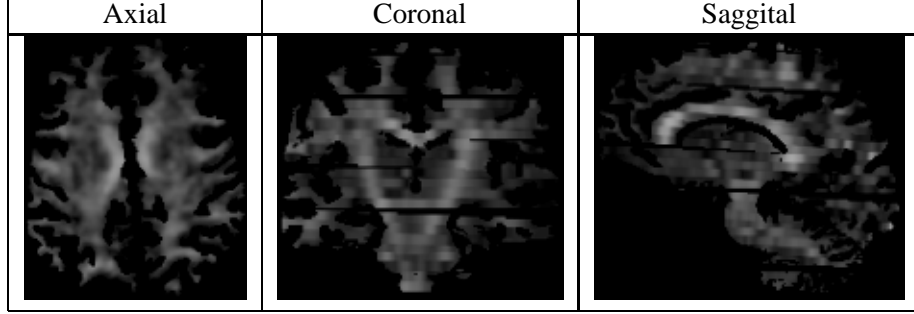
Figure 3.6: *Fractional anisotropy index, FA (see Equation (3.16)), of the DT-MRI, masked with the WM mask.*

When extracting the anisotropic part of the matrix of the diffusion tensor, $\mathbf{A} \in \mathbb{R}^{3 \times 3}$, by means of

$$\mathbf{A} := \mathbf{D} - \frac{\operatorname{trace} \mathbf{D}}{3} \mathbf{Id}, \tag{3.15}$$

the *fractional anisotropy index* FA is defined as [17]

$$\mathrm{FA} := \sqrt{\frac{3}{2}} \frac{\sqrt{\mathbf{A} : \mathbf{A}}}{\sqrt{\mathbf{D} : \mathbf{D}}} \quad \text{with} \quad \mathbf{B} : \mathbf{C} \equiv \sum_{i,j=1}^{3} B^{[ij]} C^{[ij]}. \tag{3.16}$$

Figure 3.6 shows a map of the fractional anisotropy index of the registered DT data, masked with the WM mask. With $FA = 0.74$, the highest value for fractional anisotropy was found in the splenium of the corpus callosum. Note also the strong anisotropy of the pyramidal tract in the figure.

Modeling the WM conductivity eigenvectors

It is assumed that the conductivity and the measured diffusion tensor share the eigenvectors, following the proposition of Basser et al. [16]. Let us thus consider the WM conductivity tensors in diagonalized form,

$$\underline{\sigma} = \mathbf{S} \, \mathbf{diag}(\sigma^{\mathrm{long}}, \sigma^{\mathrm{trans}}, \sigma^{\mathrm{trans}}) \, \mathbf{S}^{T},$$

with $\mathbf{S}$ the orthogonal matrix of eigenvectors of the measured diffusion tensors and $\sigma^{\mathrm{long}} \in \mathbb{R}^{+}$ and $\sigma^{\mathrm{trans}} \in \mathbb{R}^{+}$ the eigenvalues parallel (longitudinal) and perpendicular (transverse) to the fiber directions, resp..

Simulated eigenvalues using the volume and Wang's constraint

Again, Wang's (see Equation (3.1)) and the volume constraint (see Equation (3.2)) will be used for the simulation of the WM conductivity tensor eigenvalues,
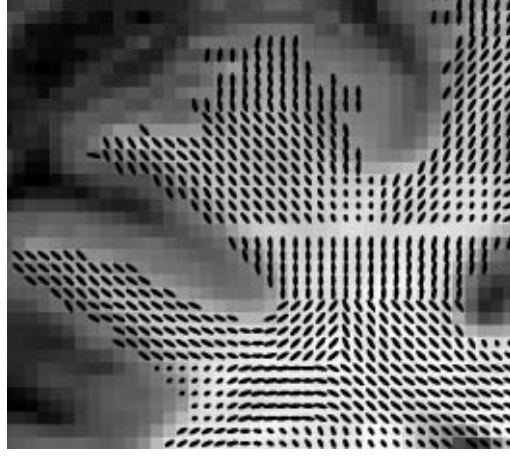
Figure 3.7: *Detail of the projection of the conductivity tensor ellipsoids $\underline{\underline{\sigma}}$ onto a coronal cut of the T1-MRI through the Commissura anterior. The gap, where no measurement data was available, is not yet filled with isotropic conductivity tensors. Top right: Fibers going up to the Gyrus frontalis superior; top left: Fibers going up to the Gyrus frontalis medius; bottom right: Fibers going through the Truncus corporis callosi; bottom left: Fibers going up to the Gyrus precentralis and down to Gyrus frontalis inferior, pars opercularis.*

σ^{long} and σ^{trans}, while exploiting measured values for the anisotropy ratio [165]. Figure 3.7 shows a detail of the projection of the conductivity tensor ellipsoids for 1:10 anisotropy (transverse:longitudinal) onto a coronal slice of the T1-MRI. The gap, where no measurement data was available, is not yet filled with isotropic conductivity tensors. Tensor validation and visualization was carried out with the software tool VM (Visualization Module), developed within the project SimBio (see Appendix D).

Effective medium approach for WM conductivity tensor eigenvalues

The second approach for the determination of the WM conductivity tensor eigenvalues uses the differential EMA, i.e., Equation (3.14). Following Haueisen et al. [106], the intracellular diffusion d_i was assumed to be negligible. The factor σ_e/d_e in (3.14) was chosen so that the average volume of the computed conductivity tensors was equal to the volume generated by an isotropic tensor with the isotropic WM bulk conductivity as eigenvalues (see Table 4.2). Note that the EMA is still insufficiently validated for the considered application, only the study of Tuch et al. [224] is known. Furthermore, in our DT measurements the

maximal ratio of largest to smallest DT eigenvalue was much lower than the ratio of about 1:9, reported for direct measurements of conductivity anisotropy in the WM compartment [165]. Therefore, most of the computations in this thesis are based on simulated eigenvalues as described above.

3.5   Summary and Conclusions

Within this chapter, possibilities for a realistic modeling of skull and WM anisotropy were presented. First, the notion of a tensor of order two was given.

For the determination of conductivity tensor eigenvectors in radial skull direction, the surface normals of a strongly smoothed triangular mesh, shrunken onto the outer spongiosa surface, were exploited. Since both tangential eigenvalues are assumed to be identical, the vector product was used for the generation of both tensor eigenvectors in tangential skull direction. Following the assumption of Basser et al. [16], the water diffusion tensor eigenvectors in brain WM, measured by means of whole-head DT-MRI, were taken over as the eigenvectors for the corresponding conductivity tensor.

Two constraints for the simulation of skull and WM tensor eigenvalues, the volume and Wang's constraint, were introduced. For a given anisotropy ratio, the volume constraint retains the volume between the anisotropic and the corresponding isotropic tensor. This eigenvalue simulation will be mainly used throughout the thesis. As a second possibility, formulas for radial and tangential eigenvalues in a simplified 3-layer skull model were presented. A self-consistent differential effective medium approach in the porous WM medium was described as a further model to determine the brain WM conductivity eigenvalues. Therefore, a linear relationship was derived to the corresponding water diffusion tensor eigenvalues as measured by DT-MRI.

Chapter 4

The forward problem

The book of nature is written in the language of mathematics.

Galileo Galilei

4.1   Introduction

In this chapter the differential equations together with the boundary conditions
are derived which describe the forward problem, i.e., the relationship between the
primary currents in the brain, which are directly driven by the neuronal processes,
and the measured potentials and magnetic fields at the head surface. Therefore,
the volume conductor head has to be modeled.

   The nowadays standard for head modeling are BE models, which can take
into account the realistic geometry of the surfaces skin, outer and inner skull and
which are adequate for piecewise homogeneous isotropic compartments. Some
further historical remarks to BE models are made in the following. For the
BE method, a Fredholm-type integral equation of the second kind is exploited
which can be derived from the Poisson equation by means of the integral equa-
tion method using double layer potential, as described in Wolters [254]. The
numerical accuracy of the BEM forward computation can be increased using
the isolated-problem approach, presented by Hämäläinen and Sarvas [97] and
by Meijs et al. [156], the analytical expressions for the solution of the surface in-
tegral of the BEM kernel function (de Munck [50], implemented and tested, e.g.,
in [254]), the virtual triangle refinement (Fuchs et al. [70]) and using local mesh
refinement around superficial sources (Yvert et al. [267]).

   This thesis focuses on the FE method, since it is able to treat both realistic
geometry and tissue anisotropy. In the first sections of this chapter, the physical

modeling based on Maxwell's equations, the mathematical formulation for the primary current sources and the description of the EEG and the MEG forward problem are presented. A summary of series expansion formulas for the potential distribution of a dipolar current source in a multilayer sphere volume conductor is then given. These formulas are later used for numerical validation purposes. In Section 4.7, an FE formulation for the Poisson equation is presented and FE meshing and discretization aspects are discussed. Diverse FE models, which are used later in the thesis, as well as numerical error criteria are then defined. The last section is concerned with numerical studies for FE forward problem accuracy.

4.2   The Maxwell equations

The electric and magnetic fields are described by the Maxwell equations

$$
\begin{aligned}
\operatorname{div} \mathbf{D} &= \rho & \text{(Coulomb)} \\
\operatorname{curl} \mathbf{E} &= -\delta_t \mathbf{B} & \text{(Faraday)} \\
\operatorname{curl} \mathbf{H} &= \mathbf{j} + \delta_t \mathbf{D} \\
\operatorname{div} \mathbf{B} &= 0
\end{aligned}
$$

with $\mathbf{D}$ the electric displacement, ρ the electric free charge density, $\mathbf{H}$ and $\mathbf{B}$ the magnetic field and induction, resp., $\mathbf{E}$ the electric field and $\mathbf{j}$ the electric current density (see, e.g., Nolting [167]). Since biological tissue mainly behaves as an electrolyte (Plonsey and Heppner [183]), the material equations

$$
\begin{aligned}
\mathbf{D} &= \varepsilon \mathbf{E} \\
\mathbf{B} &= \mu \mathbf{H}
\end{aligned}
$$

are used with ε and μ the electric and magnetic permeability, resp.. In the considered low frequency band (frequencies below 1000 Hz), the capacitive component of tissue impedance, the inductive effect and the electromagnetic propagation effect and thus the temporal derivatives can be neglected in the above formulas [183; 254]. It can be assumed, that the magnetic permeability μ is constant over the whole volume and equal to the permeability of vacuum [183; 254]. Therefore, Maxwell's equations reduce to

$$
\begin{aligned}
\operatorname{div} \mathbf{D} &= \rho \\
\operatorname{curl} \mathbf{E} &= 0 \\
\operatorname{curl} \mathbf{B} &= \mu \mathbf{j} & (4.1) \\
\operatorname{div} \mathbf{B} &= 0 & (4.2)
\end{aligned}
$$
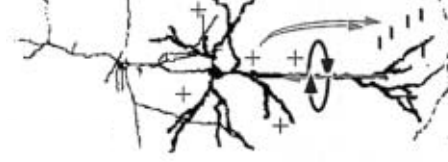
Figure 4.1: *Distribution of negative and positive current monopoles of an excited pyramidal cell (from Andrä and Nowak [6]).*

and the electric field can be expressed as a negative gradient of a scalar potential,

$$\mathbf{E} = -\operatorname{grad} u. \tag{4.3}$$

The current density is generally divided into two parts [183], the so-called *primary* or impressed current, $\mathbf{j}^p$, and the *secondary* or return currents, $\underline{\underline{\sigma}}\mathbf{E}$,

$$\mathbf{j} = \mathbf{j}^p + \underline{\underline{\sigma}}\mathbf{E}, \tag{4.4}$$

where $\underline{\underline{\sigma}}$ denotes the 3×3 conductivity tensor.

4.3 The primary currents

The sources to be localized during the inverse problem and to be modeled in the forward problem, the primary currents, are movements of ions within the dendrites of the large pyramidal cells of activated regions in the cortex sheet of the human brain. Stimulus-induced activation of a large number of excitatory synapses of a whole pattern of neurons leads to negative current monopoles under the brain surface and to positive monopoles quite closely underneath [6; 170]. This is shown in Fig. 4.1, taken from Andrä and Nowak [6].

One source model is *Feynman's dipole* [170; 184], consisting of a monopolar source at $\mathbf{x}_{so} \in \mathbb{R}^3$ and a closely neighbored sink at $\mathbf{x}_{si} \in \mathbb{R}^3$, i.e.,

$$\mathbf{J}^p_{\mathrm{Fey}}(\mathbf{x}) := M_{\mathrm{mon}} \left(\delta(\mathbf{x} - \mathbf{x}_{so}) - \delta(\mathbf{x} - \mathbf{x}_{si}) \right) \tag{4.5}$$

with $M_{\mathrm{mon}} \in \mathbb{R}$ the scalar monopolar strength. A distance of about 2 mm between source and sink can be seen as realistic (see, e.g., Nunez [170]). Nolting [167] claimed for the "δ function"

$$\int_\Omega \delta(\mathbf{x} - \mathbf{x}')d\mathbf{x} = \begin{cases} 1, & \text{if } \mathbf{x}' \in \Omega \\ 0, & \text{otherwise} \end{cases}$$
$$\delta(\mathbf{x} - \mathbf{x}') = 0 \qquad \forall\, \mathbf{x} \neq \mathbf{x}'.$$

Note, that δ is not a function in the mathematical sense, but a distribution, i.e., a continuous linear functional (see, e.g., Jantscher [114]).

It is surely more realistic to assume $\delta_n \in C_0^\infty(\Omega)$ instead of a distribution with $Tr(\delta_n(\mathbf{x})) = \{|\mathbf{x}| \leq \frac{1}{n}\}$ and $\int_\Omega \delta_n d\Omega = 1$ (see discussion in [254, §5.4]).

The neurogenesis of evoked fields was studied with isolated turtle brains by Okada [172]. Okada's measurements showed that at already small distances equal to the size of the activated region only the dipolar moment of the source term is visible. The so-called *mathematical dipole* $\mathbf{j}_{\text{Math}}^p := \mathbf{M}\delta(\mathbf{x} - \mathbf{x}_0)$ at the position $\mathbf{x}_0 \in \mathbb{R}^3$ with the moment $\mathbf{M} \in \mathbb{R}^3$ can be formulated as

$$J_{\text{Math}}^p(\mathbf{x}) = \text{div}\, \mathbf{j}_{\text{Math}}^p(\mathbf{x}) := \text{div}\, \mathbf{M}\delta(\mathbf{x} - \mathbf{x}_0). \tag{4.6}$$

The mathematical dipole has been shown to be an adequate model for the synchronous polarization of a cortical surface of about 30mm^2 [53].

4.4 The electric forward problem

Taking the divergence of Equation (4.1) (divergence of a curl of a vector is zero) and using Equations (4.3) and (4.4) gives the Poisson equation

$$-\text{div}\left(\underline{\underline{\sigma}}\,\text{grad}\,u\right) = -\text{div}\,\mathbf{j}^p = -J^p \quad \text{in } \Omega, \tag{4.7}$$

which describes the potential distribution in the head domain Ω due to a primary current $\mathbf{j}^p$ in the brain. The boundary condition

$$\left(\underline{\underline{\sigma}}_1\,\text{grad}\,u_1, \mathbf{n}\right)\Big|_{\text{at surface}} = \left(\underline{\underline{\sigma}}_2\,\text{grad}\,u_2, \mathbf{n}\right)\Big|_{\text{at surface}}$$

with $\mathbf{n}$ the unit surface normal expresses the continuity of the current density across any surface between regions of different conductivity. We find homogeneous Neumann conditions on the head surface $\Gamma = \partial\Omega$,

$$\left(\underline{\underline{\sigma}}\,\text{grad}\,u, \mathbf{n}\right)\Big|_\Gamma = 0, \tag{4.8}$$

and, additionally, a reference electrode with given potential, i.e.,

$$u_{\text{ref}} = 0. \tag{4.9}$$

A compatibility condition has to be respected, i.e., following Gauss' theorem, the condition

$$\int_\Omega J^p d\Omega = 0 \tag{4.10}$$

has to be fulfilled (see, e.g., Hackbusch [92, Example 7.4.8] or Braess [25, p.45]).

4.4.1 The subtraction approach

Strong singularities of the source model can be treated with the so-called *subtraction method* [10; 227; 151; 201; 236; 184]. The subtraction method splits the total potential u into two parts, the *singularity potential*, u^∞, and the *correction potential*, u^{corr},

$$u = u^\infty + u^{corr}. \tag{4.11}$$

The singularity potential is the solution for a dipole in an unbounded homogeneous conductor with constant conductivity $\underline{\underline{\sigma}}_0 = \sigma_0\,\mathbf{Id}$ (the isotropic tensor at the dipole location $\mathbf{x}_0$, $\sigma_0 \in \mathbb{R}^+$ the scalar conductivity value). Therefore, the solution of Poisson's equation

$$\Delta u^\infty = J^p/\sigma_0 \tag{4.12}$$

can be given by (Sarvas [199])

$$u^\infty(\mathbf{x}) = \frac{1}{4\pi\sigma_0} \int_\Omega \frac{J^p(\mathbf{x}')}{|\mathbf{x} - \mathbf{x}'|} d\mathbf{x}'.$$

For Feynman's dipole model (4.5), we thus get

$$u^\infty_{Fey}(\mathbf{x}) = \frac{M_{mon}}{4\pi\sigma_0}\left(\frac{1}{|\mathbf{x} - \mathbf{x}_{so}|} - \frac{1}{|\mathbf{x} - \mathbf{x}_{si}|}\right). \tag{4.13}$$

For the mathematical dipole (4.6), the use of the vector identity

$$\mathrm{div}'(\mathbf{j}^p_{Math}(\mathbf{x}')|\mathbf{x} - \mathbf{x}'|^{-1}) = |\mathbf{x} - \mathbf{x}'|^{-1}\,\mathrm{div}'\,\mathbf{j}^p_{Math}(\mathbf{x}') + \mathbf{j}^p_{Math}(\mathbf{x}') \cdot \mathrm{grad}\,|\mathbf{x} - \mathbf{x}'|^{-1}$$

and, since it is $\int_\Gamma \mathbf{j}^p_{Math}(\mathbf{x}')|\mathbf{x} - \mathbf{x}'|^{-1}d\mathbf{x}' = 0$, the application of Gauss' theorem leads to [199]

$$u^\infty_{Math}(\mathbf{x}) = \frac{1}{4\pi\sigma_0}\frac{(\mathbf{M},(\mathbf{x} - \mathbf{x}_0))}{|\mathbf{x} - \mathbf{x}_0|^3}. \tag{4.14}$$

Subtracting (4.12) from (4.7) yields the following equation for the correction potential

$$-\mathrm{div}\left(\underline{\underline{\sigma}}\,\mathrm{grad}\,u^{corr}\right) = \mathrm{div}\left(\left(\underline{\underline{\sigma}} - \underline{\underline{\sigma}}_0\right)\mathrm{grad}\,u^\infty\right) \quad \text{in } \Omega \tag{4.15}$$

and the inhomogeneous Neumann boundary conditions at the surface

$$\underline{\underline{\sigma}}\frac{\partial u^{corr}}{\partial \mathbf{n}}\bigg|_\Gamma = -\underline{\underline{\sigma}}\frac{\partial u^\infty}{\partial \mathbf{n}}\bigg|_\Gamma. \tag{4.16}$$

When solving this towards u^{corr}, the unknown scalar potential u can then be calculated using (4.11).

4.4.2   The direct approach

A smoother current term than the one used for the mathematical dipole (4.6) is surely more realistic. The so-called *blurred dipole*, proposed by Buchner et al. [30], has those smoothness properties. The dipole moment is approximated by a whole collection of closely neighbored sources and sinks. Since the blurred dipole is mesh-dependent, it will be discussed in Section 4.7.4.

The *direct method* then consists of solving Equation (4.7) with Neumann boundary conditions (4.8) and a fixed reference potential (4.9) in combination with the blurred dipole.

4.5   The magnetic forward problem

Since the divergence of $\mathbf{B}$ is zero (see Maxwell equation (4.2)) and the head domain is convex, a magnetic potential $\mathbf{A}$ with $\mathbf{B} = \operatorname{curl}\mathbf{A}$ can be introduced and, using Coulomb's gauge $\operatorname{div}\mathbf{A} = 0$, Maxwell's equation (4.1) transforms to

$$\mu\left(\mathbf{j}^p - \underline{\underline{\sigma}}\operatorname{grad}u\right) = \operatorname{curl}\left(\operatorname{curl}\mathbf{A}\right) = \operatorname{grad}\left(\operatorname{div}\mathbf{A}\right) - \Delta\mathbf{A} = -\Delta\mathbf{A}.$$

The source term is vanishing outside the volume conductor, so that the solution of this Poisson equation is given by [167]

$$\mathbf{A}(\mathbf{x}) = \frac{\mu}{4\pi}\int_{\Omega}\frac{\mathbf{j}^p(\mathbf{y}) - \underline{\underline{\sigma}}(\mathbf{y})\operatorname{grad}u(\mathbf{y})}{|\mathbf{x} - \mathbf{y}|}d\mathbf{y}.$$

The magnetic flux Ψ through an MEG magnetometer flux transformer Υ (see Figure 4.5) is determined as a surface integral over the magnetic induction for the coil area F enclosed by Υ, or, using Stokes theorem [167; 271], as

$$\Psi = \int_{F}\mathbf{B}dF = \oint_{\Upsilon}\mathbf{A}(\mathbf{x})d\mathbf{x}.$$

If we consider the mathematical dipole (4.6) and define

$$\mathbf{C}(\mathbf{y}) = \oint_{\Upsilon}\frac{1}{|\mathbf{x} - \mathbf{y}|}d\mathbf{x}, \tag{4.17}$$

the final equations for *primary magnetic flux*, Ψ_p, and *secondary magnetic flux*, Ψ_s, emerging from primary and secondary (return) currents, resp., are given by

$$\Psi_p \stackrel{(4.6)}{=} \frac{\mu}{4\pi}(\mathbf{M}, \mathbf{C}(\mathbf{x}_0)) \tag{4.18}$$

$$\Psi_s = -\frac{\mu}{4\pi}\int_{\Omega}(\underline{\underline{\sigma}}(\mathbf{y})\operatorname{grad}u(\mathbf{y}), \mathbf{C}(\mathbf{y}))d\mathbf{y} \tag{4.19}$$

$$\Psi = \Psi_p + \Psi_s.$$
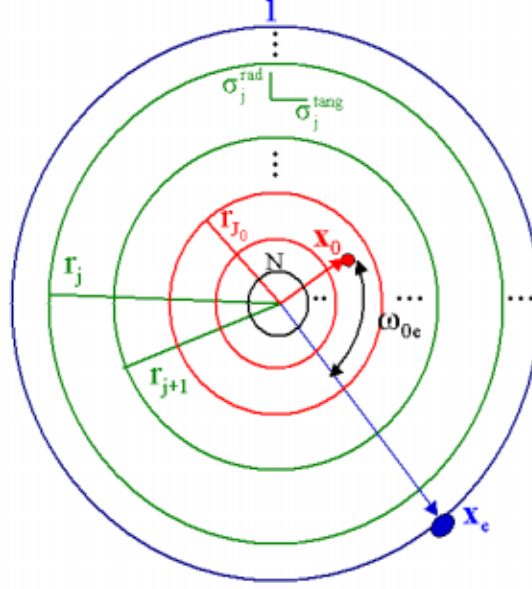
Figure 4.2: *The multilayer sphere model.*

4.6   The potential in a multilayer sphere model

De Munck [49] and de Munck and Peters [52] derived series expansion formulas for the direct problem (4.7) with boundary condition (4.8) and reference potential (4.9) for a mathematical dipole in a multilayer sphere model. The series expansions are used later in this thesis for numerical validation purposes. Therefore, a rough overview of the formulas will now be given. Refer to Appendix B for a more detailed derivation or to the original literature.

The model consists of shells N up to 1 with radii $r_N < r_{N-1} < \ldots < r_1$ and constant radial, $\sigma^{\mathrm{rad}}(r) = \sigma_j^{\mathrm{rad}} \in \mathbb{R}^+$, and tangential conductivity, $\sigma^{\mathrm{tang}}(r) = \sigma_j^{\mathrm{tang}} \in \mathbb{R}^+$, within each layer $r_{j+1} < r < r_j$. It is assumed in the following, that the source at position $\mathbf{x}_0$ with radial coordinate $r_0 \in \mathbb{R}$ is in a more interior layer than the measurement electrode at position $\mathbf{x}_e \in \mathbb{R}^3$ on the outer surface with radial coordinate $r_e = r_1 \in \mathbb{R}$ and $r_0 < r_{J_0} \leq r_e$. The multilayer sphere model is shown in Figure 4.2.

4.6.1 Series expansion formulas for a monopole source

The potential for a monopole source, $J^P(\mathbf{x}) = \delta(\mathbf{x} - \mathbf{x}_0)$, can be expressed by the spherical harmonics expansion

$$4\pi u_{\text{mon}} = \sum_{n=0}^{\infty} (2n+1) R_n(r_0, r_e) P_n(\cos \omega_{0e}) \tag{4.20}$$

with ω_{0e} the angular distance between source and electrode as shown in Figure 4.2, P_n the Legendre polynomials [271] and R_n the solution of the inhomogeneous differential equation

$$\frac{\partial}{\partial r}\left(r^2 \sigma^{\text{rad}}(r)\frac{\partial}{\partial r}R_n(r_0,r)\right) - n(n+1)\sigma^{\text{tang}}(r)R_n(r_0,r) = \delta(r_0 - r). \tag{4.21}$$

As will be shown in Appendix B.1, the solution of the above equation, i.e., the coefficients R_n, can be computed analytically and the series (4.20) converges.

4.6.2 Series expansion formulas for a dipole source

The spherical harmonics expansion for the mathematical dipole (4.6) was expressed in terms of the gradient of the monopole potential (4.20) with respect to the source point $\mathbf{x}_0$ [49; 52],

$$u(\mathbf{x}_0, \mathbf{x}_e) = (\mathbf{M}, \text{grad}_0 \, u_{\text{mon}}(\mathbf{x}_0, \mathbf{x}_e)).$$

With the help of

$$\text{grad}_0 \, r_0 = \frac{\mathbf{x}_0}{r_0} = \hat{\mathbf{x}}_0 \qquad \text{grad}_0 \cos \omega_{0e} = \text{grad}_0 \frac{(\mathbf{x}_0, \mathbf{x}_e)}{r_0 r_e} = \frac{1}{r_0}(\hat{\mathbf{x}}_e - \cos \omega_{0e} \hat{\mathbf{x}}_0),$$

a simple substitution yields the dipole potential

$$4\pi u(\mathbf{x}_0, \mathbf{x}_e) = (\mathbf{M}, S_0 \hat{\mathbf{x}}_e + (S_1 - \cos \omega_{0e} S_0)\hat{\mathbf{x}}_0)$$

with

$$S_0 = \frac{1}{r_0} \sum_{n=1}^{\infty} (2n+1) R_n(r_0, r_e) P_n'(\cos \omega_{0e}) \tag{4.22}$$

and

$$S_1 = \sum_{n=1}^{\infty} (2n+1) R_n'(r_0, r_e) P_n(\cos \omega_{0e}). \tag{4.23}$$

The derivative of the Legendre polynomial can be computed by means of the recursion

$$P_n'(\cos \omega) \equiv \frac{d}{d\cos\omega} P_n(\cos \omega) = n P_{n-1}(\cos \omega) + \cos \omega P_{n-1}'(\cos \omega).$$

The computation of $R'_n(r_0, r_e)$ can again be performed analytically, as shown in Appendix B.2.

A low convergence speed of the series (4.22) and (4.23) is found if the source approaches the electrode (see Appendix B.2). Therefore, an asymptotic approximation was proposed [52], yielding the series of differences

$$S_0 = \frac{F_0}{r_0}\frac{\Lambda}{R^3} + \frac{1}{r_0}\sum_{n=1}^{\infty}\left\{(2n+1)R_n(r_0, r_e) - F_0\Lambda^n\right\}P'_n(\cos\omega_{0e}) \qquad (4.24)$$

and

$$S_1 = F_1\frac{\Lambda\cos\omega_{0e} - \Lambda^2}{R^3} + \sum_{n=1}^{\infty}\left\{(2n+1)R'_n(r_0, r_e) - F_1 n\Lambda^n\right\}P_n(\cos\omega_{0e}) \quad (4.25)$$

with a higher speed of convergence. Refer to Appendix B.2 or to the original literature for the definition of F_0, F_1, Λ and R (all those terms are independent of n and can be computed from the given radii and conductivities of layers between source and electrode and of the radial coordinate of the source) and for a derivation of the above series of differences. The computation of the series (4.24) and (4.25) are stopped after the k's term, if the following criterion is fulfilled

$$\frac{t_k}{t_0} \leq \upsilon, \qquad t_k := (2k+1)R'_k - F_1 k\Lambda^k. \qquad (4.26)$$

4.7 FE formulation and discretization aspects

Numerical methods are needed for field simulations in realistically shaped volume conductors. As described in the introduction to this chapter, the nowadays standard for realistic head modeling are three compartment BE models. Within this thesis, the FE method is used because of its ability to treat geometries of arbitrary shape and inhomogeneous and anisotropic material parameters. FE models for the electromagnetic field simulation in the head have been developed by various research groups (see e.g. [21; 103; 227; 30; 10; 152]).

In the following, the basic Poisson equation is first transformed into a variational formulation, which is then discretized using a Ritz-Galerkin approach. FE meshing aspects are then discussed and EEG and MEG forward modeling is described.

4.7.1 Variational formulation

We will consider the direct approach described in Section 4.4.2, i.e., PDE (4.7) with Neumann boundary conditions (4.8) and the assumption of a smooth source load. Here, we assume $J_p \in L^2(\Omega)$. In order to derive an FE formulation for the direct approach, the problem has to be transformed into a variational formulation.

Definition 4.7.1. *The bilinear form $a(\cdot,\cdot)$ and the functional $l(\cdot)$ for problem (4.7) with Neumann boundary conditions (4.8) are defined as follows:*

$$a(\mathrm{u},v) \quad := \quad \int_{\Omega} \mathrm{grad\, u}\ \underline{\underline{\sigma}}\ \mathrm{grad\, v}\ d\Omega$$

$$l(v) =< l,v > \quad := \quad -\int_{\Omega} J_p \mathrm{v} d\Omega$$

We assume here, that $\mathrm{u} \in H^1(\Omega)$ (for the definition of Sobolev-spaces see, e.g., Adams [1]) and we further define

$$H_U^1 := \{\mathrm{v} \in H^1(\Omega), \int_{\Omega} \mathrm{v} d\Omega = 0\}$$

For the following theorems, certain properties of $a(\cdot,\cdot)$ and $l(\cdot)$ are necessary, whose validity were proved by Wolters [254]. Continuity in $H^1(\Omega) \times H^1(\Omega)$ and ellipticity in H_U^1 was shown for $a(\cdot,\cdot)$ with the aid of Cauchy-Schwarz' inequality and a variant of Friedrich's inequality, resp.. $l(\cdot)$ was shown to be bounded in $H^1(\Omega)$, so that $l \in (H_U^1)'$. Let us define $\mathbb{V} := H_U^1(\Omega)$ and $H := H^1(\Omega)$ for the following theorem:

Theorem 4.7.2 (Existence and Uniqueness). *Let Ω be a bounded domain and Γ a sufficiently smooth boundary. Let $\mathbb{V}$ be a closed convex set in a Hilbert space H and $a : \mathbb{V} \times \mathbb{V} \to \mathbb{R}$ an elliptic bilinear form. The variational problem*

$$Var(\mathrm{v}) := \frac{1}{2}a(\mathrm{v},\mathrm{v}) - < l,\mathrm{v} > \to min! \tag{4.27}$$

then has one and only one solution in $\mathbb{V}$ for each $l \in \mathbb{V}'$. In particular, the solution u is characterized through

$$a(\mathrm{u},\mathrm{v}) =< l,\mathrm{v} > \quad \forall \mathrm{v} \in \mathbb{V}. \tag{4.28}$$

Because of the compatibility condition (4.10), (4.28) is also valid for $\mathrm{v} = const$ and therefore $\forall \mathrm{v} \in H$.

Proof: Theorem of Lax-Milgram, Characterization theorem, see, e.g.,[25; 254].

Theorem 4.7.3. *If the conductivities are discontinuous, the solution u of Equation (4.27) is generally not a classical solution, i.e., $\mathrm{u} \notin C^2(\Omega) \cap C^1(\bar{\Omega})$, but it has discontinuous derivatives on each boundary with jumping conductivity. Only the tangential derivatives along those boundaries can be continuous.*

Proof: Hackbusch [92, Chapter 10.1.1].

4.7.2 Ritz-Galerkin approach

In practice, H_U^1 is difficult to discretize (see Hackbusch [92, Theorem 8.3.23]) and the uniqueness of the potential distribution can easier be realized by means of the Dirichlet condition (4.9) (see, e.g., Schwarz [206, Chapter 3.1.3]). After FE discretization with, from now on, $\mathbb{V} = H^1(\Omega)$, the reference potential is implemented in the linear equation system using a row-column-deletion [206].

Let us now consider the following problem: We are searching for $u \in \mathbb{V}$, so that

$$a(\mathrm{u},\mathrm{v}) = < l, \mathrm{v} > \quad \forall \mathrm{v} \in \mathbb{V}. \tag{4.29}$$

For the numerical solution, we choose a finite dimensional subspace $\mathbb{V}_h \subset \mathbb{V}$ with dimension $\dim \mathbb{V}_h = N_h$ and basis $\psi_1, \ldots, \psi_{N_h}$. The subscript h denotes the average mesh-size and $N_h = O(h^{-3})$ is the number of unknowns. We now approximate u using a Ritz-Galerkin approach:
Search $u_h \in \mathbb{V}_h$, so that

$$a(\mathrm{u}_h, \mathrm{v}_h) = l(\mathrm{v}_h) \quad \forall \mathrm{v}_h \in \mathbb{V}_h. \tag{4.30}$$

For each coefficient vector $\underline{u}_h \in V_h$ with $V_h := \mathbb{R}^{N_h}$, we define $P : V_h \to \mathbb{V}_h$ with

$$\mathrm{u}_h(\mathbf{x}) = P\underline{u}_h := \sum_{i=1}^{N_h} \underline{u}_h^{[i]} \psi_i(\mathbf{x}),$$

where $\underline{u}_h^{[i]}$ denotes the ith component of the vector $\underline{u}_h$. The discrete variational problem (4.30) can thus be transformed into a linear equation system

$$\mathsf{K}_h \underline{u}_h = \underline{j}_h \tag{4.31}$$

with

$$\begin{aligned}
\mathsf{K}_h^{[ij]} &:= a(\psi_j, \psi_i) \quad \forall 1 \le i, j \le N_h \\
\underline{j}_h^{[i]} &:= l(\psi_i) \quad \forall 1 \le i \le N_h.
\end{aligned} \tag{4.32}$$

The matrix K_h is SPD, where the positive definiteness follows from the ellipticity of the bilinear form $a(\cdot,\cdot)$ for all $u_h \in \mathbb{V}_h \backslash \{1\}$,

$$\underline{u}_h^{tr} \mathsf{K}_h \underline{u}_h = \sum_{i,j} \underline{u}_h^{[j]} \mathsf{K}_h^{[ij]} \underline{u}_h^{[i]} = a(\sum_j \underline{u}_h^{[j]} \psi_j, \sum_i \underline{u}_h^{[i]} \psi_i) = a(\mathrm{u}_h, \mathrm{u}_h) \ge \alpha \|\mathrm{u}_h\|_1^2,$$

with $\alpha > 0$ the ellipticity constant and from the comments of Schwarz [206, Chapter 3.1.3] concerning the implementation of the Dirichlet condition. Let us cite the following convergence theorem:

Theorem 4.7.4 (Convergence). *Let $\mathbb{V}_h^i \subset \mathbb{V}$ ($i \in \mathbb{N}$) be a sequence of subspaces with*

$$\lim_{i \to \infty} d(\mathrm{u}, \mathbb{V}_h^i) = 0 \quad \forall \mathrm{u} \in \mathbb{V}, \tag{4.33}$$

where d is an appropriate distance function. Let $a(\cdot, \cdot)$ be a continuous and $\mathbb{V}$-elliptic bilinear form. The Ritz-Galerkin approximation $\mathrm{u}_h^i \in \mathbb{V}_h^i$ is then converging against u:

$$||\mathrm{u} - \mathrm{u}_h^i||_{\mathbb{V}} \xrightarrow{i \to \infty} 0.$$

A sufficient condition for (4.33) is

$$\mathbb{V}_1 \subset \mathbb{V}_2 \subset \ldots \subset \mathbb{V}, \bigcup_{i=1}^{\infty} \mathbb{V}_i \text{ dense in } \mathbb{V}.$$

Proof: Hackbusch [92, Theorem 8.2.2, Lemma 6.5.7].

For the numerical realization, the volume conductor Ω is decomposed into finite elements. As an example, the subspace $\mathbb{V}_h \subset \mathbb{V}$ can be chosen as the subspace of piecewise linear functions:

$$\mathbb{V}_h := \{\mathrm{u}_h \in C^0(\overline{\Omega}); \mathrm{u}_h \text{ linear on each finite element}\} \tag{4.34}$$

As a basis, we then find the Lagrange FE functions with $\psi_i(\mathbf{x}_j) = \delta_{ij}$ ($1 \leq i, j \leq N_h$) with $\mathbf{x}_j$ the jth FE vertex. The dimension $N_h = \dim \mathbb{V}_h$ is equal to the number of vertices.

Let us discuss estimates for the FE-approximation $\mathrm{u}_h \in \mathbb{V}_h$ of the form

$$||\mathrm{u} - \mathrm{u}_h||_{\mathbb{V}} \leq O(h^k)$$

with largest possible order k. Generally, the order depends on the regularity of the solution, on the degree of the FE Ansatz-functions ψ_i, on the chosen Sobolev norm and on the approximation properties of the triangulation to the geometry. For our problem with jumping coefficients, we can only assume $\mathrm{u} \in H^1(\Omega)$. Following Hackbusch [92, Chapter 10.1.2], we can hope, that the general error bounds $||\mathrm{u} - \mathrm{u}_h||_1 = O(h)$ and $||\mathrm{u} - \mathrm{u}_h||_0 = O(h^2)$ can be achieved by means of isoparametric, i.e., geometry conforming, finite elements. However, we do not make use of such elements here.

4.7.3   Volume conductor FE mesh generation

An essential prerequisite for FE modeling is the generation of a mesh which represents the geometric and electric properties of the head volume conductor. Two different approaches were used and will be summarized now, a tetrahedra and a nodeshift cube mesh generation approach.
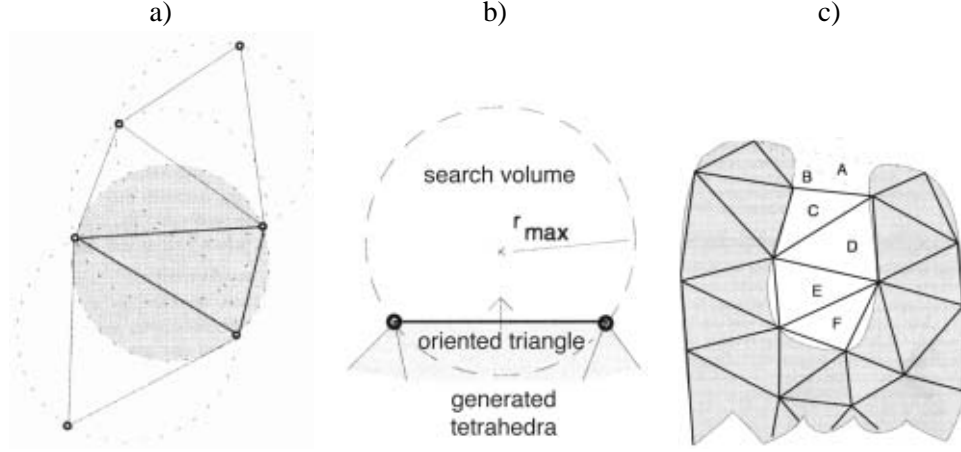
Figure 4.3: *Illustrations for tetrahedrization algorithm (Wagner [239]): a) The delaunay criterion: no vertex remains in the circumsphere of a tetrahedron. b) A maximal 3D circumsphere of an oriented triangle with given radius r_{max}. c) The tetrahedra A and B wouldn't have been generated during tetrahedrization, since the radii of their circumspheres are larger than r_{max}. The tetrahedra C up to F are spurious tetrahedra, being deleted in the last step of the algorithm.*

Tetrahedra mesh generation

The first approach uses a surface-based tetrahedral tessellation of the segmented six compartments skin, OSC, RS, CSF (ventricular system included), GM and WM. A possibility for the generation of compact and regular tetrahedra is the application of the Delaunay-criterion [239], which is shown in Fig. 4.3a.

Vertex generation: As described by Wagner [239, Chapter 4.2], the first step of the tetrahedra mesh generation process consists of the computation of FE vertices on the six segmented surfaces, using the thinning-distance parameter d_{min}^{comp} for the compartment surfaces. The algorithm begins with a seed-point on the segmented surface and deletes all neighbored vertices with a distance (defined on the surface) smaller d_{min}^{comp}, then repeating this process recursively. This leads to vertex distances between d_{min}^{comp} and $d_{max}^{comp} = \sqrt{3}d_{min}^{comp}$ [239]. Auxiliary surfaces are then generated using erosions of the compartment surfaces. The first erosion and the consequent thinning of the generated auxiliary surface is done with d_{min}^{comp}. Further erosions and consequent thinnings are carried out with $d_{min}^{aux} = \text{WIDER} * d_{min}^{comp}$ while preventing an erosion inside a more interior compartment border. The process leads to a set of layered surfaces containing the vertices of the model.

Tetrahedrization: The kernel procedure of the subsequent tetrahedrization of

the vertices consists of the following steps ([239, Chapter 6.3]): A seed triangle $(\mathbf{p}_1, \mathbf{p}_2, \mathbf{p}_3)$ with $\mathbf{p}_i \in \mathbb{R}^3$ is build using three neighbored vertices of a thinned surface. This triangle as well as the seed triangle with inverted orientation, $(\mathbf{p}_1, \mathbf{p}_3, \mathbf{p}_2)$, are put into a queue Q. As long as Q is not empty, a triangle $(\mathbf{p}_a, \mathbf{p}_b, \mathbf{p}_c)$ is taken out of it and its maximal (correctly oriented) 3D-circumsphere with fixed radius r_{max}, $SPHERE_{max}(\mathbf{p}_a, \mathbf{p}_b, \mathbf{p}_c, r_{max})$, is computed. This is shown in Fig. 4.3b. r_{max} is a function of d_{max}^{comp} or d_{max}^{aux}, dependent on the location of $(\mathbf{p}_a, \mathbf{p}_b, \mathbf{p}_c)$ on a compartment surface or an auxiliary surface, resp.. The fourth vertex $\mathbf{p}_d$ is then determined from all possible fourth vertices, which reside inside $SPHERE_{max}$ and on the correct side of the triangle (the "search volume" in Fig. 4.3b). Therefore, the center point $\mathbf{c}_d$ of its tetrahedron circumsphere, $\mathbf{c}_d = SPHERE\_CENTER(\mathbf{p}_a, \mathbf{p}_b, \mathbf{p}_c, \mathbf{p}_d)$, has to have minimal distance from the oriented triangle. If such a vertex $\mathbf{p}_d$ could be determined, the tetrahedron is taken into the tessellation T and its three new surface triangles, $(\mathbf{p}_a, \mathbf{p}_b, \mathbf{p}_d)$, $(\mathbf{p}_a, \mathbf{p}_d, \mathbf{p}_c)$ and $(\mathbf{p}_b, \mathbf{p}_c, \mathbf{p}_d)$ are put into Q. If no $\mathbf{p}_d$ could be determined, triangle $(\mathbf{p}_a, \mathbf{p}_b, \mathbf{p}_c)$ is a surface triangle and goes into the queue Q_s. The tetrahedra A and B in Fig. 4.3c wouldn't have been generated, since the radii of their circumspheres would have been larger than r_{max}.

Deletion of spurious tetrahedra: Since the outer surface of the model has concavities, spurious tetrahedra spanning vertices around such concavities have to be deleted in a last step of the tetrahedra mesh generation process (see Fig. 4.3c) ([239, Chapter 6.4]). Therefore, as long as Q_s is not empty, a surface triangle $(\mathbf{p}_a, \mathbf{p}_b, \mathbf{p}_c)$ is taken out of it and the associated tetrahedron $(\mathbf{p}_a, \mathbf{p}_b, \mathbf{p}_c, \mathbf{p}_d)$ is determined. If the tetrahedron is lying outside the model, it is deleted and $(\mathbf{p}_a, \mathbf{p}_b, \mathbf{p}_d)$, $(\mathbf{p}_a, \mathbf{p}_d, \mathbf{p}_c)$ and $(\mathbf{p}_b, \mathbf{p}_c, \mathbf{p}_d)$ are put into Q_s.

Nodeshift cube mesh generation

The second mesh generation approach takes advantage of the spatial discretization inherent in MRI images [255; 102].

Hexahedrization: The voxel-based approach directly converts image voxels to eight-noded hexahedral or cube elements. In order to keep the computation amount for the FE method in reasonable limit, lower resolutions with edge lengths of e times the edge length of a voxel-sized cube can be chosen for the final elements. In this case, the generated cube is assigned the most frequent label of its e^3 interior voxels.

Nodeshifting: Material interfaces of cubic models are characterized by abrupt transitions and right angles. Camacho et al. [35] proposed a nodeshift approach in order to smooth these irregular boundaries. For a biomechanical application in a circular ring model, where an analytical solution for Von Mises stress exists, they found a decreased error in nodeshift smoothed circular ring models compared to
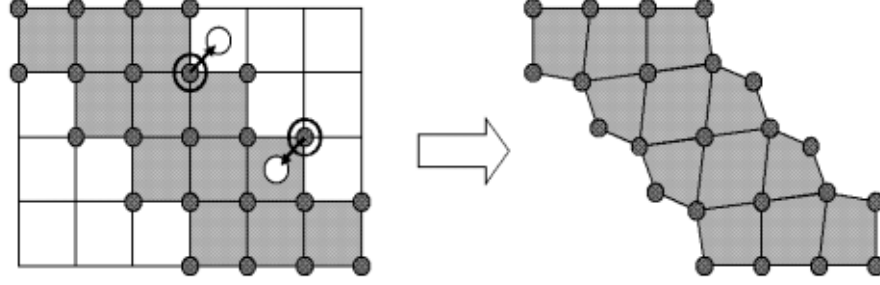
Figure 4.4: *Concept of the nodeshift approach, taken from Hartmann and Kruggel [102].*

models with unsmoothed surfaces at various tested mesh densities.

The nodeshift approach is presented in Fig. 4.4 and consists of the following steps: For each node, the material types of all eight elements (or 4 in 2D) sharing the node are determined. If more than one material type is present, the node is a material interface node and the following smoothing procedure is applied. If less than four (2 in 2D) of the eight (4 in 2D) elements share the same material type, they are designated as the minority elements. Relative to the considered material interface node, the spatial position of the centroid of the minority elements is determined (Fig. 4.4, left, exemplarily shown for 2 interface nodes) and assigned the coordinates (x, y, z). The node is then displaced by the vector

$$(\Delta x, \Delta y, \Delta z) = (ns * x, ns * y, ns * z)$$

with the user-defined nodeshift factor $ns \in [0, 0.49]$ (Fig. 4.4, right).

4.7.4 FE formulation for EEG forward problem

As in Section 4.4, direct and subtraction approach will again be distinguished for the FE formulation of the EEG forward problem. Before discussing the FE formulation for the direct method of Section 4.4.2, the mesh-dependent blurred dipole model will be presented.

The blurred dipole model

The blurred dipole model is made up from a monopole source vector $\underline{j}_l \in \mathbb{R}^K$ with entries $\underline{j}_l^{[k]}$, calculated for all $k \in \{1, \ldots, K\}$ neighboring FE mesh nodes $\mathbf{x}_k$ around the location $\mathbf{x}_l$ (not necessarily an FE mesh node), so that the moment $\mathbf{M}$ of a mathematical dipole at location $\mathbf{x}_l$, denoted by $\mathbf{M}_l$, is approximated as well as

possible and the source load is smoother than the one of the mathematical dipole. The visualization of the blurred dipole can then still be carried out by means of the vector $\mathbf{M}_l$. The calculation of the $\underline{j}_l^{[k]}$ is explained in the following.

Schönen et al. [205] reported the following basic relation for a dipole moment $\mathbf{T}_l \in \mathbb{R}^3$,

$$\mathbf{T}_l = \int_\Omega (\mathbf{x} - \mathbf{x}_l) \mathrm{J}^p(\mathbf{x}) d\mathbf{x}$$

(see also [167, p.88] and [170]). When assuming discrete sources on only neighboring FE mesh nodes, the equation is transformed in

$$\mathbf{T}_l = \sum_{k=1}^K \Delta\mathbf{x}_{kl}\, \underline{j}_l^{[k]}$$

with $\Delta\mathbf{x}_{kl}$ denoting the vector from node k to node l. This equation is well known from mechanical engineering, where small forces in combination with long lever arms have the same effect on the system as large forces in combination with short lever arms.

The use of higher dipole orders was proposed by Rienäcker et al. [190]. They introduced the dipole moment at $\mathbf{x}_l$ of rth $(r = 1,2,3)$ Cartesian direction and n^{th} order $(n \in \mathbb{N})$ by means of the higher dipole order vector $\underline{\bar{T}}_l^r \in \mathbb{R}^{n_0+1}$, $(n_0 \in \mathbb{N}$, generally, it is $n_0 = 1,2)$, with

$$\left(\underline{\bar{T}}_l^r\right)^{[n]} = \left(\underline{\bar{T}}_l^r\right)^{[n]} \left(\underline{j}_l\right) := \sum_{k=1}^K \left(\Delta\bar{x}_{kl}^r\right)^n \underline{j}_l^{[k]} \qquad \forall n = 0,\dots,n_0. \tag{4.35}$$

The bar indicates a scaling with a reference length a_{ref}, so that

$$\Delta\bar{x}_{kl}^r = \Delta x_{kl}^r / a_{\mathrm{ref}} \overset{!}{<} 1 \tag{4.36}$$

is dimensionless and the physical dimension of the resultant scaled n^{th} order moment, $\left(\underline{\bar{T}}_l^r\right)^{[n]}$, is that of a current (i.e., A, Ampère). If we now define the matrix $\bar{X}_l^r \in \mathbb{R}^{(n_0+1)\times K}$, the vector $\underline{\bar{M}}_l^r \in \mathbb{R}^{n_0+1}$, computed from the given $\mathbf{M}_l$, and the diagonal source weighting matrix $\bar{W}_l^r \in \mathbb{R}^{K\times K}$ by [190; 30]

$$\begin{aligned}
\left(\bar{X}_l^r\right)^{[nk]} &:= \left(\Delta\bar{x}_{kl}^r\right)^n & \left(\underline{\bar{M}}_l^r\right)^{[n]} &:= M_l^r \left(\frac{1}{2a_{\mathrm{ref}}}\right)^n \left(1 - (-1)^n\right) \\
\bar{W}_l^r &:= \mathrm{DIAG}\left(\left(\Delta\bar{x}_{1l}^r\right)^s, \dots, \left(\Delta\bar{x}_{Kl}^r\right)^s\right)
\end{aligned} \tag{4.37}$$

with $s = 0$ or $s = 1$, then we have to solve the minimization problem

$$F_\lambda(\underline{j}_l) = \|\underline{\bar{M}}_l^r - \underline{\bar{T}}_l^r(\underline{j}_l)\|_2^2 + \lambda\|\bar{W}_l^r \underline{j}_l\|_2^2 = \|\underline{\bar{M}}_l^r - \bar{X}_l^r \underline{j}_l\|_2^2 + \lambda\|\bar{W}_l^r \underline{j}_l\|_2^2 \overset{!}{=} \min.$$

The first part of the functional F_λ ensures a minimal difference between the resultant higher moments of the blurred dipole and the ones of the mathematical dipole, while the second part, a Tikhonov-Phillips regularizer (see Section 6.5.1) with λ the *dipole regularization parameter*, smoothes the monopole distribution and enables a unique minimum for F_λ. The solution of the minimization problem is given by

$$\left((\bar{X}_l^r)^{tr}\bar{X}_l^r + \lambda(\bar{W}_l^r)^{tr}\bar{W}_l^r\right)\underline{j}_l = (\bar{X}_l^r)^{tr}\underline{\bar{M}}_l^r$$

(see Theorem 6.5.2), so that the final solution for the monopole source vector $\underline{j}_l$ of the blurred dipole with moment $\mathbf{M}_l$ is given by

$$\sum_{r=1}^3 \left\{\bar{X}_l^r)^{tr}\bar{X}_l^r + \lambda(\bar{W}_l^r)^{tr}\bar{W}_l^r\right\}\underline{j}_l = \sum_{r=1}^3 \left\{(\bar{X}_l^r)^{tr}\underline{\bar{M}}_l^r\right\} \tag{4.38}$$

The highest order is generally chosen as $n_0 = 1$ or $n_0 = 2$, where the latter effects a spatial concentration of loads in the dipole axis. Furthermore, $s = 1$ stresses the spatial concentration of loads around the dipole.

The direct approach exploiting the blurred dipole model

The direct application of variational and FE techniques to Equation (4.7) with boundary conditions (4.8) and reference potential (4.9) together with the above described blurred dipole model thus yields the system of linear equations (4.31) with the stiffness or geometry matrix (4.32), i.e.,

$$\mathsf{K}_h^{[ij]} = \int_\Omega \operatorname{grad}\psi_j\,\underline{\underline{\sigma}}\,\operatorname{grad}\psi_i\,d\Omega \quad \forall 1 \le i,j \le N_h \tag{4.39}$$

and the right hand side vector $\underline{j}_h$, determined by

$$\underline{j}_h^{[i]} := \begin{cases} \underline{j}_l^{[k]} & if\ \exists k \in \{1,\dots,K\}: i = \mathrm{GLOB}(k) \\ 0 & \text{otherwise}, \end{cases} \tag{4.40}$$

for a source at location $\mathbf{x}_l$, where the function GLOB determines the global index i to each of the local indices k.

The subtraction approach

The subtraction method in Section 4.4.1 led to the differential equation (4.15) with inhomogeneous Neumann conditions (4.16) and thus to an equation system

$$\mathsf{K}_h\underline{u}_h^{\mathrm{corr}} = \underline{j}_h^\infty \tag{4.41}$$
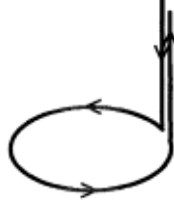
Figure 4.5: *A typical magnetometer flux transformer.*

with the same stiffness matrix as in the direct approach (see 4.39), but with a right hand side vector with entries

$$
\begin{aligned}
(\underline{j}_h^\infty)^{[i]} \;=\; & -\sum_{j=1}^{N_h} \left[\int_\Omega \operatorname{grad}\psi_j \left(\underline{\underline{\sigma}} - \underline{\underline{\sigma}}_0 \right) \operatorname{grad}\psi_i d\Omega \right. \qquad (4.42) \\
& \left. + \int_\Gamma \bar{\sigma}_0 (\operatorname{grad}\psi_j, \mathbf{n})\psi_i d\Gamma \right] \, \mathrm{u}^\infty(\mathbf{x}_j),
\end{aligned}
$$

where $\mathrm{u}^\infty(\mathbf{x}_j)$ is the evaluation of the function for the singularity potential at the FE mesh node $\mathbf{x}_j$, i.e., the evaluation of either Equation (4.13) or Equation (4.14), dependent on the chosen source model.

The solution vector $\underline{u}_h^{\mathrm{corr}}$ is the FE approximation of the correction potential, the total potential can then be computed using Equation (4.11). Note, that since the stiffness matrix is the same for the direct and the subtraction approach, the FE solver performance results presented in the next chapter are equally valid for the subtraction approach. In theory, the performance results are independent of the right hand side of the equation system.

4.7.5   FE formulation for MEG forward computation

For the magnetic forward problem, i.e., the computation of primary (Equation (4.18)) and secondary (Equation (4.19)) magnetic flux, the flux transformers of the MEG device have to be modeled (see Equation (4.17)). A typical magnetometer coil Υ is shown in Figure 4.5. Pohlmeier [184] modeled such a coil by means of a thin, closed conductor loop, using isoparametric quadratic row elements. Errors slightly below the data noise between this realistic and a point-like representation were reported, showing the necessity of the chosen approach. With

regard to these results, equation (4.17) was discretized by means of

$$\mathbf{C}(\mathbf{y}) = \sum_n \int_{-1}^{1} \frac{1}{|\sum_{i(n)} \chi_i(\xi)\mathbf{x}_i - \mathbf{y}|} \sum_{i(n)} \frac{\partial \chi_i(\xi)}{\partial \xi} \mathbf{x}_i d\xi, \qquad (4.43)$$

where n is the index for the row element and an isoparametric FE Ansatz with quadratic Ansatz-functions χ_i was made for the coil position vector,

$$\mathbf{x}(\xi) = \sum_i \chi_i(\xi)\mathbf{x}_i,$$

with $\mathbf{x}_i$ the vertices of the row element. The determination of the primary flux Ψ_p in Equation (4.18) is straight-forward. After the FE calculation of the potential distribution, the secondary flux Ψ_s in Equation (4.19) is computed using a Gauss integration, where the integrand consists of the interpolated functions in the FE space. For more detailed information, refer to Pohlmeier [184].

4.8 Definition of forward models and error criteria

4.8.1 Summary of former validations

Buchner et al. [30] validated the blurred dipole model in combination with the direct method in a one layer sphere model (radius R), where an analytical formula for the potential of two closely neighbored monopoles, a source and a sink, exists (Smythe [211]).

The correlation C in Fig. 4.6 [30] is defined as

$$C = \frac{\int_{\Gamma} u_h u_{ana} d\Gamma}{\int_{\Gamma} u_{ana} u_{ana} d\Gamma}$$

with u_{ana} denoting the analytically computed potential of Smythe. The figure shows high correlation values for practically interesting dipole eccentricities of $\varepsilon = r/R < 0.8$ with r the distance of the radial dipole to the sphere center. Note, that the mesh resolution is very low compared to the resolution, used later in this thesis. As a second validation, Buchner et al. [30] performed forward potential calculations for 64 electrodes in a four layer sphere FE model with 17196 vertices and an average edge length of 4mm for various radially and tangentially oriented blurred dipole sources. Inverse dipole fits were then carried out based on series expansion formulas in the corresponding analytical sphere model, using the software package CURRY. Mislocalizations were below 2mm in most cases and never exceeded 3mm [30].
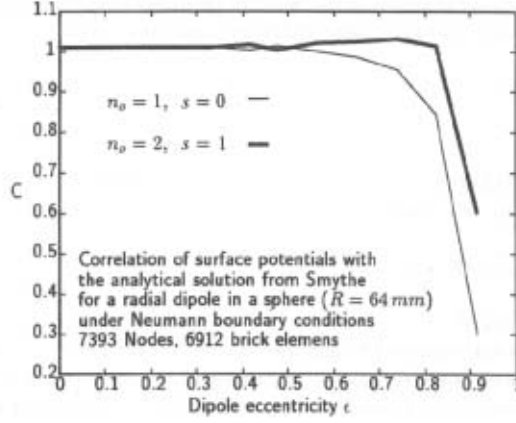
Figure 4.6: *Correlation of surface potentials with the analytical solution from Smythe for typical dipole model parameters from Buchner et al. [30].*

A preliminary examination of the subtraction method using Feynman's dipole (4.5) was carried out by Pohlmeier [184], who validated the approach in a one layer sphere model, where an analytical solution for the magnetic flux density of a mathematical dipole exists. For dipoles with an eccentricity below 0.8, the subtraction method yielded slightly better results for the magnetic flux density than the blurred dipole.

In Section 4.9, further validations of both forward approaches together with the nodeshift hexahedra mesh generation approach will be carried out.

4.8.2   Simulated sources

Except for Section 4.9.2, the blurred dipole in combination with the direct method will be used throughout this thesis. This approach was sufficiently validated, as shown above and as will be shown in Section 4.9.

Exploiting Fig. 4.6 and the simulation results of Rienäcker et al. [190], the parameters of the blurred dipole were chosen as follows throughout this thesis: The maximal dipole order n_0 (Equation (4.35)) and the scaling reference length a_{ref} (Equation (4.36)) were set to $n_0 = 2$ and $a_{\text{ref}} = 20.0 mm$, resp.. Since the chosen mesh size (see next subsection) is about a factor 10 times smaller than the reference length, the second order term $\left(\Delta \bar{x}_{ki}^{r}\right)^2$ is already very small and the model focuses on fulfilling the dipole moments of the zeros and first order. The exponent of the source weighting matrix in (4.37) was fixed to $s = 1$ and the regularization parameter in (4.38) was chosen as $\lambda = 10^{-6}$. The settings effected

Somato(tang)   Somato(rad)   Thal(rad)   Mesial-Temp
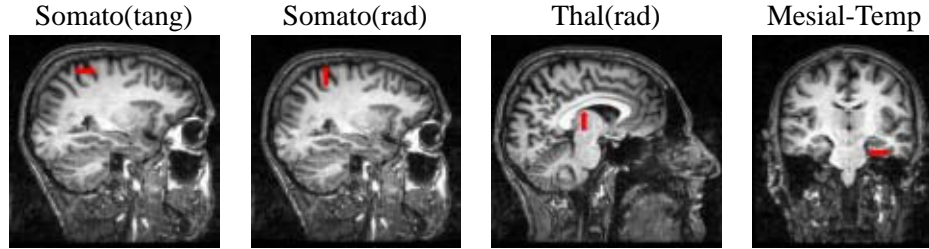
Figure 4.7: *Simulated sources on underlying T1-MRI, used throughout this thesis.*

a spatial concentration of the monopole loads in the dipole axis around the dipole location and are considered to well model the realistic primary currents [30].

Later in the thesis, forward simulation studies will be carried out with four dipole sources at three different locations in the brain (see Figure 4.7). The first two sources, one of them almost tangentially oriented (in y-direction, left) and the other radially (in z-direction, middle left), were chosen in the right somatosensory cortex as an example for eccentric, i.e., superficial sources. The second location was chosen in the left thalamus as an example for deeper sources, where the orientation is always almost radial (middle right). The third source was placed in the mesial-temporal lobe (right), since this area is of special interest in epilepsy surgery [111].

4.8.3   The modeled EEG and MEG sensors

For the EEG forward computation, 71 electrodes were placed interactively on the head surface according to the international 10/20 system [178]. The electrode configuration is shown in Fig. 4.8 (top row). The sensors were projected onto the FE head models, i.e., the electrode potential is modeled with the value of the closest neighboring FE mesh node. For visualization, the software packages CURRY (Fig. 4.8, top left) and SimBio-VM (Fig. 4.8, top right) were used (see Appendix D).

The Max-Planck-Institute of Cognitive Neuroscience Leipzig is equipped with a BTI 148 channel whole-head MEG system. Each magnetometer flux transformer of this system (see Figure 4.5) was modeled by means of a thin, closed conductor loop with a diameter of 11.5 mm, using 8 isoparametric quadratic finite row elements. In Figure 4.8 (bottom row), the position of the 148 magnetometer coils, each represented by its row elements, are visualized together with the outer surface of the head model, using the software package EIPP (see Appendix D).
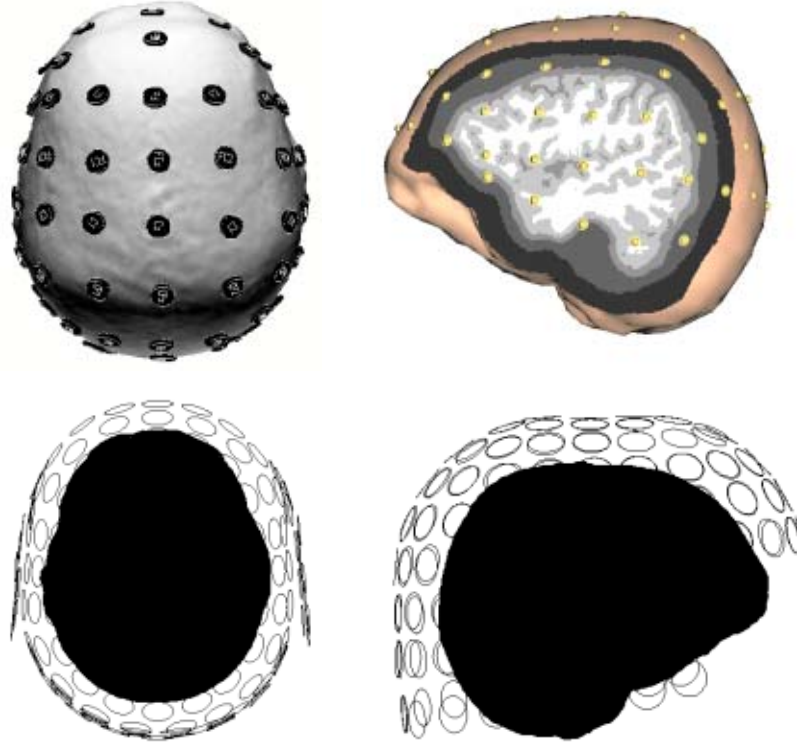
Figure 4.8: *EEG and MEG sensors: Top row: 71 electrodes of the chosen EEG system on underlying outer model surface (left) and on underlying cut 5 tissue model (right). Electrode size was enlarged for visualization purposes. Bottom row: The chosen whole head BTI-148-channel MEG system together with the outer surface of the head model.*

4.8.4   Definition of the FE volume conductor models

Mesh generation

For the tetrahedra mesh generation approach (see 4.7.3), the 6 tissue head model from Section 2.6.5 builds the basis for the generation of the FE Models 1 and 3, shown in Table 4.1. $d_{\min}^{\mathrm{comp}} = 2$ mm enabled a very exact representation of the six compartments. In order to keep the computation amount in reasonable limit with regard to the inverse problem, a factor WIDER $= 1.3$ was chosen for auxiliary surfaces. The meshed compartments skin, OSC and RS were visualized and inspected to be closed and free of holes. The vertex generation process resulted in 147287 nodes and the tetrahedrization in 895611 elements. 3496 spurious surface

Model	Type	Parameter settings	Compartments	Nodes	Elements
1	tet	$d_{min}^{comp} = 2$ WIDER = 1.3	Skin, Skull, CSF GM, WM	147287	892115
2	cube	e=2 ns 0.49	Skin, Skull, CSF GM, WM	385901	366043
3	tet	$d_{min}^{comp} = 2$ WIDER = 1.3	Skin, OSC, RS CSF, GM, WM	147287	892115

Table 4.1: *Realistically shaped volume conductor models: The model reference, the FE type, the parameter settings during mesh generation, the compartment labels and the resulting number of nodes and elements.*

tetrahedra were deleted in the last step. The program package CURRY was used for tetrahedrization (App. D). Model 1 will not distinguish between elements in the OSC and RS compartments. A cut through this model is shown in Fig. 4.9a. For visualization, the software tool SimBio-VM was used (App. D). Model 3 uses the same FE mesh geometry as Model 1, but a distinction is drawn between OSC and RS elements.

Concerning cube meshing, it was found for a biomechanical application that a minimum of 2-4 cube elements is required across the thickness of relevant structures in order to produce solutions with less than 10% error in Von Mises stress [35]. Therefore, the 5 tissue head model from Section 2.6.5 is used for a nodeshift cube mesh generation approach (see 4.7.3). For Model 2, a mesh resolution of $e = 2$ was chosen and the nodeshift was applied with $ns = 0.49$. The meshed compartments skin and skull were visualized (see Fig. 4.9b) and inspected, no holes were found. For the hexahedra mesh generation, the program VGRID from the Simbio project was used (App. D).

Isotropic bulk conductivity labeling

The finite elements were then labeled according to their compartment membership. Table 4.2 illustrates the chosen isotropic bulk values. For the conductivities of skin-, GM and WM elements, refer to Haueisen [103; 77], while the value for

Compartment	Skin	Skull	OSC	RS	CSF	GM	WM
Cond.(1/Ωm)	0.33	0.0042	0.00118	0.061	1.79	0.33	0.14

Table 4.2: *Isotropic bulk conductivity labels for the volume conductor compartments.*
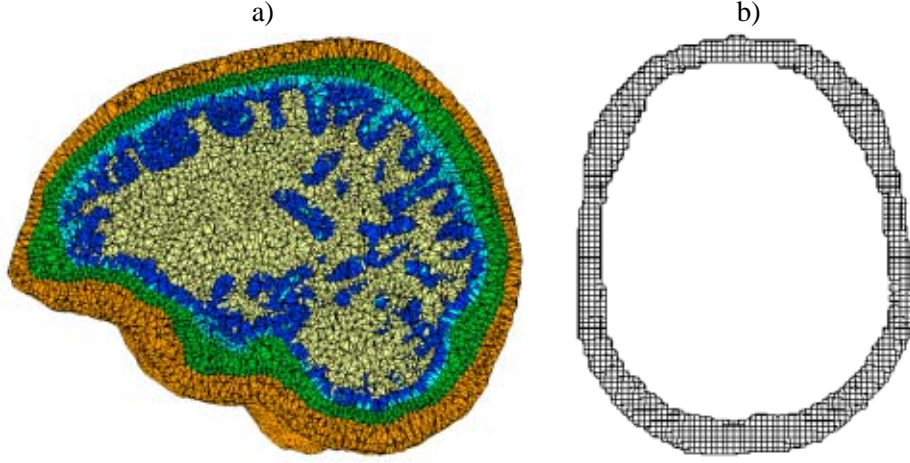
Figure 4.9: *Mesh generation: a) Axial cut through the 5 tissue tetrahedra Model 1 from Table 4.1. b) Axial slice of a cut through the skull compartment of the nodeshift cube Model 2 from Table 4.1.*

CSF is taken from the measurements of Baumann [18]. In source localization, the skull is generally regarded as one unit with the indicated bulk conductivity value σ_{skull}, resulting in the well-known conductivity ratio of about 1 : 80 between skull and skin compartment (see, e.g., [227; 73]). This is surely only a rough approximation of its resistor properties. As discussed in Section 2.6.5, Akhtari et al. [3] reported for the OSC compartment an approximately constant thickness of $l_{OSC} = 2$mm and the indicated bulk conductivity value σ_{OSC}. The value for σ_{RS} in Table 4.2 was then determined using Equation (3.3) under the (rough) assumption $l_{RS} = 5.5$mm, i.e., using

$$\frac{l_{RS}}{\sigma_{RS}} = \frac{l_{skull}}{\sigma_{skull}} - \frac{l_{OSC}}{\sigma_{OSC}}.$$

Anisotropic conductivity labeling for the skull

The Models 1 and 2 from Table 4.1 are considered now. For both models, the conductivity tensor eigenvectors in the barycenters of finite elements in the skull were determined by means of the procedure, described in Section 3.3.1. The corresponding eigenvalues were simulated under Wang's (Equation (3.1)) or the volume constraint (Equation (3.2)). Table 4.3 shows the 5 chosen anisotropy ratios and the calculated eigenvalues under constraint of the respective approach. Anisotropy ratios of 1:2, 1:5, 1:10 and 1:100 were chosen, where the last should

	Volume constraint		Wang's constraint	
$\sigma^{rad} : \sigma^{tang}$	σ^{rad}	σ^{tang}	σ^{rad}	σ^{tang}
1:1 (iso)	0.0042	0.0042	0.0042	0.0042
1:2	0.0026	0.0053	0.003	0.0058
1:5	0.00143	0.0072	0.00188	0.00938
1:10	0.000905	0.00905	0.00133	0.01326
1:100	0.000195	0.0195	0.00042	0.042

Table 4.3: *Simulated values for the skull conductivity tensor eigenvalues: The ratio was given and the eigenvalues were computed under the respective constraint.*

	Volume constraint		Wang's constraint	
$\sigma^{trans} : \sigma^{long}$	σ^{trans}	σ^{long}	σ^{trans}	σ^{long}
1:1 (iso)	0.14	0.14	0.14	0.14
1:2	0.111	0.222	0.099	0.19798
1:5	0.0818	0.41	0.0626	0.31309
1:10	0.065	0.65	0.04427	0.4427
1:100	0.03016	3.016	0.014	1.4

Table 4.4: *Simulated values for the WM conductivity tensor eigenvalues: The ratio was given and the eigenvalues were computed under the respective constraint.*

be considered to be out of the realistic range. According to Rush and Driscoll [197], the skull has a ratio of 1:10 and this ratio is used by most authors for skull anisotropy simulations [49; 180; 52; 227; 152]. Note, that under the assumption of a simplified 3x3x3 model of the skull as in Fig. 3.4 and when using the Equations (3.3) for the radial and (3.4) for the tangential skull conductivity eigenvalue with values for thicknesses and conductivities of the three skull layers as measured by Akhtari et al. [3], a ratio of about 1:3 results. Figure 4.10 shows the conductivity tensors of the skull roof (left) and of an axial cut through the skull model on the underlying T1-MRI (right). Tensor validation and visualization was again carried out using SimBio-VM (App. D).

Anisotropic conductivity labeling for the WM compartment

The procedure for modeling the WM conductivity tensors was described in Section 3.4.4. The eigenvectors of the measured diffusion tensors in the barycenters of finite elements in the WM compartment were taken as the conductivity tensor eigenvectors.

For the Models 1 and 2 from Table 4.1, the eigenvalues were simulated as shown in Table 4.4. In the literature, measured ratios between 1:6 and 1:10

a)   b)
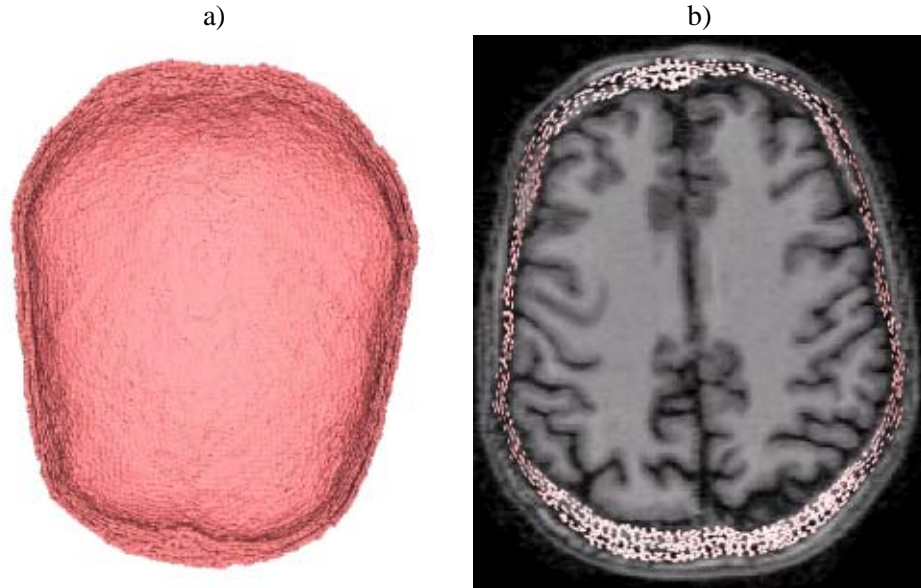
Figure 4.10: *Conductivity tensor ellipsoids in the barycenters of skull elements of Model 1 from Table 4.1 with 1:5 skull anisotropy: a) Tensors of the skull roof. b) Tensors of an axial cut through the skull model on the underlying T1-MRI. A stronger scaling of the eigenvalues of the tensors was chosen in a) compared to b).*

were found [165; 77]. Fig. 4.11 presents the conductivity tensor ellipsoids in the barycenters of the WM finite elements of Model 1 from Table 4.1 with 1:10 WM anisotropy on the underlying T1 MRI. Note the strong left-right and top-bottom anisotropy of the corpus callosum and the pyramidal tract, resp.. SimBio-VM was again exploited for tensor validation and visualization (App. D).

For the determination of eigenvalues for Model 3 from Table 4.1, the differential EMA was used as described in Section 3.4.4.

4.8.5   Error criteria for forward simulation accuracy

We now define the two error criteria, which shall describe the influence of skull and WM anisotropy on the field distribution. These criteria were introduced for BE calculations [156]. The first, the Relative Difference Measure (RDM), is

Figure 4.11: *Conductivity tensor ellipsoids in the barycenters of the WM elements of Model 1 from Table 4.1 with 1:10 WM anisotropy on underlying T1-MRI.*

defined as

$$
\text{RDM} = \sqrt{\sum_{i=1}^{m} \left(\frac{\underline{\phi}_{\text{iso}}^{[i]}}{\sqrt{\sum_{i=1}^{m} \left(\underline{\phi}_{\text{iso}}^{[i]} \right)^2}} - \frac{\underline{\phi}_{\text{ani}}^{[i]}}{\sqrt{\sum_{i=1}^{m} \left(\underline{\phi}_{\text{ani}}^{[i]} \right)^2}} \right)^2}, \qquad (4.44)
$$

where m denotes the number of sensors and $\underline{\phi}_{\text{iso}} \in \mathbb{R}^m$ and $\underline{\phi}_{\text{ani}} \in \mathbb{R}^m$ the measurement vector in the isotropic and the anisotropic case, resp.. The RDM is a measure for the topography error (Minimal error: RDM = 0). The second error measure, the MAGnification factor (MAG), defined as

$$
\text{MAG} = \frac{\sqrt{\sum_{i=1}^{m} \left(\underline{\phi}_{\text{ani}}^{[i]} \right)^2}}{\sqrt{\sum_{i=1}^{m} \left(\underline{\phi}_{\text{iso}}^{[i]} \right)^2}}, \qquad (4.45)
$$

Type	Parameter settings	Compartments Cond.($1/\Omega$m)			Nodes	Elements
tet	$d_{\min}^{\text{comp}} = 2$ WIDER $= 1.3$	Skin 0.33	Skull 0.0042	Brain 0.33	133332	793950
cube	e=2 $ns \in \{0.0, 0.35, 0.49\}$	Skin 0.33	Skull 0.0042	Brain 0.33	385901	366043

Table 4.5: *The realistically shaped 3 compartment models used for nodeshift validation and discretization error studies.*

gives an indication of errors in the magnitude (Minimal error: MAG $= 1$).

4.9   Numerical studies

4.9.1   Studies on discretization error and mesh quality

In order to validate the nodeshift approach for cubic FE meshes and to study the discretization error with regard to especially skull layer and skin surface, EEG and MEG simulation results were compared in the realistically shaped three compartment models, shown in Table 4.5. For the hexahedrization, three different nodeshift values were chosen. The meshed compartments skin and skull of all models were visually inspected to be free of holes. The electrodes were modeled with 71 finite row elements with a conductivity of 1.0 between exact electrode position and closest mesh node. For the cube models, the mean row element length was 1.1mm, 0.9mm and 0.8mm for $ns = 0.0$, $ns = 0.35$ and $ns = 0.49$, resp.. This can be seen as a first nodeshift validation with respect to a better representation of the smooth skin surface. The accuracy studies were carried out with the somatosensory source with both tangential and radial orientation and the mesial-temporal source (see Section 4.8.2), using the blurred dipole model and the direct approach. The former source is close to a convex, whereas the latter is close to a concave part of the skull. Since the tetrahedra mesh generation approach better represents the smooth skin and especially the skull surfaces, the model was treated as the reference. RDM and MAG error at the 71 electrode locations and 148 MEG sensors for the chosen sources between reference and nodeshift cube models were computed. The results are shown in Table 4.6. The errors are generally acceptable relative to other inaccuracies such as material property uncertainty, as will be shown in the last chapter. For the somatosensory source (for both orientations), the nodeshift reduced RDM and MAG errors for both EEG and MEG. Nevertheless, for the EEG modality and the mesial-temporal source, a strong smoothing with $ns = 0.49$ seems to reduce the skull's

Source	Mod.	$ns = 0.0$		$ns = 0.35$		$ns = 0.49$	
		RDM	MAG	RDM	MAG	RDM	MAG
Somato(tang)	EEG	3.3%	1.10	2.9%	1.03	2.9%	1.01
	MEG	0.4%	1.00	0.4%	1.00	0.3%	1.00
Somato(rad)	EEG	5.1%	1.10	4.1%	1.01	4.1%	1.00
	MEG	0.5%	0.99	0.5%	0.99	0.5%	0.99
Mesial-Temp	EEG	4.4%	1.05	4.2%	0.98	4.1%	0.96
	MEG	2.5%	0.95	2.6%	0.96	2.7%	0.96

Table 4.6: *Realistically shaped 3 compartment models: RDM and MAG error between the tetrahedra model and the cube models with different nodeshift factors for EEG and MEG and various sources.*

Type	Parameter settings	Radii of comp. (mm) Cond.(1/Ωm)				Nodes	Elements
cube	e=2	100	90	80	70	521062	544802
	$ns \in \{0.0, 0.49\}$	0.33	0.0042	1.0	0.33		

Table 4.7: *The finite element 4 layer sphere models for numerical accuracy studies.*

thickness leading to an increased MAG error when compared to the more moderate nodeshift of 0.35. A reason could be the concavity of the skull close to that source. Note, that the vertices of the tetrahedra model are image lattice points of the corresponding MRI, whereas, when considering a cube model with $e = 1$, the image lattice points are barycenters of cube elements. This means, that the representation of a surface in the tetrahedra model is shifted by half a voxels size compared to its representation in the cube model.

4.9.2 Further validation in multilayer sphere model

In Section 4.8.2, first validations from Buchner et al. [30] and Pohlmeier [184] of both the direct and the subtraction method were summarized. In order to validate both approaches with regard to the nodeshift hexahedra mesh generation approach, finite element four layer sphere models were generated (Table 4.7). The distance between source and sink in Feynman's source model (Equation (4.5)) was chosen to be 1mm. A tangentially oriented dipolar source with eccentricity $\varepsilon = 50\text{mm}/70\text{mm}$ was placed in the model and the surface potentials were evaluated at six electrodes (plus one reference electrode) at all extreme sphere surface positions. Fig. 4.12 shows the computed potential distributions for the

a)   b)   c)
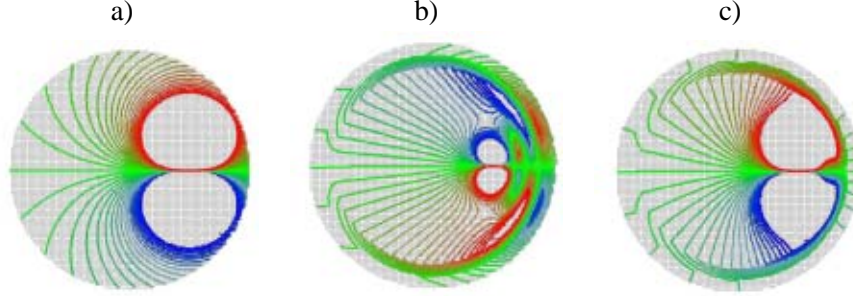
Figure 4.12: *Isopotential lines in nodeshift-model: a) Feynman's singularity potential from -0.5 to 0.5 µV b) FE correction potential from -0.5 to 0.5 µV c) total potential from -1 to 1 µV.*

Source	numerical	$ns = 0.0$		$ns = 0.49$	
model	approach	RDM	MAG	RDM	MAG
blurred	direct	2.8%	1.11	1.7%	1.04
Feynman	subtraction	2.7%	1.11	2.3%	1.05

Table 4.8: *EEG RDM and MAG error between reference solution and numerical solution in cube models without and with nodeshift surface smoothing.*

subtraction method in combination with Feynman's source model, the singularity potential $\underline{u}_{\text{Fey}}^{\infty}$ (left, see Equation (4.13)), the numerically computed correction potential $\underline{u}_{h}^{\text{corr}}$ (middle, see (4.41)) and the total potential $\underline{u}_{h} = \underline{u}_{\text{Fey}}^{\infty} + \underline{u}_{h}^{\text{corr}}$ (right, see (4.11)). RDM and MAG errors were then computed between reference and numerical solutions. The results are presented in Table 4.8. The reference is the analytically computed potential, using the series expansion formulas, presented in Section 4.6 (see Appendix D concerning the software). The computation of the series, formulas (4.24) and (4.25), was controlled by means of the criterion (4.26) with $\upsilon = 10^{-6}$. No more than 30 terms were then needed for the series computation for each electrode when using the asymptotic expansion. The nodeshift approach improved the numerical accuracy for both source models and corresponding numerical approaches. The blurred dipole better approximated the mathematical dipole, RDM and MAG were closer to the optimum when compared to Feynman's source model in combination with the subtraction method.

4.10 Summary and Conclusions

In the first sections of this chapter, a mathematical formulation for the primary current source was given and the Poisson equation was presented for modeling the potential distribution in the volume conductor. The Biot-Savart's law was exploited for the magnetic field. A variational formulation for the forward problem was then derived and FE discretization aspects were discussed. For FE meshing, a surface-based tetrahedral tessellation, using the Delaunay-criterion, and hexahedra mesh generation approaches were presented. A nodeshift approach for hexahedra meshes was used in order to smooth the boundaries of standard cubic meshes at material interfaces. Various forward models, used throughout the thesis, were then defined. This included the definition of sources which are later used for forward sensitivity considerations, the EEG and MEG sensor configurations and various isotropic and anisotropic tetrahedra and hexahedra volume conductor models. Furthermore, the RDM and MAG error criteria for forward modeling accuracy were defined.

Numerical validation studies were carried out in the last section. It was shown in a realistically shaped 3-compartment model that the nodeshift generally decreased the discretization error between tetrahedra and cube models. Furthermore, it improved the numerical accuracy in a four layer sphere model when compared to the analytical results of the series expansion formulas. It was also shown that a mesh-dependent blurred dipole model in combination with a direct solution of the forward problem better approximated the analytical results for a mathematical dipole than the subtraction approach together with Feynman's dipole. The blurred dipole in combination with the direct solution technique is used throughout the following chapters.

Chapter 5

Efficient FE solver methods

5.1   Introduction

The solution of hundreds or even thousands of large scale systems of equations
(4.31) with identical stiffness matrix (4.32) and varying right hand sides is the
major time consuming part within the inverse source localization process. There-
fore, fast solver methods in combination with parallel computing platforms are
needed.

Saad [198] mentioned in the introduction to his book that memory and com-
putational requirements for solving large scale 3D systems of equations stem-
ming from PDE discretizations may seriously challenge the most efficient di-
rect solvers available today. He pointed out that iterative methods, especially
Krylov subspace iterations in combination with preconditioning methods, could
provide efficient procedures and are almost mandatory for such problems. This
chapter will therefore focus on such iterative techniques. Note that also mod-
ern approaches based on hierarchical matrices exist [94], which could be very
interesting with regard to the presented application.

Large condition numbers are the reason for slow convergence of common
iterative solvers such as Krylov subspace methods [93; 198]. The spectral condi-
tion (condition belonging to the Euclidean norm) of the SPD matrix K_h is equal
to

$$\kappa_2(\mathsf{K}_h) = \frac{\lambda_{\max}}{\lambda_{\min}}$$

with $\lambda_{\max}$ the largest and $\lambda_{\min}$ the smallest eigenvalue of K_h [93, §2.10]. It be-
haves asymptotically like $O(h^{-2})$. Table 5.1 shows condition numbers[1] of the

---

[1]Courtesy of A.Basermann, C&C Research Laboratories, NEC Europe Ltd.. To solve the large
sparse symmetric eigenvalue problems, a Jacobi-Davidson method was applied (Basermann [13]).
The iterative process was carried out up to a maximal l_2 relative residual of 10^{-10}.

FE volume conductor model	λ		κ_2 number
	max	min	
Model 1, isotropic	327.96	$0.1133 * 10^{-4}$	$2.894 * 10^7$
Model 1, 1:10 anisotropic	328.02	$0.1117 * 10^{-4}$	$2.936 * 10^7$
Model 2, isotropic	15.165	$0.1722 * 10^{-5}$	$8.806 * 10^6$
Model 2, 1:10 anisotropic	15.167	$0.1711 * 10^{-5}$	$8.864 * 10^6$

Table 5.1: *Eigenvalues and condition numbers of the Models 1 and 2 of Table 4.1 with isotropic (Table 4.2) and 1:10 anisotropic layers skull and WM as defined in the Tables 4.3 and 4.4 (volume constraint).*

Models 1 and 2 of Table 4.1 with isotropic (Table 4.2) and 1:10 anisotropic layers skull and WM (Tables 4.3 and 4.4 {volume constraint}). These models will be used throughout this chapter. The presented large condition numbers can cause severe accuracy and performance problems for Krylov subspace methods. These problems will be recovered by the application of appropriate preconditioners such that the condition number of the resulting preconditioned stiffness matrix gets small. The results in Table 5.1 show a minor influence of the modeled anisotropy on the condition number. A minor influence of the nodeshift on the condition number was reported in Wolters et al. [255]. Note that, in theory, the convergence speed is independent on the right-hand side of the linear equation system [93, §3.4], so that the results of this chapter are valid for both the direct and the subtraction approach (see Section 4.7.4) and all possible source configurations.

The chapter begins with the description of the algorithm for the preconditioned CG method and the presentation of different preconditioners, appropriate for the considered application. The different approaches will be compared within solver performance tests on a single processor. A parallelization strategy for the most successful method will then be developed. Further performance tests on a multi-processor machine terminate the chapter. All numerical solver studies were carried out on an SGI ORIGIN 2000 with 16 processors [2], a main memory size of 6 Gbytes [3], an instruction cache size of 32 Kbytes, a data cache size of 32 Kbytes and a secondary unified instruction/data cache size of 4 Mbytes.

---

[2]195MHZ, IP27, CPU: MIPS R10000, proc. chip rev.: 2.6, FPU: MIPS R10010, rev.: 0.0.

[3]The SGI Origin is a high performance computer of the MIMD (Multiple Instruction Multiple Data) class [63]. The MIMD class can be divided into distributed and shared memory architectures. Since all processors have access to the whole address space, the SGI-Origin belongs in a first approximation to the shared memory class. In order to speed-up computation, each processor has faster access to a certain sub-address space. This is why the SGI-Origin is also called a distributed shared memory computer.

5.2 The preconditioned conjugate gradient method

Algorithm 8 (Par.) PCG algorithm $\text{PCG}(\mathsf{K}_h, \underline{u}_h, \underline{j}_h, \mathsf{C}_h)$

$\underline{r}_h \leftarrow \underline{j}_h - \mathsf{K}_h \underline{u}_h$

$\underline{w}_h \Leftarrow \mathsf{C}_h^{-1} \cdot \underline{r}_h$

$\underline{s}_h \leftarrow \underline{w}_h$

$\gamma \Leftarrow (\underline{w}_h, \underline{r}_h)$

repeat

$\quad \underline{v}_h \leftarrow \mathsf{K}_h \cdot \underline{s}_h$

$\quad \alpha \Leftarrow \gamma / (\underline{s}_h, \underline{v}_h)$

$\quad \underline{u}_h \leftarrow \underline{u}_h + \alpha \underline{s}_h$

$\quad \underline{r}_h \leftarrow \underline{r}_h - \alpha \underline{v}_h$

$\quad \underline{w}_h \Leftarrow \mathsf{C}_h^{-1} \cdot \underline{r}_h$

$\quad \gamma \Leftarrow (\underline{w}_h, \underline{r}_h)$

$\quad \beta \leftarrow \gamma / \gamma_{\text{OLD}}, \ \gamma_{\text{OLD}} \leftarrow \gamma$

$\quad \underline{s}_h \leftarrow \underline{w}_h + \beta \underline{s}_h$

until TERMINATION

The Krylov subspace of dimension n is defined as

$$Kry_n(\mathsf{K}_h, \underline{r}_0) = \text{span}\{\underline{r}_0, \mathsf{K}_h \underline{r}_0, \dots, \mathsf{K}_h^{n-1} \underline{r}_0\}$$

with $\underline{r}_0$ the initial residual. The CG method for solving SPD linear systems is a realization of an orthogonal projection technique onto Kry_n. Saad [198] derived the CG algorithm from a full orthogonalization method (Arnoldi's method for linear systems), using simplifications resulting from the three-term Lanczos recurrence for symmetric matrices.

The goal of a preconditioner, $\mathsf{C}_h \in \mathbb{R}^{N_h \times N_h}$, is the reduction of $\kappa_2(\mathsf{C}_h^{-1} \mathsf{K}_h)$ for the preconditioned equation system $\mathsf{C}_h^{-1} \mathsf{K}_h \underline{u}_h = \mathsf{C}_h^{-1} \underline{j}_h$. Further requirements are that it is cheap with regard to arithmetic and memory costs to solve linear systems $\mathsf{C}_h \underline{w}_h = \underline{r}_h$ with $\underline{w}_h$ the residual for the preconditioned system and that this operation can well be parallelized. The PCG method (see, e.g.,[93; 198; 206]) is shown in Algorithm 8.

Theorem 5.2.1 (Error estimate for PCG method). *Let K_h and C_h be positive definite. If $\underline{u}_h^*$ denotes the exact solution of the equation system, then the k's iterate of the PCG method $\underline{u}_h^k$ fulfills the following energy norm estimate*

$$\|\underline{u}_h^k - \underline{u}_h^*\|_{\mathsf{K}_h} \leq c^k \frac{2}{1 + c^{2k}} \|\underline{u}_h^0 - \underline{u}_h^*\|_{\mathsf{K}_h}, \qquad c := \frac{\sqrt{\kappa_2(\mathsf{C}_h^{-1} \mathsf{K}_h)} - 1}{\sqrt{\kappa_2(\mathsf{C}_h^{-1} \mathsf{K}_h)} + 1}.$$

The theorem was proven by, e.g., Hackbusch [93, Theorem 9.4.14]. Note that the above error estimate is only an upper bound that may be too pessimistic. In fact, the convergence of the PCG method is influenced by the whole spectrum of $C_h^{-1}K_h$ and superconvergence results are known [93, Remark 9.4.13].

5.2.1 Jacobi preconditioning or scaling

It can be shown, that the smallest (largest) eigenvalue of a symmetric matrix is at most (at least) as large as the smallest (largest) diagonal element, so that the condition number is at least as large as the quotient of maximal and minimal diagonal element (Schwarz, [206, p.258]). Diagonal entries in K_h of FE nodes from inside the skull are much smaller than from outside (jumping conductivity coefficients). The simplest preconditioner is thus the scaling or Jacobi-preconditioning ([198, pp.265f], [206, pp.257f]), where

$$C_h := D_h^2, \qquad D_h := \mathrm{DIAG}(\sqrt{K_h^{[11]}}, \ldots, \sqrt{K_h^{[N_h N_h]}}).$$

When splitting the Jacobi-preconditioner between left and right (row and column scaling), we have to solve $\tilde{K}_h \underline{v}_h = D_h^{-1} \underline{j}_h$ with $\tilde{K}_h = D_h^{-1} K_h D_h^{-tr}$ and $\underline{u}_h = D_h^{-tr} \underline{v}_h$. Row and column scaling preserves symmetry, so that the scaled matrix $\tilde{K}_h$ is again SPD with unit diagonal entries. The scaling may therefore lead to a first substantial condition improvement. Hackbusch [93, Theorem 8.3.3] mentioned the following theorem:

Theorem 5.2.2. *Let K_h be SPD and $C_h := D_h^2$ the Jacobi-preconditioner. Assume that each row of K_h does not contain more than* d *nonzero entries. Then, for all diagonal matrices $\tilde{D}_h^{-1}$, it is*

$$\kappa_2(C_h^{-1}K_h) \leq d\, \kappa_2(\tilde{D}_h^{-1}K_h),$$

i.e., the chosen diagonal preconditioner is close to the optimal one.

5.2.2 Incomplete factorization preconditioners

The second class are the incomplete factorization preconditioners. The first presented one, the IC0, is an approximation to the Cholesky-decomposition $K_h = L_h L_h^{tr}$ (see Algorithm 9, Schwarz [206, pp.209f]). The second, the ILDLT, approximates an LDLT-decomposition $K_h = L_h D_h L_h^{tr}$ (Golub and Van Loan [79, p.139]). Scaling of the equation system is performed before incomplete factorization preconditioning in the PCG solution process. For incomplete factorizations, the preconditioning operation $C_h \underline{v}_h = \underline{r}_h$ in Algorithm 8 is solved by a forward-back sweep.

Algorithm 9 Cholesky decomposition $\mathsf{K}_h = L_h L_h^{tr}$

---

for $p = 1, \ldots, N_h$ **do**
  $L_h^{[pp]} = \sqrt{\mathsf{K}_h^{[pp]}}$
  for $i = (p+1), \ldots, N_h$ **do**
    $L_h^{[ip]} = \mathsf{K}_h^{[ip]} / L_h^{[pp]}$
    for $k = (p+1), \ldots, i$ **do**
      $\mathsf{K}_h^{[ik]} = \mathsf{K}_h^{[ik]} - L_h^{[ip]} / L_h^{[kp]}$
    end for
  end for
end for

IC0-factorization: The IC0-factorization preconditioner exploits an incomplete Cholesky-decomposition $\mathsf{C}_h := L_0 L_0^{tr}$ with zero fill-in, i.e., L_0 has the same non-zero-pattern as the lower triangular part of $\tilde{\mathsf{K}}_h$. The principle for the first step of IC0 is presented in Figure 5.1. The figure shows the nonzero pattern of the start matrix $\check{\mathsf{K}}_h \in \mathbb{R}^{N_h \times N_h}$ (left) (generally a copy of the scaled stiffness matrix), the situation after the first step of Algorithm 9 (fill-in is marked with *) and the situation after the first step of IC0 (fill-in rejected). Note, that the Cholesky decomposition is carried out on the memory space of $\check{\mathsf{K}}_h$.

The existence of IC0 is not necessarily guaranteed for general SPD matrices while it can be proven, e.g., for the subclass of symmetric M-matrices [93, Theorem 8.5.10]. Therefore, a reduction of non-diagonal stiffness matrix entries has to be carried out in certain applications before IC0 computation is possible [206, p.266]. If the scaled geometry matrix is decomposed by means of $\tilde{\mathsf{K}}_h = E_h + \mathrm{Id}^{N_h} + E_h^{tr}$ with $E_h \in \mathbb{R}^{N_h \times N_h}$ its strict lower triangular part, the reduction can be formulated as

$$\check{\mathsf{K}}_h = \mathrm{Id}^{N_h} + \frac{1}{1+\varsigma}(E_h + E_h^{tr}). \tag{5.1}$$

For sufficiently large $\varsigma \in \mathbb{R}_0^+$, the existence of IC0 is guaranteed, but with increasing ς, the preconditioning effect decreases.

Note that for certain special cases a condition improvement to $O(h^{-1})$ can be proven as, e.g., when using a modified ILU_ω-preconditioning with $\omega = -1$ (in the symmetric case, the ILU_0 is equal to the ICO) for diagonally dominant symmetric matrices arising from a 5-point discretization of a 2D Poisson equation (Hackbusch [93, Theorem 8.5.15 and Remarks 8.5.16,17]).

ILDLT-factorization with threshold: Jacobi-preconditioning and IC0 factorizations are "blind" to numerical values. Elements that are dropped in IC0 depend only on the non-zero pattern of K_h. Therefore, as a second class of incomplete
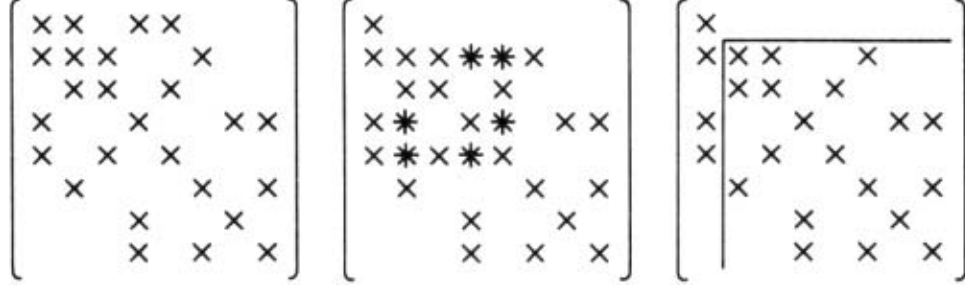
Figure 5.1: *Principle of IC0 (taken from Schwarz [206]): nonzero matrix pattern (left), situation after first step of Algorithm 9 (fill-in is marked with *), situation after the first step of IC0.*

factorization methods, a threshold-technique, as it is the incomplete LDL^{tr} factorization with threshold value ε, ILDLT(ε) [198; 13], are studied where elements are dropped according to their magnitudes rather than their locations. With such techniques, the zero pattern (elements smaller ε) is determined dynamically during preconditioner construction.

5.2.3 Theoretical considerations to multigrid iterations

The above preconditioning methods have the disadvantage that the convergence rate, i.e., the factor by which the error is reduced in each iteration, is still dependent on the mesh size h. With decreasing mesh size and thus increasing order of the equation system, the convergence rate tends to 1 from below, so that the number of iterations needed to achieve a given accuracy increases.

A solver method is called asymptotically optimal with respect to the operation count and memory demand, if both are proportional to N_h. The Geometric Multi-Grid (GMG) method can be shown to be asymptotically optimal, requiring an order of $O(N_h)$ arithmetical operations per iteration [93, Theorem 10.4.2] and a memory demand of $O(N_h)$.

h-independent convergence with respect to the spectral norm can be shown for the W-cycle GMG method even for unsymmetric and indefinite sparse linear systems of equations [93, Theorem 10.6.25]. The assumptions for such proofs are that the so-called smoothing [93, §10.6.2] and approximation properties [93, §10.6.3] are fulfilled, the number of smoothing steps is sufficiently large and the mesh size on the coarsest level is not too coarse. A detailed description of GMG is given in [91].

We now make use of the conditions that the system matrix is SPD, the restric-

tion is adjoint to the prolongation (Equation (5.4)), the post-smoother adjoint to the pre-smoother and the Galerkin product property (Equation (5.5)) is valid. In this case, the GMG method can be designed as a symmetric iteration [93, §4.8, Lemma 10.7.1]. If we denote with M_h the MG iteration matrix (see, e.g., [93, Theorem 10.4.5]), monotone convergence with respect to the energy norm and an h-independent convergence rate

$$\rho := \rho(M_h) = ||M_h||_{K_h} < 1$$

can be shown using the same assumptions as above [93, §10.7.2]. In particular, if with C_h we now denote the matrix of the third normal form (see [93, §3.2]) of the iteration resulting from m steps of the GMG method (note that m steps of the GMG method yield the rate ρ^m), the condition number of the m-step GMG-preconditioned equation system fulfills

$$\kappa_2(C_h^{-1}K_h) \leq \frac{1}{1 - \rho^m}, \tag{5.2}$$

i.e., it is h-independent, too, and thus of an order $O(1)$ [93, Lemma 10.7.1]. If, furthermore, a symmetric smoothing iteration is chosen, h-independent monotone convergence with respect to the energy norm can even be proven for the V-cycle GMG for all smoothing step numbers larger zero without any restriction to the coarsest mesh size [93, Theorem 10.7.15].

5.2.4 The multigrid-preconditioned CG method

For our application, it is not easy to generate the necessary grid hierarchy and to choose the MG components (smoothing, prolongation etc.) so that the rate observed is really small (e.g., $\rho \leq 0.1$). A robust method which provides a small convergence rate for a wide class of real-life problems is given by exploiting the MG-method as a basis for the CG method (see, e.g., [93; 115; 219]). With MG(m)-CG, we will now denote the MG-preconditioned CG method with m the number of MG iterations for the CG preconditioning step.

Theorem 5.2.3. *The exact solution of the preconditioning equation $C_h \underline{w}_h = \underline{r}_h$ for MG(m)-CG is equivalent to the application of m MG cycles to the so-called a priori preconditioning equation*

$$K_h \underline{w}_h = \underline{r}_h. \tag{5.3}$$

Proof: The preconditioner has the special form

$$C_h^{-1} = \left(\text{Id}^{N_h} - (M_h)^m\right) K_h^{-1}$$

[93, Theorem 3.2.2, Remark 3.2.4]. If the linear MG iteration is applied to (5.3) with the zero start vector $\underline{w}_h^0 = \underline{0}^{N_h}$, it produces iterates of the form

$$\underline{w}_h^m = (M_h)^m \underline{w}_h^0 + \sum_{i=0}^{m-1} \left\{ (M_h)^i \left(\mathrm{Id}^{N_h} - M_h \right) \right\} \mathsf{K}_h^{-1} \underline{r}_h = \left(\mathrm{Id}^{N_h} - (M_h)^m \right) \mathsf{K}_h^{-1} \underline{r}_h$$

[93, Theorem 3.2.5].   □

Using Theorem 5.2.1 and Equation (5.2), an error estimate of

$$\|\underline{u}_h^k - \underline{u}_h^*\|_{\mathsf{K}_h} \le c^k(\rho) \frac{2}{1 + c^{2k}(\rho)} \|\underline{u}_h^0 - \underline{u}_h^*\|_{\mathsf{K}_h}$$

with

$$c(\rho) = \frac{\sqrt{\kappa_2(\mathsf{C}_h^{-1}\mathsf{K}_h)} - 1}{\sqrt{\kappa_2(\mathsf{C}_h^{-1}\mathsf{K}_h)} + 1} = \frac{1 - \sqrt{1 - \rho^m}}{1 + \sqrt{1 - \rho^m}}$$

can be derived for the k's iterate $\underline{u}_h^k$ of GMG(m)-CG. If ρ is considered to be small, then $c(\rho) \approx \rho/4 + \mathcal{O}(\rho^2)$ can be achieved by means of a Taylor expansion. This means that the convergence ρ of the pure GMG-method can be accelerated to $\rho/4$ by means of the CG method [93, §10.8.3]. Nevertheless, in practice, ρ is relatively unfavorable. In this case, Jung and Langer carried out the operation count for standard boundary value problems and showed that GMG(1)-CG is more efficient than the pure GMG solver for $\rho \in [0.4, 1)$ (see [115] and references therein).

5.2.5   Algebraic multigrid preconditioners

In contrast to GMG, where a grid hierarchy is required explicitly, AMG is able to construct matrix hierarchy and corresponding transfer operators by only knowing the entries in the geometry matrix K_h (see, e.g., [196; 26; 219; 189]). It is well known, that the classical AMG works robust for M-matrices and, with regard to our application, that small positive off-diagonal entries are admissible [196; 219; 189]. The method is especially suited for our problem with discontinuous and anisotropic coefficients, where an optimal tuning of the GMG is difficult or even impossible ([196, §4.1,4.6.4],[219, §4.1]).

Feuchter et al. [59] recently presented another interesting approach that should be mentioned here, since it bridges in a certain way the gap between GMG and AMG. As in AMG, their approach only needs the finest grid and the corresponding system matrix in order to generate the coarser grids and to set up the prolongation and restriction operators in a "black-box fashion". All grids between

the coarsest and the second finest level are nested so that the general GMG convergence theory can be exploited. Only the embedding of the second finest grid into the given finest grid is "non-nested". Feuchter et al. elaborate a convergence theory for the non-nested case and present numerical results for complicated 2D domains.

Nevertheless, this work focuses on an AMG approach. Ruge and Stüben [196] have proven AMG V-cycle convergence for SPD matrices when assuming that the interpolation operators have full rank, the Equations (5.4) for the restriction and (5.5) for the coarse grid operators are fulfilled and an algebraic smoothing and an algebraic approximation property are supposed to hold [196, §4.3]. The smoothing property could be proven under quite general circumstances [196, §4.4], while the approximation property presented the most problems. Therefore, a weaker condition was introduced with which uniform two-level convergence could be proven [196, Theorem 5.2], but which was not sufficient to guarantee a level-independent V-cycle convergence rate [196, §4.5.5]. Nevertheless, the weaker condition is necessary for the approximation property and implies a useful property for the prolongation operator to be constructed, i.e., that the prolongation has to preserve the kernel of K_h ([196, §4.5.5] and [189, §3.4]).

Stand-alone AMG will hardly ever be optimal. There may be some very specific error components which are reduced significantly less efficient, causing a few eigenvalues of the AMG iteration matrix to be much closer to 1 than all the rest [219, §3.3]. In such a case, acceleration by means of using AMG as a basis for the CG method (see Section 5.2.4) eliminates these particular frequencies very efficiently.

As in GMG, the basic idea in AMG is to reduce high and low frequency components of the error by the efficient interplay of smoothing and coarse grid correction, respectively. In analogy to GMG, the denotation "coarse grids" will be used, although these are purely virtual and do not have to be constructed explicitly as coarse FE meshes. The diagonal entry of the ith row of K_h is considered as being related to a grid point in ω_h (the index set of nodes) and an off-diagonal entry is related to an edge in an FE grid.

A description of AMG will now be given for a symmetric two grid method where h is related to the fine grid and H to the coarse grid. Each AMG algorithm consists of the following components:

(a) Coarsening: define the splitting $\omega_h = \omega_C \cup \omega_F$ of ω_h into sets of coarse and fine grid nodes ω_C and ω_F, respectively.

(b) Transfer operators: prolongation $\mathfrak{P}_{h,H} : V_H \mapsto V_h$ ($V_h = \mathbb{R}^{N_h}$, Section 4.7.2) and the adjoint as the restriction

$$\mathfrak{R}_{H,h} := \mathfrak{P}_{h,H}^{tr}. \tag{5.4}$$

"fine grid"   "coarse grid"
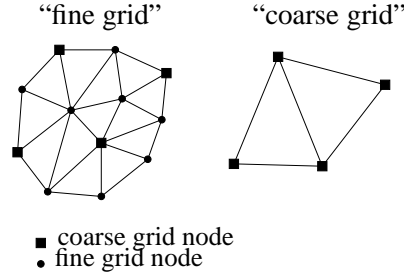

■ coarse grid node
• fine grid node

Figure 5.2: *Illustration of a two grid method.*

(c) Definition of the coarse matrix by Galerkin's method, i.e.,

$$\mathsf{K}_H := \mathfrak{R}_{H,h}\mathsf{K}_h\mathfrak{P}_{h,H}. \tag{5.5}$$

Because of (b), $\mathsf{K}_H \in \mathbb{R}^{N_H \times N_H}$ is again SPD.

(d) Appropriate smoother for the considered problem class: In order to achieve a symmetric method, e.g., a forward Gauss-Seidel method for pre-smoothing and the adjoint, a backward Gauss-Seidel method for post-smoothing [93, §4.8.3,§10.7.1,2]. For the Gauss-Seidel method, the algebraic smoothing property can be proven for sparse SPD matrices so that it is generally chosen for smoothing in AMG [196, §4.4].

Coarsening: The coarsening process has the task to reduce the nodes such that $N_H = |\omega_C| < N_h = |\omega_h|$. Here, $|\omega|$ denotes the number of elements in the set ω. Motivated from Figure 5.2, the grid points ω_h can be split into two disjoint subsets ω_C (coarse grid nodes) and ω_F (fine grid nodes), i.e., $\omega_h = \omega_C \cup \omega_F$ and $\omega_C \cap \omega_F = \emptyset$ such that there are (almost) no direct connections between any two coarse grid nodes and the resulting number of coarse grid nodes is as large as possible [219, p.12]. Instead of considering all connections between nodes as being of the same rank, the following sets are introduced

$$
\begin{aligned}
N_h^i &= \left\{ j \,|\, |\mathsf{K}_h^{[ij]}| \geq \varsigma |\mathsf{K}_h^{[i,i]}|, i \neq j \right\} & (5.6)\\
S_h^i &= \left\{ j \in N_h^i \,|\, |\mathsf{K}_h^{[ij]}| > \text{coarse}(i,j,\mathsf{K}_h) \right\}\\
S_h^{i,T} &= \left\{ j \in N_h^i \,|\, i \in S_h^j \right\} & (5.7)
\end{aligned}
$$

where N_h^i is the index set of neighbors (a pre-selection is carried out by the threshold-parameter $\varsigma \in \mathbb{R}_0^+$), S_h^i denotes the index set of nodes with a "strong connection" from node i and $S_h^{i,T}$ is related to the index set of nodes with a "strong

---

Algorithm 10 : COARSE:$(\{S_h^{i,T}\}, \omega_h) \rightarrow (\omega_C, \omega_F)$

$\omega_C \leftarrow \emptyset, \quad \omega_F \leftarrow \emptyset$
while $\omega_C \cup \omega_F \neq \omega_h$ **do**
   $i \leftarrow \text{PICK}(\omega_h \setminus (\omega_C \cup \omega_F))$
   if $|S_h^{i,T}| + |S_h^{i,T} \cap \omega_F| = 0$ **then**
      $\omega_F \leftarrow \omega_h \setminus \omega_C$
   else
      $\omega_C \leftarrow \omega_C \cup \{i\}$
      $\omega_F \leftarrow \omega_F \cup (S_h^{i,T} \setminus \omega_C)$
   end if
end while

---

connection" to node i. In addition $\text{coarse}(i, j, K_h)$ is an appropriate cut-off (coarsening) function, e.g.,

$$\text{coarse}(i, j, K_h) := \alpha \cdot \max_{j, j \neq i}\{|K_h^{[ij]}|\}, \tag{5.8}$$

with $\alpha \in [0, 1]$ (see, e.g., [196, §4.6.1]). With those definitions a splitting into coarse and fine grid nodes can be done. For our application, a modified splitting algorithm of Ruge and Stüben [196, §4.6] was used, which is shown in Algorithm 10. Therein, the function

$$i \leftarrow \text{PICK}(\omega_h \setminus (\omega_C \cup \omega_F))$$

returns a node i where the number $|S_h^{i,T}| + |S_h^{i,T} \cap \omega_F|$ is maximal. Note, that tissue conductivity inhomogeneity and anisotropy is taken into account within the coarsening algorithm.

Prolongation: Next the prolongation operator $\mathfrak{P}_{h,H} : V_H \mapsto V_h$ has to be defined correctly. As already mentioned, the weakened algebraic approximation property implies that the kernel of K_h has to be preserved by $\mathfrak{P}_{h,H}$ ([196, §4.5.5] and [189, §3.4]). In our case, if $\mathbb{V}_h$ is chosen as the subspace of piecewise linear functions (4.34), the kernel simply consists of the constant potential distributions. Another important property is, that $\mathfrak{P}_{h,H}$ has full rank. Reitzinger [189, Corollary 4.1.2] showed that a full rank prolongation operator, which satisfies

$$\sum_{j=1}^{N_H} \mathfrak{P}_{h,H}^{[ij]} = 1 \quad \forall i = 1, \ldots, N_h,$$

fulfills the above necessary conditions. There are a lot of possibilities to define such transfer operators with pure algebraic information. The simplest is given

---

Algorithm 11 (Parallel) $V(\nu_F, \nu_B)$-cycle MG($K_h, \underline{u}_h, \underline{j}_h$)

---

if COARSEGRID **then**
    $\underline{u}_h \Leftarrow$ DIRECTSOLVE$(K_h \cdot \underline{u}_h = \underline{j}_h)$
else
    $\widetilde{\underline{u}}_h \Leftarrow \nu_F$ TIMES SMOOTH FORWARD$(K_h, \underline{u}_h, \underline{j}_h)$
    $\underline{d}_h \leftarrow K_h \cdot \widetilde{\underline{u}}_h - \underline{j}_h$
    $\underline{d}_H \leftarrow \mathfrak{P}_{h,H}^{tr} \cdot \underline{d}_h$
    $\underline{\mathfrak{w}}_H \leftarrow 0$
    $\underline{\mathfrak{w}}_H \Leftarrow$ MG$(K_H, \underline{\mathfrak{w}}_H, \underline{d}_H)$
    $\underline{\mathfrak{w}}_h \leftarrow \mathfrak{P}_{h,H} \cdot \underline{\mathfrak{w}}_H$
    $\widehat{\underline{u}}_h \leftarrow \widetilde{\underline{u}}_h - \underline{\mathfrak{w}}_h$
    $\underline{u}_h \Leftarrow \nu_B$ TIMES SMOOTH BACKWARD$(K_h, \widehat{\underline{u}}_h, \underline{j}_h)$
end if

---

by a piecewise constant interpolation [26]. Another possible setting and the one which turned out to be the most efficient for the presented application was proposed by Kickinger [120] and is given by

$$
\mathfrak{P}_{h,H}^{[ij]} = \begin{cases} 1 & i = j \in \omega_C \\ 1/|S_h^{i,T} \cap \omega_C| & i \in \omega_F, \, j \in S_h^{i,T} \cap \omega_C \\ 0 & \text{else} \, . \end{cases} \tag{5.9}
$$

Ruge and Stüben [196, §4.5.4] (for a good motivation see also [89]) proposed the discrete harmonic extension for $\mathfrak{P}_{h,H}$. This is the best interpolation proposed here but it suffers from the fact that $\mathfrak{P}_{h,H}$ has more nonzero entries so that cycling gets more expensive. In our application, its numerical work per cycle (see [196, §4.6.3] or a general definition in [93, §3.3]) was increased compared to the approach in (5.9).

AMG-CG: After the proper definition of the prolongation and coarse grid operators a matrix hierarchy can be setup in a recursive way. Finally, a multigrid cycle can be assembled, shown in Algorithm 11. Therein the variable COARSEGRID denotes the level where a direct solver is applied. For an m-$V(\nu_F, \nu_B)$-cycle AMG preconditioned CG method, the operation $\underline{\mathfrak{w}}_h \Leftarrow C_h^{-1} \cdot \underline{r}_h$ in Algorithm 8 is realized by m calls of MG$(K_h, \underline{\mathfrak{w}}_h, \underline{r}_h)$ (see Theorem 5.2.3).

5.3 Performance studies on a single processor

In the following, the performance of the different solver methods will be compared on a single processor for Model 2 of Table 4.1 with isotropic and 1:10 anisotropic layers skull and WM. Comparable results were achieved for Model 1.
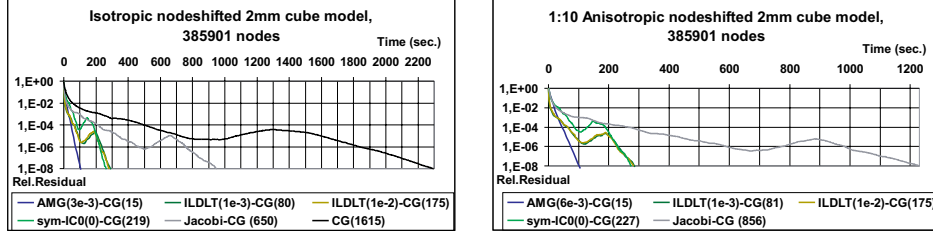
Figure 5.3: *Model 2 of Table 4.1: l_2-relative residual against wall clock time on 1 processor for the solver part of different solver methods up to an accuracy of 10^{-8}.*

Solver parameter settings, used throughout this chapter, are now discussed. The FE space $\mathbb{V}_h$ consisted of the piecewise linear Ansatz-functions (see Equation (4.34)). The selected values of ς for the IC0, ε for the ILDLT and ζ (see (5.6)) for the AMG are indicated behind the preconditioner in the solver performance figures. The setup-times for the preconditioners were neglected in the figures since this has to be performed only once with regard to the inverse problem. All solvers were started with the zero potential vector. For the AMG-CG, the 1-$V(1,1)$-cycle AMG-preconditioner was used. Even if the W-cycle has a smaller convergence rate, the V-cycle was found to be cheaper in practice (see [93, §3.3] for a definition of effectiveness). Equation (5.8) was taken as the cut-off coarsening function with $\alpha = 0.01$ and the prolongation was chosen as in (5.9). The factorization in Algorithm 11 was carried out, if the size of the coarsest grid (COARSEGRID) in the preconditioner-setup was below 1000 for the cube models. The coarse system was solved using a Cholesky-factorization (Algorithm 9).

In order to take advantage of the large number of zero elements, special schemes are implemented to store the sparse stiffness matrix and the sparse pre-conditioners. All presented methods use the Compressed Sparse Row (CSR) format (see Saad [198, pp.84f]). Symmetry in IC0 and ILDLT is exploited by storing only the lower triangular part of those preconditioners. Nevertheless, in the implementation of sym-IC0-CG, also the stiffness matrix is stored in symmetric CSR format (this explains the prefix "sym", see Schwarz [206, pp.268f]), while, with regard to their parallelization, Jacobi-CG, ILDLT-CG and AMG-CG memorize the full stiffness matrix. This implies, that a stiffness matrix-vector multiplication in the PCG Algorithm 8 will be computed faster by sym-IC0-CG than by the other solvers.

Figure 5.3 shows the required time of the different solver methods in order to reduce the initial l_2 residual by a factor of 10^{-8} for the isotropic cube model (left) and the anisotropic cube model (right). For the isotropic model, the performance

of the pure Krylov-method was presented additionally to the PCG results. The number of iterations are marked behind the Krylov-method. Note, that the peaks in the residuals are due to the fact that the Krylov-method minimizes the K_h-energy-norm instead of the l_2-norm, visualized in the above figures.

For relative residuals in the range 10^{-3} up to 10^{-8}, AMG-CG is the fastest solver due to its superior preconditioning properties. Because of the strong potential decrease from the source through the low-conducting skull to the electrodes, the interesting residuals begin at about 10^{-6}. As will be seen in Chapter 7, the accurate reconstruction of multiple dipolar sources can even necessitate relative residuals of about 10^{-8}. For 10^{-6}, AMG-CG is about a factor 3 times faster than the class of incomplete factorization PCG methods for both isotropic and anisotropic model. For 10^{-8}, it is a factor 9 (12) times faster than the Jacobi-CG for the isotropic (anisotropic) model. The factor between AMG-preconditioned CG and the pure Krylov approach is about 22 for the isotropic model. Compared to ILDLT(1e-2)-CG, where 175 (175) iterations with 5375551 (5483394) incomplete factorization non-zeros were required for the isotropic (anisotropic) model, the ILDLT(1e-3)-CG needed only 80 (81) iterations. Nevertheless, this advantage is lost since, with 17091344 (16616026) non-zeros, ILDLT(1e-3)-CG iterations are computationally more expensive. Note again, that sym-IC0-CG is only faster than the ILDLT-threshold solvers because of the different implementations of the stiffness matrix storage. IC0 had about the same amount of non-zeros than ILDLT(1e-2), so that, with regard to its parallelization, IC0-CG would be 219/175 (227/175) times slower than ILDLT(1e-2)-CG for the isotropic (anisotropic) model. To give an impression about the time for the computation of the preconditioners, the setup for the isotropic cube model took 128 seconds (s) for the AMG, 53 s for ILDLT(1e-3) and 12 s for ILDLT(1e-2) and IC0.

ILDLT- and AMG-preconditioners take conductivity inhomogeneity and anisotropy into account, symIC0- and Jacobi-CG only do to a minor degree. Note that with 850 to 650 iterations, the Jacobi-CG is a factor 1.3 slower in the anisotropic case and refer to the discussion about the influence of anisotropy onto the solver times in Section 5.5.2.

5.4   Parallelization of FE solver methods

If the inverse problem has to be solved with many calls to FE forward simulations, the results cannot be produced within an acceptable time on one processor. However, a parallel computer may provide sufficient capacity such that time limitation can be fulfilled. In Haase et al. [88] it has been shown for a Poisson equation on the geometry of a simplified crank shaft that AMG-CG solvers exhibit high speed-ups on parallel computers including PC clusters and an SGI

ORIGIN 2000. The speed-up was especially good (superlinear) for the solver-part of the algorithm. Within this Section, the data partitioning aspects and the concepts of the parallel solver approaches will be presented, which mainly rely on ideas reported by Haase, Kuhn and Reitzinger in [87; 88; 189]. The parallel solvers will be applied to source localization problems and their performance will be compared in realistic head volume conductor models.

5.4.1 Data Partitioning

The aim of parallelization is to split both data and operations to the $P \in \mathbb{N}$ processors available. The consistency of the algorithms is preserved by message passing. In our case, the parallelization is based on a non-overlapping domain decomposition, i.e., we decompose $\overline{\Omega}$ into P subdomains $\overline{\Omega}_s$ such that

$$\overline{\Omega} = \bigcup_{s=1}^{P} \overline{\Omega}_s$$

with

$$\Omega_s \cap \Omega_q = \emptyset \quad \forall q \neq s, \quad s, q = 1, \ldots, P$$

holds. Each subdomain Ω_s is discretized by a mesh $\tau_{h,s}$ such that the whole decomposition

$$\tau_h = \bigcup_{s=1}^{P} \tau_{h,s}$$

of Ω forms a conforming mesh. A global FE space $\mathbb{V}_h$ is defined with respect to τ_h and the local spaces $\mathbb{V}_{h,s}$ are restrictions of $\mathbb{V}_h$ onto $\tau_{h,s}$. The index set of nodes in $\overline{\Omega}_s$ is denoted by ω_s. Note, that

$$\omega_h = \bigcup_{s=1}^{P} \omega_s \quad \text{but} \quad N_h = |\omega_h| \leq \sum_{s=1}^{P} |\omega_s| =: \sum_{s=1}^{P} N_s$$

holds, i.e., different subdomains may share unknowns although elements from different subdomains do not overlap. "Interface nodes" are those nodes which belong to at least two processors, whereas "inner nodes" only belong to one.

The mesh partitioning of realistic FE head geometries with unstructured meshes is critical for the efficiency of the parallel solver method, described in the next subsection. The distribution must be done so that the number of elements assigned to each processor is the same and the number of adjacent elements assigned to different processors is minimized in order to balance the computation amount among the processors and to minimize the communication between them, resp.. Therefore, graph partitioning algorithms are used which model the

FE mesh by a graph (V, E) with vertices V and edges E. The interest is in an "element-wise-" [87; 88; 189] in contrast to a "node-wise-" [13] distribution, i.e., the dual graph of the FE mesh is partitioned. The finite elements are the vertices of the dual graph and adjacent elements are the corresponding edges. A balanced k-way partitioning is used (Karypis and Kumar [118]), minimizing the number of edges which straddle partitions. The algorithm is based on a multilevel approach, first reducing the size of the dual graph by collapsing vertices and edges, then partitioning the dual graph on the lowest level and further refine during the uncoarsening steps.

5.4.2 Data types and basic operations

Data types

A subdomain connectivity matrix $A_{s,h} \in \mathbb{R}^{N_s \times N_h}$

$$A_{s,h}^{[ij]} := \begin{cases} 1 & \text{if} \quad j = \text{LOC2GLOB}(i) \\ 0 & \text{else} \end{cases} \quad \forall i \in \omega_s, \, \forall j \in \omega_h,$$

($\text{LOC2GLOB}(\cdot)$ maps a local index to the global one) symbolically represents the mapping of a vector $\underline{u}_h \in \mathbb{R}^{N_h}$ in global numbering onto a local vector $\underline{u}_s \in \mathbb{R}^{N_s}$ in subdomain $\overline{\Omega}_s$, while the transpose maps a local vector back onto the global one. The index set of all those subdomains to which an unknown $u_h^{[j]}$, $j \in \omega_h$ belongs, is denoted by

$$\Sigma^j := \{ s \,|\, u_h^{[j]} \in \omega_s \}. \tag{5.10}$$

The data related to the ith node is stored in the subdomain Ω_s, if $s \in \Sigma^i$. This approach results in local data denoted by index s of two types [87]: *accumulated data* (vectors $\underline{u}_h$, $\underline{s}_h$ and $\underline{w}_h$, matrix $\mathfrak{M}_h \in \mathbb{R}^{N_h \times N_h}$) represented by

$$\underline{u}_s := A_{s,h} \cdot \underline{u}_h \ , \qquad \mathfrak{M}_s := A_{s,h} \cdot \mathfrak{M}_h \cdot A_{s,h}^{tr}$$

with $\mathfrak{M}_s \in \mathbb{R}^{N_s \times N_s}$ and *distributed data* (vectors $\underline{j}_h$, $\underline{v}_h$, $\underline{r}_h$, $\underline{d}_h$, matrix K_h) represented by

$$\underline{d}_h = \sum_{s=1}^{P} A_{s,h}^{tr} \cdot \underline{d}_s, \qquad \mathsf{K}_h := \sum_{s=1}^{P} A_{s,h}^{tr} \cdot \mathsf{K}_s \cdot A_{s,h}.$$

The local FE accumulation with respect to $\mathbb{V}_{h,s}$ produces automatically distributed matrices K_s.

Basic operations

The inner product of different type vectors only requires one global reduce operation of the local inner products, since it is

$$(\underline{\mathfrak{w}}_h, \underline{\mathfrak{r}}_h) = \underline{\mathfrak{w}}_h^{tr} \sum_{s=1}^{P} A_{s,h}^{tr} \underline{\mathfrak{r}}_s = \sum_{s=1}^{P} (A_{s,h} \underline{\mathfrak{w}}_h)^{tr} \underline{\mathfrak{r}}_s = \sum_{s=1}^{P} (\underline{\mathfrak{w}}_s, \underline{\mathfrak{r}}_s).$$

It can be further shown that the multiplication of a distributed matrix K_h with the accumulated vector $\underline{\mathfrak{s}}_h$ results in a distributed vector $\underline{\mathsf{v}}_h$:

$$\mathsf{K}_h \cdot \underline{\mathfrak{s}}_h = \sum_{s=1}^{P} A_{s,h}^{tr} \mathsf{K}_s A_{s,h} \cdot \underline{\mathfrak{s}}_h = \sum_{s=1}^{P} A_{s,h}^{tr} (\mathsf{K}_s \cdot \underline{\mathfrak{s}}_s) = \sum_{s=1}^{P} A_{s,h}^{tr} \underline{\mathsf{v}}_s = \underline{\mathsf{v}}_h$$

The realization requires no communication at all because $\underline{\mathsf{v}}_s = \mathsf{K}_s \cdot \underline{\mathfrak{s}}_s$ only has to be computed locally.

Theorem 5.4.1 (Admissible interpolation pattern). *If an accumulated matrix* $\mathfrak{M}_{h,H} \in \mathbb{R}^{N_h \times N_H}$ *fulfills the condition*

$$\forall i \in \omega_h, j \in \omega_C : \Sigma^i \not\subseteq \Sigma^j \implies \mathfrak{M}_{h,H}^{[ij]} = 0, \tag{5.11}$$

then the operations

$$\underline{\mathfrak{w}}_h = \mathfrak{M}_{h,H} \cdot \underline{\mathfrak{w}}_H, \qquad \underline{\mathsf{d}}_H = \mathfrak{M}_{h,H}^{tr} \cdot \underline{\mathsf{d}}_h, \qquad \mathsf{K}_H = \mathfrak{M}_{h,H}^{tr} \mathsf{K}_h \mathfrak{M}_{h,H} \tag{5.12}$$

can be performed locally without any communication.

Proof: Haase [87, Theorems 5.1,5.2].

5.4.3 Parallel algebraic multigrid

Now it can be observed that Algorithms 8 and 11 are also the appropriate parallel formulations, where double-line arrows "$\Leftarrow$" indicate that communication is required for the corresponding operation. In Algorithm 11, the coarse grid system is accumulated globally once in the setup phase. During the iteration only a vector has to be assembled (indicated by "$\Leftarrow$") for computing the coarse grid solution.

In AMG the coarsening and prolongation operators are components which can be chosen. The main idea in the design of parallel AMG is to choose these components such that the resulting prolongation operators $\mathfrak{P}_{h,H}$ are of accumulated type, satisfying the pattern condition (5.11). The operations (5.12) can then be performed locally without any communication. Therefore, the sets of strong connections $\{S_h^{i,T}\}$ have to be controlled in the coarsening step, which will be described in the following.
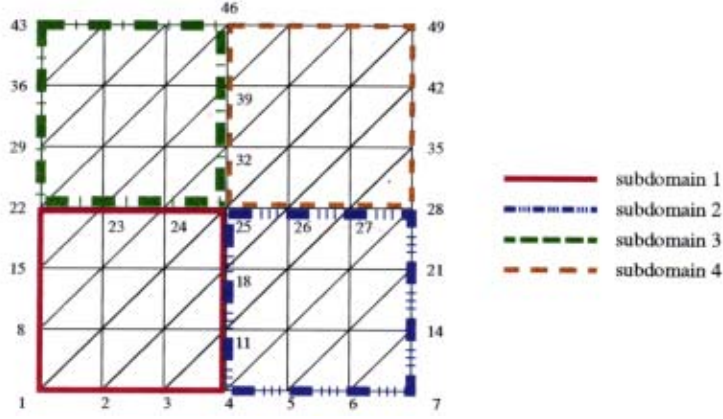
Figure 5.4: *Four non-overlapping subdomains with triangular mesh and row-wise numbering, taken from Haase et al. [88].*

Ordering of communication groups

Haase et al. [88] introduced a "communication group" Σ_k as being the subset of processors, which are involved in a next neighbor communication. They ordered these groups uniquely by means of their cardinality

1. $|\Sigma_k| > |\Sigma_\ell| \quad \Rightarrow \quad k < \ell$,

2. $|\Sigma_k| = |\Sigma_\ell|$ and Σ_k lexicographically smaller than $\Sigma_\ell \quad \Rightarrow \quad k < \ell$.

The ordering guarantees the consistency of local and global ordering and prevents communication deadlocks in the algorithm. The nodes ω_s of subdomain Ω_s were then locally grouped into four classes with respect to a certain communication group Σ_k :

1. active nodes: $\omega_a := \{i \in \omega_s : \Sigma^i \equiv \Sigma_k\}$

2. visible nodes: $\omega_v := \{i \in \omega_s : \Sigma^i \subset \Sigma_k\}$

3. grouped nodes: $\omega_g := \{i \in \omega_s : \Sigma^i \supset \Sigma_k\}$

4. invisible nodes : $\omega_s \setminus (\omega_a \cup \omega_v \cup \omega_g)$

Let nc_s be the number of communication groups of subdomain Ω_s. The following example helps in understanding the above definitions:

Example 5.4.2. *In the 2D model in Figure 5.4, subdomain Ω_2 possesses the $nc_2 = 4$ communication groups $\Sigma_1 = \{1,2,3,4\}$, $\Sigma_2 = \{1,2\}$, $\Sigma_3 = \{2,4\}$ and $\Sigma_4 = \{2\}$, where the last one does not require any communication, but simplifies the parallel coarsening algorithm. It is $\Sigma_1 = \Sigma^{25}$, $\Sigma_2 = \Sigma^{18}$, $\Sigma_3 = \Sigma^{26}$ and $\Sigma_4 = \Sigma^7$. For Ω_2 and $\Sigma_2 = \{1,2\}$, it is $\omega_a = \{4,11,18\}$, $\omega_v = \{5,6,7,12,13,14,19,20,21\}$ and $\omega_g = \{25\}$. Invisible nodes are 26, 27 and 28.*

Parallel coarsening and prolongation

For the parallel coarsening and the determination of the prolongation weights, the admissible interpolation pattern (5.11) has to be respected for the prolongation matrix $\mathfrak{P}_{h,H}$. Therefore, Haase et al. [88] proposed the following three steps:

1. The geometry matrices K_s are locally compiled in parallel for each subdomain Ω_s. In order to determine the strong connections to each node $i \in \omega_h$, i.e., $S_h^{i,T}$ (see (5.7)), the system matrix has to be globally accumulated. A first step to control (5.11) consists in a special accumulated matrix

$$\widetilde{\mathfrak{K}} = \sum_{s=1}^{P} A_{s,h}^{tr} \widetilde{\mathsf{K}}_s A_{s,h}$$

with

$$\widetilde{\mathsf{K}}_s^{[ij]} = \begin{cases} \mathsf{K}_s^{[ij]} & \text{iff} \quad \Sigma^i \subseteq \Sigma^j \vee \Sigma^i \supseteq \Sigma^j \\ 0 & \text{else} \end{cases}, \qquad (5.13)$$

which is locally stored as $\widetilde{\mathfrak{K}}_s = A_{s,h} \widetilde{\mathfrak{K}} A_{s,h}^{tr}$. For the example in Figure 5.4, this means, e.g., that $\widetilde{\mathfrak{K}}^{[18,26]} = \widetilde{\mathfrak{K}}^{[26,18]} = 0$, i.e., nodes from different interfaces will not be interpolated from each other. The preliminary sets of strong connections $S_h^{i,T}$ can then be computed using the matrix $\widetilde{\mathfrak{K}}_s$ instead of K_h in Equations (5.7) and (5.8).

2. The second step exploits the ordering of the communication groups by subsequently performing a local coarsening on the active nodes ω_a (see "step two" in the routine **PARCOARSE** in Algorithm 12). It has to be guaranteed that the decomposition of interface nodes into coarse and fine nodes is coherent over all processes of the respective communication group. Therefore, the coarsening is carried out only on Σ_k's root process, the result is broadcasted to the waiting group, which then proceeds with its coarsening while respecting the marked coarse nodes ω_m. The coarsening parts are handled by the routine **COARSEP** (see Algorithm 13), which is derived from the sequential coarsening routine from Algorithm 10. The sequential

---

Algorithm 12 : PARCOARSE: $(\{S_h^{i,T}\}, \omega_{C,s}, \omega_{F,s}) \rightarrow (\{S_h^{i,T}\}, \omega_{C,s}, \omega_{F,s})$

Determine communication groups $[\Sigma_k]_{k=1,\ldots,\mathrm{nc}_s}$, $\omega_{C,s} \leftarrow \emptyset$, $\omega_{F,s} \leftarrow \emptyset$.

for all $k = 1, \ldots, \mathrm{nc}_s$ **do**

  /* Step two */

  Determine ω_a, ω_v and ω_g

  if $s ==\mathrm{ROOT}(\Sigma_k)$ **then**

    $(\omega_{C,s}, \omega_{F,s}) \leftarrow$ **COARSEP**$(\{S_h^{i,T}\}, \omega_a, \omega_a, \omega_v, \omega_{C,s}, \omega_{F,s})$

    $\omega_m \leftarrow \omega_{C,s} \cap \omega_a$

  end if

  $\omega_m \Leftarrow \mathrm{BROADCAST}(\Sigma_k, \omega_m)$

  if $s \neq \mathrm{ROOT}(\Sigma_k)$ **then**

    $(\omega_{C,s}, \omega_{F,s}) \leftarrow$ **COARSEP** $(\{S_h^{i,T}\}, \omega_m, \omega_a, \omega_v, \omega_{C,s}, \omega_{F,s})$

  end if

  /* Step three */

  for all $i \in \omega_a$ **do**

    if $i \in \omega_{F,s}$ **then**

      $S_h^{i,T} \leftarrow S_h^{i,T} \cap (\omega_a \cup \omega_g)$

    else

      $S_h^{i,T} \leftarrow S_h^{i,T} \cap (\omega_a \cup \omega_v)$

    end if

  end for

end for

---

routine is contained in the parallel one via the call

$$(\omega_C, \omega_F) \leftarrow \textbf{COARSEP}(\{S_h^{i,T}\}, \omega_h, \omega_h, \omega_h, \omega_C, \omega_F),$$

with $\omega_C = \omega_F = \emptyset$ as initial parameters.

3. Step three (see Algorithm 12) restricts the strong connections with regard to the prolongation such that no fine node from the active set has connections to the visible nodes. Fine interface nodes are thus only allowed to be interpolated from neighboring coarse nodes from the same interface and not from inner nodes.

Parallel smoothing

Finally, the parallel smoother in Algorithm 11 requires communication and has to be adapted appropriately. A Gauss-Seidel smoother for the inner nodes and an ω-Jacobi smoother for the interface nodes was used. The ω-Jacobi-smoother involves a vector conversion from distributed to accumulated type, i.e., one next

---

Algorithm 13 : COARSEP:$(\{S_h^{i,T}\}, \omega_m, \omega_a, \omega_v, \omega_C, \omega_F) \rightarrow (\omega_C, \omega_F)$

> **while** $\omega_C \cup \omega_F \not\supseteq \omega_a$ **do**
>> $i \leftarrow \text{PICK}(\{S_h^{k,T}\}, \omega_m \setminus (\omega_C \cup \omega_F), \omega_F)$
>> **if** $|S_h^{i,T}| + |S_h^{i,T} \cap \omega_F| = 0$ **then**
>>> $\omega_F \leftarrow \omega_F \cup (\omega_a \setminus \omega_C)$
>> **else**
>>> $\omega_C \leftarrow \omega_C \cup \{i\}$
>>> $\omega_F \leftarrow \omega_F \cup \left((S_h^{i,T} \setminus \omega_C) \cap (\omega_a \cup \omega_v)\right)$
>> **end if**
> **end while**

---

neighbor communication across interfaces is required per smoothing step. The exact algorithm for the parallel smoother can be found in Haase [87, Alg.6.10].

5.5 Numerical studies on multiple processors

Parallel solver performance studies were carried out for the Models 1 and 2 of Table 4.1 with isotropic and 1:10 anisotropic layers skull and WM.

5.5.1 Data partitioning

The FE meshes were partitioned into 2, 4, 6, 8, 10 and 12 subdomains for parallel computations. For the balanced k-way partitioning (Section 5.4.1), no weighting of the graphs edges (the finite elements), e.g., with regard to jumping conductivities between elements at tissue-boundaries, was carried out. The partitioning process thus only exploited the pure mesh geometry, not the conductivity labels. The software package METIS [117] was used for data partitioning. The results were achieved in a few seconds on a single processor. A first examination of the partitioning results was carried out by means of zooming, rotating, translating, scaling, and applying explosion factors, using the visualization tool PMVIS [176]. Figure 5.5 shows the partitioned geometries of the tetrahedra and the nodeshifted hexahedra models. Later, the number of interface and inner nodes and the number of elements were controlled during the parallel computations (see Figure 5.8). In all cases, the quality of the partitioning results was very satisfactory.

5.5.2 Comparison of parallel preconditioners

On multiple processors, the parallel AMG-CG was compared with the parallel Jacobi-CG. Most parameter settings were already discussed in Section 5.3. For
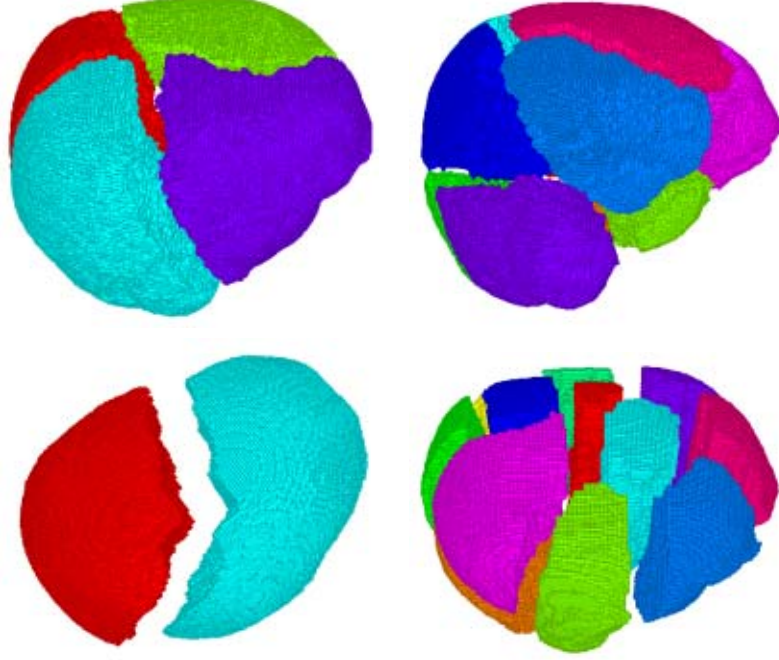
Figure 5.5: *Realistic FE head models partitioned with METIS and visualized with PMVIS: Top row: Model 1 from Table 4.1, partitioned for 4 processors (left) and for 12 processors (right). Bottom row: Model 2 from Table 4.1, partitioned for 2 processors (left) and for 12 processors (right).*

the tetrahedra models, the factorization in Algorithm 11 was carried out, if the size of the coarsest grid (COARSEGRID) in the preconditioner-setup was below 800. The influence of the coarse grid size towards the solver times was observed to be small, when, e.g., increasing from 800 to 1000, the value, chosen for the cube models. Pattern condition (5.11) was respected during the coarsening and the construction of the prolongation operator, using the three-step algorithm presented in Section 5.4.3. The parallel solver process was stopped after the ith iteration if the relative error in the controllable $\mathsf{K}_h \mathsf{C}_h^{-1} \mathsf{K}_h$-energy norm was below $\varepsilon = 10^{-8}$, i.e.,

$$\frac{\langle \underline{\mathsf{w}}^i, \underline{\mathsf{r}}^i \rangle}{\langle \underline{\mathsf{w}}^0, \underline{\mathsf{r}}^0 \rangle} \leq \varepsilon^2.$$

The process of determining the index set (5.10) for each node and scattering the data to the processors, both of which are carried out by the root processor, and the local arrangement of nodes to groups according to their index-set and
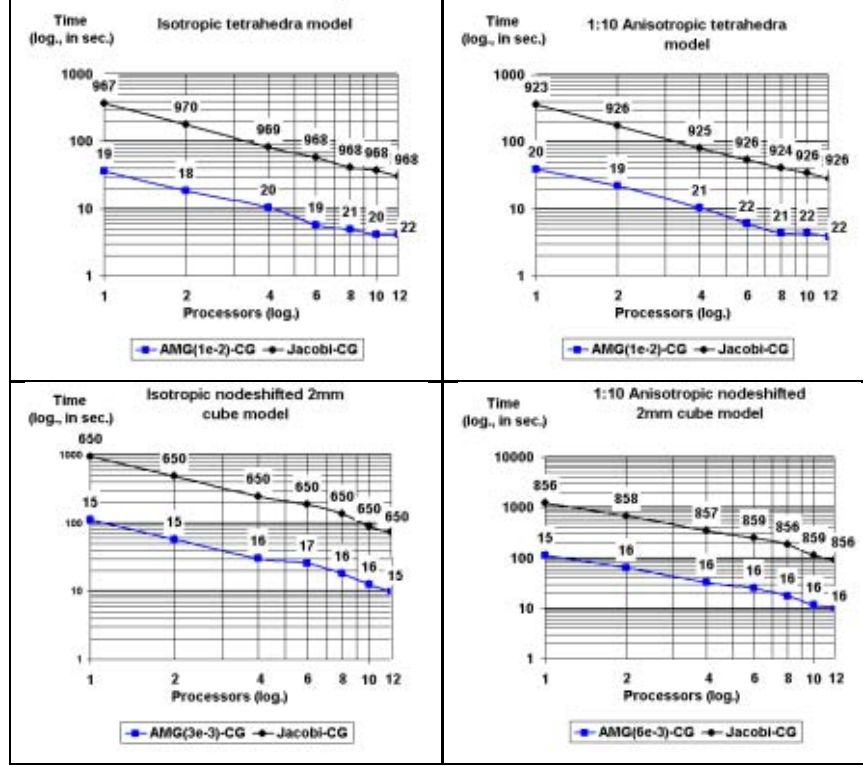
Figure 5.6: *SGI ORIGIN: Wall clock times from 1 to 12 processors for the solver part of the parallel AMG(ζ)-CG (for ζ see (5.6)) compared to the parallel Jacobi-CG up to an accuracy of 10^{-8} for the isotropic (left) and the anisotropic (right) Model 1 (top row) and Model 2 (bottom row) from Table 4.1. The numbers of iterations are shown over the curves.*

the allocation of corresponding communicator groups takes about half a minute. The accumulation of the geometry matrix K_s on 1 processor took about 225 s, parallelized on 12 processors a local matrix generation time of 19 s and thus a speed-up of about 12 was achieved (the times were nearly identical for all four models). The setup of the AMG on 1 processor took about 39 s for the tetrahedra and 135 s for the cube models, parallelized on 12 processors about 8 s and 30 s, resp.. The above computation times can be neglected with regard to the inverse problem since these processes have to be performed only once per head geometry.

Figure 5.6 shows the wall clock time of the parallel AMG(ζ)-CG solver (for ζ see (5.6)) compared to the parallel Jacobi-CG. The number of iterations for both solver methods, necessary for the required accuracy, is shown over the curves. If
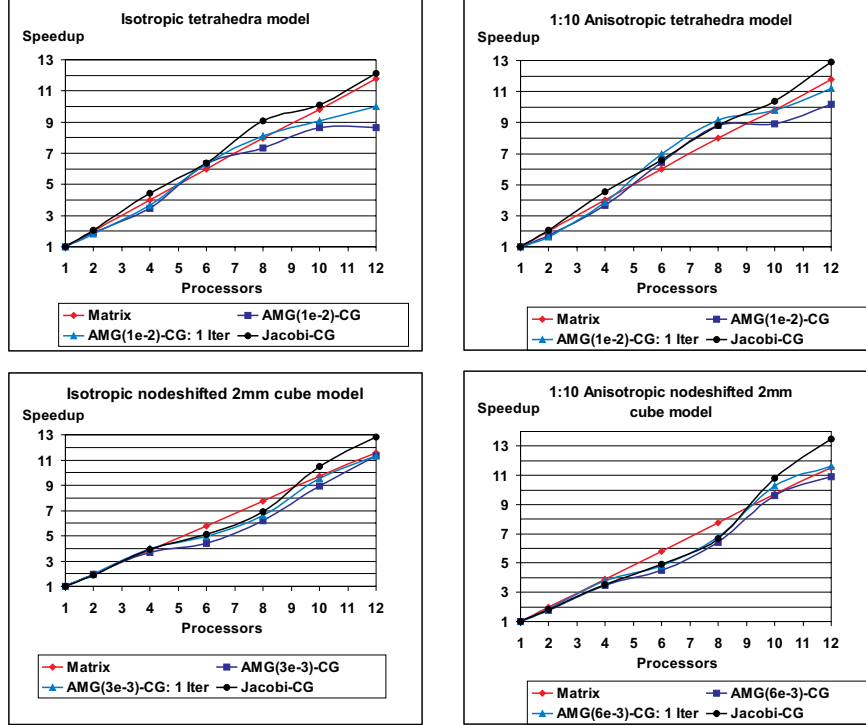
Figure 5.7: *SGI ORIGIN: Speed-up results from 1 to 12 processors for the isotropic (left) and the anisotropic (right) Model 1 (top row) and Model 2 (bottom row) from Table 4.1.*

the Jacobi-CG on one processor, which can be seen as the standard solver method in FE-based EEG/MEG source reconstruction, is taken as the reference, using 361 s for the 1:10 anisotropic Model 1, then the parallel AMG-CG method on 12 processors, using 3.8 s, was a factor of about 95 faster (9.3 through MG preconditioning and 10.2 through parallelization on 12 processors). For the anisotropic nodeshifted cube model, the Jacobi-CG on one processor needed 1231 s, while the parallel AMG-CG on 12 processors only 10.3 s. This is a factor of even 119 (10.9 through MG preconditioning and 10.9 through parallelization on 12 processors).

The speed-up results from 1 to 12 processors are shown in Figure 5.7. The matrix generation is purely local and gives the reference curve for the quasi optimal speed-up. This curve can also be seen as an indicator for the quality of the mesh partitioning, described in Section 5.5.1. The speed-ups for the parallel AMG-CG solver, for one iteration of this solver and for the parallel Jacobi-CG

Figure 5.8: *Relation interface nodes to all nodes (interface plus inner nodes) on the five levels of the AMG, exemplarily for the decompositions for 2, 6 and 12 processors for the anisotropic Model 1 (left) and the anisotropic Model 2 (right) from Table 4.1.*
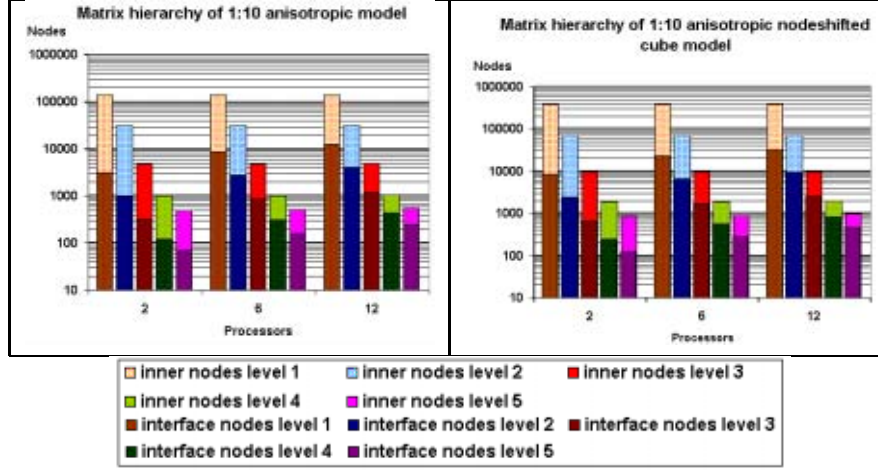
solver are compared for all four head models. Nearly linear speed-ups for AMG-CG can be observed in the figure.

The quality of the smoother, the coarse grids and the prolongation matrices depend on the mesh partitioning and a strongly increasing number of interface-nodes would spoil the preconditioning effect. Therefore, it is interesting to have a look at the relation of interface nodes to all nodes (interface plus inner nodes) on the different levels of the AMG. Figure 5.8 shows these relations exemplarily for 2, 6 and 12 processors for the anisotropic models. For the anisotropic tetrahedra model, the decomposition into two domains led to 3084 and thus 2% interface nodes on the finest level. On the 4th level (there is no more smoothing and restriction on the coarsest level), 120 out of 1022 nodes were interface nodes and thus a percentage of 12%. On 12 processors, 12462 and thus 8% were interface nodes on the finest level and on the fourth level, 443 out of 1066, i.e., 42%. For the anisotropic nodeshifted cube model and for both corresponding isotropic models (not shown), about the same percentages of interface nodes to all nodes were observed.

The parallel AMG-preconditioner takes conductivity inhomogeneity and anisotropy into account, while the parallel Jacobi-CG mainly ignores anisotropy. This could be one reason for the fact that, in the anisotropic case, the AMG is still a stable preconditioner and the large difference in the preconditioning effect

between AMG and Jacobi remains. Nevertheless, in Section 5.3, it was found that a factor 1.3 more iterations were needed for the anisotropic cube model than for the corresponding isotropic volume conductor. With 967 to 923 iterations (Jacobi-CG, one processor), the inverse can now be observed for the tetrahedra model. Fewer iterations are needed for the anisotropic model. It can thus be concluded from the small difference in the condition numbers between isotropic and anisotropic models in Table 5.1 and from the observed solver results that the iteration count differences are only of an order $O(1)$. It thus seems that realistic conductivity anisotropy with a ratio of up to 1:10 does not spoil the convergence behavior of both solvers. Nevertheless, it may be, that this is only the case for the AMG preconditioner since it deals with the inhomogeneity and anisotropy during coarsening and set up of the interpolation operators.

5.6   Summary and Conclusions

High resolution FE head modeling allows the inclusion of head tissue conductivity inhomogeneities and anisotropies. The bottleneck for a broader application of FE modeling in EEG/MEG source reconstruction is the time for solving the large linear equation system with hundreds or even thousands of different right hand sides arising from the FE discretization. Within this chapter, an efficient and memory-economical way was presented to face this problem. Very short calculation times were achieved through the combination of AMG preconditioning techniques and the parallelization on distributed memory platforms.

On one processor, AMG-, IC- and Jacobi-preconditioners were compared. For the class of IC-preconditioners, a variant without fill-in, the IC0, and a threshold-based ILDLT method were tested, where the latter allows fill-in during preconditioner construction. From relative residuals of 10^{-4} up to 10^{-8}, the AMG-preconditioned CG method was the fastest for all tested models. For the 2mm nodeshifted cube model and for a relative residual of 10^{-8}, it was a factor 2.5 times faster than the class of IC-preconditioned CG methods for both the isotropic and the 1:10 anisotropic model. It was faster by a factor of 8.5 in the isotropic and a factor of 11 in the anisotropic model than the Jacobi-preconditioned-CG method. Because of the loss of digits for the potential from the source to the electrodes, the interesting residuals begin at about 10^{-6}. As will be seen in Chapter 7.3.2, the accurate reconstruction of multiple dipolar sources can even necessitate relative residuals of about 10^{-10}.

On multiple processors, the parallel AMG-CG was compared with the parallel Jacobi-CG. If the Jacobi-CG on a single processor is taken as a reference, a speed-up of 95 was achieved for a realistically shaped high resolution 1:10 anisotropic tetrahedra head model with 118299 nodes when comparing to the

parallel AMG-CG on 12 processors, 9.3 through multigrid preconditioning and 10.2 through parallelization on 12 processors. The factor for the realistically shaped high resolution 1:10 anisotropic cube model with 325384 nodes was even 119, 10.9 through multigrid preconditioning and 10.9 through parallelization on 12 processors. On 12 processors, the parallel AMG-CG was a factor 7.4 faster than the parallel Jacobi-CG for the tetrahedra model and a factor 8.9 for the cube model. The required relative solution accuracy was 10^{-8}. For a solution accuracy of 10^{-6} with respect to the limitations within the inverse problem (e.g. data noise), factors in the same range were found.

The solver process was shown to be stable with respect to realistic tissue anisotropy. The partitioning of the dual graph of a convex head geometry generally leads to a relatively large percentage of interface nodes. Nevertheless, for the examined moderate processor numbers between 1 and 12, the AMG-preconditioner was found to be stable, i.e., a sensible increase of the number of subdomains did not result in a deterioration of the AMG-preconditioner and thus an increasing need for iterations. It was shown that the latter is true both for the isotropic and for the anisotropic models. Nevertheless, in our application, the parallel AMG-CG solver process for single right-hand-sides does not show superlinear speed-ups as reported by Haase et al. [88] for a Poisson equation on the geometry of a simplified crank shaft. This is because the partitioning of the long and thin crank shaft only leads to very few interface nodes, the communication need is thus lower and superlinear speed-ups result from a more efficient use of the cache memories since the local problem size decreases with increasing number of subdomains. However, for our application superlinear speed-ups will finally be achieved through a simultaneous treatment of a moderate number of right-hand-sides within a single parallel AMG-CG solver process [8].

The chosen modern numerical approach in combination with high performance computing on a parallel machine was shown to yield computation times, which should push high resolution realistically shaped anisotropic forward modeling within the EEG/MEG inverse problem into the application fields. A first performance test of the NeuroFEM software on a Linux PC-cluster with a simple ethernet showed acceptable parallelization speed-ups and, because of the 1 GB processors, a strongly reduced computation time compared to the presented results on the SGI ORIGIN 2000 [61]. The presented algorithms can thus be used on a simple (modern) PC-cluster.

The new results of this chapter have been published in Wolters et al. [261; 255; 258; 263; 262] and Fingberg et al. [61]. A further manuscript is in an advanced state [8].

Chapter 6

The inverse problem

6.1 Introduction

Source localization of cerebral activity with respect to the individual anatomy is a prominent goal of EEG and MEG. The non-uniqueness of the inverse problem implies that assumptions on the source model, as well as anatomical and physiological a-priori knowledge about the source region and sometimes even results from other techniques like fMRI [158; 175] should be taken into account to obtain a unique solution. Different source models for continuous and discrete source parameter spaces have been proposed during the last years [230; 264; 95; 200; 161; 242; 30; 122; 191; 72; 259; 203; 204].

One possibility is the restriction to a limited number of dipoles, the *focal source model* [230; 200; 161; 259]. The various spatio-temporal focal source models differ in the manner in which they describe the time dependence of the data. Generally, they are grouped into three classes, the unconstrained dipole model (so-called *moving dipole*), dipoles with temporally fixed location (*rotating dipole*) and dipoles with fixed location and fixed orientation (*fixed dipole*). If only one single time "snapshot" is taken into account, the three classes merge in a spatial dipole model, the so-called *instantaneous state dipole model* [264].

Another proposition is the *distributed source model*, where the restriction to a limited number of focal sources is abolished. The non-uniqueness of the resulting problem is compensated by the assumption that the dipole distribution should be minimal with regard to a specific norm. Different norms have been proposed, such as the L2-norm [95], leading to a smooth current distribution with minimal source energy and the L1-norm [191; 242], which results in a more focal distribution [72]. Most distributed source models are instantaneous models, but newest developments show, that spatio-temporal approaches can help stabilizing the inverse reconstruction process [202; 203; 204].

This chapter begins with the definition of the EEG/MEG lead-field matrix and the node-oriented EEG lead-field basis. Once, the lead-field is computed, the inverse methods are provided with fast forward solutions. The reconstruction algorithms are then divided into two classes, the first class contains inverse methods for the focal source model while the second deals with current density reconstructions for distributed source models.

6.2   The EEG/MEG lead-field matrix for discrete parameter space

A *physiological* a-priori information about the source region (*influence space*) is the assumption that the generators must be located on the folded surface of the brain inside the cortex, ignoring white matter and deeper structures such as basal ganglia, brain stem and cerebellum. If convolutions of the cortical surface are appropriately modeled by the segmentation procedure, another addition is the *anatomical* information that the generators are perpendicular to this surface [143; 170]. This limitation to normally oriented dipoles is called the *normal-constraint*. Because a mathematical dipole models an active source region with a certain extent and the resolution of the inverse current reconstruction by means of noisy EEG- or MEG-data is limited, most inverse methods are based on a discretized influence space, represented for example by the vertices of a cortical triangulation when using the physiological constraint. Other approaches use regular 3D discretizations of the whole brain volume. The so-called *influence nodes* are the n_{inf} vertices of the discretized influence space.

Let us introduce the denotation $\underline{x}_i$ for the ith column of an arbitrary matrix X. Since the differential equation is linear, it is possible to set up a so-called *influence* or *lead-field matrix* $\mathrm{L} \in \mathbb{R}^{m \times r}$. A column of L is established by calculating a forward solution at the m EEG/MEG measurement sensors for a dipole on one of the n_{inf} influence nodes with unit strength in one Cartesian direction. If the physiological a-priori information and the normal-constraint are applied, there is only one possible dipole direction for each influence node and thus every dipole location $i \in \{1, \ldots, n_{\text{inf}}\}$ is represented by only one column in the lead-field matrix (the column $\underline{l}_i$), i.e., $r = n_{\text{inf}}$. For the unconstrained case, three columns in L represent the three orthogonal unit dipoles at a specific location, i.e., $r = 3n_{\text{inf}}$. Let us assume for the latter case, that the columns of L are ordered blockwise according to the Cartesian coordinate, i.e., the columns $\underline{l}_i$, $\underline{l}_{i+n_{\text{inf}}}$ and $\underline{l}_{i+2n_{\text{inf}}}$ represent the forward results for a unit dipole at influence node i in x, y and z direction, resp.. For an arbitrary dipole source configuration at T timepoints with dipole strength matrix $\mathrm{J} \in \mathbb{R}^{r \times T}$, the resulting simulated EEG/MEG fields, $\mathrm{U}^c \in \mathbb{R}^{m \times T}$, can then

be inexpensively calculated by

$$U^c = LJ.$$

If once, the discretization of the influence space has been fixed, the block of the r right-hand sides for which generally a computation expensive EEG/MEG FE forward problem has to be solved, is known. The lead-field matrix L can then be computed using the parallel solver techniques presented in Chapter 5. The parallel solvers can be combined with techniques for multiple right hand sides to speed up the calculation using the fast cache memory [37; 90; 8]. The lead-field matrix L can then be used for the whole variety of inverse reconstruction methods which are based on the underlying influence space discretization. Note that the interpolation techniques proposed by Yvert et al. [268] also enable the use of the discrete lead-field matrix for inverse methods in continuous parameter space.

6.3 Node-oriented EEG lead-field basis

If all m measurement sensors are EEG electrodes, i.e., no MEG modeling is required, then the so-called *node-oriented EEG lead-field basis* proposed by Weinstein et al. [247] can be computed, which strongly reduces computational work.

Let us consider the equation system $K_h \underline{u}_h = \underline{j}_h$ of Section 4.7.4 with the stiffness matrix $K_h \in \mathbb{R}^{N_h \times N_h}$ as defined in (4.39), the FE solution for the electric potential at all FE nodes, $\underline{u}_h \in \mathbb{R}^{N_h}$, and the right-hand side vector $\underline{j}_h \in \mathbb{R}^{N_h}$ as defined in (4.40) (or (4.42)). If the only interest is the computation of the potentials for an arbitrary source at the $m-1$ non-reference EEG sensors, $\underline{u}_h^{EEG} \in \mathbb{R}^{m-1}$, then we can make use of the relation

$$\underline{u}_h^{EEG} = R\underline{u}_h = RK_h^{-1}\underline{j}_h \tag{6.1}$$

for efficiently computing the node-oriented EEG lead-field basis $RK_h^{-1} \in \mathbb{R}^{(m-1) \times N_h}$. Each of the $m-1$ rows of matrix $R \in \mathbb{R}^{(m-1) \times N_h}$ has only one non-zero entry, the value 1.0 at the column corresponding to the FE node index for that electrode, denoted by i in the following. Therefore, only the ith row of K_h^{-1}, or, since K_h^{-1} is symmetric, its ith column, denoted by $\underline{k^{-1}}_i \in \mathbb{R}^{N_h}$, is needed, which can be computed by means of

$$K_h \underline{k^{-1}}_i = \underline{e}_i \qquad \forall i \in \{\text{GLOBEL}(1), \ldots, \text{GLOBEL}(m-1)\}$$

with the function GLOBEL determining the global FE index i to each of the local electrode indices, and with $\underline{e}_i \in \mathbb{R}^{N_h}$ being the ith unit vector. The computation of the EEG lead-field basis RK_h^{-1} thus only needs $m-1$ instead of r fast parallel FE forward solutions. Certain source models yield vectors $\underline{j}_h$ with only few non-zero

entries at known indices, e.g., the blurred dipole (4.40). The forward computation (6.1) for such source models can thus even exploit the sparse structure of the right-hand side vector. Note that the EEG lead-field basis can be exploited by inverse methods in discrete and continuous parameter space.

6.4   Reconstruction of focal sources

Mosher et al. [161] showed how a common linear algebraic framework can be formulated for the three spatio-temporal focal source models, described in the introduction to this chapter. One can conclude from this formulation that measured fields depend nonlinearly on dipole location (and, for the fixed dipole, the fixed orientation) and linearly on dipole moment strength. Thus, after having chosen the number of sources, nonlinear algorithms should determine their locations (and possibly fixed orientations) and embedded linear methods their moment strength.

It is thus the goal to find an influence node location tuple q for a chosen number of p dipoles (in practice from $p = 1$ up to $p = 4$) and the corresponding $r \times T$ strength matrix J_q such that

$$H(q) = ||U^c - U^{me}||_F^2 = ||L_q J_q - U^{me}||_F^2 \overset{!}{=} \min \qquad (6.2)$$

where the $m \times r$ matrix L_q is the overdetermined lead-field matrix (thus $m > r$), corresponding to the location tuple q, the $m \times T$ matrix U^{me} are the noise-free measurements (EEG/MEG) and $|| \cdot ||_F$ is the Frobenius-norm. Using the normal-constraint, the number r of columns of L_q and rows of J_q equals the number p of dipoles, without this constraint it is $r = 3p$.

The minimization task can thus be split into two problems. The first problem is to find the dipole location tuple q which gives a good approximation of the global minimum of H in a feasible calculation time. Second, a physiologically and mathematically suitable model should be developed for the shape of the functional graph H. Every evaluation of H for a given location tuple q contains the construction of the corresponding lead-field matrix L_q and the subsequent determination of the dipole direction and strength matrix J_q with respect to the noise U^ε in the measured data $U_\varepsilon^{me} = U^{me} + U^\varepsilon$.

6.4.1   A downhill simplex optimizer in continuous parameter space

Nelder and Mead's simplex method [162], formulated as an uphill approach in Section 2.4.3 (Algorithm 1), was described as a nonlinear optimization approach for the maximization of the mutual information between two MR images within the registration process. The concept of the Continuous Downhill Simplex (CDS) method used here is quite comparable. The CDS is used for the determination of

the nonlinear parameters for simple focal source models in continuous parameter space, e.g., the continuous one dipole model (see the application in the next chapter). Main differences to Algorithm 1 are that the ordering is reversed and a downhill pivoting based on H instead of an uphill pivoting based on the mutual information is carried out. Furthermore, in order to speed up the optimization, the restriction to a Freudenthal triangulation was abolished. After each simplex reflection, which is still constructed to conserve the volume of the simplex and thus avoid degeneracy, the possibility of a moderate expansion in order to take larger steps was implemented.

The CDS method generally cannot exploit the lead-field approach, discussed in Section 6.2. For a computed source configuration q, the corresponding matrix L_q of Equation (6.2) has to be determined during the inverse optimization by means of FE forward computations. To alleviate the computation amount, the mentioned lead-field interpolation techniques for inverse methods in continuous parameter space may be used [268].

The CDS optimizer needs a-priori chosen seedpoints and, dependent on the seed dipoles, it can converge to local minima. This was shown for brain-stem auditory evoked potentials by Gerson et al. [78], where the CDS produced larger errors for even a simple one dipole model. Huang et al. [109] examined a multi-start CDS in order to imitate a global optimization technique for fitting multidipole, spatio-temporal MEG data.

6.4.2 A simulated annealing algorithm on discretized influence space

The second presented optimization approach for the nonlinear source parameters tries to globally minimize the cost function H in a discretized parameter space and does not need any seedpoints. Theoretically, it would be possible to test all

$$\left(\begin{array}{c} n_{\text{inf}} \\ \text{p} \end{array} \right) = \frac{n_{\text{inf}}!}{(n_{\text{inf}} - \text{p})! \ \text{p}!}$$

combinations of a choice of p source locations without repetition out of n_{inf} influence nodes for their functional value H. In practice, this is generally not senseful because the number of elements in the configuration space is too large and cannot be explored exhaustively. The method of Simulated Annealing (SA) utilizes concepts of combinatorial optimization for searching the minimum of H in acceptable time [187; 19; 30; 78; 99; 259]. It simulates the process of a slow cooling (annealing) of a melted solid. If the annealing process is carried out slowly enough, then the crystal lattice of the solid finds the most regular and stress-free state, i.e., the state of lowest energy. If the heated solid is frozen too fast, then it can be that only a local energy minimum is achieved and stress remains in

---

Algorithm 14 SA:$(H, p, \text{MAX} \in \mathbb{N}, t_{\text{step}}, \text{TOL} \in \mathbb{R}) \rightarrow q_{\text{opt}}$

DETERMINE t_{start} CHOOSE q_{utd}, $d_{\text{utd}} = d_{\text{opt}} = \text{BIGNUM}$, $t = t_{\text{start}}$, $n_{\text{sum}} = 0$

while $((d_{\text{utd}} > \text{TOL}) \wedge (n_{\text{sum}} < \text{MAX}))$ **do**

  $n_{\text{count}} = n_{\text{accept}} = 0$

  while $\big((n_{\text{accept}} < n_{\text{inf}}) \wedge (n_{\text{count}} < 10 * n_{\text{inf}})\big)$ **do**

    $q_{\text{tmp}} = RANDOM(q_{\text{utd}})$, $n_{\text{count}} = n_{\text{count}} + 1$

    $d_{\text{tmp}} = H(q_{\text{tmp}})$

    if $d_{\text{tmp}} < d_{\text{opt}}$ **then**

      $q_{\text{opt}} = q_{\text{tmp}}$, $d_{\text{opt}} = d_{\text{tmp}}$

    end if

    if $\text{dif} = (d_{\text{tmp}} - d_{\text{utd}}) > 0$ **then**

      $a = RANDOM([0, 1])$ /* Metropolis */

      if $e^{-\text{dif}/t} > a$ **then**

        $q_{\text{utd}} = q_{\text{tmp}}$, $d_{\text{utd}} = d_{\text{tmp}}$, $n_{\text{accept}} = n_{\text{accept}} + 1$

      end if

    else

      $q_{\text{utd}} = q_{\text{tmp}}$, $d_{\text{utd}} = d_{\text{tmp}}$, $n_{\text{accept}} = n_{\text{accept}} + 1$

    end if

  end while

  $t = t - t_{\text{step}}$, $n_{\text{sum}} = n_{\text{sum}} + n_{\text{count}}$

end while

---

the crystal lattice. Analogous to the described annealing, the final state of the SA is determined by control parameters in the minimization algorithm. If the cooling is slow enough, the global minimum of the considered process will be found [112]. At high temperatures, the atomic mobility of the solid and therefore the probability of a displacement is increased. The mobility is lost proportionally to the cooling. In the minimization algorithm, this process is simulated with the Metropolis-criterion [159].

The transfer of the SA algorithm into the application field of the focal inverse source reconstruction is shown in Algorithm 14, following Beckmann [19]. Within the inner loop, one source location of the up-to-date combination q_{utd} is randomly changed by the function *RANDOM* and saved in q_{tmp}, the temporary source combination. The functional H is then evaluated for the temporary sources. If the residual d_{tmp} is smaller than the current optimum, d_{opt}, then the sources are saved as the new optimal combination together with its discrepancy to the data. The temporary combination becomes the up-to-date one, if its defect to the data is smaller than d_{utd}. Especially for the case of high system temperature, also a deterioration with regard to the defect is accepted. The coupling of the acceptance of a less favored source configuration to the temperature of the

system is controlled by the Metropolis criterion. If the criterion is fulfilled, the less-favored source configuration becomes the up-to-date one. The starting high temperature results in a high probability of accepting a less favored configuration in order not to get stuck in a local extremum. The temperature is decreased by means of t_{step}, if either the number of accepted configurations, n_{accept}, reaches the number of influence nodes, or the number of all tested source tuples, n_{count}, gets larger than many times the number of n_{inf}. At the beginning of the algorithm, the starting temperature has to be determined. Therefore, an initial value for t_{start} is chosen and this value is increased during initial SA iterations as long as the condition $n_{\text{accept}}/n_{\text{count}} < 0.99$ is true. The algorithm thus adapts itself to the size of the influence space and, concerning the starting temperature, to the different scaling of EEG and MEG data. SA is terminated, if either the defect is falling under a given tolerance or a maximum of source configurations has been tested.

6.4.3 Determination of the linear parameters

Assuming that a dipole location tuple q has been proposed, the problem (6.2) with noisy data $\mathrm{U}_{\varepsilon}^{me}$ should then be solved in order to compute the dipole strengths. Linear least square methods have to yield the "best" (will be defined) fit between measured and simulated fields. Refer to Zeidler [270, Chapter 37] or Lawson and Hansen [136] for a survey. If dipole components are proposed which "numerically" (nearly) project into the data null space, the corresponding lead-field matrix becomes ill-conditioned. In combination with noisy data, simple least square algorithms such as the generalized inverse can yield physiologically unexplainable results for dipole moment strengths, especially when overestimating the number of active sources. This problem can be alleviated with dipole fit regularization methods as shown in the following.

Singular Value Decomposition and Generalized Inverse

The first three presented methods to solve the linear least square problem (6.2) do not take the noise in the measured data into account. They are based on different decompositions of the overdetermined $m \times r$ ($m > r$) lead-field matrix L_{q}. The first two methods, the *QR decomposition* and the *Complete Orthogonal Factorization* (COF), are discussed in Appendix C. The third strategy is based on the *Singular Value Decomposition* (SVD) of the lead-field matrix

$$\mathrm{L}_q = \mathrm{VSW}^{tr} = (\underline{v}_1, \ldots, \underline{v}_m) \begin{pmatrix} \Sigma \\ 0_{m-r} \end{pmatrix} (\underline{w}_1, \ldots, \underline{w}_r)^{tr}$$

with the orthogonal $m \times m$ matrix V, the $m \times r$ matrix S with $\Sigma = \mathrm{DIAG}(\varsigma_1, \ldots \varsigma_r)$ and the orthogonal $r \times r$ matrix W [250]. $\varsigma_i^2 \in \mathbb{R}$ are the eigenvalues and $\underline{v}_i \in \mathbb{R}^m$

the eigenvectors of $L_q L_q^{tr}$ and ς_i^2 the eigenvalues and $\underline{w}_i \in \mathbb{R}^r$ the eigenvectors of $L_q^{tr} L_q$. Furthermore, it is

$$L_q \underline{w}_i = \varsigma_i \underline{v}_i \qquad i = 1, \ldots, r, \tag{6.3}$$

and

$$\begin{aligned} \underline{v}_i^{tr} L_q &= \varsigma_i \underline{w}_i^{tr}, & i &= 1, \ldots, r, \\ \underline{v}_i^{tr} L_q &= (\underline{0}^r)^{tr}, & i &= r+1, \ldots, m. \end{aligned}$$

Thus, the space spanned by $\{\underline{v}_1, \ldots, \underline{v}_r\}$ is called the *column space* and $\mathrm{span}\{\underline{v}_{r+1}, \ldots, \underline{v}_m\}$ is the so-called *left null space* of L_q. The *singular values* ς_i are automatically arranged by the SVD such that $\varsigma_1 \geq \varsigma_2 \geq \ldots \geq \varsigma_r > 0$, if full rank of L_q has been assumed. In practice, the *right singular vectors* $\underline{w}_i$ and the *left singular vectors* $\underline{v}_i$ are both arranged with increasing spatial frequency. In vector notation, the SVD can be written in the form

$$L_q \underline{j}_q = \sum_{i=1}^r \varsigma_i (\underline{j}_q, \underline{w}_i) \underline{v}_i.$$

Without respect to the noise in the data and using the above SVD, the least square problem (6.2) can be solved by means of the *generalized inverse* of the lead-field matrix, in matrix form

$$\begin{aligned} L_q^+ U_\varepsilon^{me} &= \left(L_q^{tr} L_q\right)^{-1} L_q^{tr} U_\varepsilon^{me} = WS^+ V^{tr} U_\varepsilon^{me} \\ &= (\underline{w}_1, \ldots, \underline{w}_r) \left(\begin{array}{cc} \Sigma^{-1} & 0 \end{array} \right) (\underline{v}_1, \ldots, \underline{v}_m)^{tr} U_\varepsilon^{me}, \end{aligned}$$

or, in vector notation,

$$L_q^+ \underline{u}_\varepsilon^{me} = \sum_{i=1}^r \frac{1}{\varsigma_i} (\underline{u}^{me} + \underline{u}^\varepsilon, \underline{v}_i) \underline{w}_i. \tag{6.4}$$

As with the QR and the COF decomposition (see Appendix C), the only goal of the generalized inverse is to minimize the residual variance to the noisy data. Non-regularized dipole fit methods use this algorithm to solve the linear least square problems embedded in the nonlinear optimization process.

Note the following as an additional remark. With $V_r := (\underline{v}_1, \ldots, \underline{v}_r) \in \mathbb{R}^{m \times r}$, the matrix $P_L := L_q L_q^+ \in \mathbb{R}^{m \times m}$ projects data $\underline{u} \in \mathbb{R}^m$ onto the column space of L_q,

$$P_L \underline{u} = L_q L_q^+ \underline{u} \overset{(6.4)}{=} L_q \sum_{i=1}^r \frac{1}{\varsigma_i} (\underline{u}, \underline{v}_i) \underline{w}_i \overset{(6.3)}{=} \sum_{i=1}^r (\underline{u}, \underline{v}_i) \underline{v}_i = V_r V_r^{tr} \underline{u}.$$

Mosher et al. [161] presented an efficient form of calculating $H(q)$, which is based on an SVD of the data matrix $U_\varepsilon^{me} = V_u S_u W_u^{tr}$ (orthogonal $V_u \in \mathbb{R}^{m \times m}$, $S_u \in \mathbb{R}^{m \times T}$ and orthogonal $W_u \in \mathbb{R}^{T \times T}$):

$$
\begin{aligned}
H(q) &= ||U_\varepsilon^{me} - L_q(L_q^+ U_\varepsilon^{me})||_F^2 = ||U_\varepsilon^{me}||_F^2 - ||P_L U_\varepsilon^{me}||_F^2 \\
&= ||V_u S_u W_u^{tr}||_F^2 - ||V_r V_r^{tr} V_u S_u W_u^{tr}||_F^2 = ||S_u||_F^2 - ||V_r^{tr} V_u S_u||_F^2
\end{aligned}
$$

Orthogonal matrices were dropped in the derivation since they preserve the Frobenius-norm. When using SVD-versions of the lead-field matrix, in which only the left singular vectors V_r are iteratively calculated and when r is small relative to m, this procedure of calculating $H(q)$ will outperform methods based on noniterative QR-decompositions.

Truncated singular value decomposition

In practice, L_q often suffers from large condition numbers $\text{cond}_2(L_q) = \frac{\varsigma_1}{\varsigma_r}$ during the SA-optimization process. Thus, the singular values, ς_i, get very small and the high spatial frequency components of the noise in the data in Equation (6.4) can be extremely amplified. This has an effect on those spatial dipole components, which "numerically" (nearly) lie in the kernel of L_q. It can lead to source configurations, where dipoles with a large strength nearly cancel each other with regard to their surface field distribution and only explain noise (for both EEG and MEG inverse problem), the so-called *ghost sources*. When considering the MEG inverse problem, radial dipoles are such ghosts and they can get a big strength only to explain MEG noise. Both problems especially appear if the number of active sources is overestimated. The problem can be alleviated with a regularization T_λ of the generalized inverse

$$
\underline{j}_q^\lambda = T_\lambda \underline{u}_\varepsilon^{me} := \sum_{i=1}^r \frac{1}{\varsigma_i} F_\lambda(\varsigma_i)(\underline{u}_\varepsilon^{me}, \underline{v}_i) \underline{w}_i,
$$

where F_λ is called a *filter*, as described by Louis [145].

The choice of

$$
F_\lambda(\varsigma) = \frac{\varsigma^2}{\varsigma^2 + \lambda^2}
$$

leads to the so-called *Tikhonov-Phillips regularization*, where the high spatial frequency components in the source space, strongly influenced by the noise in the data space, are attenuated. As discussed with more detail in Section 6.5.1, Tikhonov-Phillips regularization amounts to minimizing the functional

$$
||L_q \underline{j}_q - \underline{u}_\varepsilon^{me}||_2^2 + \lambda^2 ||\underline{j}_q||_2^2,
$$

or, in equivalent denotation,

$$||\bar{\mathrm{L}}_q \underline{j}_q - \underline{\bar{u}}_\varepsilon^{me}||_2^2$$

with

$$\bar{\mathrm{L}}_q = \left(\begin{array}{c} \mathrm{L}_q \\ \lambda \mathrm{Id}^r \end{array} \right) \qquad \text{and} \qquad \underline{\bar{u}}_\varepsilon^{me} = \left(\begin{array}{c} \underline{u}_\varepsilon^{me} \\ \underline{0}^r \end{array} \right).$$

As shown by Hämmerlin and Hoffmann [98], the condition number of the Tikhonov regularized least square problem is then ameliorated to

$$\mathrm{cond}_2(\bar{\mathrm{L}}_q) = \sqrt{\frac{\varsigma_1^2 + \lambda^2}{\varsigma_r^2 + \lambda^2}},$$

This regularization concept for nonlinear dipole fit methods has recently been applied to source localization by Fuchs et al. [73].

Another way is to choose the filter

$$F_\lambda(\varsigma) = \left\{ \begin{array}{l} 1, \text{ if } \varsigma \geq \lambda \\ 0, \text{ if } \varsigma < \lambda \end{array} \right.,$$

leading to a regularization called the Truncated Singular Value Decomposition (TSVD), which was proposed for source localization by Wolters et al. [256]. This algorithm is simple to implement and has the effect of a lowpass filter. The high spatial frequency components of the data, $\varsigma_i(\cdot, \underline{w}_i)\underline{v}_i$, are lying below the noise level and as a consequence, the high spatial frequency components in the source space cannot be reconstructed. Using regularization, information will be lost but otherwise the amplification of the high frequency data components would have a more negative effect on the solution, especially in combination with an overestimation of the number of active sources. Like Tikhonov-Phillips regularization, the TSVD ameliorates the condition of the problem.

The SA-TSVD algorithm, published in Wolters et al. [260; 259] and described in the following, is an iterative procedure. In every step of the SA optimization, L_q is changing and thus the condition of the least square problem. Therefore, an automatic determination of the regularization parameter λ is essential. One possibility is provided by the so-called *discrepancy principle* (see, e.g., the overview article of Hanke and Hansen [100]) where the defect *d* to the

measured data

$$
\begin{aligned}
d := ||(I - L_q T_\lambda)\underline{u}_\varepsilon^{me}||_2^2 \quad &= \quad ||\underline{u}_\varepsilon^{me} - \sum_{i=1}^{r} F_\lambda(\varsigma_i)(\underline{u}_\varepsilon^{me}, v_i)v_i||_2^2 \\
&= \quad ||\underline{u}_\varepsilon^{me}||_2^2 - \sum_{i=1}^{r} F_\lambda(\varsigma_i)|(\underline{u}_\varepsilon^{me}, v_i)|^2 \\
&\overset{\text{TSVD}}{=} \quad ||\underline{u}_\varepsilon^{me}||_2^2 - \sum_{\varsigma_i > \lambda} |(\underline{u}_\varepsilon^{me}, v_i)|^2
\end{aligned}
$$

is not only minimized, but chosen in dependence of the condition number of L_q and of the noise $\underline{u}^\varepsilon$ in the data.

Let C be the $m \times m$ sample noise covariance matrix, determined e.g. from the signal-free pre-stimulus interval of the measurements, averaged over all epochs. This matrix reflects the spatial distribution and correlation of the measurement noise. C is a symmetric and positive definite matrix, which can be decomposed into $C = DD^{tr}$ by means of a singular value decomposition. If the noise statistics are known, i.e., if the number of epochs is sufficiently high in order to obtain a good estimate of the noise covariance matrix, the process of data *pre-whitening* can be used, as described by Knösche et al. [123]. Thus, we can restrict the theory to spatially uncorrelated noise where D is a diagonal weighting matrix.

If we consider only one time point and Gaussian distributed and heteroscedastic (different in each channel) noise with zero mean, every channel i should be weighted according to its own noise standard deviation $\varepsilon_i = |(\underline{u}^\varepsilon)^{[i]}|$ using the diagonal weighting matrix D^{-1} with entries $1/\varepsilon_i$. We thus get the weighted least square problem

$$
H^w(q) \quad = \quad ||L_q \underline{j}_q - \underline{u}_\varepsilon^{me}||_{C^{-1}}^2 = ||D^{-1}(L_q \underline{j}_q - \underline{u}_\varepsilon^{me})||_2^2 \overset{!}{=} \min,
$$

the weighted regularized inverse

$$
\underline{j}_\lambda^w = T_\lambda^w D^{-1} \underline{u}_\varepsilon^{me} := \sum_{i=1}^{r} \frac{1}{\varsigma_i^w} F_\lambda(\varsigma_i^w)(D^{-1}\underline{u}_\varepsilon^{me}, \underline{v}_i^w)\underline{w}_i^w,
$$

where $\{\varsigma_i^w, \underline{v}_i^w, \underline{w}_i^w\}$ is the singular system of the weighted lead-field matrix $D^{-1}L_q$ and the weighted defect

$$
d^w \quad = \quad ||\left(I - D^{-1}L_q T_\lambda^w\right) D^{-1}\underline{u}_\varepsilon^{me}||_2^2 \overset{\text{TSVD}}{=} ||D^{-1}\underline{u}_\varepsilon^{me}||_2^2 - \sum_{\varsigma_i^w > \lambda} |(D^{-1}\underline{u}_\varepsilon^{me}, \underline{v}_i^w)|^2.
$$

The instantaneous state ($T = 1$, α_i is a scalar) TSVD regularization procedure with so-called *a-posteriori* regularization parameter choice [145; 147], exploiting

---

Algorithm 15 TSVD:$(R) \rightarrow d$

$\underline{j}^w_\lambda = 0$, $i = 0$, $\bar{d} = \|\mathrm{D}^{-1}\underline{u}^{me}_\varepsilon\|^2_2$

Compute $\{\varsigma^w_i, \underline{v}^w_i, \underline{w}^w_i\} = \mathrm{SVD}(\mathrm{D}^{-1}\mathrm{L_q})$

while $(i \leq r) \wedge (\bar{d} > R^2)$ **do**

$\quad i = i + 1$

$\quad \alpha_i = (\underline{v}^w_i)^{tr}\mathrm{D}^{-1}\underline{u}^{me}_\varepsilon$

$\quad \underline{j}^w_\lambda = \underline{j}^w_\lambda + \frac{1}{\varsigma^w_i}\underline{w}^w_i\alpha_i$, $\bar{d} = \bar{d} - \alpha^{tr}_i\alpha_i$

end while

$d = \bar{d}$

---

the discrepancy principle, is presented in Algorithm 15. Within this algorithm, the regularization parameter is coded by the free parameter R. The TSVD can be shown to be an order optimal regularization procedure [226; 145]. The larger R is chosen, the stronger the regularization will be. Because of the small number r of source components, good experience has been made with a choice of $R = 1.0$.

The extension of the SA-TSVD to spatio-temporal modeling ($T > 1$) is straightforward for the moving and for the rotating dipole model. In these cases, $\underline{\alpha}_i$ is the $1 \times T$ vector

$$\underline{\alpha}_i = (\underline{v}^w_i)^{tr}\mathrm{D}^{-1}\mathrm{U}^{me}_\varepsilon,$$

$\frac{1}{\varsigma^w_i}\underline{w}^w_i\underline{\alpha}_i$ is an $r \times T$ matrix and the euclidian norm should be exchanged for the Frobenius-norm. The SA-TSVD can also simply be applied to the approximate approach of the fixed dipole model, described by Mosher et al. [161]. In this approach, the dipole strengths for each dipole location tuple q are initially calculated under the assumption of rotating orientations. After that, the orientations are fixed by SVD's of the $3 \times T$ submatrices J_i in $\mathrm{J}_q = (\mathrm{J}_1, \ldots, \mathrm{J}_p)^{tr}$, which describe the strengths in the three unit directions of every dipole. The fixed orientations are defined as the first left singular vectors of the submatrices J_i. The appeal for this approximate approach lies in the reduced computational effort. A computationally more intensive implementation for the fixed dipole model could be the embedding of a projected gradient method or a penalty method (see, e.g., Zeidler [270, Chapter 46] or Polak [186]) for the determination of the two nonlinear orientation parameters into the SA-optimization process for the dipole locations and the calculation of the linear dipole strength parameters by means of the TSVD.

6.4.4   Choosing the number of sources

An important parameter is the number p of focal sources, which is normally unknown in advance, but which is required as an input parameter for spatio-

temporal dipole modeling. One possibility for the determination of the number parameter was described by Mosher et al. [161]. They proposed to separate the signal and noise subspaces and thus to visually determine the number of source components through the drop in the magnitude of the smallest signal eigenvalue to the greatest noise eigenvalue of the estimated spatial data covariance matrix $\frac{1}{(T-1)} U_\varepsilon^{me} (U_\varepsilon^{me})^{tr}$. This procedure assumes that the signals have a sufficient strength and that they are sufficiently uncorrelated during the time interval. An algorithmic way for the determination of the number parameter is offered by information criteria, as described by Knösche et al. [123]. Under the assumption that the measurements are noise-free and the rank of the projection or lead-field operator is maximal (i.e. no source component projects in the data null space), the number of non-zero eigenvalues of the data covariance matrix equals the number of independent source components. Information criteria are based on a statistical concept of separating the space spanned by the principal components of the estimated data covariance matrix into a signal and a noise part.

In Wolters et al. [260; 259], a "trial and error" strategy was proposed to combine the determination of the unknown number parameter with the localization of the sources using the nonlinear dipole fit method SA in combination with the regularization approach TSVD. It will be shown in the next chapter, that the SA-TSVD is more stable with regard to an overestimation of the number of focal sources. Together with the SVD of the spatio-temporal data, giving an estimate for the minimal source number, the exact number of dipoles can better be enclosed.

6.5 Instantaneous current density reconstructions

Current density reconstruction methods are used for the distributed source model, where active dipolar sources are admitted at all n_{inf} influence nodes. The data functional for instantaneous state modeling ($m \times 1$ measurement vector $\underline{u}_\varepsilon^{me}$) is thus given by

$$\text{DATA}(\underline{j}) := ||D^{-1}(L\underline{j} - \underline{u}_\varepsilon^{me})||_2^2 = ||\bar{L}\underline{j} - \underline{\bar{u}}_\varepsilon^{me}||_2^2 \qquad (6.5)$$

with the $r \times 1$ source strength vector $\underline{j}$ and the $m \times r$ lead-field matrix L with $r = 3n_{\text{inf}}$ or, if the normal-constraint can be applied, $r = n_{\text{inf}}$ and the $m \times m$ diagonal weighting matrix D^{-1} as defined in Section 6.4.3. In order to simplify denotation, we set $\bar{L} = D^{-1}L$ and $\underline{\bar{u}}_\varepsilon^{me} = D^{-1}\underline{u}_\varepsilon^{me}$. Minimization of the data functional is an ill-posed problem. Unknowns outnumber by far the measurements and noise in the observations has the tendency to amplify high frequency components in the source reconstruction result. A cure of the problem is to add an additional

constraint for the sources by a Lagrangian multiplier:

$$F_\lambda^\nu(\underline{j}) := \text{DATA}(\underline{j}) + \lambda \cdot \text{MODEL}_\nu(\underline{j}) \stackrel{!}{=} \min \tag{6.6}$$

The index ν denotes the norm for the model term. In the following, this term will consist of two operators. The first one is a source space regularization operator, denoted by an $r \times r$ matrix B. The second, the $r \times r$ diagonal source depth weighting matrix $\text{W} = \text{DIAG}(w_i)$ will be discussed in Subsection 6.5.4.

In order to simplify denotations, let us introduce the Kronecker product.

Definition 6.5.1. *The Kronecker product* $\text{A} \otimes \text{B}$ *of two matrices* $\text{A} \in \mathbb{R}^{m \times n}$ *and* $\text{B} \in \mathbb{R}^{r \times s}$ *is defined by means of the block-matrix*

$$\text{A} \otimes \text{B} = \begin{bmatrix} a_{11}\text{B} & a_{12}\text{B} & \dots & a_{1n}\text{B} \\ a_{21}\text{B} & a_{22}\text{B} & \dots & a_{2n}\text{B} \\ \vdots & \vdots & & \vdots \\ a_{m1}\text{B} & a_{m2}\text{B} & \dots & a_{mn}\text{B} \end{bmatrix} \in \mathbb{R}^{(mr) \times (ns)}.$$

6.5.1   Linear Tikhonov-Phillips regularization using the L_2 norm

The model term for the linear Tikhonov-Phillips regularization is chosen as

$$\text{MODEL}_2(\underline{j}) := \|\text{BW}\underline{j}\|_2^2 \tag{6.7}$$

as it was first proposed for source localization by Hämäläinen et al. [95].

Theorem 6.5.2 (Tikhonov-Phillips). *Let* $\underline{j}_\lambda$ *be the solution of the regularized normal equations, i.e.,*

$$\underline{j}_\lambda = \text{A}^{-1}\underline{b} \tag{6.8}$$

with

$$\text{A} := \bar{\text{L}}^{tr}\bar{\text{L}} + \lambda \text{W}^{tr}\text{B}^{tr}\text{BW} \in \mathbb{R}^{r \times r} \ \ and \ \ \underline{b} := \bar{\text{L}}^{tr}\underline{\bar{u}}_\varepsilon^{me} \in \mathbb{R}^r,$$

then it is also solution of the minimization problem (6.6) in combination with the model term (6.7).

Proof: Louis [145, Theorem 4.2.1]. $\blacksquare$

The above solution is presented on a deterministic way. It can also be derived by means of probabilistic methods from estimation theory, where the sources are treated as random variables, being equipped with a probability distribution. In Vauhkonen [231], e.g., the maximum a posteriori estimate (MAP) is derived by a maximization of the posterior density with Gaussian assumptions. The solution is identical to Equation (6.8), if the operator $\text{W}^{tr}\text{B}^{tr}\text{BW}$ is interpreted as the inverse of a source covariance matrix.

Choice of the source space regularization operator

In the following, the source space regularization or smoothing operator is written in the form

$$B^{tr}B = Id^s \otimes G,$$

with $Id^s \in \mathbb{R}^{s \times s}$ the identity matrix of rang $s \in \{1,3\}$ ($s = 1$ in case of the normal-constraint, otherwise $s = 3$) and $G \in \mathbb{R}^{n_{inf} \times n_{inf}}$. If no normal-constraint is applied, then the formulation implies, that each of the three Cartesian dipole components is regularized separately with the smoothing operator G, defined in the following. The choice of

-
$$G = Id^{n_{inf}} \tag{6.9}$$

  is denoted by the so-called *discrete L_2 norm* approach.

-
$$G^{[ij]} = \int_\Omega \psi_i \psi_j d\Omega \qquad G^{[ij]} = \int_{\Gamma_S} \bar{\psi}_i \bar{\psi}_j d\Gamma_S \qquad \forall i,j = 1,\dots,n_{inf}$$

  for volume or cortical surface regularization, resp., is denoted by the so-called *continuous L_2 norm* approach. For the volume regularization, ψ_i are the basis function of the finite element subspace $\mathbb{V}_h$ from Subsection 4.7.2, while $\bar{\psi}_i$ are surface basis functions for the regularization on the cortical surface Γ_S, as described by Buchner et al. [30].

-
$$G^{[ij]} = \int_\Omega \operatorname{grad} \psi_i \operatorname{grad} \psi_j d\Omega \qquad G^{[ij]} = \int_{\Gamma_S} \operatorname{grad} \bar{\psi}_i \operatorname{grad} \bar{\psi}_j d\Gamma_S$$

  for volume or cortical surface regularization, resp., is denoted by the so-called *continuous (gradient) L_2 norm* approach.

Iterative solution for the L_2 norm approach

The equation system $A\underline{j}_\lambda = \underline{b}$ in (6.8) has an SPD system matrix A and can thus be solved with a Jacobi-CG method, presented in Subsection 5.2.1. In the implementation of the PCG method, the matrix-vector multiplication exploits the special form of A using a tailored stepwise application of the involved matrices so that A does not have to be compiled and stored explicitly. This reduces arithmetic costs and memory access [30]. In order that high frequency noise will not be amplified within the iterative solution process, one option in our implementation is the interpretation of the CG-method as a regularization approach, i.e., the iteration may be stopped in dependence of the noise level in the data (for a theoretical overview see [145, §4.3.3] or [69]).

6.5.2 L_2 norm regularization in the data space

Lawson and Hanson [136] present an elegant way for solving the regularized least squares problem (6.6) in combination with the L_2 model term (6.7):

Theorem 6.5.3 (Data space regularization). *Let $\underline{j}_\lambda$ be computed by means of*

$$\underline{j}_\lambda = \left(W^{tr}B^{tr}BW\right)^{-1}\bar{L}^{tr}\bar{A}^{-1}\underline{\bar{u}}_\varepsilon^{me} \tag{6.10}$$

with

$$\bar{A} := \bar{L}\left(W^{tr}B^{tr}BW\right)^{-1}\bar{L}^{tr} + \lambda\,\mathrm{Id}^m \in \mathbb{R}^{m\times m},$$

then it is also solution of the minimization problem (6.6) in combination with the model term (6.7).

Proof: If the operators of Equations (6.10) and (6.8) are equated, we get

$$\left(W^{tr}B^{tr}BW\right)^{-1}\bar{L}^{tr}\bar{A}^{-1} = A^{-1}\bar{L}^{tr}.$$

By means of multiplying this equation with $\bar{A}$ from the right and with A from the left, it is easy to see that both are identical.   □

The crucial point is that the dimension of the matrix to invert, $\bar{A}$, is only of the order m, while matrix A in Equation (6.8) has an order r. If the source space regularization and depth weighting operator $W^{tr}B^{tr}BW$ is chosen so that it is easy to invert, then the above regularization in data space is computationally cheaper than solving Equation (6.8). This is the case with the operator B, arising from the discrete L_2 norm approach (6.9). The LORETA method, proposed by Pascual-Marqui and Michel [177], uses a discretization of the Laplace operator for B, whose inversion is more computation expensive.

6.5.3   Nonlinear regularization by means of the L_1 norm

The choice of $\nu = 1$ in Equation (6.6) leads to the L1-norm regularization approach, introduced by Wagner et al. [242]. Here, we choose $B = \mathrm{Id}^s \otimes \mathrm{Id}^{n_{\inf}}$ ($s = 1$ in case of the normal-constraint, otherwise $s = 3$) and, in case of the normal-constraint, the model term

$$\mathrm{MODEL}_1(\underline{j}) = \sum_{i=1}^{n_{\inf}} |w_i\underline{j}^{[i]}| \tag{6.11}$$

and otherwise ($s = 3$)

$$\mathrm{MODEL}_1(\underline{j}) = \sum_{i=1}^{n_{\inf}} \sqrt{\left(w_i\underline{j}^{[i]} + w_{i+n_{\inf}}\underline{j}^{[i+n_{\inf}]} + w_{i+2n_{\inf}}\underline{j}^{[i+2n_{\inf}]}\right)^2}. \tag{6.12}$$

Iterative solution for the L_1 norm approach

Since the derivative of the functional (6.6) in combination with the model term (6.12) can easily be evaluated analytically, a nonlinear Polak-Ribiere CG method was used for its minimization [191]. The general principle of the method was described by Polak [186] and will be summarized in the following. If we take a particular point $\underline{j}^{(i)}$ as the origin of the coordinate system with coordinates $\underline{j}$, the functional can be approximated by means of its Taylor series

$$
\begin{aligned}
F_\lambda^1(\underline{j}) &= F_\lambda^1(\underline{j}^{(i)}) + \sum_{k=1}^r \frac{\partial F_\lambda^1(\underline{j}^{(i)})}{\partial \underline{j}^{[k]}} \underline{j}^{[k]} + \frac{1}{2} \sum_{k,l=1}^r \frac{\partial^2 F_\lambda^1(\underline{j}^{(i)})}{\partial \underline{j}^{[k]} \partial \underline{j}^{[l]}} \underline{j}^{[k]} \underline{j}^{[l]} + \ldots (6.13) \\
&\approx c - (\underline{b}, \underline{j}) + \frac{1}{2} \underline{j}^{tr} A \underline{j} =: \bar{F}_\lambda^1(\underline{j}) \quad\quad (6.14)
\end{aligned}
$$

with

$$
c := F_\lambda^1(\underline{j}^{(i)}) \in \mathbb{R}, \quad \underline{b} := -\operatorname{grad} F_\lambda^1 |_{\underline{j}^{(i)}} \in \mathbb{R}^r, \quad A^{[kl]} := \left. \frac{\partial^2 F_\lambda^1}{\partial \underline{j}^{[k]} \partial \underline{j}^{[l]}} \right|_{\underline{j}^{(i)}} \in \mathbb{R}^{r \times r}.
$$

Starting with an initial vector $\underline{r}^0 \in \mathbb{R}^r$ and setting $\underline{s}^0 = \underline{r}^0$, the CG method for the minimization of the quadratic form $\bar{F}_\lambda^1$ in (6.14), which is equivalent to the solution of the linear equation system $A\underline{j} = \underline{b}$ [93, §9.1], constructs the following two sequences of vectors

$$
\underline{r}^{(i+1)} = \underline{r}^{(i)} - \alpha^{(i)} A \underline{s}^{(i)} \quad , \quad \underline{s}^{(i+1)} = \underline{r}^{(i+1)} + \beta^{(i)} \underline{s}^{(i)} \quad\quad (6.15)
$$

with

$$
\alpha^{(i)} = \frac{(\underline{r}^{(i)}, \underline{s}^{(i)})}{(\underline{s}^{(i)}, \underline{s}^{(i)})_A} \quad , \quad \beta^{(i)} = \frac{(\underline{r}^{(i+1)}, \underline{r}^{(i+1)})}{(\underline{r}^{(i)}, \underline{r}^{(i)})},
$$

where i ($i = 0, 1, 2, \ldots$) is the iteration index. Remember therefore the PCG-Algorithm 8 without preconditioning. If the Hessian matrix A were known, then the construction (6.15) could be used to find a sequence of conjugate directions $\underline{s}^i$ along which to line-minimize. It can be shown that the minimum of the quadratic form (6.14) would be achieved on this way after maximally r iterations [93, §9.4]. Since A is not known, Fletcher-Reeves version of the CG method exploits the following theorem:

Theorem 6.5.4. *Let us suppose that $\underline{r}^{(i)} = -\operatorname{grad} \bar{F}_\lambda^1(\underline{j}^{(i)})$ and that we start from $\underline{j}^{(i)}$ and determine the local minimum, $\underline{j}^{(i+1)}$, of $\bar{F}_\lambda^1$ along the direction $\underline{s}^{(i)}$ and then set $\underline{r}^{(i+1)} := -\operatorname{grad} \bar{F}_\lambda^1(\underline{j}^{(i+1)})$. Under the above assumptions, $\underline{r}^{(i+1)}$ (which is now constructed without any knowledge of A) is the same vector as the one constructed by the use of (6.15).*

Proof: Exploiting the assumption, it is $\underline{r}^{(i)} = -\mathrm{A}\underline{j}^{(i)} + \underline{b}$, and, with an $\alpha \in \mathbb{R}$ chosen so that $\underline{j}^{(i+1)} = \underline{j}^{(i)} + \alpha \underline{s}^{(i)}$ (use recursion (6.15) for the computation of $\underline{s}^{(i)}$) is at the line minimum,

$$\underline{r}^{(i+1)} := -\operatorname{grad} \bar{F}_\lambda^1(\underline{j}^{(i+1)}) = -\mathrm{A}\underline{j}^{(i+1)} + \underline{b} = \underline{r}^{(i)} - \alpha\mathrm{A}\underline{s}^{(i)}. \qquad (6.16)$$

But at the line minimum, it is $0 = \left(\underline{s}^{(i)}, \operatorname{grad} \bar{F}_\lambda^1(\underline{j}^{(i+1)})\right) = -\left(\underline{s}^{(i)}, \underline{r}^{(i+1)}\right)$. If this condition is combined with Equation (6.16), the arising α is equal to $\alpha^{(i)}$ from recursion (6.15). $\qquad\qquad\square$

In practice, the functional F_λ^1 in (6.13) is not a real quadratic form. Therefore, Polak and Ribiere introduced a small change,

$$\beta^{(i)} = \frac{(\underline{r}^{i+1} - \underline{r}^i, \underline{r}^{i+1})}{(\underline{r}^i, \underline{r}^i)},$$

to the above algorithm. Line minimization along the direction $\underline{s}^i$ by means of a routine for initially bracketing a minimum ([187, p.400]) combined with Brent's method in one dimension ([187, p.404]) finally completes the Polak-Riviere CG method ([187, p.423]).

6.5.4 Depth weighting

Three different choices for the $r \times r$ source depth weighting matrix $\mathrm{W} = \mathrm{DIAG}(w_i)$ are discussed now.

- Since deeper sources can only explain measurements with a higher source strength compared to more superficial sources, a regularization without depth weighting, i.e. $w_i = 1$, gives preference to superficial sources.

- If it is not clear from the experiment that superficial sources are searched for, a depth weighting has to be carried out in order not to discriminate deeper sources [177; 74]. The choice of

$$w_i = \|\underline{l}_i\|_2 \qquad \forall i = 1, \ldots, r$$

leads to a *column-wise depth normalization*.

- It is well known that radial sources in a sphere model are silent with regard to the MEG. With the column-wise normalization, zero lead-field columns could thus be possible, leading to a singular matrix W. Motivated by this fact, a *regularized location-wise normalization* $W = \mathrm{Id}^s \otimes \tilde{W}$ with the $n_{\mathrm{inf}} \times$

n_{inf} diagonal matrix $\tilde{W} = \mathrm{DIAG}(\tilde{w}_i)$ was proposed by Fuchs et al. [74]. In case of the normal-constraint ($s = 1$), the weights $\tilde{w}_i$ are chosen as

$$\tilde{w}_i = (k_i^2 + \beta^2)/k_i \qquad k_i = \|\underline{l}_i\|_\infty \qquad \forall i = 1, \ldots, n_{\mathrm{inf}} \qquad (6.17)$$

and otherwise ($s = 3$)

$$\begin{aligned} \tilde{w}_i &= (k_i^2 + \beta^2)/k_i \qquad \forall i = 1, \ldots, n_{\mathrm{inf}} \qquad (6.18) \\ k_i &= \max_{j=1,\ldots,m} \left\{ \sqrt{(\underline{l}_i^{[j]})^2 + (\underline{l}_{i+n_{\mathrm{inf}}}^{[j]})^2 + (\underline{l}_{i+2n_{\mathrm{inf}}}^{[j]})^2} \right\} \end{aligned}$$

By means of the choice

$$\beta = \max_{i=1,\ldots,n_{\mathrm{inf}}} k_i / \mathrm{SNR},$$

the regularization was carried out with respect to the signal-to-noise ratio SNR of the measured data.

6.5.5 Choice of the regularization parameter

Much research has been done with regard to the choice of the regularization parameter λ for the above procedures, especially for the L_2 norm methods. Refer, for example, to the overview article of Hanke and Hansen [100] and the references therein. Most often, two cases are distinguished, the case where the variance of the noise is known in advance and the case where it is unknown. In Section 6.4.3, the discrepancy principle was presented as a member of the first class. For Tikhonov regularization, a second representative of the first class is the *Greferer/Raus-method*, which may be seen as an improved variant of the discrepancy principle [100]. If the variance of the noise is unknown, the regularization parameter can be chosen following the *quasi-optimality criterion* or using the *generalized cross-validation* (GCV) method [100].

Besides the discrepancy principle, the so-called *L-curve criterion* is used here and will now be described. The L-curve criterion can be seen as a more heuristic approach when comparing it to the above procedures. No convergence results are known, but numerical experiments demonstrated that the criterion is robust in practical applications, as reported by Hansen [101]. The L-curve criterion is based on a graph of the model term $\mathrm{MODEL}_v(\underline{j})$ (either (6.7) for the L_2 norm or (6.11,6.12) for the L_1 norm) versus the data term $\mathrm{DATA}(\underline{j})$ (see (6.5)) as a function of the regularization parameter λ, as presented in Figure 6.1 [187]. When plotted in log-log scale, the graph will have a characteristic L-shaped appearance with a steep part (almost parallel to the y-axes), a flat part (almost parallel to the
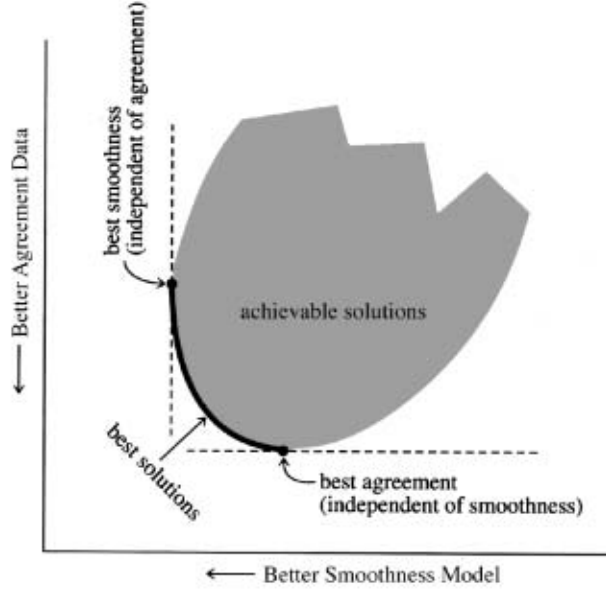
Figure 6.1: *Concept of the L-curve criterion for choosing the regularization parameter [187].*

x-axes) and a "distinct" corner separating these two parts. The steep part corresponds to solutions which are dominated by regularization errors, i.e., parameter λ is chosen too large and not all the available information in the measurements is extracted. The flat part corresponds to a solution that is dominated by perturbation errors. The curve becomes almost parallel to the x-axes in the vicinity of $\lambda = 0$, where the data part approaches its limit and high frequency components of the measurement noise are strongly amplified into the solution vector, so that a large model term results. The corner of the L-curve, chosen by hand within this thesis (an automatic procedure was presented by Hanke and Hansen [100]), thus corresponds to a good balance between minimizing data and model term and therefore to an appropriate choice of λ.

The last presented method, the χ^2 criterion, was introduced to source localization by Rienäcker et al. [191]. The χ^2 criterion chooses the regularization parameter λ so that the data term is brought in its "statistical range" $m \pm \sqrt{m}$, i.e.,

$$\text{DATA}(\underline{j}) \overset{!}{=} m$$

(m the number of measurement sensors).

6.6 Spatio-temporal current density reconstructions

Only the a-priori assumption of *spatial smoothness* of the current distribution within the brain was used for the above regularization procedures. A second physiologically meaningful assumption is the *temporal smoothness* property of the current density reconstruction, which is now considered additionally.

Let us introduce the spatio-temporal regularization problem in a more general form. With Y^{me} denoting the $m \times T$ matrix of measurement data ($\underline{y}_i$ the vector of measurements at timepoint t_i and $\underline{y} := (\underline{y}_1^{tr}, \ldots, \underline{y}_T^{tr})^{tr} \in \mathbb{R}^{mT}$), X the $r \times T$ matrix with the properties of the investigated object that we are searching for and W an $r \times r$ diagonal depth weighting matrix, we define the (generally time-dependent) $m \times r$ matrix A_i at timepoint t_i as the operator, which maps the property vector $\underline{x}_i$ onto the observation vector $\underline{y}_i$. The spatio-temporal regularization problem is then given by the minimization problem

$$F_{\lambda,\mu}(X) := \sum_{i=1}^{T} ||A_i \underline{x}_i - \underline{y}_i||_2^2 + \lambda^2 \sum_{i=1}^{T} ||W\underline{x}_i||_2^2 + \mu^2 \sum_{i=1}^{T-1} \frac{||W\underline{x}_{i+1} - W\underline{x}_i||_2^2}{(t_{i+1} - t_i)^2} \to \min,$$

and, if we substitute $\hat{\underline{x}}_i := W\underline{x}_i$, by

$$F_{\lambda,\mu}(\hat{X}) := \sum_{i=1}^{T} ||\tilde{A}_i \hat{\underline{x}}_i - \underline{y}_i||_2^2 + \lambda^2 \sum_{i=1}^{T} ||\hat{\underline{x}}_i||_2^2 + \mu^2 \sum_{i=1}^{T-1} \frac{||\hat{\underline{x}}_{i+1} - \hat{\underline{x}}_i||_2^2}{(t_{i+1} - t_i)^2} \to \min \quad (6.19)$$

with $\tilde{A}_i = A_i W^{-1}$. The μ penalty term models the temporal smoothness of the problem. The extreme cases $\mu = 0$ and $\mu \to \infty$ can thus be interpreted as regularizations of the temporally uncoupled and static problem, resp..

6.6.1 A deterministic approach

Let us consider problem (6.19) and let us define the block diagonal matrix

$$\tilde{A} := \text{DIAG}\left(\tilde{A}_1, \ldots, \tilde{A}_T\right) \in \mathbb{R}^{(mT) \times (rT)} \tag{6.20}$$

and the temporal regularization operator

$$D := \begin{bmatrix} \frac{1}{t_2-t_1} & -\frac{1}{t_2-t_1} & & & \\ & \frac{1}{t_3-t_2} & -\frac{1}{t_3-t_2} & & \\ & & \ddots & \ddots & \\ & & & \frac{1}{t_T-t_{T-1}} & -\frac{1}{t_T-t_{T-1}} \end{bmatrix} \in \mathbb{R}^{(T-1) \times T}. \tag{6.21}$$

Remember the Definition 6.5.1 of the Kronecker product of two matrices. An efficient method for solving the minimization problem (6.19) is then presented in Algorithm 16, which can be derived on a deterministic way, as shown by Schmitt and Louis [203; 202].

Algorithm 16 STR:$(\underline{\mathbf{y}}, \lambda, \mu) \to X$

(i) Compute $Q \in \mathbb{R}^{(T-1)\times(T-1)}$ and $R \in \mathbb{R}^{T\times T}$ (D from (6.21))

$$
\begin{aligned}
Q &= \left(DD^{tr} + \frac{\lambda^2}{\mu^2} \mathrm{Id}^{T-1} \right)^{-1} \\
R &= \mathrm{Id}^T - D^{tr}QD
\end{aligned}
$$

(ii) With $\tilde{A}$ from (6.20), define the block matrix $C \in \mathbb{R}^{(mT)\times(mT)}$ as

$$
C := \tilde{A} \left(R \otimes \mathrm{Id}^{rT} \right) \tilde{A}^{tr}
$$

(iii) Solve for $\underline{\mathbf{v}} = (\underline{v}_1^{tr}, \ldots, \underline{v}_T^{tr})^{tr} \in \mathbb{R}^{mT}$

$$
\left(C + \lambda^2 \mathrm{Id}^{mT} \right) \underline{\mathbf{v}} = \underline{\mathbf{y}}
$$

(iv) Finally, $\forall i = 1, \ldots, T$, compute the ith column vector of matrix $X \in \mathbb{R}^{r\times T}$

$$
\underline{x}_i = W^{-1} \sum_{j=1}^{T} R^{[ij]} \tilde{A}_j^{tr} \underline{v}_j
$$

6.6.2 Estimation theoretical approaches

The so-called *Kalman-filters* and *smoothers* are spatio-temporal regularization approaches, which are derived using methods from estimation theory. Kalman-filters estimate $\hat{\underline{x}}_i$ by means of only the current and past observations, $\{\underline{y}_1, \ldots, \underline{y}_i\}$, while a Kalman-smoother exploits the whole measurement interval, $\{\underline{y}_1, \ldots, \underline{y}_T\}$. It will be renounced here to deeper present the underlying estimation theoretical methodology. For an introduction to the theory of Kalman-filters, see Melsa and Cohn [157], for Kalman-smoothers, refer to Grewal and Andrews [84]. Since the Kalman filtering estimates are based on the current and past observations only, slight delays are often induced in the reconstruction results for dynamic processes, while this problem is less distinct when using a Kalman-smoother, as shown by Kaipio et al. [116].

6.6.3 Applications of dynamic inverse problems

The application of Algorithm 16 to two different problems, namely spatio-temporal current density reconstructions and dynamic electrical impedance tomography, will be shortly described now. For more details, refer to Schmitt et al. [204].

Algorithm 17 STR-C:$(U^{me}, \lambda, \mu) \to J$

(i) Calculate Q and R as in Algorithm 16.

(ii) Solve the generalized Sylvester equation for $V \in \mathbb{R}^{m \times T}$

$$\left(\tilde{L} \tilde{L}^{tr} \right) VR + \lambda^2 V = U^{me}$$

(iii) Compute the current density matrix $J \in \mathbb{R}^{r \times T}$

$$J = W^{-1} \tilde{L}^{tr} VR$$

Spatio-temporal current density reconstruction

For spatio-temporal current density reconstructions, matrix Y^{me} consists of the measured spatio-temporal EEG/MEG data, i.e., U^{me}, X consists of the spatio-temporal current density reconstructions, i.e., J, and W is the diagonal source strength depth weighting matrix as defined in Section 6.5.4. Matrix A_i is replaced by the lead-field matrix L, which is independent of time, so that C in Algorithm 16 simplifies to $C = R \otimes \tilde{L} \tilde{L}^{tr}$ with $\tilde{L} := LW^{-1} \in \mathbb{R}^{m \times r}$. As shown by Schmitt and Louis [203; 202], Algorithm 16 can then be transformed to Algorithm 17. The Sylvester type equation in this algorithm can be efficiently solved by methods proposed by Gardiner et al. [76].

In Schmitt et al. [204], we compared the reconstruction results of Algorithm 17 with the reconstructions of the temporally uncoupled linear Tikhonov-Phillips regularization from Section 6.5.1 with the discrete regularization operator (6.9). For two dipoles with smooth activation curves in a very simple volume conductor model, Algorithm 17 resulted in a reconstruction with smaller localization error and a more exact activation curve. We concluded, that the a-priori information of temporal smoothness leads to higher robustness against noise in the data.

Dynamic electrical impedance tomography

A second application of Algorithm 16 can be found in the field of dynamic Electrical Impedance Tomography (dyn-EIT) [212; 231; 234; 232; 233; 116; 235; 204; 146]. EIT tries to reconstruct a conductivity distribution inside a given object by means of injecting currents and measuring resultant potentials at the objects surface. It may be difficult for EIT to reconstruct the anisotropic conductivity distribution within the WM compartment with the necessary resolution, since the low-conducting closed skull compartment poses a big problem. Nevertheless, the method may help in reducing systematic errors in the EEG

inverse problem [80], in determining conductivity inhomogeneities of the skull layer [174; 173] and may also be useful in better estimating the WM conductivity tensor eigenvalues, while exploiting the eigenvectors as an a-priori information, measured by DT-MRI [213].

We consider the so-called *complete electrode model*

$$
\begin{aligned}
\operatorname{div}(\sigma \operatorname{grad} u) &= 0 && \text{in } \Omega \\
\int_{e_l} \sigma \frac{\partial u}{\partial \mathbf{n}} d\Gamma &= I_l && l = 1, \dots, L \\
\left. \left(u + z_l \sigma \frac{\partial u}{\partial \mathbf{n}} \right) \right|_{e_l} &= U_l && l = 1, \dots, L \\
\left. \sigma \frac{\partial u}{\partial \mathbf{n}} \right|_{\Gamma \setminus \cup_{l=1}^L e_l} &= 0
\end{aligned}
$$

with z_l the effective contact impedance between the lth electrode e_l and tissue, I_l the injected current at e_l and U_l the measured voltage at this electrode. As shown by Somersalo et al. [212], the conditions $\sum_l I_l = 0$ and $\sum_l U_l = 0$ ensure existence and uniqueness of the solution and the complete electrode model predicts the measured voltages at the precision of the measurement system. In the following, the resistivity ρ is used, which is defined as the inverse of the conductivity σ, i.e., $\rho = 1/\sigma$ ([127, p.69]). Using variational and FE methods, a discrete deterministic forward model for EIT of rang N_h can be derived (an overview is given in Vauhkonen [231]). By means of the operator

$$
U^c : \mathbb{R}^{N_h} \times \mathbb{R}^L \to \mathbb{R}^L \qquad U^c(\underline{\rho}_i) := U^c(\underline{\rho}_i, \underline{I}_i) = R(\underline{\rho}_i)\underline{I}_i \qquad i = 1, \dots, T,
$$

with an $L \times L$ matrix R arising from the FE discretization and depending nonlinearly on the resistivity vector $\underline{\rho}_i \in \mathbb{R}^{N_h}$ at timepoint t_i, the simulated voltage vector can be computed from the vector of injected currents at timepoint t_i, $\underline{I}_i \in \mathbb{R}^L$. The operator U^c can be linearized in $\underline{\rho}_i$,

$$
U^c(\underline{\rho}) = U^c(\underline{\rho}_i) + J(\underline{\rho}_i)(\underline{\rho} - \underline{\rho}_i) + o(\|\underline{\rho} - \underline{\rho}_i\|),
$$

with $J(\underline{\rho}_i)$ denoting the $L \times N_h$ Jacobian matrix, which can be computed as described by Vauhkonen [231, Chapter 4.1]. Using the linearization, a Gauss-Newton type algorithm can be formulated for the dyn-EIT inverse problem [231; 202; 204]

$$
\begin{aligned}
\rho^{k+1} &= \min_{\rho = (\underline{\rho}_1, \dots, \underline{\rho}_T)} \left\{ \sum_{i=1}^T \| U^c(\underline{\rho}_i^k) + J(\underline{\rho}_i^k)(\underline{\rho}_i - \underline{\rho}_i^k) - \underline{u}_i^{me} \|_2^2 \right. \\
&\quad + \left. \lambda^2 \sum_{i=1}^T \| \underline{\rho}_i - \underline{\rho}^0 \|_2^2 + \mu^2 \sum_{i=1}^{T-1} \frac{\| \underline{\rho}_{i+1} - \underline{\rho}_i \|_2^2}{(t_{i+1} - t_i)^2} \right\}.
\end{aligned}
$$

The index k in this equation denotes the Gauss-Newton iteration count. The vector $\underline{\rho}^0 = \text{const} \cdot (1, \ldots, 1)^{tr} \in \mathbb{R}^{N_h}$ can be estimated from the data [231]. The measured voltages are denoted by the matrix $\text{U}^{me} = (\underline{u}_1^{me}, \ldots, \underline{u}_T^{me}) \in \mathbb{R}^{L \times T}$. If we now substitute $\underline{x}_i := \underline{\rho}_i - \underline{\rho}^0$, we obtain

$$
\begin{aligned}
\rho^{k+1} \quad = \quad & \rho^0 + \min_{X=(\underline{x}_1,\ldots,\underline{x}_T)} \left\{ \sum_{i=1}^{T} ||\text{J}(\underline{\rho}_i^k)\underline{x}_i - \left[\underline{u}_i^{me} + \text{J}(\underline{\rho}_i^k)(\underline{\rho}_i^k - \underline{\rho}^0) - \text{U}^c(\underline{\rho}_i^k)\right] ||_2^2 \right. \\
+ \quad & \left. \lambda^2 \sum_{i=1}^{T} ||\underline{x}_i||_2^2 + \mu^2 \sum_{i=1}^{T-1} \frac{||\underline{x}_{i+1} - \underline{x}_i||_2^2}{(t_{i+1} - t_i)^2} \right\},
\end{aligned}
\tag{6.22}
$$

which has the form (6.19), so that Algorithm 16 can be applied.

In Schmitt et al. [204], we carried out a numerical study to test accuracy and efficiency of the presented deterministic approach for dyn-EIT. The considered model consisted of a two-dimensional cut through a tube with high resistive content and the dynamic process of a low-resistive "rising bubble" perpendicular to the 2D observation plane. The results of Algorithm 16 for solving the dyn-EIT problem (6.22) for $k = 1$ and $k = 2$, i.e., one or two Gauss-Newton iterations, was compared with the result of a (fixed interval) Kalman-smoother estimation theoretical approach (see Section 6.6.2). It was found that for both noiseless and noisy data, one Gauss-Newton iteration with Algorithm 16 already yielded slightly better reconstruction results than the Kalman-smoother, while the results for two iterations were again enhanced. Note also that the Kalman-smoother is more memory and computation expensive and has to be controlled by three parameters while Algorithm 16 only needs two. It should finally be annotated that the so-called *fixed-lag Kalman smoother*, used by Vauhkonen et al. [235], should be computationally more interesting than the fixed-interval smoother.

6.7 Summary and Conclusions

In this chapter, a selection of approaches to the bioelectromagnetic inverse problem was presented. After introducing the concept of the lead field matrix and the node-oriented EEG lead field basis, algorithms were discussed that are either based on the assumption of a limited number of pointlike sources, the focal source model, or on the assumption of a distributed source model.

For the reconstruction of focal sources, a downhill simplex optimizer in combination with methods for solving the linear least square problem was presented. Among other conceivable applications, this procedure is especially appropriate for reconstructing single dipolar sources in continuous parameter space. The main focus of the section about focal inverse methods was placed on a new dipole

fit method, the SA-TSVD, a discrete simulated annealing approach in combination with the truncated singular value decomposition for solving the embedded linear least square problem. By means of an adjusted discrepancy principle, the TSVD regularization is automatically controlled by the noise in the data and the condition of the occurring least square problems. Although the singular value decomposition of the spatio-temporal EEG/MEG data gives an estimate for the minimal number of sources contributing to the measurements, the exact number is unknown in advance and noise complicates the reconstruction. Classical non-regularized nonlinear dipole fit algorithms (as an example of this class the SA-COF was presented) do not give an estimate for the correct number because they are not stable with regard to an overestimation of this parameter. Too many sources may only describe noise but can still attain a large magnitude during the inverse procedure and may be indiscernible from the true sources. The SA-TSVD annihilates this problem by better filtering ghost source components. Such ghosts can be radial components (MEG) or components with deep dipoles (EEG and MEG) or sources which nearly cancel each other (EEG and MEG). In the next chapter, the superior ability of the SA-TSVD to estimate the number and reconstruct "sure" sources will be demonstrated through simulation studies.

As the second class of inverse methods, instantaneous current density reconstruction approaches were presented. The distributed source models were divided into L_2 and L_1 norm methods and various regularization operators for 3D brain- or 2D cortical surface- regularization together with their numerical solution strategies were described. The concepts of channel and source space depth weighting were introduced and the choice of the regularization parameter was discussed. The instantaneous current density reconstruction methods will be used in the next chapter.

In the last section, recently developed linear spatio-temporal regularization approaches [203] were described, which do not only use the a-priori assumption of spatial smoothness as the instantaneous Tikhonov-Phillips L_2 norm methods, but which additionally consider temporal smoothness properties of the underlying distribution, also measured in the L_2 norm. The application of the methods to spatio-temporal current density reconstruction and, as a second application area, to the dynamical electrical impedance tomography (dyn-EIT) showed a stabilizing effect of the additional temporal smoothness term. In dyn-EIT, the presented method was compared to a fixed-interval Kalman smoother and was found to be superior with respect to reconstruction accuracy and memory and computational effort.

The new results of this chapter have been published in Wolters et al. [256; 260; 259] and Schmitt et al. [204].

Chapter 7

Sensitivity towards tissue anisotropy

7.1 Introduction

The last chapters were concerned with the generation of realistically shaped volume conductor models, the solution of the forward problem and the theory of various inverse methods, used in the field of EEG/MEG source reconstruction. The gold standard for the forward approach are multi-compartment models with isotropic conductivities within each compartment. EEG and MEG are most often simulated by means of the BE method, while the FE approach was only rarely used because of the large computation amount.

In spherical models of the head, some studies exist for the influence of layer conductivity anisotropy (radial versus tangential) on forward and inverse problem in EEG and MEG [180; 273], but especially GM and WM compartments are only poorly represented by such a model. In realistic FE models, sensitivity studies exist for the influence of 1:10 skull anisotropy on forward problem (EEG and MEG, [228]) and inverse problem (EEG, [152]), while only one study is known for the influence of WM anisotropy onto the forward simulation (EEG and MEG, [106]). The sensitivity of source reconstruction methods on realistic WM anisotropy for both EEG and MEG was not yet studied.

In the first section of this chapter, the influence of skull and WM anisotropy onto the forward problem will be presented and compared with results from the literature. The second section concerns about the sensitivity of inverse approaches towards tissue anisotropy. The results of this chapter are summarized in the last section.
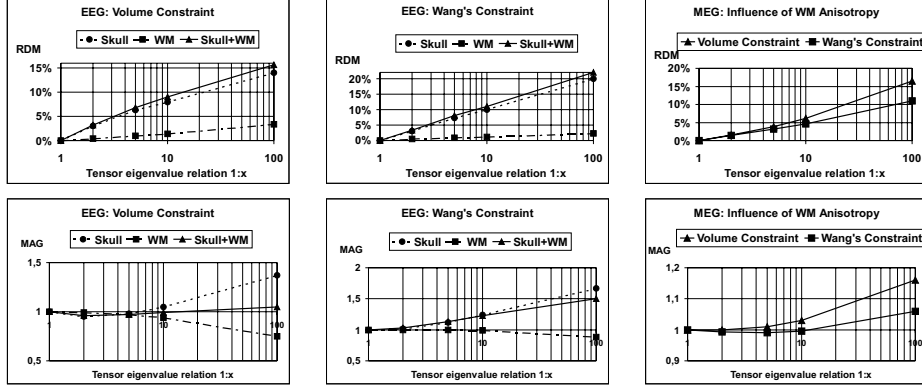
Figure 7.1: *EEG and MEG topography error (top row) and magnitude error (bottom row) for different anisotropy ratios: For the EEG, errors due to anisotropy effects of skull, WM and both skull and WM are presented for the tensor volume retaining (left) and Wang's constraint (middle). For MEG, only WM anisotropy effects for both constraints are presented (right), since skull anisotropy was found to have no influence.*

7.2   Influence on EEG/MEG forward problem

In this section, the influence of skull and WM anisotropy onto the EEG and MEG forward problem is studied for a neocortical source and for a deep source. For the neocortical source, it is distinguished between a mainly tangential and a mainly radial orientation component. EEG and MEG sensors are simulated as described in Section 4.8.3.

7.2.1   A tangentially oriented eccentric source

Forward calculations for the eccentric source with a large tangential orientation component ("Somato(tang)" in Fig. 4.7) and a strength of 10 nAm were carried out in the volume conductor model 1 (Table 4.1) and the sensitivity of EEG and MEG towards anisotropy of the skull layer (see Table 4.3), the WM compartment (Table 4.4), and of both skull and WM was determined. Fig. 7.1 shows the resulting RDM (top row) and MAG (bottom row) errors for an increasing anisotropy ratio, when either obeying the volume constraint or Wang's constraint. EEG and MEG sensors were modeled as described in Section 4.8.3.

The EEG results concerning 1:10 anisotropic skull in combination with an isotropic WM compartment are generally in agreement with the observations of Marin et al. [152], where a topography error of about 10% and a magnification
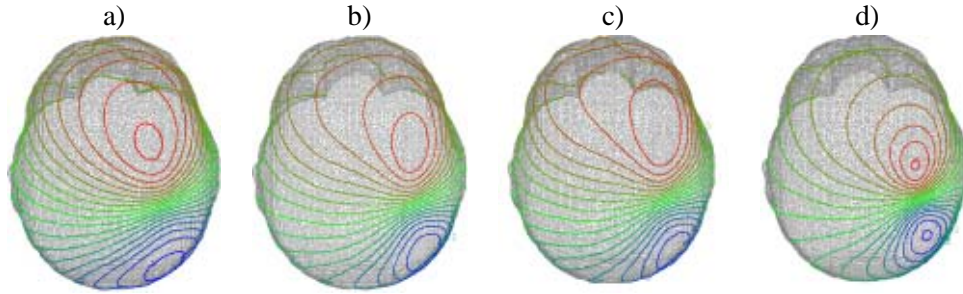
Figure 7.2: *Topography of isopotential distribution on upper part of the head: a) isotropic skull; from -0.9 to 0.2 μV b) 1:10 anisotropic skull; volume method; from -1.1 to 0.3 μV c) 1:10 anisotropic skull with $\sigma^{rad} = 0.00042$ and $\sigma^{tang} = 0.0042$; from -0.7 to 0.1 μV d) 1:10 anisotropic skull with $\sigma^{rad} = 0.0042$ and $\sigma^{tang} = 0.042$; from -2.2 to 0.9 μV.*

factor larger than 1 was reported for an eccentric tangentially oriented dipole in a realistic FE head model. However, Marin et al. [152] modeled 1:10 skull anisotropy by fixing the radial and increasing the tangential conductivity eigenvalues by a factor of 10. If we do so, a much larger topography error (RDM=20%) and a much larger magnification factor (MAG=1.72) was observed (see Fig. 7.2 and compare (a) with (d)). This difference could be attributed to different simulation parameters like skull thickness and source location, and to the definition/evaluation of RDM and MAG. Marin et al. [152] evaluated an integral over the whole head surface, whereas only the potentials at the 71 EEG electrodes were considered here. The focus is on the influence of anisotropy on the inverse EEG problem, where in practice, only a limited number of sensors is available. The electrodes are often placed around the "center of interest" in order to sample the whole measurable dipolar pattern, which is illustrated for example in Fig. 1.2.

Fig. 7.2 shows the isopotential distribution interpolated on the head surface for various anisotropy ratios. The isopotential distribution for the isotropic skull layer is shown in (a), and the result for 1:10 anisotropy with volume constraint in (b). The two 1:10 skull anisotropy isopotential distributions in (c) and (d) were calculated either by means of a fixation of the tangential conductivity eigenvalues and a reduction of the radial one by a factor of 10 (c) or by means of a fixation of the radial conductivity eigenvalue and an increase of the tangential ones by a factor of 10 (d).

The result of a computation in the isotropic nodeshifted cube model 2 (Table 4.1) is shown on an axial cut through the model in the vicinity of the source in Fig. 7.3(a). In (b), the computation was carried out in the corresponding model
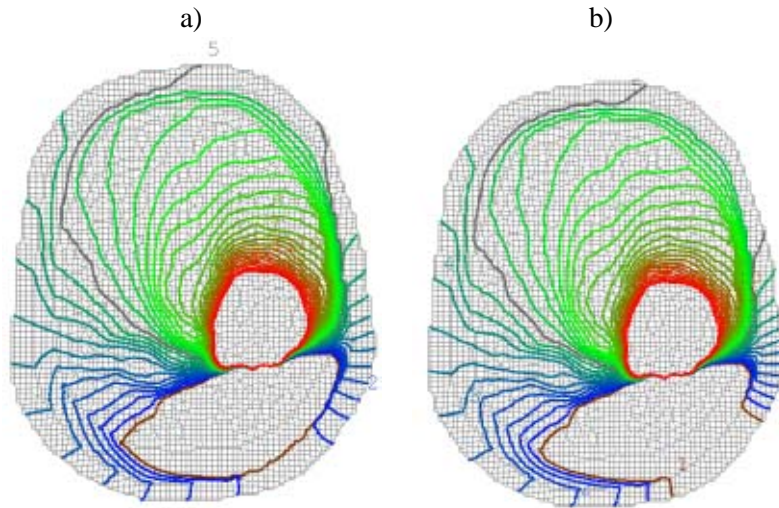
a)   b)

Figure 7.3: *Isopotential distribution from -0.1 to 0.2 μV on axial cut through the nodeshifted cube model a) isotropic model b) 1:10 anisotropic skull, volume constraint; isotropic WM.*

with 1:10 anisotropic skull (volume constraint), while retaining the isotropic WM compartment. The influence of anisotropy can well be studied when comparing the run of the marked (grey and brown) isopotential lines in both models.

When comparing the results on skull anisotropy in realistic FE models with examinations in multilayered sphere models [273; 152], the important difference is found that the EEG topography error between isotropic and 1:10 anisotropic skull modeling in the realistic FE head model (in agreement with the realistic FE head model in Marin et al. [152]) is much larger than the EEG topography error between isotropic and 1:10 anisotropic spherical layer modeling, reported by Zhou et al. [273] and Marin et al. [152]. Additionally, a MAG close to 1 was pointed out for the spherical model [273], whereas for the realistic FE model, a MAG larger 1 was found here, and was also reported by Marin et al.. Spherical symmetry effects could thus play a role, reducing topography and magnitude errors for the multilayered sphere model. However, these errors seem to be apparent in realistically shaped head models.

1:10 skull anisotropy was found to have no influence (RDM $< 1\%$, MAG ≈ 1) on the MEG topography and magnitude for both volume and Wang's constraint. This is in agreement with the results of van den Broek [228] in a realistic FE head model and with the generally accepted idea that volume currents in the skull and scalp layer give negligible contributions to the magnetic field [96].

The observations regarding the influence of WM anisotropy on EEG and MEG for an isotropic skull layer in Fig. 7.1 agree well with the results in Haueisen et al. [106]. They reported small topography and magnitude errors for EEG and MEG for an eccentric source with large tangential orientation component. Here, a negligible influence for a ratio of 1:10 on the EEG topography with an RDM close to 1% and on the MEG topography with an RDM of about 5% was observed. The MAG is close to the optimum in the realistic anisotropy range for both EEG and MEG.

Haueisen et al. [104] reported a strong influence of local conductivity changes around the source to EEG and MEG. Therefore, 41 finite elements in the neighborhood around the source were determined in the 1:10 anisotropic tetrahedra model 1, five of which were isotropic CSF, 30 isotropic GM and 6 anisotropic WM elements. Isotropic WM conductivity was then assigned to the latter 6 elements and EEG and MEG were computed in this *locally isotropic* model. For both EEG and MEG, an RDM smaller than 1% and a MAG of about 1 was found. Note that only 6 out of the 41 neighboring elements to the source were WM elements so that the small influence should be mainly attributed to this fact.

In summary, for the EEG, 1:10 anisotropy of both skull and WM layer, leads to a topography error of about 9% for the volume constraint and 11% for Wang's constraint. The topography error is mainly due to skull anisotropy, whereas WM anisotropy has only a small influence on the potential distribution for the chosen eccentric source with large tangential orientation component. When choosing the volume constraint, the magnitude error MAG for 1:10 anisotropy of skull and WM layer is kept close to the optimum of 1.0, whereas Wang's constraint leads to a MAG of 1.23. An increase of radial or tangential skull conductivity contracts (in Figure 7.2, compare (a) with (d)), whereas a decrease spreads out the isopotential distribution on the surface. The pattern is also distorted (in Figure 7.2, compare (a) with (c)), so that an approximation of skull anisotropy effects by means of an increase or a decrease of the scalar isotropic skull conductivity value in BE head models seems to be impossible. This is in particular true, because further computations with different source locations and orientations showed that contraction or spreading out depends on parameters such as location/orientation of the source and skull shape and thickness (see Section 7.3.1).

For the MEG, no influence of skull anisotropy was observed. The influence of WM was small for realistic anisotropy ratios.

7.2.2 A radially oriented eccentric source

Forward calculations for the eccentric source with large radial orientation component ("Somato(rad)" in Fig. 4.7) and a strength of 10 nAm were carried out in the tetrahedra FE model 1 (Table 4.1). Fig. 7.4 shows the resulting RDM (left)
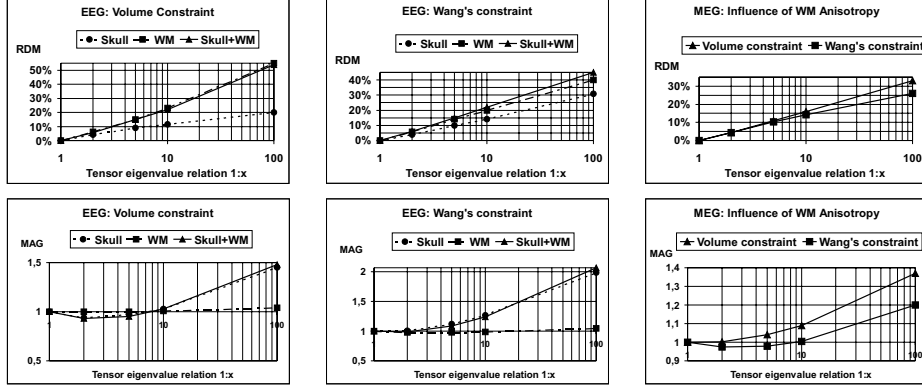
Figure 7.4: *EEG and MEG topography error (top row) and magnitude error (bottom row) for different anisotropy ratios: For the EEG, errors due to anisotropy effects of skull, WM and both skull and WM are presented for the tensor volume retaining (left) and Wang's constraint (middle). For MEG, only WM anisotropy effects for both constraints are presented (right), since skull anisotropy was found to have no influence.*

and MAG (right).

1:10 realistic WM anisotropy for the radially oriented eccentric source has a strong influence on the topography of EEG and MEG, a result which again mainly agrees with the results of Haueisen et al. [106]. They reported a large topography error for both EEG and MEG (our MEG results have to be compared to the flux density component B_y in Haueisen's Table 2) and a moderate magnitude error for an eccentric almost radially oriented source. Here, an EEG topography error was observed of RDM=23% for the volume and RDM=20% for Wang's constraint and an MEG topography error of about 15% for both constraints. The large MEG topography error can be explained by the fact that WM anisotropy influences the secondary (return) currents and that the ratio of the secondary to the whole magnetic flux increases with increasing ratio of the radial dipole orientation component [105]. Note that for radially oriented sources in spherical head models, the primary magnetic flux (and because of spherical symmetry effects also the secondary magnetic flux) is zero outside the model. For both EEG and MEG, the MAG was again close to the optimum 1.0 for realistic WM anisotropy ratios except for the MEG in combination with the volume constraint, where the error was close to 1.1.

Again, an RDM smaller than 1% and a MAG of about 1 was found for the comparison with the 1:10 anisotropic but locally isotropic model (see Sec-
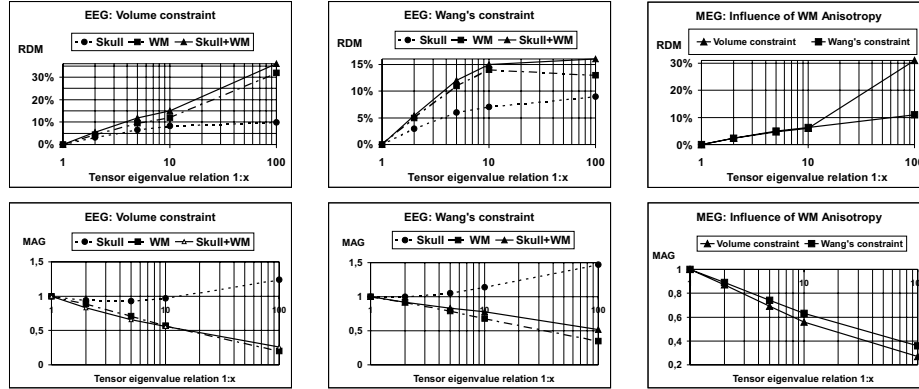
Figure 7.5: *Deep thalamic source: EEG and MEG topography error (top row) and magnitude error (bottom row) for different anisotropy ratios: For the EEG, errors due to anisotropy effects of skull, WM and both skull and WM are presented for the tensor volume retaining (left) and Wang's constraint (middle). For MEG, only WM anisotropy effects for both constraints are presented (right), since skull anisotropy was found to have no influence.*

tion 7.2.1) for both EEG and MEG.

The EEG results concerning 1:10 anisotropy of the skull agree well with the observations of Marin et al. [152]. With an RDM of 12% for the volume and 14% for Wang's constraint, the influence on the potential topography is in the range as seen for the tangential dipole. A MAG close to 1 for the volume and a MAG of 1.27 for Wang's constraint was achieved. For MEG, as for the tangential eccentric source, no influence (RDM < 1%, MAG ≈ 1) of skull anisotropy was found [96; 228].

In summary, 1:10 anisotropy of both considered compartments leads to a non-negligible topography error for both EEG and MEG. This error is mainly due to WM anisotropy. Skull anisotropy has no influence on the MEG, but a non-negligible influence on the EEG. For EEG, the volume constraint led to a smaller MAG error than Wang's constraint, whereas we observed the inverse for the MEG. The local change from anisotropic to isotropic conductivity of (some few) WM elements in the neighborhood of the source did not influence the error considerations.

7.2.3 A deep source

In a last simulation, forward calculations in the tetrahedra FE model 1 (Table 4.1) were carried out for a deep and thus almost radial source ("Thal(rad)" in Fig. 4.7)
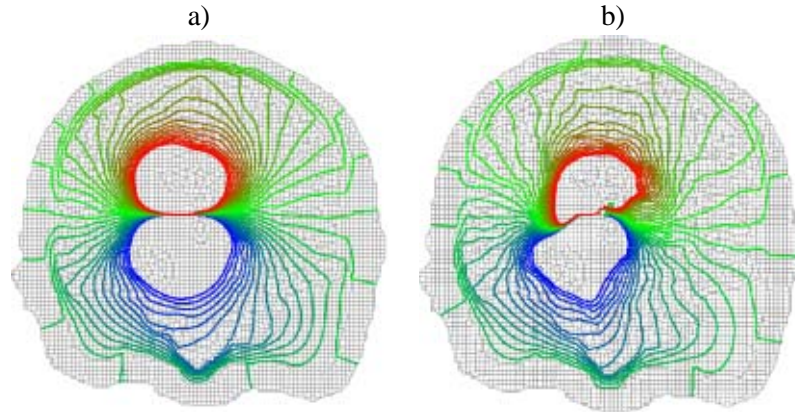
a)   b)

Figure 7.6: *Isopotential distribution from -0.3 to 0.3 μV on coronal cut through the nodeshifted cube model a) isotropic model b) 1:10 anisotropic, but locally isotropic WM compartment.*

with a strength of 10 nAm. In the thalamus, tissue structure is almost radially oriented. Fig. 7.5 shows the resulting RDM and MAG errors.

It can be observed from both figures, that 1:10 WM anisotropy in combination with an isotropic skull layer leads to a non-negligible topography error larger 10% for the EEG, whereas with 6%, the error is moderate for the MEG, but it is then strongly increasing for larger anisotropy ratios. WM anisotropy strongly decreased the surface potential (MAG=0.57 in Fig. 7.5) and the magnetic fields (MAG≈0.6 in Fig. 7.5). The former is related to the results of Zhou and van Oosterom [273], who reported a decreased (increased) potential magnitude for increased (decreased) radial conductivity in the inner sphere of a multilayer sphere model, whereas for a change in the tangential conductivity component, no influence was found.

Again, the influence of local conductivity changes around the source was studied. Therefore, for the thalamic source, 29 neighbored finite elements in the 1:10 anisotropic tetrahedra model 1 and 45 neighbored finite elements in the nodeshift cube model 2 with 1:10 anisotropic WM compartment were determined, all of which were transformed from anisotropic to isotropic WM elements. When comparing the forward simulations in the tetrahedra model, an RDM of 16% and a MAG of 1.34 was found for the EEG and an RDM of 14% and a MAG of 1.19 for the MEG. These results show the importance of local conductivity changes, as reported by Haueisen et al. [104]. Fig. 7.6 shows the isopotential distribution for model 2 for the isotropic case (a) and for the corresponding case with 1:10 anisotropic but locally isotropic WM compartment.
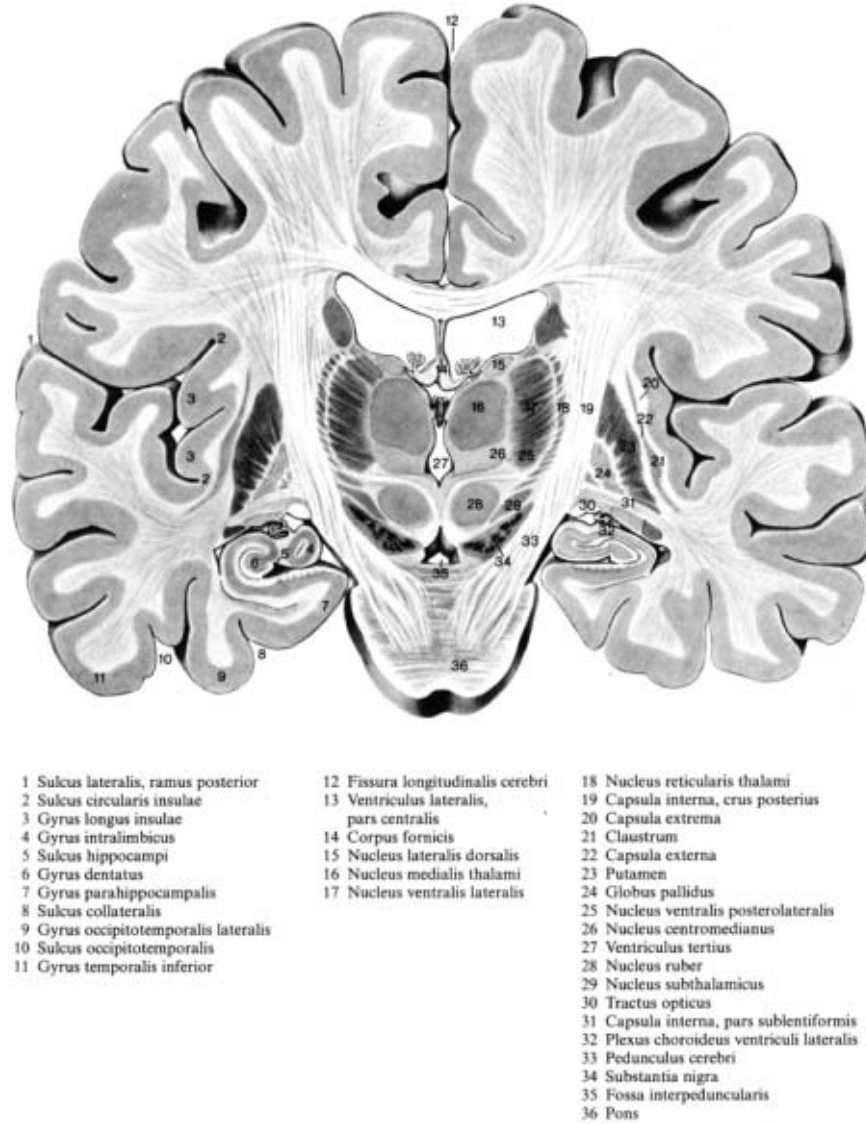
Figure 7.7: *Cut through the thalamus, the Pedunculus cerebri and the Pons [166].*

1 Sulcus lateralis, ramus posterior	12 Fissura longitudinalis cerebri	18 Nucleus reticularis thalami
2 Sulcus circularis insulae	13 Ventriculus lateralis, pars centralis	19 Capsula interna, crus posterius
3 Gyrus longus insulae	14 Corpus fornicis	20 Capsula extrema
4 Gyrus intralimbicus	15 Nucleus lateralis dorsalis	21 Claustrum
5 Sulcus hippocampi	16 Nucleus medialis thalami	22 Capsula externa
6 Gyrus dentatus	17 Nucleus ventralis lateralis	23 Putamen
7 Gyrus parahippocampalis		24 Globus pallidus
8 Sulcus collateralis		25 Nucleus ventralis posterolateralis
9 Gyrus occipitotemporalis lateralis		26 Nucleus centromedianus
10 Sulcus occipitotemporalis		27 Ventriculus tertius
11 Gyrus temporalis inferior		28 Nucleus ruber
		29 Nucleus subthalamicus
		30 Tractus opticus
		31 Capsula interna, pars sublentiformis
		32 Plexus choroideus ventriculi lateralis
		33 Pedunculus cerebri
		34 Substantia nigra
		35 Fossa interpeduncularis
		36 Pons

The increased volume current flow along the fibre bundles of the corticospinal tract, shown in Fig. 7.7, can be observed from the isopotential distribution in the anisotropic case (isopotential lines are perpendicular to the volume current flow).

For the EEG, an RDM of about 7% for 1:10 anisotropic skull in combination with an isotropic WM compartment (Fig. 7.5, left column) and an increase in the magnitude for Wang's constraint (Figure 7.5, bottom row, right, MAG = 1.14) was observed, while the magnitude was kept close to the optimum for the volume constraint (Figure 7.5, top row, right, MAG = 0.97). For the MEG, only a small influence (RDM < 3%, MAG=0.98) was found for Wang's constraint (not shown).

In summary, for the deep thalamic source, a non-negligible influence of 1:10 skull and WM anisotropy on the EEG topography was found. The EEG topography error is mainly due to WM, but to a minor extent also to skull anisotropy. For the MEG, we assume that WM anisotropy has a non-negligible influence on the topography, whereas skull anisotropy can be neglected. WM anisotropy strongly reduced EEG and MEG field magnitude. Local conductivity changes were strongly influencing our error considerations.

7.3 Influence on EEG/MEG source reconstruction

The sensitivity of the EEG/MEG inverse source reconstruction process towards realistic head tissue conductivity anisotropy is now examined. In various medical application fields such as epilepsy and brain tumors, simple one dipole models are used [78; 81; 195; 110; 237; 111; 48]. Therefore, in the first part of this section, the EEG single dipole fit reconstruction error is examined for a variety of sources. In the second part, a more complicated source model from cognition is studied. The sensitivity of EEG and MEG inverse reconstruction methods towards tissue anisotropy is described for the reconstruction of early syntactic processes in frontal and temporal cortical areas, referring to the examinations of Friederici et al. [68].

7.3.1 EEG reconstruction error for single dipole fit

A variety of sources with different locations and orientations in the brain were used for examining the sensitivity of EEG single dipole fitting towards realistic skull and WM anisotropy. The EEG was computed in the 5 tissue tetrahedra model 1 (Table 4.1) for 46 neocortical sources with large tangential and for 42 with large radial orientation component and for 46 dipoles in deeper brain areas, each with a strength of 10 nAm. The reference dipoles are presented in Figs. 7.8 and 7.9 as red arrows or poles, resp.. They are scaled so that 1mm arrow length corresponds to 1nAm source strength. The 71 EEG electrodes are fixed as described in Section 4.8.3. The inverse dipole fit method uses the downhill simplex optimizer in continuous parameter space (Section 6.4.1) for the dipole localiza-
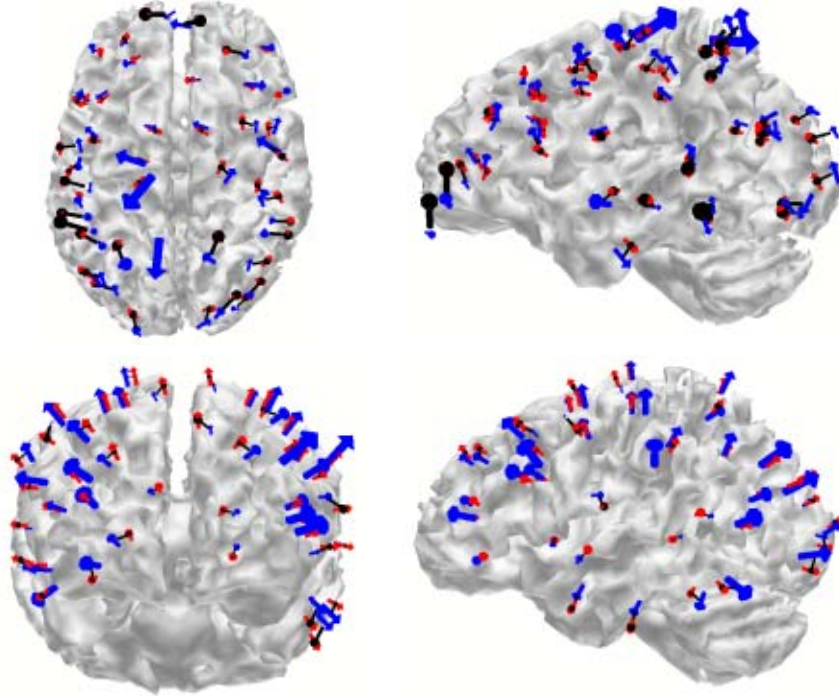
Figure 7.8: *EEG reconstruction errors due to 1:10 anisotropy of the skull compartment (1nAm source strength scaled as 1mm, figure scale 1:4): The red arrows are the reference dipoles, 46 mainly tangentially oriented (top) and 42 mainly radially oriented ones (bottom), and the blue arrows are the fitted ones. The pair of reference and corresponding reconstructed source is connected with a black pole, representing the localization error. Dipoles are shown on underlying transparent WM surface.*

tion, while orientation and strength are determined by means of the generalized inverse (Section 6.4.3). The midpoint of the brain was chosen as the seedpoint and the simplices could then move freely in space without further constraints.

In order to study the accuracy of the 71 electrode fit in combination with the blurred dipole source model, each source was fitted in the isotropic model by means of its EEG result in the isotropic volume conductor. A maximal localization error of 0.6mm was found, which emphasizes the accuracy of chosen method and source model.

In the following, mean μ, standard deviation Σ and maximum and minimum are computed for the (absolute) localization error, the (absolute) orientation error and the (relative) amplitude error for each of the three source classes (tangential,

ref. sour.	(Abs.) Localization error (in mm)				(Abs.) Orientation error θ (in degrees)				(Rel.) Strength error AMP (in percent)			
	μ	Σ	Max	Min	μ	Σ	Max	Min	μ	Σ	Max	Min
tang.	8.6	3.5	18	3.6	19	11	55	1.9	29	40	201	2.8
rad.	4.6	1.9	8.8	1.3	10	7	35	1.1	56	41	154	2
deep	6.8	2.6	12	2.1	11	7	29	0.7	31	34	174	1.9

Table 7.1: *Influence of 1:10 skull anisotropy on single dipole fit for the class of tangentially and radially oriented neocortical sources and the class of deep sources.*

radial, deep). If $\mathbf{x}$ (x) is the orientation (strength) of the reference source and $\mathbf{y}$ (y) the one of the corresponding fitted dipole, the orientation (strength) error θ (AMP) is measured by means of

$$\theta := \mathrm{GRAD}\left(\arccos\frac{(\mathbf{x},\mathbf{y})}{\|\mathbf{x}\|\|\mathbf{y}\|}\right) \qquad \mathrm{AMP} = \left|\frac{x-y}{x}\right| \cdot 100,$$

where the function GRAD denotes a conversion of the measure of angle in radians to a measure of angle in degrees.

Note that the orientation error as well as the strength error are also important criteria besides the localization error. In certain experiments, different dipole locations are fixed (e.g., if fMRI results are available) and those dipole location is considered as the correct one, where the reconstructed source orientation and strength fits best to the anatomical normal-constraint, described in Section 6.2. Other experiments exist, where dipole locations as well as their orientations are fixed and only the fitted strengths are evaluated. The latter procedure was used, e.g., for discovering an isolated influence of repetitive sensorimotor training on the activation in motor areas [244].

Skull anisotropy

A dipole fit in the isotropic model was then carried out exploiting its EEG result in the model with 1:10 skull anisotropy. In Fig. 7.8, the fitted dipoles are shown as blue arrows for the neocortical sources with mainly tangential (top) and with mainly radial orientation (bottom). The localization error for each pair is visualized by means of a black pole, whose location is the location of the reference source and who points to the location of the fitted source.

As Fig. 7.8 and Table 7.1 show, with 8.6mm for the localization and 19 degrees for the orientation, the largest mean errors appear for the class of neocortical sources with mainly tangential orientation component. The tangential sources

ref. sour.	(Abs.) Localization error (in mm)				(Abs.) Orientation error θ (in degrees)				(Rel.) Strength error AMP (in percent)			
	μ	Σ	Max	Min	μ	Σ	Max	Min	μ	Σ	Max	Min
tang	2.5	1.3	5.8	0.6	11	6.4	26	1.3	15	12	43	0.1
rad	2.1	1.1	6.3	0.4	7	5.8	25	0.8	18	16	63	0.2
deep	3.3	1.5	6.2	0.9	11	6.0	24	1.9	21	22	116	0.2

Table 7.2: *Influence of WM anisotropy on single dipole fit for the class of tangentially and radially oriented neocortical sources and the class of deep sources.*

have in particular localization errors in depth, which was already observed in spherical models by Peters and de Munck [180]. They are localized too deep in the temporal lobe (Fig. 7.8, top left) and too superficial in particular in parietal and occipital areas (Fig. 7.8, top right). A correlation seems to exist between the thickness of the skull layer and the depth mislocalization of tangentially oriented sources: tangential sources are localized too deep in temporal areas, where the skull layer is quite thin and too superficial in parietal and occipital areas, where it is quite thick.

In Dümpelmann et al. [55] we showed that reconstruction errors, resulting from inaccuracies in the conductivity ratio assumptions for a BEM forward model, can be alleviated by better optimizing the electrode configuration with regard to the examined source. As it can be observed in Fig. 7.8 (top right), the localization errors are especially large in frontal cortical areas. For such regions, the fixed electrode configuration may be less appropriate for sampling the dipolar pattern with sufficient accuracy, as Fig. 4.8 (top right) indicates. Note that because of eyes and nose it may be difficult in practice to improve the situation in frontal areas.

While localization and orientation errors seem to be nearly a factor two smaller, with a mean of 56 percent, the amplitude error is conspicuously large for the class of radially oriented reference sources (Table 7.1 and Fig. 7.8, bottom row).

An anisotropy ratio of 1:10 was chosen for the above study following the measurements of Rush and Driscoll [197]. This ratio was also taken in other skull anisotropy studies [49; 52; 228; 152]. Nevertheless, if Akhtari et al's [3] recently measured values for thicknesses and conductivities of the three skull layers and the formulas (3.3) and (3.4) for the simplified 3x3 model of the skull are considered, an anisotropy ratio of only about 1:3 results, which would reduce the reconstruction errors, as reported by Fuchs et al. [71].
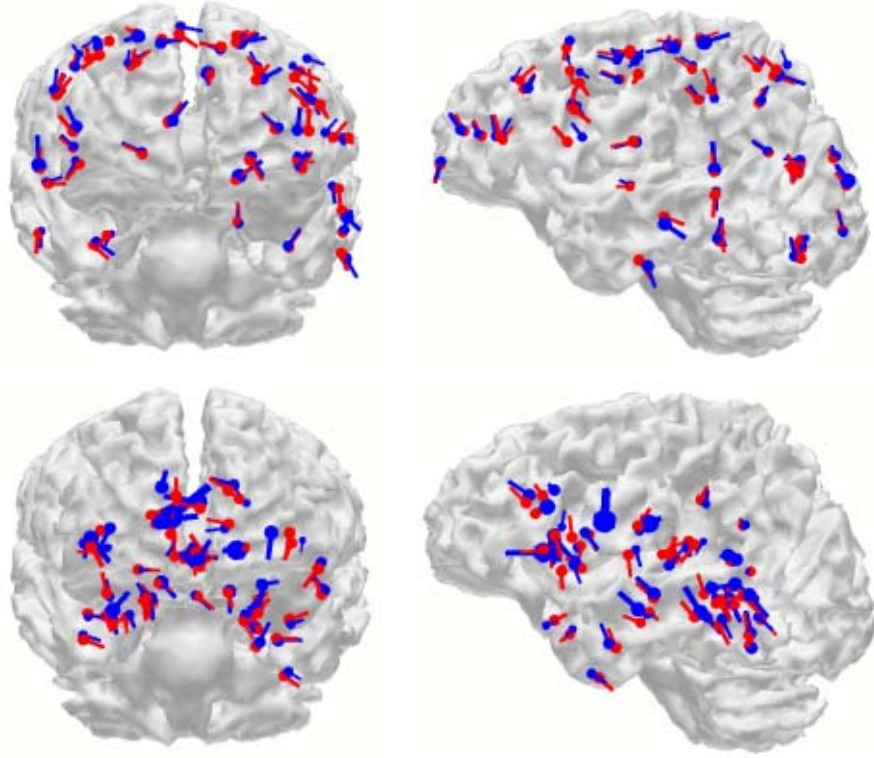
Figure 7.9: *EEG reconstruction errors due to 1:10 anisotropy of the WM compartment (1nAm source strength scaled as 1mm, figure scale 1:4): The red poles are the reference dipoles, 46 mainly tangentially oriented (top) and 46 deep ones (bottom). The blue poles are the reconstructed dipoles. Dipoles are presented on underlying transparent WM surface.*

WM anisotropy

Each dipole was then reconstructed in the isotropic model by means of its EEG result in the model with anisotropic WM compartment. A ratio of 1:10 was assumed, which is the upper bound found in measurements [165; 77]. In Fig. 7.9, the reference and reconstructed sources are shown for the class of mainly tangentially oriented neocortical sources (top row) and for the class of deep sources (bottom row). Since the localization errors are in general smaller than for skull anisotropy, the pairs of reference and fitted source can well be identified without indicating them by means of black poles as in Fig. 7.8. The reconstruction errors are presented in Table 7.2. With 3.3mm for localization, 11 degrees for orien-

tation and 21 percent for source strength, the largest mean reconstruction errors were observed for the class of deep sources. Maximal errors for that class were 6.2mm/24°/116%.

As discussed in Section 7.2, especially in 7.2.3, the influence of WM anisotropy increases, the more the source is surrounded by WM fibre structures. In the study of Haueisen et al. [106] and in 7.2.3, large amplitude changes were observed for deep sources when including realistic WM anisotropy in the forward simulation. It was expected that those amplitude changes translate with approximately the same percentage value into source strength changes. This is now confirmed with the large maximal strength error of 116 percent for the class of deeper sources.

Note that all reference sources (also the deep ones) were placed in the GM compartment, which was modeled with an isotropic conductivity value throughout this thesis. In reality, also brain GM is equipped with an anisotropy. A ratio of 1:2 was measured in cat cerebellar cortex [266], while the ratio measured in the cortex of a frog was even much higher [164]. If we then take into account that local conductivity variations around the source strongly influence the forward computations as observed in 7.2.3, larger errors than presented here have to be expected if the GM anisotropy is modeled additionally.

7.3.2 Localization of early syntactic processes: An EEG/MEG simulation study

Language processing is a very complex cognitive task. On the way to a deeper understanding how it is performed, the reconstruction of the involved brain regions as well as their dynamical interaction is an important step. Since a long time, the cortical representation of language is examined through patients with circumscribed brain lesions (Broca [28], 1861, Wernicke [251], 1874, and see, e.g.,[54; 65; 67]). In the past century, this knowledge has been strongly enlarged through the use of electrophysiological methods such as EEG ERP's (see, e.g., [163; 66; 65; 67]) and by means of brain imaging techniques such as PET (see, e.g., [218]), fMRI (see, e.g., [160]), EEG source reconstruction (see, e.g., [125]) and MEG source reconstruction (see, e.g., [124; 68]).

Friederici et al. [66; 65; 67] identified three ERP components, which correlate with language comprehension processes. Their studies are based on comparisons between correct and either syntactically incorrect or semantically incorrect sentences: An Early Left Anterior Negativity component (ELAN), reaching its peak mostly between 130 and 200ms after stimulus, was observed and interpreted as a phase where the input is parsed into an initial syntactic structure. In a second phase, a centroparietal negativity component, the so-called N400 ("N" stands for Negativity and "400" for an average peak latency of 400ms after stimulus), was seen in correlation with processes of lexical-semantic access and integration. A

late centroparietal positivity (P600) was observed in correlation with secondary syntactic processes of reanalysis and repair in a third phase.

Up to now, it is not clear which generators in the brain support the ELAN processes. While PET and fMRI succeeded in identifying a number of brain structures that seem to contribute to the processing of syntactic structures, their dynamic interaction remains unclear due to the low temporal resolution of the methods. ERP studies have revealed a great deal of the temporal dimension of syntax processing, but EEG source localization was not able to provide more than very coarse information on the reconstruction of the underlying sources. MEG has the same temporal resolution as EEG combined with a better spatial resolution for mainly tangentially oriented primary currents in source reconstruction (as seen later in this section). Friederici et al. [65; 67] suggested that frontal cortical structures support early parsing processes, while specific subcortical regions of the basal ganglia may not be crucial for the ELAN. This resulted from lesion studies where patients with left frontal cortical lesions demonstrated a selective absence of the ELAN, whereas the component was present in patients with subcortical lesions involving the basal ganglia. On the other hand, in an fMRI study, Meyer et al. [160] also found an increase in activation as a function of syntactic correctness in the mid-portion of the superior temporal gyrus. Note that due to low temporal resolution, the study may have reflected an additive effect of the early and the late syntactic processes. Dronkers et al. [54] reported that patients with a temporal lesion including the anterior part of the superior temporal gyrus displayed a syntactic comprehension deficit. In a 148 channel whole-head MEG study using instantaneous Tikhonov-Phillips current density reconstruction on the cortical surface in a realistically shaped one compartment BE model, Knösche et al. [124] revealed a significant difference between correct and syntactically incorrect sentences for the early phase in frontal and temporal areas in both hemispheres. Since the current density approach did not allow precise spatial conclusion, Friederici et al. [68] carried out a second MEG study, using a dipole fit approach with seedpoints from the fMRI results of Meyer et al. [160]. The dipoles, fitted within a time interval of 20ms around the ELAN peak of the syntactically incorrect condition, were allowed to move within a sphere region centered at the respective seedpoint with a radius of 1cm. The study provided a clear indication that both temporal as well as fronto-lateral cortical regions in both hemispheres support early syntactic processing with a dominance in the left hemisphere. The contribution of the left temporal region seemed to be larger than the contribution of the left fronto-lateral region.

Our interest will now be focused on the influence of volume conduction effects on the reconstruction of the ELAN sources. Therefore, a cortical influence space surface was generated by means of a dilation of the white matter mask
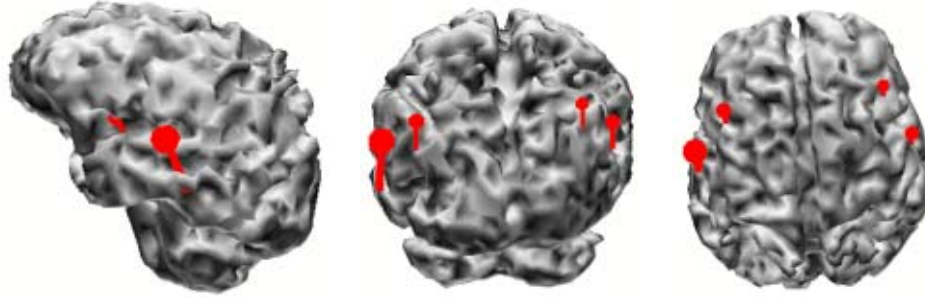
Figure 7.10: *The four reference dipoles supposed to underlie the ELAN component (1nAm source strength scaled as 1mm, figure scale 1:4).*

from Section 2.6.2 by 1mm, while taking care that the dilated mask was topologically equivalent to a sphere, i.e., had no cavities or handles (Euler number 1, see Def. 2.2.6). In a subsequent step, the surface of the resulting mask was triangulated. Therefore, the tetrahedrization algorithm from Section 4.7.3 with $d_{\min}^{\mathrm{comp}} = 5$mm was used and the resulting surface queue Q_s was exploited, yielding a triangulation with 6742 regularly shaped triangles and a number of $n_{\mathrm{inf}} = 3373$ vertices. For triangulation, the software package CURRY was used. The triangles were controlled to be similarly orientated so that their normal vectors pointed in one direction, i.e., either outside or inside the surface [121]. The solid angle of a closed surface with regard to the origin is 0, 2π or 4π for the origin lying outside, on or inside the surface, resp. [229]. In our case, the origin is lying outside the influence space mesh and the solid angle was computed to be $0.5 \cdot 10^{-5}$ (necessary condition for closed surface fulfilled). The mesh with 5mm resolution is considered to only be a rough representation of the neocortical surface, neglecting deeper GM structures such as the basal ganglia. It is not supposed to represent all important neocortical curvatures and as a consequence, the normal-constraint was not applied, i.e., sources in all cartesian directions were allowed for each mesh vertex during source reconstruction ($r = 3n_{\mathrm{inf}}$, see Section 6.2). Two lead field matrices for the isotropic tetrahedra model 1 (Tables 4.1 and 4.2) with a relative solver accuracy of 10^{-10} (10^{-7}), in the following referred to as the *isotropic lead field matrix with high (low) accuracy*, were then computed for combined 71 electrode EEG and 148 channel MEG (Section 4.8.3).

Four ELAN reference dipoles as presented in Fig. 7.10 were simulated on vertices of the influence space mesh, a source with 33nAm strength in the vicinity of the left auditory cortex, a left fronto-lateral source with 20nAm strength and their right hemisphere homologue dipoles with 18nAm and 16nAm, resp..

In a first study, forward computations for the left temporal ELAN source were
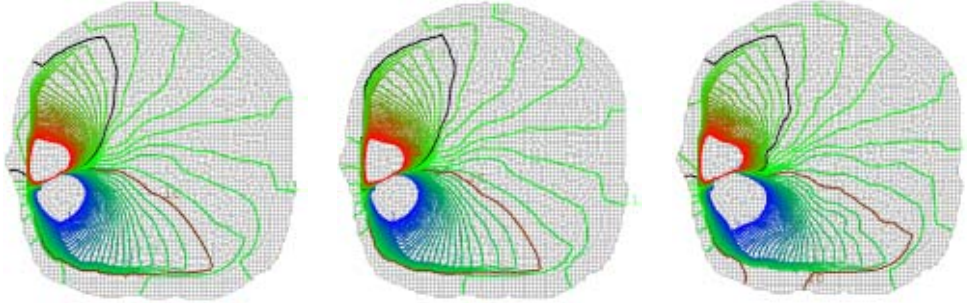
Figure 7.11: *Isopotential distribution for the left temporal ELAN source from -0.5 to 0.5 μV on a coronal slice through the location of the source for the isotropic nodeshifted cube model 2 (left) and the corresponding models with 1:10 anisotropy of skull (middle) and WM (right) compartment (both volume constraint).*

carried out in the nodeshifted cube model 2 (Table 4.1). Fig. 7.11 shows the resultant isopotential distributions on a coronal slice through the location of the source for the isotropic case (left) and for the corresponding cases with 1:10 anisotropy of skull (middle) and WM (right) compartment (both volume constraint). Skull anisotropy leads to a shift of the ELAN ERP component from lateral in medial direction on the head surface. This can be seen when following the black marked iso-line with a potential of $-0.075 \mu V$, which is the strongest negative isopotential line in the presented figure which reaches the model surface in the isotropic case (left). In the anisotropic case, the same isopotential is not able to break through the skull layer, the strongest is the line with a potential of $-0.06 \mu V$, which reaches the surface more medially (middle). The brown marked iso-line with a potential of $0.06 \mu V$ shows the effect of WM anisotropy. An interpretation may be that in the anisotropic WM case (right), this isopotential line is forced to stronger follow a direction perpendicular to the fibre bundles of the corticospinal tract because of an increased volume current flow along the fibres, so that it enters the skull compartment at a different location and, in contrast to the isotropic case, is then able to break through the skull.

A next study consisted of reconstructing the ELAN dipoles using an inverse method for focal sources. Therefore, the SA Alg. 14 in discrete parameter space (Section 6.4.2) was used. With a choice of $t_{step} = 0.99$, $TOL =$1E-08 and $MAX =$1E07 for all of the following SA optimization runs, a very slow annealing was simulated so that a high probability for SA convergence to the global minimum was given [112]. In a first validation step, the four reference dipoles

were reconstructed by means of their simulated isotropic EEG and MEG data with high solver accuracy. A number of $p = 4$ sources was used in combination with the functional H, determined by means of the COF, i.e., assuming noise-free data (Section 6.4.3 and Appendix C.2). When using the isotropic lead field matrix with high accuracy, all four reference sources were reconstructed without any reconstruction error for both simulated datasets. When using the isotropic lead field matrix with low accuracy and the simulated highly accurate EEG data, only three of four sources were correctly found, the reconstructed dipole in the right temporal area already had a localization error of 3mm to the corresponding reference source, while again no reconstruction error was observed when using the MEG data. This shows the high sensitivity of EEG multiple dipole reconstruction towards model inaccuracies. The isolating skull layer is reducing the surface electrode potentials by several orders of magnitude compared to the potentials close to the source so that high solver accuracy is needed for accurate source reconstruction. Therefore, the isotropic lead field matrix with high accuracy was used in the following.

EEG and MEG reference data were then simulated in the 6 tissue tetrahedra volume conductor model 3 (Table 4.1). For the two skull layers OSC and RS and for skin, CSF and GM compartments, the isotropic conductivity values from Table 4.2 were used. The EMA was applied for the conductivities of the WM elements (Section 3.4.4), yielding an anisotropic and inhomogeneous WM compartment. For the inverse dipole fit, the isotropic lead field matrix and the methods SA-COF and SA-TSVD were used. For the computation of the SVD within the TSVD, we use subroutine DGESVD from the software package LAPACK [132]. In the MEG case, with $p = 8$, the number of sources was overestimated while the correct number of $p = 4$ sources was chosen for the EEG. The regularization parameter for the TSVD in Alg. 15 was set to $R = 1.0$ and the entries of the diagonal weighting matrix D were determined by means of $\varepsilon_i = \text{ABS}(\underline{u}_{iso}^{[i]} - \underline{u}_{sim}^{[i]})$, i.e., the absolute value of the difference between reference, $\underline{u}_{iso}$, and simulated, $\underline{u}_{sim}$, data. If we define the Signal-to-Noise Ratio

$$SNR := \frac{1}{m} \sum_{i=1}^{m} \left| \frac{u_{sim}^{[i]}}{\varepsilon_i} \right|, \tag{7.1}$$

$SNR = 101.2$ was achieved for the simulated MEG data ($m = 148$), whereas only $SNR = 11.7$ was found for the EEG ($m = 71$).

As Fig. 7.12 (top row) shows, both inverse dipole fit methods SA-TSVD (blue) and SA-COF (green) were able to reconstruct the 4 ELAN reference sources for the MEG case with only a neglegible error, even when overestimating the number of sources with the choice of $p = 8$. In contrast to the SA-COF, the regularization approach SA-TSVD avoids, that the remaining defect to the data is
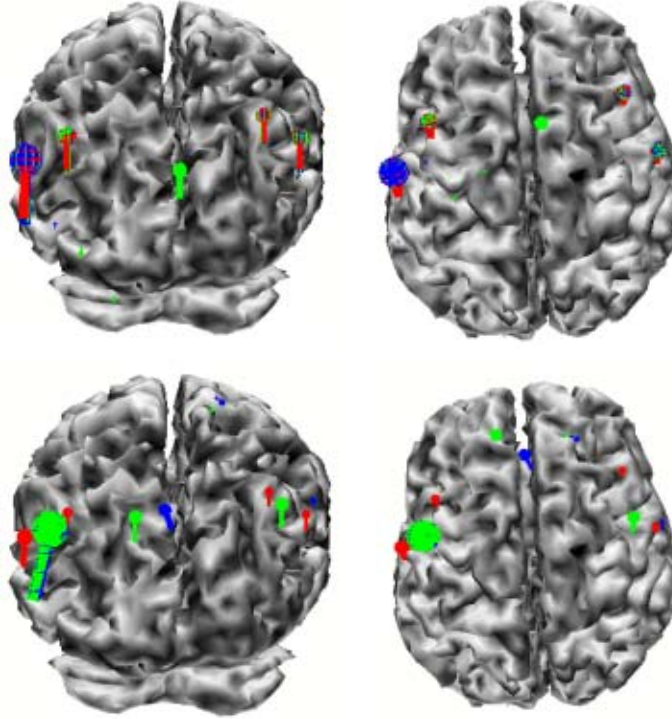
Figure 7.12: *Influence of volume conduction effects of model 3 with two-layer skull and EMA WM compartment on the reconstruction of the ELAN sources (red) using SA-COF (green) and SA-TSVD (blue): MEG, overestimated number of 8 dipoles (top row, 1nAm source strength scaled as 1mm, figure scale 1:4) and EEG, 4 dipoles (bottom row, 2nAm source strength scaled as 1mm, figure scale 1:4).*

explained by a strong dipole, which has only small influence on the flux distribution. Remember that deep dipoles are mainly radial and that, in a multilayer sphere model, radial dipoles do not produce any magnetic field. For the (correct) choice $p = 4$, the MEG reconstruction error was also close to zero.

The reference ELAN sources could not be correctly reconstructed when using the EEG data and optimizing without any further constraints to the sources, as shown in Fig. 7.12 (bottom row). If we assume that the large fitted source in the left temporal lobe (for both SA-COF and SA-TSVD) corresponds to the left temporal ELAN source, its reconstruction error amounts to 12mm/28°/132%. The reconstruction errors for the right temporal ELAN source are 11.6mm/11.5°/56% for SA-COF and 4.2mm/42°/48% for SA-TSVD. The two fronto-lateral ELAN
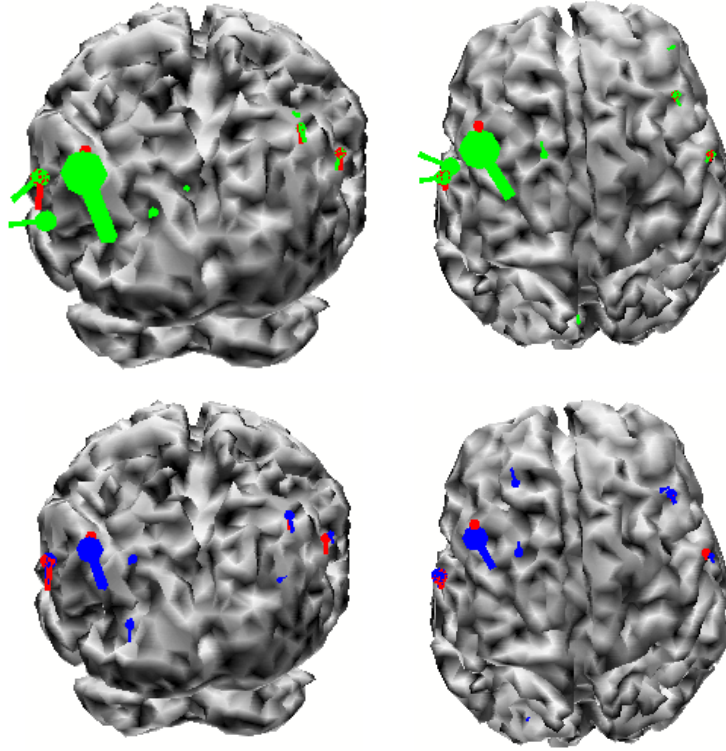
Figure 7.13: *Influence of 1:10 WM anisotropy on the MEG reconstruction of the ELAN sources (red) when overestimating the number of dipoles ($p = 8$): Reconstruction result of SA-COF (green, top row) and SA-TSVD (blue, bottom row) (2nAm source strength scaled as 1mm, figure scale 1:4).*

sources were replaced by a surface-near and a deep fronto-medial source.

As a last study to the reconstruction of the ELAN sources with focal inverse methods, MEG data were simulated in the 5 tissue model 1 with 1:10 anisotropy of the WM compartment (Table 4.4), yielding a signal-to-noise ratio of $SNR = 12.9$. The sensitivity of the inverse fit using SA-COF and SA-TSVD when overestimating the number of sources with a choice of $p = 8$ was examined. Fig. 7.13 shows the result for the SA-COF (top row) and for the regularization approach SA-TSVD (bottom row). Even for 1:10 WM anisotropy and the strong overestimation of the number of sources, both methods are able to localize quite exactly the ELAN reference dipoles without any further constraint to the sources during optimization. The reconstruction errors are summarized in Table 7.3. Note that the tangentially oriented superficial ELAN sources are especially well suited

ref.	SA-COF			SA-TSVD		
sour.	Loc.Err.	θ	AMP	Loc.Err.	θ	AMP
left temp.	0mm	50°	3%	0mm	5°	0%
left front.	13mm	24°	333%	8mm	23°	169%
right temp.	0mm	14°	3%	3mm	11°	37%
right front.	0mm	20°	9%	0mm	11°	28%

Table 7.3: *Influence of 1:10 WM anisotropy on the MEG reconstruction when overestimating the number of dipoles ($p = 8$): Localization, orientation and strength errors for the four ELAN reference sources when using SA-COF and SA-TSVD.*

for MEG reconstruction. Much larger errors have to be expected for dipoles with stronger radial source components. Furthermore, as discussed at the end of Section 7.3.1, the modeling of realistic 1:2 GM anisotropy is expected to increase reconstruction errors significantly.

The SA-COF was found to produce larger errors in orientations and strengths for the four ELAN dipoles and also assigned larger strengths to the additionally fitted sources than the SA-TSVD (see Fig. 7.13 and Table 7.3). This is because radial source components were not filtered out as done by the regularized dipole fit. As described in Wolters et al. [260; 259], the SA-TSVD shows better separational abilities to disentangle real and ghost sources. Sources (or better: source components) which have a measurable effect on the data are reconstructed and do not sink into insignificance beside stronger sources which only explain noise such as radial (MEG, see Fig. 7.13, top row) or deep dipoles (EEG and MEG, see Fig. 7.12, top row) or sources which nearly cancel each other (EEG and MEG). For the latter two classes, a further series of EEG reconstructions in a simulated sulcus structure was presented in Wolters et al. [259], showing the superiority of the regularized over the non-regularized fit. In all of these examinations, SA-TSVD was shown to be more stable regarding an overestimation of the number of active dipoles. In combination with the SVD of the spatio-temporal measurement data, giving an estimate for the minimal number, the exact number of dipoles can thus better be enclosed. As a final note, the regularized focal reconstruction method is used as a more stable method for the inverse reconstruction of rotor unbalance sources in an aircraft engine, as described by Rienäcker et al. [192].

Current density reconstruction

The reconstruction properties of inverse instantaneous current density methods from Section 6.5 are now examined for the four focal ELAN reference dipoles from Fig. 7.10. Knowing that we are confronted with superficial reference sources,
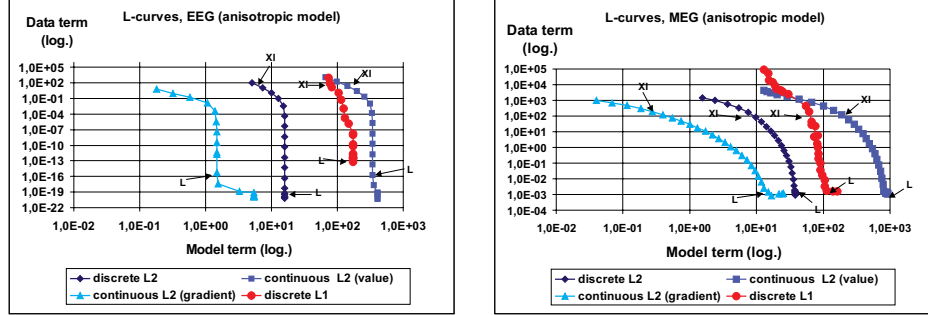
Figure 7.14: *L-curves for various instantaneous current density reconstruction methods for model 1 with 1:10 anisotropy of skull and WM compartments, EEG (left) and MEG (right).*

the depth weighting operator W (Section 6.5.4) was chosen as the identity operator, i.e., the reconstructed current distribution gives preference to superficial sources. For the simulations using anisotropic data, the channel weighting matrix D was computed as described in the last subsection.

The regularization parameters for the various current density methods first have to be determined. Therefore, L-curves were computed for the isotropic 5 tissue tetrahedra model 1 and the corresponding model with 1:10 anisotropic skull and WM compartments, following the description of Section 6.5.5. The simulated anisotropic data were equipped with a signal-to-noise ratio (see Equation 7.1) of $SNR = 36.2$ for EEG and $SNR = 12.9$ for MEG. The resulting graphs, i.e., the model term versus the data term, is shown in log-log-scale in Fig. 7.14 for EEG data (left) and for MEG data (right), both for the anisotropic case. The corresponding choices of parameter λ for the L-curve-criterion is marked with an "L" and for the χ^2 criterion with a "Xi". As the figure shows, some curves do not have the characteristic L-shaped appearance. The flat part of the L-curve is missing for example for the discrete L_2 norm method for both EEG and MEG, i.e., in this case, perturbation errors do not become dominant for decreasing λ values. A reason could be that high frequency noise in the simulated data is missing, since the modeled noise consists only of the absolute value of the difference between isotropic and anisotropic forward simulations. Therefore, the solution does not get spoiled with high frequency source components.

We begin with the current density reconstruction using simulated EEG data and the L_1 norm method from Section 6.5.3. The method is well known to be favorable for the reconstruction of focal sources when compared to L_2 norm model term formulations [242; 191; 72]. By means of using the non-linear Polak-
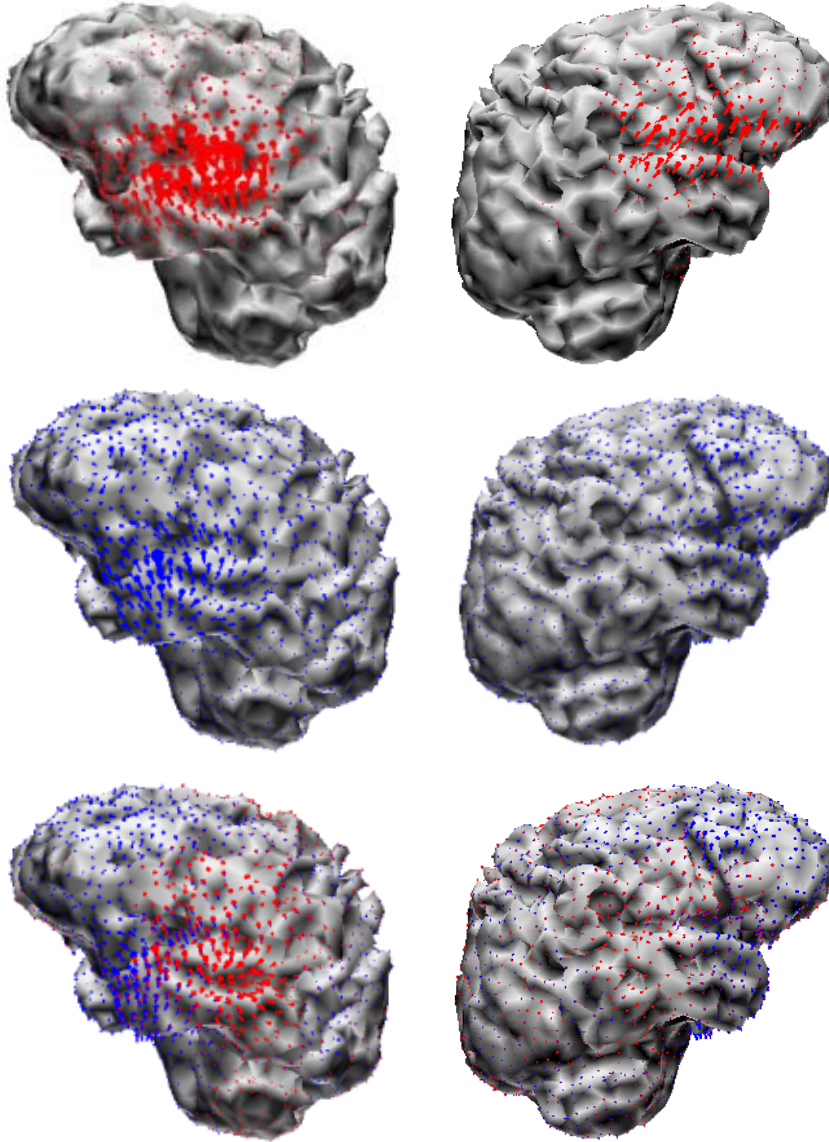
Figure 7.15: *Influence of volume conduction effects of model 1 on the EEG based current density reconstruction of the ELAN sources, using the L-curve-criterion for the regularization parameter (50pAm source strength scaled as 1mm, figure scale 1:4): discrete L1 norm (top and middle row) and continuous gradient L2 norm (bottom row), results in the isotropic model (red), results in the model with 1:10 anisotropy of skull and WM compartments (blue).*

Ribiere CG method for the minimizing of the functional with L_2 norm model term and comparing the result with the one of the linear Jacobi-CG solver from Section 6.5.1, a necessary (not sufficient) validation for the numerical solver was carried out. Fig. 7.15 shows the result for the isotropic EEG data (top row) and for the anisotropic EEG data (middle row). The L-curve criterion was used for the determination of the regularization parameter. 1mm pole length corresponds to a current amplitude of 50pAm. As the isotropic result shows (top row), even the focusing L_1 norm is not able to distinguish between the temporal and the fronto-lateral center of activity. Instead of two centers, the activity is smeared out over the whole cortical area between both ELAN sources. The reconstructed activity on the left hemisphere dominates over the right hemisphere. This is the error which is introduced through the choice of the source model (focal reference sources reconstructed by means of a current density method). The error is much more distinct for the anisotropic data (middle row), where, additionally, the center of activity was strongly shifted in anterior direction along the Sylvian fissure so that the sources would no longer be expected in the vicinity of the auditory cortex. The results for the continuous gradient L_2 norm in the bottom row of Fig. 7.15 show comparable properties only that the current density distribution is even more spread out. Similar results were achieved when using the discrete or the continuous L_2 norm (not shown here). The sensitivity of two instantaneous current density reconstruction methods towards skull anisotropy was already studied for EEG by Marin et al. [152]. They used the linear Tikhonov-Phillips L_2 norm approach and an S-MAP regularization [11], i.e., a non-linear method which produces more focalized results like the presented L_1 norm approach. In agreement with the above results, Marin et al. [152] reported that 1:10 skull anisotropy totally annihilated any localization ability for the Tikhonov-Phillips approach and that the restoration of very close active regions was profoundly disabled for both the linear and the non-linear regularization method because of too strongly blurred solutions.

Current density reconstructions were then carried out using the simulated MEG data. Fig. 7.16 shows the result of the discrete L_1 norm (top row, visualized as poles) and the discrete L_2 norm (bottom row, visualized as spheres in order to focus on strength differences). 200pAm current strength corresponds to 1mm for the left and to 2mm for the right hemisphere. The results using isotropic MEG data are shown in red, the results for 1:10 anisotropic MEG data (skull and WM compartment) using the L-curve-criterion in blue. Examplarily, the χ^2-criterion was used for the L_1 norm reconstruction (top row, in green). The solution of the L_1 norm for isotropic MEG data (and thus the error introduced through the choice of the source model) shows three centers of activity. Surprisingly, the left (which is stronger than the right) fronto-lateral ELAN source could not be re-
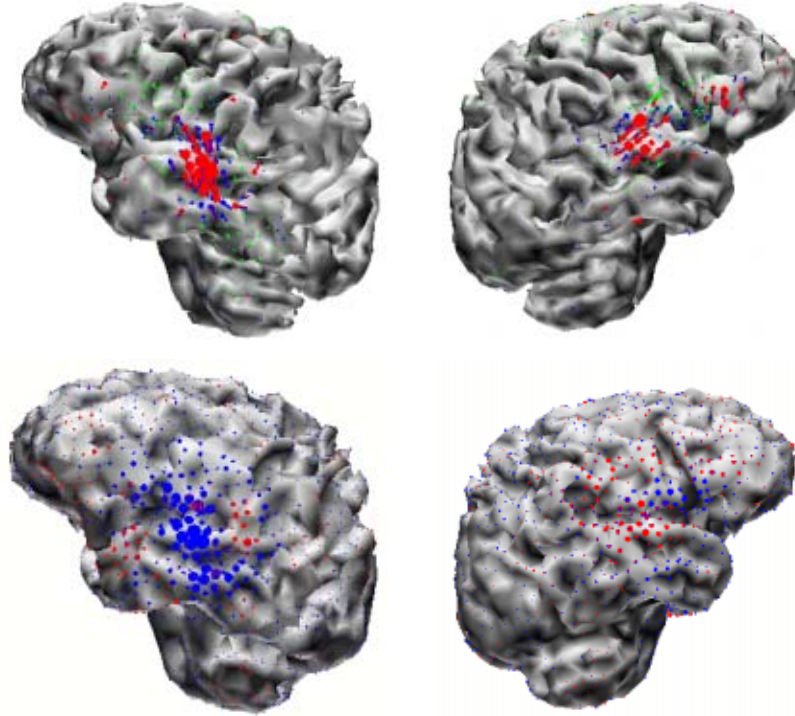
Figure 7.16: *Influence of volume conduction effects of model 1 on the MEG based current density reconstruction of the ELAN sources, isotropic model (red), 1:10 anisotropic model using the L-curve- (blue) and the χ^2-criterion (green) (200pAm corresponds to 1mm for the left and to 2mm for the right hemisphere, figure scale 1:4): L1 discrete, results presented as poles (top row), L2 discrete, results presented as spheres (bottom row).*

constructed, but both temporal and the right fronto-lateral center. The temporal activities are much better focused around the reference sources than in the EEG case. The result of the L_1 norm reconstruction (L-curve-criterion) by means of the anisotropic MEG data is only a little more smeared out, but the three activity centers are still distinguishable. This is no longer the case when using the χ^2-criterion, where the activity between the fronto-lateral and the temporal reference centers is strongly smeared out on both hemispheres. Since this property of the χ^2-criterion was also observed for L_2 norm methods for both EEG and MEG (not shown) and, furthermore, was reported from another study by Rienäcker et al. [191], it can be concluded that the criterion "over-regularizes" and should not be used. As Fig. 7.16 (bottom row) shows, the reconstructed current distribu-

tion between the fronto-lateral and the temporal reference centers are also much more smeared out on both hemispheres when using the discrete L_2 norm for both isotropic and anisotropic MEG data. The reconstructed activity on the left hemisphere is stronger for the anisotropic data than for the isotropic data, whereas the inverse is true for the right hemisphere.

7.4   Summary and Conclusions

The influence of realistic conductivity anisotropy of the human skull and the human brain WM compartments on forward and inverse problem in EEG and MEG was studied in this chapter using high resolution FE head models.

Concerning the influence on the forward problem, the presented results are mainly in agreement with the literature (for skull anisotropy, see [273; 228; 152], for WM anisotropy only one study exists, see [106]).

It can be concluded for the EEG forward problem that the influence of 1:10 anisotropy of both skull and WM compartments depends on location and orientation of the source. For a tangentially oriented superficial source, the modeling of skull anisotropy was found to have a non-negligible influence, whereas the effect of WM anisotropy was less distinct. For a radially oriented superficial source, the relative influence of WM anisotropy to skull anisotropy increased. The more the source is surrounded by WM structure and the more the source orientation is parallel to the WM fibre orientation, the larger the influence of WM anisotropy seems to be. The relative influence of WM to skull anisotropy was much increased for a deep thalamic source.

For the MEG forward problem, skull anisotropy or thickness variations only have a negligible effect, whereas the accurate modeling of the inner skull surface is important. This was also reported in [96; 97]. The influence of 1:10 anisotropy of the WM compartment depends on location and orientation of the source. For a tangentially oriented superficial source, the influence was also negligible. Since WM anisotropy influences the secondary (return) currents and the ratio of the secondary to the whole magnetic flux increases with increasing ratio of the radial dipole orientation component (see, e.g., [105]), the effect was distinct for a radially oriented superficial source. Since the radial dipole orientation component increases with source depth, WM anisotropy modeling gets more and more important, the deeper the source is.

It was found that local conductivity (anisotropy) changes around the source have a strong influence on EEG and MEG forward problem. This is in agreement with a study of local (isotropic) conductivity changes [104]. The sources are embedded in brain GM structure, modeled here with an isotropic conductivity. In reality, brain GM is equipped with an anisotropy of 1:2 (tangentially:perpendicular

to the cortical surface), which could therefore be expected to be important.

The influence of various inverse reconstruction methods on skull and WM anisotropy was then examined. The influence on WM anisotropy for both EEG and MEG was not yet studied.

In a first examination, the sensitivity of an EEG single dipole fit method, widely used in many application areas [81; 195; 110; 237; 111; 48], was profoundly studied for three classes of sources (superficial tangentially and radially oriented and deep sources). Each class consisted of more than 40 reference dipoles, placed in the GM compartment and spread over the whole domain of interest. For the class of deep sources, 1:10 WM anisotropy led to maximal errors of 6.2mm/24°/116% (localization, orientation, strength). Because of the strong effect of local conductivity changes, larger errors have to be expected if GM anisotropy is additionally taken into account. Errors for 1:10 anisotropy of the skull are significantly larger. With 18mm/55°/201% maximal errors, the tangentially oriented superficial sources were found to be most affected. This is in agreement with a study in a spherical model by Peters and de Munck [180]. They were localized too deep in temporal areas, where the skull layer is quite thin and too superficial in parietal and occipital areas, where it is quite thick. An approximation of skull anisotropy effects by means of an increase or a decrease of the scalar isotropic skull conductivity value in BE head models thus seems to be impossible.

The last study was concerned with the restoration sensitivity for more complicated source models. The ELAN sources [68] were chosen as an example. It was shown for the EEG that neglecting both the partitioning of the skull (into outer skull compacta and the remaining layer) and the EMA-WM anisotropy annihilated the restoration ability of the dipole fit methods SA-TSVD and SA-COF. For the MEG, since the ELAN sources were modeled superficial and tangentially oriented [68], the dipole fit reconstruction was still sufficiently accurate when neglecting a 1:10 WM anisotropy (stronger than EMA-WM anisotropy). For SA-TSVD, the latter is even true if the number of sources is overestimated. In this case, the result of the non-regularized dipole fit approach SA-COF was spoiled by either strong radial dipole components or strong components with deep dipoles. This shows the superiority of the regularized dipole fit method. The sensitivity of instantaneous current density methods was then examined. For EEG, it was found that the L_2 and even the focalizing L_1 norm methods are no longer able to distinguish between the fronto-lateral and the temporal ELAN source. Even without any error in the head model, the activity is smeared out between both centers on both hemispheres. This is the error which is introduced through the choice of the source model (focal reference sources reconstructed by means of a current density method). MEG in combination with the L_1 norm approach is already able

to reconstruct both temporal and the right fronto-lateral ELAN source. Neverthe-less, when using the discrete L_2 norm approach, the activity is again smeared out between both centers on both hemispheres. For EEG, 1:10 anisotropy annihilated the restoration ability of L_1 norm model terms and L_2 norm methods, the latter being in agreement with the results of Marin et al. [152]. The centers of activity were strongly shifted along the Sylvian fissure in anterior direction. For MEG, the additional errors through 1:10 anisotropy were negligible.

The new results of this chapter are summarized in Wolters et al. [258; 257] and Anwander et al. [9].

Chapter 8

Conclusions and Perspective

Die von mir nicht selten beobachtete Tatsache, daß sich das E.E.G. in manchen Fällen nur vom Bereich einer Schädellücke ableiten ließ und dann, wenn die Nadeln unmittelbar daneben auf dem unversehrten Knochen lagen, keine Kurve zu erzielen war, sprach meiner Ansicht nach eindeutig für die Entstehung des menschlichen E.E.G. im Großhirn.

Hans Berger

8.1 Summary and Conclusions

This thesis deals with EEG/MEG source reconstruction in realistically shaped high resolution anisotropic Finite Element (FE) models of the human head. It covers four major topics: the first is concerned with methods to generate a realistically shaped head model with anisotropic conducting compartments skull and brain White Matter (WM) and techniques to incorporate physiological and anatomical constraints to the inverse problem; the second topic deals with algorithms for the fast solution of the EEG/MEG FE forward problem; the third is concerned with an overview of different techniques for solving the inverse problem and with the presentation of new regularization algorithms for the reconstruction of multiple and extensive sources and the fourth is the study of the sensitivity of EEG/MEG source reconstruction towards skull and brain WM conductivity anisotropy.

In Chapter 2, techniques were presented for constructing a multi-compartment head model from a matched set of T1- and PD-MRI. The chapter focused on an improved segmentation of the skull compartment, since larger errors were observed in EEG-based [42; 43; 110; 111] or MEG-based [96; 97] source recon-

197

struction due to misspecifications of skull shape or incorrect modeling of the inner skull surface, resp.. These imprecisions were reported to be detrimental in certain clinical applications [110; 111]. In this thesis, the T1-MRI was used for the segmentation of skin, brain grey matter and WM compartments, whereas the registered PD-MRI was exploited for a correct modeling of the inner skull surface. When comparing the T1/PD-MRI inner skull surface result with the result of the standard technique in EEG/MEG-source reconstruction, which exclusively exploits the T1-MRI and uses a closing and inflation of the segmented brain surface, errors of up to 8.5 mm were found in areas, where the thickness of the cerebro-spinal fluid was underestimated by the conventional method. Furthermore, an improved incorporation of physiological and anatomical constraints to the inverse problem was enabled by means of the presented exact segmentation of the brain grey matter compartment when compared to standard techniques such as region-growing procedures. This is especially due to the segmentation method which takes into account the scanner inhomogeneities. As described in Chapter 3, realistic skull conductivity tensors were obtained by means of the surface normals of a smooth surface spongiosa model, for which the segmentation results of inner and outer skull were exploited. For the WM compartment, whole head DT-MRI measurements were used to determine the WM conductivity tensor eigenvectors, following the proposition of Basser et al. [16]. The skull and WM tensor eigenvalues were either simulated, following direct conductivity measurements (measured anisotropy ratio of 1:10 for the skull [197] and up to 1:10 for WM [165; 77]), or, for brain WM, they were modeled by means of a differential effective medium approach, as reported by Tuch et al. [223; 224].

An overview of the underlying theory for the EEG/MEG FE forward simulations and the definition of the head volume conductor models, used throughout the thesis, was given in Chapter 4. By means of accuracy studies in multilayer sphere models, hexahedra FE meshes exploiting a nodeshifting on compartment surfaces were shown to be more accurate than conventional hexahedra meshes. The presented modern FE solver approach in Chapter 5, being well suited for tissue inhomogeneity and anisotropy, yielded computation times, which should push high resolution realistically shaped anisotropic volume conductor modeling within the EEG/MEG inverse problem into the application fields. When comparing the presented parallel algebraic multigrid preconditioned conjugate gradient technique on 12 processors with the standard in source reconstruction, a single processor Jacobi conjugate gradient method, speed-ups of more than 100 were achieved for high resolution anisotropic FE head models.

An overview of methods for the reconstruction of focal and distributed sources and new algorithmic developments for the inverse problem were presented in Chapter 6. The single dipole fit in continuous parameter space was first intro-

duced to FE modeling. For multiple sources, a new regularized dipole fit algorithm was presented, a simulated annealing algorithm in discrete parameter space in combination with the truncated singular value decomposition for solving the embedded linear least square problem. Its application to the reconstruction of the sources of the Early Left Anterior Negativity component (ELAN) in Chapter 7 and further studies in a simulated sulcus structure in Wolters et al. [259] showed better separational abilities to disentangle real and ghost sources and estimate the unknown number of dipoles. This is due to the filtering properties of the regularized fit method, where source components, which only have a small contribution to the measurements, are suppressed. Concerning the distributed source model, a recently developed linear spatio-temporal regularization approach with additional temporal smoothness term, introduced by Schmitt and Louis [203], was applied to spatio-temporal current density reconstruction and, as a second application area, to the dynamical electrical impedance tomography (dyn-EIT). The spatio-temporal approach was shown to have a stabilizing effect on the reconstruction results. In dyn-EIT, the presented method was compared to a fixed-interval Kalman smoother and was found to be superior with respect to reconstruction accuracy and memory and computational effort.

Finally, in Chapter 7, the sensitivity of EEG/MEG source reconstruction towards skull and WM conductivity anisotropy was studied. As mentioned in the introduction, to the knowledge of the author, no study exists for the sensitivity towards WM anisotropy and the sensitivity towards skull anisotropy was only insufficiently explored. In a first part, the influence on the forward problem was studied. The results were mainly in agreement with the literature. Skull anisotropy was found to have a non-negligible influence on the EEG and nearly no influence on the MEG (see also [227; 151; 228; 152]). It seems that, the more the source is surrounded by WM structure, the more important WM anisotropy modeling becomes for both EEG and MEG (see also [104; 106]). For MEG, this influence was especially strong for sources with mainly a radial orientation component (see also [105]). Local conductivity changes around the source were important for both, EEG and MEG. The sensitivity of an EEG continuous single dipole fit, widely used in various application fields [81; 195; 110; 237; 111; 48], was then studied. With 18 mm maximal error, the localization of tangentially oriented superficial sources was found to be especially sensitive to 1:10 skull anisotropy, in agreement with a study in a spherical model [180]. Since tangential sources were localized too deeply in temporal areas, where the skull layer is quite thin and too superficially in parietal and occipital areas, where it is quite thick, an approximation of skull anisotropy effects by means of a change of the isotropic skull conductivity parameter in boundary element models seems to be impossible. Of course, the sensitivity decreases, if a smaller ratio for skull anisotropy

will be found to be more appropriate. With a maximal localization error of 6.2 mm for a deeper source, the localization procedure was less affected by WM anisotropy. Nevertheless, with a maximal orientation error of 24° and a more than twice underestimated source strength, a misinterpretation of the dipole reconstruction result can not be precluded. With regard to the reconstruction of the four superficial and tangentially oriented sources, which are assumed to underly the ELAN ERP component [68], WM and skull anisotropy was found to have a negligible influence on the MEG reconstruction. In contrast, it annihilated the EEG reconstruction ability. This was found for the presented regularized multi-dipole fit procedure as well as for instantaneous current density reconstructions using discrete L_1 or L_2 norm model terms. For the EEG, anisotropy strongly shifted the center of the ELAN current density reconstruction results along the Sylvian fissure in anterior direction.

8.2   Perspective

In the future, a further effort is needed for the measurement of human head tissue conductivities, especially concerning the skull anisotropy. Animal models have to provide the necessary validation at a better controlled level. This could be done through the implantation of depths electrodes and their EEG/MEG reconstruction with and without tissue anisotropy modeling (see the validation part of the SimBio project, Appendix D, and the preliminary study by Flemming et al. [62]). Since it was shown that skull inhomogeneities have a large effect on EEG and MEG, one of the interesting application fields for high resolution FE head modeling are newborns with open sutures (see Grebe et al. [83; 82]). Because of the strong effect of local conductivity changes, additional errors have to be expected if brain gray matter anisotropy is taken into account, which can amount to ratios of much more than 1 to 2 [164; 266]. This should be figured out in future simulations, as well as the influence of the improved (bimodal) skull modeling on the inverse problem. Concerning fast FE forward computation, a further acceleration will be achieved through a simultaneous treatment of a moderate number of sources (right-hand-sides) (see preliminary results in [90; 8]). The node-oriented EEG lead-field basis of Weinstein et al. [247] (Section 6.3) has to be implemented and validated. This exploitation of the reciprocity theorem will strongly reduce the computational work for the EEG inverse problem. Furthermore, modern solver approaches based on hierarchical matrices [94] could be applied and compared to the presented approach. As a last remark, an investigation of the stabilizing effect of spatio-temporal current density modeling [203; 204] has to be carried out in realistic head models and further modern inverse approaches have to be implemented (see, e.g., [144]).

Appendix A

Basics of Magnetic Resonance Imaging

Nuclear Magnetic Resonance (NMR), the physical basis phenomenon for Magnetic Resonance Imaging (MRI), was discovered in 1946 [23; 188]. Ten years later, first attempts were made to use NMR for medical purposes [171], but it was not until 1974 that interest for clinical applications increased strongly, when it was described how magnetic field gradients could be employed to obtain images from NMR [134]. A short overview of MRI will now be given and the denotations will be defined, which were used in Sections 2.3 and 3.4.4. The reader is referred to [6; 246; 126] for a more detailed description.

A.1   Larmor relationship and macroscopic magnetization

The spin of a single hydrogen nucleus[1] and its magnetic dipole moment, $\vec{\mu}$, cannot be oriented arbitrarily in an external magnetic field $\mathbf{B}_0 = B_0\mathbf{e}_z$ (see [2]). The magnetic moment is subjected to a torque $\vec{\mu} \times \mathbf{B}_0$ that tries to align it with the z-axis [210]. The usual state would be for $\vec{\mu}$ to align itself N to S, where N refers to the north pole of the hydrogen nucleus and S refers to the south pole of the external field (rest or parallel state) [246]. However, it is possible for a nucleus to be oriented N to N (excited or antiparallel state). It then has the property that a slight perturbation causes the particle to flip back to the lower-energy state. Actually, at any instance, there are nuclei in parallel and others in antiparallel state.

---

[1]For simplicity, we will restrict ourselves to hydrogen nuclei, which make up 10% of the body weight [246] and which allow medically meaningful images to be produced. The total angular momentum of a hydrogen nucleus consists only of the spin of the nucleus and does not have an additional orbital angular momentum.

[2]For simplicity, $\mathbf{B}_0$ will be restricted to a static field aligned along the z-axis.
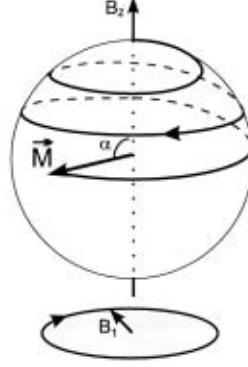
Figure A.1: *Precession of charged particles in a magnetic field from Andrä and Nowak [6].*

The axis of the spinning nucleus does not remain fixed in the magnetic field, but rather precesses or wobbles just as a spinning top does in a gravitational field (see Fig.A.1 [6]). The precessional (Larmor) frequency $\nu = \omega/(2\pi)$ can be found from the Larmor relationship

$$\omega = \gamma B \tag{A.1}$$

where B is the amplitude of the magnetic field and γ the magnetogyric ratio[3]. The energy difference of particles in rest and excited particles is $\Delta E = h\nu$ (h is Planck's constant) and the ratio of the populations of nuclei in parallel state, N_p, to nuclei in antiparallel state, N_{ap}, is $N_p/N_{ap} = \exp^{\Delta E/kT}$ where k is Boltzmann's constant and T the temperature. Therefore, a surplus of nuclear spins aligned parallel to $\mathbf{B}_0$ results[4]. This difference gives rise to a macroscopic magnetization $\mathbf{M}$ of the sample, i.e., a magnetic dipole moment per unit volume.

A.2   Resonance

Resonance occurs when a second magnetic field $\mathbf{B}_1$, a pulse of radio frequency (RF) energy which oscillates at the Larmor frequency, is applied to the system. The particles then absorb energy and the magnetic moment of the nucleus rotates. The flip angle of the rotation, α, (see Fig.A.1) is dependent on the magnitude and duration of $\mathbf{B}_1$ [126]. A pulse with Larmor frequency ν and $\alpha = \pi/2$ is called a 90° pulse.

---

[3]At $B_0 = 3$ Tesla the Larmor frequency for hydrogen nuclei is $\nu = 127.7$ MHz.
[4]At $B_0 = 1$ Tesla, it is $N_p/N_{ap} \approx 1 + 10^{-6}$ [6].

A.3 Field gradients

The effect of a spatially constant gradient field $B_z = zG_z$ during the application of an RF pulse is now discussed. Using (A.1), it is then $\omega(z) = \gamma(B_0 + zG_z)$, i.e., the Larmor frequency varies linearly along the z axis. This means that the protons in slice z^* can only be excited by an RF pulse with frequency $\omega(z^*)$.

A.4 B_0 inhomogeneities

In practice, $\mathbf{B}_0$ is not perfectly homogeneous [5]. The corresponding effects can be reduced by means of a refocusing or $180°$ RF pulse. After a $90°$ pulse, the transverse magnetization diverges due to the inhomogeneities (see Equation A.1), e.g., spins at locations with slightly larger field strength precess faster than the ones with slightly smaller field strength. A $180°$ refocusing pulse, applied a time τ after the $90°$ pulse, then reverses the order of the spins, so that the ones which have lagged behind now move ahead. After another time delay τ, a signal maximum will be achieved, the so-called Hahn-spin echo. The symbol *TE* is commonly used for the time 2τ. A $180°$ refocusing pulse in combination with field gradients is also used for diffusion weighted imaging, introduced in A.9.

A.5 Relaxation

After RF excitation, M_z and $M_\perp$ ($\perp = x, y$) return to the equilibrium value M_0 and 0, resp.. When denoting the relaxation time constants by T_1 for longitudinal (M_z) or spin-lattice relaxation and by T_2 for transverse ($M_\perp$) or spin-spin relaxation[6], this is described by the classical Bloch equations [23]

$$
\begin{aligned}
\frac{dM_z}{dt} &= \gamma(\mathbf{M} \times \mathbf{B}_0)_z - \frac{M_z - M_0}{T_1} \\
\frac{dM_{x,y}}{dt} &= \gamma(\mathbf{M} \times \mathbf{B}_0)_\perp - \frac{M_{x,y}}{T_2}
\end{aligned}
\tag{A.2}
$$

These equations represent phenomenologically the motion of $\mathbf{M}$ in time under the influence of the external field $\mathbf{B}_0$ including relaxation mechanisms. The spin-lattice relaxation is due to thermal coupling to the lattice, whereas the spin-spin

---

[5]It is technically impossible to produce an absolutely homogeneous magnetic field [126].

[6]It is the wide range of relaxation times in biological tissue that makes NMR so interesting for medical diagnostics. At $B_0 = 1.5$ Tesla, T_1 and T_2 relaxation times for brain white matter are 510 ms and 67 ms, for brain gray matter 760 ms and 77 ms and for CSF 2650 ms and 280 ms, resp. [126].

relaxation mainly relies on an exchange of magnetic energy between excited and non-excited particles [246]. For a $90°$ pulse, (A.2) is satisfied by [7] [6]

$$M_z(t) = M_0(1 - e^{\frac{-t}{T_1}}), \quad M_\perp(t) = M_0 e^{i\omega t} e^{\frac{-t}{T_2}}. \tag{A.3}$$

A.6   Magnetic resonance imaging

For simplicity, the restriction is made to a two-dimensional object and the relaxation term in (A.3) is neglected [6]. A $90°$ pulse is applied in order to excite the sample, followed by a spatially constant field Gradient G_y, switched on for the time T_y, and a subsequent Gradient G_x in x direction. The following NMR signal is then recorded [6]:

$$M_\perp(t, G_y) = \frac{1}{\sqrt{2\pi}} \iint \tilde{M}_\perp(x, y) e^{i\gamma(G_y y + B_0)T_y} e^{i\gamma(G_x x + B_0)t} dx dy$$

In the following, in line with [6], B_0 is set to 0. We only consider the phase evolution due to externally applied fields other than the main magnetic field. Repeating the above encoding procedure with various G_y, subsequently measuring the signal $M_\perp(t, G_y)$ and applying a Fourier transformation with respect to G_y yields the final result for 2D-space [6]

$$\tilde{M}_\perp(x, y) = \frac{1}{\sqrt{2\pi}} \int\limits_{-T_x}^{T_x} \int\limits_{-G_y^{max}}^{G_y^{max}} M_\perp(t, G_y) e^{-i\gamma((G_y T_y)y + (G_x t)x)} dG_y dt.$$

A similar relationship can be derived for 3D [126]:

$$\rho(\mathbf{r}) = \frac{1}{\sqrt{2\pi}} \iiint S(\mathbf{k}) e^{-i2\pi(\mathbf{k},\mathbf{r})} d\mathbf{k}. \tag{A.4}$$

In this formula, we use $\mathbf{r}$ instead of (x, y, z) and the function ρ instead of $M_\perp$ in order to underline, that we seek to get an image of the proton density of the tissues, and we denote the measured signal with S and its domain of definition with $\mathbf{k}(G_x * t, G_y * T_y, G_z * T_z)$, the so-called "$\mathbf{k}$-space" (see [126]).

A.7   Pulse sequence

A pulse sequence describes the chronological order of RF and gradient pulses in order to obtain signals from which an image can be reconstructed. Many different pulse sequences exist, each tuned to a specific problem such as the optimization
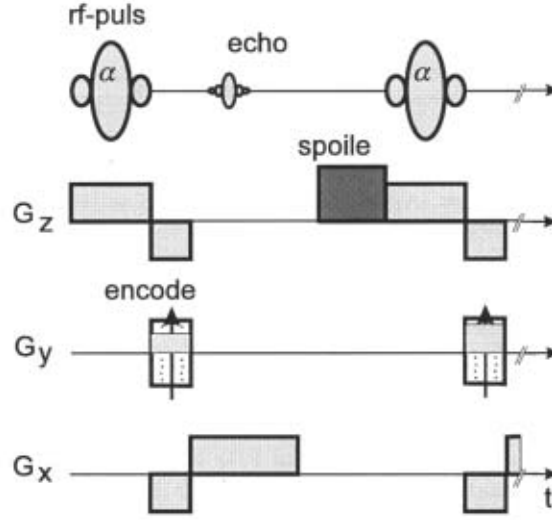
Figure A.2: *Gradient echo pulse sequence from Andrä and Nowak [6].*

of the contrast between certain tissues (see Section 2.3) or diffusion imaging (see A.9).

In the following, a simple gradient echo sequence will be discussed as an example for a pulse sequence (see Fig. A.2) [6]. This sequence is used for the acquisition of the PD-MRI in Section 2.3. The temporally constant (during a certain period of time) field gradient G_z during the application of an RF pulse with flip angle α means, that only protons within a slice of the sample are excited. The slice thickness is proportional to the width of the frequency spectrum of the RF pulse and inversely proportional to the amplitude of G_z. Protons with different z coordinates within the slice will have different phases after the excitation, so that they have to be rephased with a further gradient with inverted amplitude, $-G_z$. On the simplifying assumption that the spins are tipped instantaneously after half the duration of the RF pulse, they will be refocused if the rephasing gradient has half the duration of the slice excitation gradient pulse ([34], p.105). During this time, the phase encoding gradient G_y and a reversed readout gradient, $-G_x$, are also applied. The signal is then recorded under the influence of G_x for twice the duration of the reversed readout gradient. The pulse sequence is then repeated with different phase encoding gradients G_y, followed by the Fourier transformation for image reconstruction. The sequence repetition interval is denoted by *TR*.

The imaging of a slice can take minutes, since after each phase encoding step,

---

[7]$M_\perp = M_x + iM_y$ is a complex quantity.

at least a T_1 period is needed for a recovering before the sample can be re-excited for the next phase encoding step. If *TR* is short with respect to T_1, the effective transverse magnetization is determined by [6]

$$M_\perp(x,y) = M_0(x,y)\frac{(1 - e^{\frac{-TR}{T_1(x,y)}})sin\alpha}{1 - e^{\frac{-TR}{T_1(x,y)}}cos\alpha}.$$

If small flip angles, e.g., $10°$ or $20°$, are chosen in combination with short repetition times, the obtained signal can still be large. The resulting pulse sequence is referred to as FLASH (Fast Low Angle SHot, [86]). FLASH assumes, that the phase memory of $M_\perp$ has been lost at the end of the repetition interval; since this is not true when the repetition interval is faster than the transverse relaxation time, spoiling gradient pulses must be applied at the end of each interval [64; 6], as shown in Fig. A.2.

A.8   Bloch equations including diffusion

If we denote with c the concentration in terms of particles per unit volume, the well-known diffusion equation (Fick's second law) [60] assumes the form

$$\frac{\partial c}{\partial t} = \nabla \cdot (\mathbf{D}^{\text{eff}}\nabla c) \tag{A.5}$$

with $\mathbf{D}^{\text{eff}} \in \mathbb{R}^{3\times3}$ the effective diffusion tensor, defined in Section 3.4.1. The modified Bloch equations including anisotropic diffusion then have the form [216; 215; 126]:

$$\frac{\partial M_\perp}{\partial t} = \gamma(\mathbf{M} \times \mathbf{B}_0)_x - \frac{M_\perp}{T_2} \qquad -\nabla \cdot (\mathbf{v}M_\perp) + \nabla \cdot (\mathbf{D}^{\text{eff}}\nabla M_\perp)$$

$$\frac{\partial M_z}{\partial t} = \gamma(\mathbf{M} \times \mathbf{B}_0)_z - \frac{M_z - M_0}{T_1} \quad -\nabla \cdot (\mathbf{v}M_z) + \nabla \cdot (\mathbf{D}^{\text{eff}}\nabla M_z) \tag{A.6}$$

In these equations, additionally, the first added term accounts for flow with velocity $\mathbf{v}$. Again, a strong $\mathbf{B}_0$ in z direction has been assumed. The total time derivative in (A.2) has been replaced by a partial derivative since now the components of $\mathbf{M}$ (and also of c in A.5) depend on both position and time.

A.9   Diffusion tensor imaging

Let us consider a stationary particle, exposed to a Stejskal-Tanner type pulse sequence, shown in Fig.A.3 [126]. During the first τ period after the $90°$ pulse, the
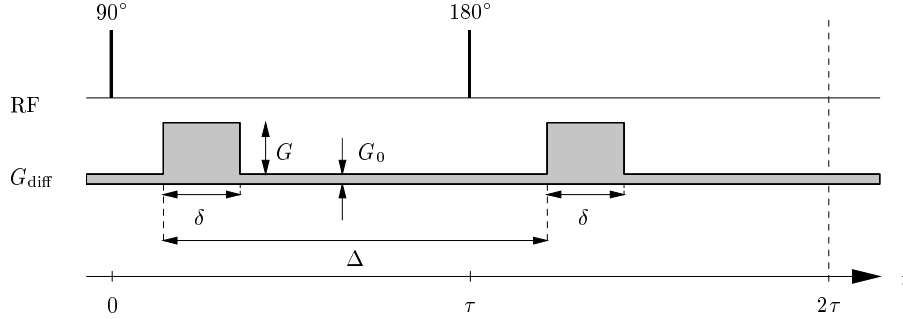
Figure A.3: *Stejskal-Tanner type spin echo preparation experiment for diffusion weighting.*

particle accumulates a phase shift, let's say, $+\Phi$, due to the applied gradient pulse with duration δ and magnitude G (see A.3). The 180° refocusing pulse then inverts the phase of the particle to $-\Phi$ (see A.4) and since it accumulates a positive shift, $+\Phi$, again in the second τ period, no phase shift remains at $t = TE = 2\tau$. In contrast, a diffusing particle changes its position, so that a net phase shift not equal to zero, lets say, a positive shift, results for the considered diffusing particle. Because diffusion is a random process, other particles in the neighborhood of the first accumulate a negative shift, and since the magnetization is a vector average over the ensemble spins (see A.1), the result is a signal attenuation.

For a Stejskal-Tanner type pulse sequence, analytic expressions have been derived based on the extended Bloch equations (A.6) that describe the signal attenuation and relate the measured echo intensity to the applied pulse gradient sequence [216]. In these expressions, the effects of diffusion, flow, reversible dephasing due to external gradients, relaxation and precession in the main magnetic field were separated [215; 126],

$$M_\perp(t) = M_x(t) + iM_y(t) = A(t)e^{i\Phi(\mathbf{v},t)}e^{-ig(t)}e^{-t/T_2}e^{-i\omega_0 t},$$

with some real-valued functions A, Φ and g. $A(TE)$, the magnitude of the magnetization at the time of the echo, was related to the diffusion tensor for anisotropic media. With $A(t) \sim S(t)$ and with the denotation S and S_0 for the echo amplitude with and without the diffusion gradient pulses, resp., the effective diffusion tensor was defined in this way by [14]

$$\frac{S}{S_0} = e^{-\mathbf{b}:\mathbf{D}^{\text{eff}}} \tag{A.7}$$

with the notation

$$\mathbf{b} : \mathbf{D}^{\text{eff}} := \sum_{i,j=1}^{3} \mathbf{b}^{[ij]}(\mathbf{D}^{\text{eff}})^{[ij]} \in \mathbb{R}$$

and

$$\mathbf{b}^{[ij]} = \gamma^2 \int_0^{TE} \left[\mathbf{F}(t') - 2H(t'-\tau)\mathbf{f}\right]^{[i]} \left[\mathbf{F}(t') - 2H(t'-\tau)\mathbf{f}\right]^{[j]} dt'$$

with

$$\mathbf{F}(t) = \int_0^t \mathbf{G}(t')dt' \quad \text{and} \quad \mathbf{f} = \mathbf{F}(\tau).$$

H is the unit Heaviside function and $\mathbf{G}(t)$ the applied gradient pulses. This expression defines the effective diffusion tensor, being averaged over the echo time.

For the Stejskal-Tanner experiment in Fig.A.3 with gradient pulses having symmetrical trapezoidal form with time rise ε, the integral can be evaluated and the elements are given by [153]

$$\mathbf{b}^{[ij]} = \gamma^2 \mathbf{G}^{[i]} \mathbf{G}^{[j]} [\delta^2(\Delta - \delta/3) + \frac{\varepsilon^3}{30} - \frac{\varepsilon^2}{6}\delta]. \tag{A.8}$$

The effective self-diffusion tensor averaged over the echo time, $\mathbf{D}^{\text{eff}}$, is thus determined by the application of different $\mathbf{b}^{[ij]}$ values (i.e., by means of a variation of gradient and time settings), the subsequent measurement of the signal *S* and a multivariate linear regression [126].

Appendix B

The multilayer sphere model

B.1 The derivation of the monopole potential

Following de Munck [49] and de Munck and Peters [52], the solution of the inhomogeneous differential equation (4.21) was expressed as the product of two linear independent solutions $H_n^{(i)}, i \in \{1,2\}$ of the corresponding homogeneous differential equation,

$$R_n(r_0, r_e) = \frac{H_n^{(1)}(r_0) H_n^{(2)}(r_e)}{r_e \sigma^{\text{rad}}(r_e) \left[H_n^{(1)}(r) \frac{d}{dr} H_n^{(2)}(r) - H_n^{(2)}(r) \frac{d}{dr} H_n^{(1)}(r) \right]_{r=r_e}}.$$

The solutions of the homogeneous equation are known to be $H_0^{(1)}(r) \equiv 1$ and, $\forall n \neq 0$ and for $r_{j+1} < r < r_j$:

$$H_n^{(i)}(r) = A_{j,n}^{(i)} P_{j,n}(r) + B_{j,n}^{(i)} Q_{j,n}(r), \qquad P_{j,n}(r) = r^{v_j(n)}, \qquad Q_{j,n}(r) = r^{-v_j(n)-1}$$

with

$$v_j(n) = \frac{1}{2} \left(-1 + \sqrt{1 + 4n(n+1)\sigma_j^{\text{tang}}/\sigma_j^{\text{rad}}} \right).$$

For a determination of the coefficients, the Dirichlet condition in the center of the multisphere model and the boundary condition at the outer surface were introduced by

$$\lim_{r \to 0} H_n^{(1)}(r) = 0 \quad \lim_{r \to 0} H_n^{(1)'}(r) = 1, \qquad \forall n \neq 0$$

$$\lim_{r \to r_1} H_n^{(2)}(r) = 1 \quad \lim_{r \to r_1} H_n^{(2)'}(r) = 0, \qquad \forall n \neq 0,$$

so that Gauss' identity, $\int_\Omega J^p d\Omega = \oint_\Gamma f d\Gamma$, was fulfilled for the monopole with

$$f := \sigma \frac{\partial u_{\text{mon}}}{\partial \mathbf{n}}\bigg|_\Gamma = \frac{1}{4\pi r_1^2}.$$

With two further conditions, the first being the continuity of the potential over a layer surface,

$$A_{j,n}^{(i)} P_{j,n}(r_j) + B_{j,n}^{(i)} Q_{j,n}(r_j) = A_{j-1,n}^{(i)} P_{j-1,n}(r_j) + B_{j-1,n}^{(i)} Q_{j-1,n}(r_j),$$

and the second being the continuity of the current normal to a layer surface,

$$\sigma_j^{\text{rad}} \left[A_{j,n}^{(i)} P'_{j,n}(r_j) + B_{j,n}^{(i)} Q'_{j,n}(r_j) \right] = \sigma_{j-1}^{\text{rad}} \left[A_{j-1,n}^{(i)} P'_{j-1,n}(r_j) + B_{j-1,n}^{(i)} Q'_{j-1,n}(r_j) \right],$$

a formula for the coefficients of the spherical harmonics expansion was derived:

$$R_n(r_0, r_e) = \frac{\left\{ M_{J_0}(r_0, r_{J_0+1}) \prod_{j=N}^{J_0-1} M_j(r_j, r_{j+1}) \right\}_{12}}{\left\{ -r_e^2 \prod_{j=N}^{1} M_j(r_j, r_{j+1}) \right\}_{22}} \varsigma_0^{v_{J_0}} \prod_{j=1}^{J_0-1} \varsigma_j^{v_j}. \tag{B.1}$$

In this formula, it is $\varsigma_0 = r_0/r_{J_0} < 1$ and $\varsigma_j = r_{j+1}/r_j < 1$, and, with

$$S_j^-(r_j, r_{j+1}) = \begin{pmatrix} \frac{r_j v_j}{r_{j+1}} & -\frac{r_j}{\sigma_j^{\text{rad}}} \\ \frac{-\sigma_j^{\text{rad}} v_j(v_j+1)}{r_{j+1}} & v_j+1 \end{pmatrix}, \quad S_j^+(r_j, r_{j+1}) = \begin{pmatrix} v_j+1 & \frac{r_{j+1}}{\sigma_j^{\text{rad}}} \\ \frac{v_j(v_j+1)\sigma_j^{\text{rad}}}{r_j} & \frac{r_{j+1} v_j}{r_j} \end{pmatrix},$$

the matrices M_j are defined as

$$M_j(r_j, r_{j+1}) = \varsigma_j^{2v_j+2} \frac{1}{2v_j+1} S_j^-(r_j, r_{j+1}) + \frac{1}{2v_j+1} S_j^+(r_j, r_{j+1}). \tag{B.2}$$

In formula (B.1), the limit $r_{N+1} \to 0$ (Dirichlet condition) has to be taken for $M_N(r_N, r_{N+1})$, using l'Hôpitals rule:

$$\lim_{r_{N+1} \to 0} \frac{d}{dr_{N+1}} M_N(r_N, r_{N+1}) = \frac{1}{2v_N+1} \begin{pmatrix} 0 & \frac{1}{\sigma_N^{\text{rad}}} \\ 0 & \frac{v_N}{r_N} \end{pmatrix} \tag{B.3}$$

To summarize, the spherical harmonics expansion (4.20) for a monopolar source can be calculated by means of (B.1), (B.2) and (B.3).

B.2 Asymptotic approximation for the dipole potential

For the computation of $R'_n(r_0, r_e)$, i.e., the derivative with respect to r_0, the 12-matrix element in Equation (B.1) has to be exchanged against the 22-matrix element and the result has to be divided by the conductivity $\sigma_{J_0}^{\text{rad}}$ [49; 52].

For $n \to \infty$, the first term in (B.2) tends to zero, since $\zeta_j < 1$. Thus, the matrix product in (B.1) tends to a rational function of v_j. It is then clear that the series convergence in Equation (4.20) is determined by the behavior of the product of the ζ_j in (B.1). De Munck and Peters [52] showed that, if the source approaches the electrode, this product tends to $A\Lambda^n$ with $\Lambda \to 1$ and

$$A = \prod_{j=1}^{J_0-1} (\zeta_j \zeta_0)^{1/2(\alpha_j - 1)} \qquad \Lambda = \prod_{j=1}^{J_0-1} (\zeta_j \zeta_0)^{\alpha_j} \qquad \alpha_j = \sqrt{\sigma_j^{\text{tang}} / \sigma_j^{\text{rad}}}.$$

Therefore, an asymptotic approximation was proposed to speed up computation of the series (4.22) and (4.23). The main point in their derivation is an approximation of the spherical harmonics expansion with a formula, which is known both in analytical form and as a spherical harmonics expansion. Such formulas are

$$\sum_{n=1}^{\infty} \Lambda^n P'_n(\cos \omega_{0e}) = \frac{\Lambda}{R^3} \qquad \sum_{n=1}^{\infty} n \Lambda^n P_n(\cos \omega_{0e}) = \frac{\Lambda \cos \omega_{0e} - \Lambda^2}{R^3},$$

with $R = \sqrt{1 - 2\Lambda \cos \omega_{0e} + \Lambda^2}$. With the definition of the terms

$$F_0 = -\frac{2A}{r_e \beta_{J_0}} \prod_{j=1}^{J_0-1} \frac{2\beta_{j+1}}{\beta_j + \beta_{j+1}} \qquad F_1 = \frac{\beta_{J_0}}{r_0 \sigma_{J_0}^{\text{rad}}} F_0,$$

with $\beta_j = \sqrt{\sigma_j^{\text{tang}} \sigma_j^{\text{rad}}}$, de Munck and Peters [52] found the following asymptotic approximations for $n \to \infty$

$$(2n+1)R_n(r_0, r_e) \to F_0 \Lambda^n \qquad (2n+1)R'_n(r_0, r_e) \to nF_1 \Lambda^n$$

and thus the series of differences (4.24) and (4.25) with a higher speed of convergence.

Appendix C

Conventional methods for the dipole fit least square problem

C.1 QR decomposition

Without respect to the noise in the data, one possibility to solve the linear least square problem (6.2) is the *QR decomposition*. If the overdetermined $m \times r$ ($m > r$) lead-field matrix L_q has full rank r, it can be decomposed into an orthogonal $m \times m$ matrix Q ($Q^{tr}Q = I$) and an $m \times r$ matrix

$$R = \left(\frac{R_1}{0} \right)$$

with a right upper triangular $r \times r$ matrix R_1 (see, e.g., Werner [250]). The coefficient matrix of the reduced system has the same condition as the lead-field matrix

$$\text{cond}_2(L_q) = \text{cond}_2(QR) = \text{cond}_2(R).$$

The application of Q^{tr} to the measured (noisy) data $U_\varepsilon^{me} \in \mathbb{R}^{m \times T}$ yields

$$Q^{tr}U_\varepsilon^{me} = \left(\frac{U_{\varepsilon 1}^{me}}{U_{\varepsilon 2}^{me}} \right)$$

with an $r \times T$ matrix $U_{\varepsilon 1}^{me}$ and an $(m-r) \times T$ matrix $U_{\varepsilon 2}^{me}$. Because orthogonal transformations preserve the Frobenius-norm, the linear least square problem

$$H(q) = ||Q^{tr}L_qJ_q - Q^{tr}U_\varepsilon^{me}||_F^2 = ||R_1J_q - U_{\varepsilon 1}^{me}||_F^2 + ||U_{\varepsilon 2}^{me}||_F^2$$

can be solved by back-substitution $R_1J_q = U_{\varepsilon 1}^{me}$.

To compute the QR-decomposition, the method of Householder [250] was used, implemented in subroutine DGEQPF in the software package LAPACK [132].

The left orthogonal matrix is represented as a product of elementary Householder rotation matrices $H^i := \mathrm{Id}_m - \tau_i \underline{x}_i \underline{x}_i^{tr}$ with a scalar τ_i and an $m \times 1$ vector $\underline{x}_i$, i.e.

$$Q = H^1 \cdot \ldots \cdot H^m.$$

C.2   Complete Orthogonal Factorization

Another possibility to solve (6.2) is the *Complete Orthogonal Factorization* (COF) of L_q. This method can also handle matrices which do not have full effective rank $r_e = r$, which cannot be guaranteed in practical applications. Generally, the COF numerically produces the same results as the QR decomposition and it also suffers from the fact not to account for the data noise. The only goal of both algorithms is to minimize the residual variance to the noisy data. In a first step of the COF, a QR-decomposition with column pivoting

$$L_q P = Q \begin{pmatrix} R_{11} & R_{12} \\ 0 & R_{22} \end{pmatrix}$$

is calculated, where the $r_e \times r_e$ matrix R_{11} is defined as the largest leading submatrix whose estimated condition number is less than $1/R_{cond}$ with a small constant R_{cond}. Thus, the order of R_{11} is the effective rank r_e of L_q. In a second step of the COF, the $(m - r_e) \times (r - r_e)$ matrix R_{22} is considered to be negligible and the $r_e \times (r - r_e)$ matrix R_{12} is annihilated by the $r \times r$ orthogonal right Householder rotation matrix Z:

$$\begin{bmatrix} R_{11} & R_{12} \end{bmatrix} = \begin{bmatrix} R_1 & 0 \end{bmatrix} Z$$

If we write

$$Q = \begin{bmatrix} Q_{r_e} & Q_{m-r_e} \end{bmatrix},$$

where Q_i contains the first i columns of Q and

$$Z = \begin{bmatrix} Z_{r_e} \\ Z_{r-r_e} \end{bmatrix},$$

where Z_i contains the first i rows of Z, we arrive at the COF of the lead-field matrix

$$L_q P = \begin{bmatrix} Q_{r_e} & Q_{m-r_e} \end{bmatrix} \begin{pmatrix} R_1 & 0 \\ 0 & 0 \end{pmatrix} \begin{bmatrix} Z_{r_e} \\ Z_{r-r_e} \end{bmatrix}.$$

The linear least square problem $H(q)$ can then be solved by

$$J_q = P Z_{r_e}^{tr} R_1^{-1} Q_{r_e}^{tr} U_{\varepsilon}^{me}.$$

Subroutine DGELSX of the Lapack-library was used for the COF [132]. In the simulations, it was chosen $R_{cond} = 0.3 \cdot 10^{-7}$.

Appendix D

Software developments: The program NeuroFEM

A new FE software package NeuroFEM [1] was developed, based on the CAUCHY-code [2] (see [30; 191; 254]). Since it would have been difficult to integrate the FORTRAN77-CAUCHY FE forward problem tools using quasistatic memory management in a new C++ class structured inverse toolbox, the old software was redesigned. The inverse toolbox contains a variety of state-of-the-art current source localization methods from the package ASA [3] (see [122]) and was developed within the frame of the project SimBio [4] (see [142]). It will ease the future integration of inverse methods from the CAUCHY project or of new developments such as the methods presented in this thesis and published in [260; 259; 203; 204]. Another argument for the code development was the possibility for a proper interface to the software package PEBBLES, including the parallel AMG solver [88] [5]. The solver code also exploits C++ principles of overloading and inheritance.

Therefore, C++ class structured software concepts in the NeuroFEM code

---

[1]NeuroFEM: A.Anwander and C.Wolters, http://www.simbio.de, 2002.

[2]CAUCHY: Anatomic source reconstruction of EEG/MEG-data, H.Buchner, Neurologische Klinik, RWTH Aachen, 1997. I would like to thank Rainer Beckmann and Adrian Rienäcker for the excellent CAUCHY support.

[3]ASA: Advanced Source Analysis, http://www.ant-software.nl, 2002.

[4]SimBio: A generic environment for bio-numerical simulation. IST-program of the European Commission, Project No.10378, http://www.simbio.de, 2000-2003. The author of this thesis was strongly involved in the definition and application phase of SimBio, in the recruitment of personal and in the realization of the project-goals.

[5]PEBBLES – User's Guide, S. Reitzinger, SFB F013 "Numerical and Symbolic Scientific Computing", http://www.sfb013.uni-linz.ac.at, 1999. Many thanks to Stefan Reitzinger and Michael Kuhn for all the help concerning solver integration and NeuroFEM parallelization.

replace old CAUCHY kernel routines. The storage management is fully dynamical so that a recompilation of the software is no longer necessary when changing the problem- and thus memory- size. The new structure facilitated parallel programming on distributed memory computers using the Message-Passing Interface (MPI) standard. The integrated software allows future comparisons with series expansion formulas in spherical shell models [6] or with BE method based forward simulations using the ASA software. Furthermore, the use of the binary VISTA-format was enabled, so that NeuroFEM was successfully coupled to the other SimBio work-packages such as the work-package for MRI registration and segmentation, the work-package for FE grid-generation, the library PILUTS, containing further parallel FE solver techniques (among others, a parallel Schur-complement ILDLT-preconditioned CG method), the SimBio-VM (Visualization Module) and the CORBA interface for component interaction and remote parallel computation. Obviously, NeuroFEM still supports the old CAUCHY ASCII formats, so that it is also coupled to EIPP, the CAUCHY visualization tool, and to CURRY [7], which, amongst many other features, offers further segmentation and visualization possibilities, surface triangulation and tetrahedra FE meshing.

The coupling of NeuroFEM to the PEBBLES parallel solver-package was carried out through an "element by element" interface. The root-process determines the index set (see Equation (5.10)) for each node of the partitioned geometry and scatters the corresponding data together with the conductivity tensors to the processors. The arrangement of the nodes to groups according to their index-sets, the ordering of the groups and the allocation of corresponding MPI-communicator groups and the local node numbering is then a fully parallel process. Element-stiffness-matrices are computed on each processor and stored in the local stiffness matrices in FE compact row format. The global Dirichlet-node information is scattered to all processors and implemented with a penalty approach in local numbering to those local stiffness matrices whose processor-number is part of the global Dirichlet-node index-set. The coarsening can then be carried out and the hierarchy of stiffness and prolongation matrices can be determined in the parallel setup-phase of the AMG preconditioner as described in Section 5.4.3.

The software NeuroFEM-PEBBLES is available under a fee-free license of the MPI of Cognitive Neuroscience Leipzig, Germany, and the University of Linz, Austria [8]. It is used by several institutions in Europe and the USA.

---

[6] I would like to thank Jan C. de Munck for handing out his C++ code for the series expansion formulas and helping me in implementing the software for the validations in Section 4.9.2.

[7] CURrent Reconstruction and Imaging, http://www.neuro.com/neuroscan/prod05.htm. Many thanks to Michael Wagner, Manfred Fuchs and Jörn Kastner for the various scientific discussions and their continuous support concerning the use of CURRY.

[8] E-mail to wolters@cns.mpg.de or anwander@cns.mpg.de.

Appendix E

Zusammenfassung (summary in german)

E.1 Motivation und Einordnung

Seit nun fast drei Jahrzehnten werden im Bereich der Kognitionswissenschaften und in klinischer Forschung und Routine die Quellen elektrischer Aktivität im menschlichen Gehirn anhand ihrer über das Elektroenzephalogramm (EEG) an der Kopfoberfläche gemessenen Potentialverteilung bzw. ihres über das Magnetoenzephalogramm (MEG) in einigen Zentimetern Entfernung davon gemessenen magnetischen Flusses rekonstruiert. Im Vergleich zu anderen funktionellen Bildgebungsmethoden wie z.B. die Positronen-Emissions-Tomographie (PET) oder die funktionelle Magnetresonanztomographie (fMRT) hat die EEG/MEG-Quellrekonstruktion den Vorteil einer sehr hohen zeitlichen Auflösung. Die gemessene Aktivität ist das Resultat von Ionenbewegungen in aktivierten kortikalen Regionen des Gehirns, den sog. *Primärströmen*. Schon im Jahr 1949 wurden erstmals die Primärströme über *Stromdipole* mathematisch modelliert. Der Primärstrom erzeugt Rückströme im leitfähigen Gewebe des Kopfes, die sog. *Sekundärströme*. Die Rekonstruktion der Dipolquellen wird das *EEG/MEG inverse Problem* genannt. Dessen Lösung erfordert die wiederholte Berechnung des *Vorwärtsproblems*, d.h. der Simulation der EEG/MEG-Feldverteilung für eine gegebene Dipolquelle im Gehirn.

Ein erstes Anwendungsgebiet findet sich in der Diagnose und Therapie von pharma-resistenten Epilepsien, von denen ca. 0,25% der Weltbevölkerung betroffen sind und für die sich in den letzten Jahrzehnten eine systematische chirurgische Behandlung entwickelt hat. Voraussetzung für einen die restlichen Gehirnregionen schonenden chirurgischen Eingriff ist die Kenntnis der Lage und Ausdehnung der epileptischen Zentren. Bisher wurden diese Charakteristika in den Pa-

tienten stark belastenden invasiven Untersuchungen wie zum Beispiel Subdural-
oder Tiefen-Elektroden gewonnen. Die bioelektrischen Signale von Epilepsie-
kranken weisen zwischen den Anfallsereignissen sog. interiktale Spikes auf. Die
nicht-invasive Messung des EEG/MEG dieser interiktalen Spikes und die an-
schließende Berechnung des epileptischen Zentrums belastet den Patienten nicht.

Ein weiteres Anwendungsfeld ist die präoperative Ermittlung der Lage wich-
tiger funktionell-zusammenhängender Zentren im Gehirn, z.B. des primär-mo-
torischen, des primär-auditorischen oder primär-somatosensorischen Cortex. Bei
Operationen in diesen Bereichen (z.B. Tumoroperationen) könnten Lähmungen,
Hör- und Sensibilitätsstörungen vermieden werden. Dazu werden über akusti-
sche oder sensorische Reize charakteristische Signale evoziert und über Summa-
tionstechniken sichtbar gemacht. Durch das Lösen des inversen Problems wird
versucht, die zugrunde liegende Quellstruktur zu ermitteln.

Neben den aufgeführten klinischen Anwendungen ergeben sich auch zahlrei-
che Anwendungsfelder in der Kognitionswissenschaft. Von Interesse sind z.B. funk-
tionelle Zusammenhänge im Gehirn und die Aufdeckung der aktivierten Areale
während der Verarbeitung eines Reizes, wie z.B. der Sprachverarbeitung im Ge-
hirn.

Die Lösung des Vorwärtsproblems impliziert die Modellierung des Kopf-
es als Volumenleiter. Es ist bekannt, dass in makroskopischer Hinsicht Gewe-
be wie die Kopfhaut, der Schädel, die Zerebrospinalflüssigkeit (engl.: CSF) und
die Hirngewebe graue und weiße Substanz (engl.: GM und WM) verschiedene
Leitfähigkeiten besitzen. Der menschliche Schädel ist aus drei Schichten auf-
gebaut, eine relativ gut leitfähige spongiöse Schicht wird von zwei stark isolie-
renden Schichten, den äußeren und inneren Kompakta, eingeschlossen. In radia-
ler Richtung durch den Schädel handelt es sich also um eine Reihenschaltung
von hohem, niedrigem und hohem Widerstand, wohingegen in den tangentia-
len Richtungen die Leiter parallel geschaltet sind. Als Ganzes gesehen besitzt
der Schädel demnach eine richtungsabhängige oder *anisotrope* Leitfähigkeit mit
einem gemessenen Verhältnis von bis zu 1 zu 10. Für die faserige WM wurde
ebenfalls eine Anisotropie mit einem ähnlichen Verhältnis (senkrecht zu parallel
zu den Fasern) nachgewiesen. Leider existiert bis heute keine direkte Methode,
die Leitfähigkeit der WM nicht-invasiv in genügender Auflösung zu ermittelt.
Seit einigen Jahren werden allerdings Formalismen diskutiert, die den gesuch-
ten Leitfähigkeitstensor in Bezug setzen zum Wasserdiffusionstensor, der in WM
nicht-invasiv über die Diffusionstensor-MRT (DT-MRT) gemessen werden kann.
Natürlich wird keine fundamentale Beziehung zwischen der freien Beweglichkeit
von Ionen und Wasserteilchen angenommen, sondern lediglich, dass die einge-
schränkte Mobilität über die Fasergeometrie der WM in Beziehung steht.

Heutzutage werden verschiedene Ansätze für die Lösung des Vorwärtspro-

blems genutzt und mit steigender Genauigkeit der Modellierung des Kopfvolumenleiters erhöht sich die Komplexität der numerischen Feldberechnungen. Einfache Modelle, die immer noch am häufigsten Gebrauchten, beschreiben den Kopf als Mehrschalenkugel-Leiter mit üblicherweise drei Schichten, die die Kopfhaut, den Schädel und das Gehirn repräsentieren. Um besser auf die Geometrie der drei modellierten Oberflächen einzugehen, wurden sog. BE-Modelle (von engl.: Boundary Element) entwickelt, die sich für isotrop leitfähige Schichten eignen. Um sowohl auf realistische Geometrien als auch auf Anisotropien und Inhomogenitäten eingehen zu können, wurden Finite-Elemente (FE) Modelle des Kopfes entwickelt.

Zwei wichtige Fragen stellen sich nun: Ist eine exakte Modellierung der vorgestellten Gewebeleitfähigkeits-Anisotropien nötig und in welchen Fällen reichen weniger berechnungsaufwendige Verfahren aus? Wie können komplexe FE-Vorwärtsmodelle hinreichend beschleunigt werden, um den Zeitrestriktionen für inverse Quellrekonstruktionen in den Anwendungen zu genügen?

Es existieren zahlreiche Arbeiten, die, basierend auf FE-Modellen des Kopfes, gezeigt haben, dass Öffnungen im Schädel wie z.B. diejenige, durch die der optische Nerv eintritt oder das okzipitale Loch des Hirnstamms, oder Inhomogenitäten wie Läsionen im Gehirn oder die Sutura des Schädels (insbesondere bei Kleinkindern, wo die Sutura noch nicht geschlossen sind) einen nicht vernachlässigbaren Einfluss auf das EEG/MEG-Vorwärtsproblem haben. Eine erste Studie bzgl. der Sensitivität zweier ausgewählter EEG-Rekonstruktionsverfahren wies teils große Fehler im Falle der Nichtbeachtung von Schädel-Anisotropie nach. Insbesondere für diverse klinische Anwendungen wird der sog. *single dipole fit* im kontinuierlichen Parameterraum verwendet. Aufgrund des hohen Berechnungsaufwands wurden solche Verfahren bisher noch nicht auf ihre Sensitivität auf Schädelanisotropie getestet. Obwohl bereits eine Studie einen nichtvernachlässigbaren Einfluss auf die EEG/MEG-Vorwärtssimulation zeigte, gibt es noch keinerlei Ergebnis zur Auswirkung der WM-Anisotropie auf inverse Rekonstruktionsverfahren.

Die Lösung des inversen Problems ist im allgemeinen nicht eindeutig. Viele Dipol-Quellkonfigurationen können ein und dieselbe EEG und MEG Feldverteilung erzeugen. Zusätzliche Annahmen über die Quellen sind dementsprechend unerlässlich. Bei den sog. *fokalen Rekonstruktionsmethoden* wird die Annahme gemacht, dass einige wenige Dipole den gemessenen Daten zugrunde liegen. Diese Dipole (Anzahl, Ort, Richtung, Stärke) sollen innerhalb des anatomisch und physiologisch sinnvollen Suchgebiets so ermittelt werden, dass die Messwerte möglichst genau erklärt werden, gleichzeitig aber das Rauschen keinen zu starken Einfluss auf die Lösung nimmt und die Algorithmen stabil in Bezug auf eine Überschätzung der Anzahl aktiver Quellen bleiben. Bei diesen, wie auch bei den

sog. *Stromdichterekonstruktionsverfahren*, wird sich das Konzept der Regularisierung als eine wichtige Methode herausstellen.

E.2   Wissenschaftliche Ergebnisse der Dissertation

Die Ergebnisse der vorgelegten Dissertation können in vier Teilbereiche aufgeteilt werden.

Im ersten Teilbereich wurden Methoden zur Registrierung und Segmentierung multimodaler MR-Bilder vorgestellt mit dem Ziel, ein **realistisches anisotropes Multigewebe Kopfmodell** zu generieren. In der Literatur wurde von größeren EEG- und MEG-Quellrekonstruktionsfehlern aufgrund mangelhafter Modellierung insbesondere der inneren Schädelkante berichtet. Ein erster Fokus dieser Arbeit lag dementsprechend auf einer verbesserten Segmentierung dieser Kante, die über ein auf dem T1-gewichteten MRT (T1-MRT) registrierten Protonendichte-gewichteten MRT (PD-MRT) gewonnen wurde. Die innere Schädelkante zeichnet sich im PD-MRT im Gegensatz zum T1-MRT durch einen hohen Kontrast zwischen CSF (protonenreich) und Knochen (protonenarm) aus. Das T1-MRT wurde hingegen für die Segmentierung der Kopfhaut, der GM und der WM verwendet. Die Standardtechnik im Bereich der EEG/MEG-Quellrekonstruktion nutzt lediglich ein T1-MRT und gewinnt die gesuchte innere Schädelkante über ein Glätten und Aufblasen der segmentierten Hirnoberfläche. Im Vergleich beider Methoden konnte eine Verbesserung der Segmentierung von bis zu 8,5mm in Gebieten erzielt werden, in denen die Standardmethode die Dicke der CSF-Schicht unterschätzte. Über die vorgestellten Methoden, insbesondere der Segmentierung unter Berücksichtigung der MR-Inhomogenitäten, konnte zudem eine sehr exakte Modellierung der GM erzielt werden, welche dann als anatomische und auch physiologische Nebenbedingung in die Quellrekonstruktion eingebettet werden kann. Zur realistischen Modellierung der Anisotropie der Schädelschicht wurde ein deformierbares Modell eingesetzt, welches eine geglättete Spongiosaoberfläche darstellt und somit ein Abgreifen der Leitfähigkeitstensor-Eigenvektoren in radialer Knochenrichtung ermöglicht. Die Eigenvektoren der WM-Tensoren wurden über Ganzkopf-DT-MRT gemessen. Schädel- und WM-Tensor-Eigenwerte wurden entweder unter Ausnutzung publizierter Werte simuliert oder gemäß einem differentialen EMA (von engl.: Effective Medium Approach) ermittelt.

Der zweite Teilbereich betraf die **schnelle hochaufgelöste FE-Modellierung** des EEG/ MEG-Vorwärtsproblems. Zunächst wurde ein Überblick über die Theorie gegeben und die praktische Realisierung der später eingesetzten hochaufgelösten anisotropen FE-Volumenleitermodelle vorgestellt. In numerischen Genauigkeitsstudien konnte nachgewiesen werden, dass Hexaeder-FE-Netze, wel-

che ein Verschieben der Stützpunkte zur Glättung an Gewebekanten nutzen, vorteilhaft sind zu herkömmlichen Hexaeder-Netzen. Dazu wurden die Reihenentwicklungsformeln für das Mehrschalenkugel-Modell eingesetzt. Ein weiterer Fokus dieser Arbeit lag auf dem Einsatz schneller FE-Lösungsmethoden, welche die praktische Anwendbarkeit von hochaufgelösten anisotropen FE-Kopfmodellen in den verschiedenen Anwendungsgebieten ermöglichen sollte. In einem Zeitvergleich zwischen dem neu in die Software integrierten parallelen (12 Prozessoren) algebraischen Mehrgitter- und dem Standard-Einprozessor-Jacobi-Vorkonditionierer für das Verfahren der konjugierten Gradienten konnte für hochaufgelöste anisotrope FE-Kopfmodelle ein Beschleunigungsfaktor von mehr als 100 erzielt werden.

Im dritten Teilbereich, den **Methoden zum inversen Problem**, wurden neben einem Überblick über fokale Rekonstruktionsverfahren und Stromdichterekonstruktionsverfahren algorithmische Neuentwicklungen präsentiert. Es wurde zunächst die Methode des *single dipole fit* in die FE-Modellierung eingeführt. Für multiple dipolare Quellen wurde ein *Simulated Annealing* Algorithmus in Kombination mit einer abgeschnittenen Singulärwertzerlegung im diskreten Parameterraum entwickelt. Im Vergleich zu Standardmethoden zeigte der Algorithmus in verschiedenen Simulationsstudien eine verbesserte Fähigkeit der Unterscheidung zwischen realen und sog. *ghost* Quellen. Des Weiteren wurde eine kürzlich in der Literatur vorgestellte raum-zeitliche Regularisierungsmethode auf die Stromdichterekonstruktion und, als zweite Anwendung, auf die dynamische Impedanztomographie angewandt. Der raum-zeitliche Ansatz konnte dabei eine stabilisierende Wirkung auf die Rekonstruktionsergebnisse erzielen und zeigte im Hinblick auf seine Genauigkeit und den Speicher- und Rechenzeitbedarf Vorteile gegenüber einem sog. *Kalman-Glätter*.

Im letzten Teilbereich der Dissertation wurden Untersuchungen zur **Anisotropie-Sensitivität** durchgeführt. Der erste Teil bezog sich dabei auf das Vorwärtsproblem, wo die Resultate im Einklang mit der verfügbaren Literatur waren. Es kann festgehalten werden, dass Schädelanisotropie einen nicht-vernachlässigbaren Einfluss auf die EEG-Simulation hatte, wohingegen das MEG unbeeinflusst blieb. Je mehr eine Quelle von WM umgeben war, desto größer war der Einfluss der WM-Anisotropie auf sowohl EEG als auch MEG. Für das MEG wirkte sich WM-Anisotropie insbesondere auf Quellen mit starken radialen Anteilen aus. Lokale Leitfähigkeitsänderungen im Bereich der Quelle sollten sowohl im Hinblick auf das EEG als auch auf das MEG modelliert werden. Im zweiten Teil wurden die Einflüsse auf die inverse Quellrekonstruktion untersucht. Mit 18mm maximalem Fehler des EEG basierten *single dipole fit* war die Lokalisation einer hauptsächlich tangential orientierten oberflächennahen Quelle besonders sensitiv gegenüber einer 1 zu 10 Schädelanisotropie. Da die tangentialen Quellen im tem-

poralen Bereich (Schädel relativ dünn) zu tief und im parietalen und okzipitalen Bereich (Schädel relativ dick) zu oberflächennah lokalisiert wurden, scheint eine Approximation der Schädelanisotropie in BE-Modellen über eine Anpassung des skalaren Schädelleitfähigkeitswertes nicht möglich zu sein. Obwohl bei Vernachlässigung der WM-Anisotropie der maximale EEG-Lokalisierungsfehler mit 6,2mm für eine tiefe Quelle wesentlich geringer ausfiel, kann aufgrund eines maximalen Orientierungsfehlers von 24° und einer mehr als zweifach unterschätzten Quellstärke eine Missinterpretation des Ergebnisses nicht ausgeschlossen werden. Für die Rekonstruktion der vier tangentialen oberflächennahen Dipole, welche als Aktivitätszentren der sog. *Early Left Anterior Negativity* (ELAN) Komponente bei der Syntaxanalyse von Sprache betrachtet werden, stellte sich WM und Schädelanisotropie als vernachlässigbar im Hinblick auf eine MEG-Rekonstruktion heraus. Im Gegensatz dazu wurde das EEG-Rekonstruktionsergebnis für alle getesteten inversen Verfahren stark verfälscht. Anisotropie verschob das Aktivitätszentrum von L_1 und L_2 Norm Stromdichterekonstruktionsverfahren entlang der Sylvischen Furche in anteriore Richtung.

References

[1] R.A. Adams. *Sobolev spaces*. Pure and Applied Mathematics, Academic Press, New York, 1975.

[2] M.K. Agoston. *Algebraic topology-A first course*. New York, Marcel Dekker, 1976.

[3] M. Akhtari, H.C. Bryant, A.N. Marmelak, L. Heller, J.J. Shih, M. Mandelkern, A. Matlachov, D.M. Ranken, E.D. Best, and W.W. Sutherling. Conductivities of three-layer human skull. *Brain Top.*, 13(1):29–42, 2000.

[4] D.C. Alexander, C. Pierpaoli, P.J. Basser, and J.C. Gee. Spatial transformations of diffusion tensor magnetic resonance images. *IEEE Trans. Biomed. Eng.*, 20(11):1131–1139, 2001.

[5] E.L. Allgower and K. Georg. *Numerical Continuation Methods - An Introduction*. Springer Verlag, Berlin, 1990.

[6] W. Andrä and H. Nowak. *Magnetism in medicine – a handbook*. Wiley–VCH, Berlin· Weinheim· New York· Chichester· Brisbane· Singapore· Toronto, 1998.

[7] A. Anwander. *Segmentation d'images couleur par un opérateur gradient vectoriel multiéchelle et contour actif: Application à la quantification des phases minéralogiques du clinker de ciment*. PhD thesis, CREATIS-UMR CNRS 5515 de l'INSA de Lyon, France, 2001.

[8] A. Anwander, G. Haase, S. Reitzinger, and C. Wolters. High performance computation for source reconstruction in the human brain. in preparation, 2002.

[9] A. Anwander, C.H. Wolters, M. Dümpelmann, and T.R. Knösche. Influence of realistic skull and white matter anisotropy on the inverse problem in EEG/MEG-source localization. In *[169]*, pages 679–681, 2002.

[10] K.A. Awada, D.R. Jackson, J.T. Williams, D.R. Wilton, S.B. Baumann, and A.C. Papanicolaou. Computational aspects of finite element modeling in EEG source localization. *IEEE Trans. Biomed. Eng.*, 44(8):736–751, 1997.

[11] S. Baillet and L. Garnero. A bayesian approach to introducing anatomo-functional priors in the EEG/MEG inverse problem. *IEEE Trans. Biomed. Eng.*, 44:374–385, 1997.

[12] D.H. Ballard and C.M. Brown. *Computer Vision*. Prentice Hall, Englewood Cliffs, NJ, 1982.

[13] A. Basermann. Parallel block ILUT/ILDLT preconditioning for sparse eigenproblems and sparse linear systems. *Num.Lin.Alg.with Appl.*, 7:635–648, 2000.

[14] P.J. Basser, D. Le Bihan, and J. Mattiello. Estimation of the effective self-diffusion-tensor from the NMR spin echo. *J. Magn. Res. B*, 103:247–254, 1994.

[15] P.J. Basser, J. Mattiello, and D. Le Bihan. Anisotropic diffusion: MR diffusion tensor imaging. In D. Le Bihan, editor, *Diffusion and Perfusion Magnetic Resonance Imaging*, pages 140–149. Raven Press, New York, 1995.

[16] P.J. Basser, J. Mattiello, and D. LeBihan. MR diffusion tensor spectroscopy and imaging. *Biophysical Journal*, 66:259–267, 1994.

[17] P.J. Basser and C. Pierpaoli. Microstructural and physiological features of tissues elucidated by quantitive-diffusion-tensor MRI. *J. Magn. Reson. B*, 111:209–219, 1996.

[18] S.B. Baumann, D.R. Wozny, S.K. Kelly, and F.M. Meno. The electrical conductivity of human cerebrospinal fluid at body temperature. *IEEE Trans. Biomed. Eng.*, 44(3):220–223, 1997.

[19] R. Beckmann. Finite Elemente Analyse der elektrischen Aktivität des Zentralnervensystems sowie Lösung des inversen problems. Diplomarbeit im Maschinenbau, Institut für Maschinenelemente und Maschinengestaltung, RWTH Aachen, 1993.

[20] H. Berger. Über das Elektrenkephalogramm des Menschen. *Arch.Psychiat.Nervenkr.*, 87(527–570), 1929.

[21] O. Bertrand, M. Thévenet, and F. Perrin. 3D finite element method in brain electrical activity studies. In J. Nenonen, H.M. Rajala, and T. Katila, editors, *Biomagnetic Localization and 3D Modelling*, pages 154–171. Report of the Dep. of Tech.Physics, Helsinki University of Technology, 1991.

[22] S.M. Blinkov and I.I. Glezer. *The human brain in figures and tables. A quantitative handbook.* Plenum Press, New York, 1968.

[23] F. Bloch, W.W. Hansen, and M. Packard. Nuclear induction. *Phys.Rev.*, 46(127), 1946.

[24] P.A. Bottomley and E.R. Andrew. RF magnetic field penetration, phase shift and power dissipation in biological tissue: implications for NMR imaging. *Phys.Med.Biol.*, 23:630–643, 1978.

[25] D. Braess. *Finite Elemente*. Springer Verlag, 1992.

[26] D. Braess. Towards algebraic multigrid for elliptic problems of second order. *Computing*, 55:379–393, 1995.

[27] M.A.B. Brazier. A study of the electric field at the surface of the head. *Electroenc. Clin. Neurophysiol.*, 2(38–52), 1949.

[28] M.P. Broca. Remarques sur le siége de la faculté du langage articulé, suivies d'une observation d'aphémie (perte de la parole). *Bull. Soc.Anat.Paris*, 6:330–357, 1861. http://psychclassics.yorku.ca/Broca/aphemie.htm.

[29] M.E. Brummer, R.M. Mersereau, R.L. Eisner, and R.R.J. Lewine. Automatic detection of brain contours in MRI data sets. *IEEE Trans. Med. Imag.*, 12(2):153–166, 1993.

[30] H. Buchner, G. Knoll, M. Fuchs, A. Rienäcker, R. Beckmann, M. Wagner, J. Silny, and J. Pesch. Inverse localization of electric dipole current sources in finite element models of the human head. *Electroenc. Clin. Neurophysiol.*, 102:267–278, 1997.

[31] S. Burkhardt. Segmentierung des Knochens aus T1- und PD-gewichteten Kernspinbildern. Diplomarbeit, Institut für Informatik, Fakultät für Mathematik und Informatik, Universität Leipzig,http://dol.uni-leipzig.de/pub/2000-32/en, 2000.

[32] S. Burkhardt, F. Kruggel, D. Saupe, and C. Wolters. Segmentierung des Knochens aus T1- und PD-gewichteten Kernspinbildern vom Kopf. In H. Handels, A. Horsch, T. Lehmann, and H.-P. Meinzer, editors, *Bildverarbeitung für die Medizin*, pages 187–191. Springer-Verlag, Berlin, 2001.

[33] S. Burkhardt, C.H. Wolters, and D. Saupe. Segmentation of human skull surfaces from bimodal MRI volumes. in preparation, 2002.

[34] P.T. Callaghan. *Principles of nuclear magnetic resonance microscopy*. Oxford University Press, Oxford, 1993.

[35] D. Camacho, R. Hopper, G. Lin, and B. Myers. An improved method for finite element mesh generation of geometrically complex structures with application to the skullbase. *J.Biomechanics*, 30(10):1067–1070, 1997.

[36] V. Caselles, R. Kimmel, G. Sapiro, and C. Sbert. Minimal surfaces based object segmentation. *IEEE Trans. Pattern Anal. and Machine Intelligence*, 19(4):394–398, 1997.

[37] T.F. Chan and W. L. Wan. Analysis of projection methods for solving linear systems with multiple right-hand sides. *SIAM J. Sci. Comput.*, 18(6):1698 – 1721, 1997.

[38] D. Cohen. Magnetoencephalography: Evidence of magnetic field produced by alpha-rythm currents. *Science*, 161:784–786, 1968.

[39] I. Cohen, L.D. Cohen, and N. Ayache. Using deformable surfaces to segment 3D images and infer differential structures. *CVGIP: Imag.Under.*, 56(2):242–263, 1992.

[40] A. Collignon, F. Maes, D. Delaere, D. Vandermeulen, P. Suetens, and G. Marchal. Automated multimodality medical image registration using information theory. In Y. Bizais and C. Barillot, editors, *Information Processing in Medical Imaging*, pages 263 – 274. Kluwer Academic Publishers, Dordrecht, 1995.

[41] J. Crank. *The mathematics of diffusion*. Clarendon Press, Oxford, 2nd edition, 1975.

[42] B.N. Cuffin. Effects of local variations in skull and scalp thickness on EEG's and MEG's. *IEEE Trans. Biomed. Eng.*, 40:42–48, 1993.

[43] B.N. Cuffin. EEG localization accuracy improvements using realistically shaped head models. *IEEE Trans. Biomed. Eng.*, 43:299–303, 1996.

[44] A.M. Dale and M.I. Sereno. Improved localization of cortical activity by combining EEG and MEG with cortical surface reconstruction: a linear approach. *Journal of Cognitive Neuroscience*, 5:162–176, 1993.

[45] D.A. Danielson. *Vectors and Tensors in Engineering and Physics*. Addison-Wesley Publishing Company, Inc., 1996. ISBN 0-201-44210-8.

[46] C. Davatzikos and R.N. Bryan. Using a deformable surface model to obtain a shape representation of the cortex. *IEEE Trans. Med. Imag.*, 15:785–795, 1996.

[47] B.M. Dawant, A.P. Zijdenbos, and R.A. Margolin. Correction of intensity variations in MR images for computer-aided tissue classification. *IEEE Trans. Med. Imag.*, 12:770–781, 1993.

[48] A. de Jongh, J.C. de Munck, J.C. Baayen, E.J. Jonkmann, R.M. Heethaar, and B.W. van Dijk. The localization of spontaneous brain activity: First results in patients with cerebral tumors. *Clin.Neurophysiol.*, 112:378–385, 2001.

[49] J.C. de Munck. The potential distribution in a layered anisotropic spheroidal volume conductor. *J. Appl. Phys.*, 64:465–469, 1988.

[50] J.C. de Munck. A linear discretization of the volume conductor boundary integral equation using analytically integrated elements. *IEEE Trans. Biomed. Eng.*, 39(9):986–990, 1992.

[51] J.C. de Munck, R. Bhagwandien, S.H. Muller, F.C. Verster, and M.B. Herk. The computation of MR image distortions caused by tissue susceptibility using the boundary element method. *IEEE Trans. Biomed. Eng.*, 15(5):620–627, 1996.

[52] J.C. de Munck and M. Peters. A fast method to compute the potential in the multi sphere model. *IEEE Trans. Biomed. Eng.*, 40(11):1166–1174, 1993.

[53] J.C. de Munck, B.W. van Dijk, and H. Spekreijse. Mathematical dipoles are adequate to describe realistic generators of human brain activity. *IEEE Trans. Biomed. Eng.*, 35(11):960–966, 1988.

[54] N.E. Dronkers, B.B. Redfernn, and C.A. Ludy. Lesion localization in chronic Wernicke's aphasia. *Brain Lang.*, 51:62–65, 1995.

[55] M. Dümpelmann, T.R. Knösche, A. Anwander, and C.H. Wolters. Sensitivity of inverse source reconstruction results towards forward model inaccuracies: Application of a universal sensitivity analysis software framework on different tissue conductivity ratios. In *[169]*, pages 694–696, 2002.

[56] A. Einstein. Über die von der molekularkinetischen Theorie der Wärme geforderte Bewegung von in ruhenden Flüssigkeiten suspendierten Teilchen. *Annalen Physik Chemie (4.Folge)*, 17:549–560, 1905.

[57] R. Falgout, Van E. Henson, J. E. Jones, and U. Meier Yang. Boomer AMG: A parallel implementation of algebraic multigrid. Techn. Report UCRL-MI-133583, Lawrence Livermore National Laboratory, March 1999.

[58] D.H. Fender. Models of the human brain and the surrounding media: Their influence on the reliability of source localization. *Journal of Clin.Neurophysiol.*, 8:381–390, 1991.

[59] D. Feuchter, I. Heppner, S.A. Sauter, and G. Wittum. Bridging the gap between geometric and algebraic multi-grid methods. *Comp.Vis.Sci.*, 6:1–13, 2003.

[60] A. Fick. Über Diffusion. *Annalen Physik Chemie*, 170:59–86, 1855.

[61] J. Fingberg, G. Berti, H. Hartmann, A. Basermann, C. Wolters, A. Anwander, A. McCarthy, and S. Woods. Bio-numerical simulations with SimBio. *NEC Research and Development*, 44(1), 2003.

[62] L. Flemming, J. Haueisen, U. Tenner, F. Giessler, and M. Eiselt. Source localization accuracy in an animal model. *Biomedizinische Technik*, 46(2):138–140, 2000.

[63] M.J. Flynn. Some computer organizations and their effectiveness. *IEEE Trans. on Comp.*, 21:948–960, 1972.

[64] R. Freeman and H.D.W. Hill. Phase and intensity anomalies in fourier transform nmr. *J. Magn. Reson.*, 4:366ff, 1971.

[65] A.D. Friederici, A. Hahne, and D.Y. von Cramon. First-pass versus second-pass parsing processes in a Wernicke's and a Broca's aphasic: electro-physiological evidence for a double dissociation. *Brain Lang.*, 62:311–341, 1998.

[66] A.D. Friederici, E. Pfeifer, and A. Hahne. Event-related brain potentials during natural speech processing: Effects of semantic morphological and syntactic violations. *Cog.Brain Res.*, 1:183–192, 1993.

[67] A.D. Friederici, D.Y. von Cramon, and S.A. Kotz. Language related brain potentials in patients with cortical and subcortical left hemisphere lesions. *Brain*, 122:1033–1047, 1999.

[68] A.D. Friederici, Y. Wang, C.S. Herrmann, B. Maess, and U. Oertel. Local-ization of early syntactic processes in frontal and temporal cortical areas: An MEG study. *Human Brain Map.*, 11:1–11, 2000.

[69] A. Frommer and P. Maaß. Fast CG-based methods for Tikhonov regular-ization. *SIAM J. Sci. Comp.*, 20(5):1831–1850, 1999.

[70] M. Fuchs, R. Drenckhahn, H.A. Wischmann, and M. Wagner. An im-proved boundary element method for realistical volume conductor model-ing. *IEEE Trans. Biomed. Eng.*, 45(8):980–997, 1998.

[71] M. Fuchs, M. Wagner, and J. Kastner. Standardized boundary and finite el-ement method volume conductor models. In *[169]*, pages 697–699, 2002. poster presentation.

[72] M. Fuchs, M. Wagner, T. Köhler, and H.A. Wischmann. Linear and nonlin-ear current density reconstructions. *Jour.Clin.Neurophysiol.*, 16(3):267–295, 1999.

[73] M. Fuchs, M. Wagner, H.A. Wischmann, T. Köhler, A. Theißen, R. Drenckhahn, and H. Buchner. Improving source reconstructions by combining bioelectric and biomagnetic data. *Electroenc. Clin. Neurophys-iol.*, 107:93–111, 1998.

[74] M. Fuchs, H.A. Wischmann, and M. Wagner. Generalized minimum norm least squares reconstruction algorithms. *ISBET Newsletter*, 5:8–11, 1994.

[75] M. Fuchs, H.A. Wischmann, M. Wagner, and J. Krüger. Coordinate sys-tem matching for neuromagnetic and morphological reconstruction over-lay. *IEEE Trans. Biomed. Eng.*, 42(4):416–420, 1995.

[76] J.D. Gardiner, A.J. Laub, J.J. Amato, and C.B. Moler. Solution of the Sylvester matrix equation $AXB^T + CXD^T = E$. *ACM Trans.Math.Softw.*, 18:223–238, 1992.

[77] L.A. Geddes and L.E. Baker. The specific resistance of biological mate-rial. A compendium of data for the biomedical engineer and physiologist. *Med.Biol.Eng.*, 5:271–293, 1967.

[78] J. Gerson, V.A. Cardenas, and G. Fein. Equivalent dipole parameter estimation using simulated annealing. *Electroenc. Clin. Neurophysiol.*, 92:161–168, 1994.

[79] G.H. Golub and C.F. Van Loan. *Matrix Computations*. The Johns Hopkins University Press, Baltimore and London, third edition edition, 1996.

[80] S. Gonçalves, J.C. de Munck, R.M. Heethaar, F.H. Lopes da Silva, and B.W. van Dijk. The application of EIT to reduce systematic errors in the EEG inverse problem–a simulation study. *Physiol.Meas.*, 21:379–393, 2000.

[81] R. Grave de Peralta Menendez and S.L. Gonzalez Andino. Single dipole localization: Some numerical aspects and a practical rejection criterion for the fitted parameters. *Brain Top.*, 6(4):277–282, 1994.

[82] R. Grebe, El Badia, and Wallois. Une nouvelle approche de localisation de sources en EEG chez l'enfant et le nouveau-né. Projet HTSC, Université de Picardie Jules Verne et CHU, Amiens, et Université de Technologie de Compiègne, France, 2002.

[83] R. Grebe, H. Zeaiter, V. Bach, F. Telliez, and R. Vandenhouten. Nonstationary time series analysis applied for evaluation of newborn sleeping stages under change of environment temperature. *Med.Biol.Eng.Comp.(Sup2,Pl)*, 37:438–439, 1999.

[84] M.S. Grewal and A.P. Andrews. *Kalman Filtering*. Prentice Hall, 1993.

[85] A. Gueziec and R. Hummel. The wrapper algorithm: surface extraction and simplification. In *IEEE Workshop on Biomedical Image Analysis*, pages 204–213. IEEE Computer Press, Los Alamitos, 1994.

[86] A. Haase, J. Frahm, D. Matthaei, W. Hänicke, and K.-D. Merboldt. FLASH imag.: rapid NMR imag. using low flip-angle pulses. *J.Magn.Reson.*, 67:258–266, 1986.

[87] G. Haase. *Parallelisierung numerischer Algorithmen für partielle Differentialgleichungen*. B.G.Teubner, Stuttgart·Leipzig, 1999.

[88] G. Haase, M. Kuhn, and S. Reitzinger. Parallel AMG on distributed memory computers. *SIAM J. Sci.Comp.*, 24(2):410–427, 2002.

[89] G. Haase and U. Langer. Multigrid-Methoden. Vorlesungsskriptum, http://www.numa.uni-linz.ac.at/, 1998.

[90] G. Haase and S. Reitzinger. Cache issues of algebraic multigrid methods for linear systems with multiple right-hand sides. Technical Report 02-05, J. Kepler Univ. Linz, SFB "Numerical and Symbolic Scientific Computing", 2002.

[91] W. Hackbusch. *Multi-Grid Methods and Applications*. Springer Verlag, Berlin, Heidelberg, New York, Tokyo, 1985.

[92] W. Hackbusch. *Theorie und Numerik elliptischer Differentialgleichungen.* Teubner Studienbücher, 1986.

[93] W. Hackbusch. *Iterative solution of large sparse systems of equations.* Springer Verlag, New York, Berlin, Heidelberg, London, Paris, Tokyo, Hong Kong, Barcelona, Budapest, 1994.

[94] W. Hackbusch. A sparse matrix arithmetic based on H-matrices. part I: Introduction to H-matrices. *Computing*, 62:89–108, 1999.

[95] M.S. Hämäläinen and R.J. Ilmoniemi. Interpreting measured magnetic fields of the brain: Estimates of current distributions. Techn. Report TKK-F-A559, Helsinki University of Technology, 1984.

[96] M.S. Hämäläinen and J. Sarvas. Feasibility of the homogeneous head model in the interpretation of neuromagnetic fields. *Phys.Med.Biol.*, 32:91–97, 1987.

[97] M.S. Hämäläinen and J. Sarvas. Realistic conductivity geometry model of the human head for interpretation of neuromagnetic data. *IEEE Trans. Biomed. Eng.*, 36:165–171, 1989.

[98] G. Hämmerlin and K.-H. Hoffmann. *Numerische Mathematik.* Springer-Verlag, 2 edition, 1991.

[99] H. Haneishi, N. Ohyama, K. Sekihara, and T. Honda. Multiple current dipole estimation using simulated annealing. *IEEE Trans. Biomed. Eng.*, 41:1004–1009, 1994.

[100] M. Hanke and P.C. Hansen. Regularization methods for large-scale problems. *Surv.Math.Ind.*, 3:253–315, 1993.

[101] P.C. Hansen. Analysis of discrete ill-posed problems by means of the L-curve. *SIAM Rev.*, 34:561–580, 1992.

[102] U. Hartmann and F. Kruggel. From segmented medical voxel datasets to high quality finite element meshes. *IEEEBiomed*, 2002. submitted.

[103] J. Haueisen. *Methods of numerical field calculation for neuromagnetic source localization.* PhD thesis, Shaker-Verlag Aachen, ISBN 3-8265-1691-5, 1996.

[104] J. Haueisen, C. Ramon, H. Brauer, and H. Nowak. The influence of local conductivity changes on MEG and EEG. *Biomedizinische Technik*, 45(7-8):211–214, 2000.

[105] J. Haueisen, C. Ramon, P. Czapski, and M. Eiselt. On the influence of volume currents and extended sources on neuromagnetic fields: A simulation study. *Annals of Biomedical Engineering*, 23:728–739, 1995.

[106] J. Haueisen, D.S. Tuch, C. Ramon, P.H. Schimpf, V.J. Wedeen, J.S. George, and J.W. Belliveau. The influence of brain tissue anisotropy on human EEG and MEG. *NeuroImage*, 15:159–166, 2002.

[107] T. Heinonen, H. Eskola, P. Dastidar, P. Laarne, and J. Malmivuo. Segmentation of T1 MR scans for reconstruction of resistive head models. *Comput.Meth.Programs Biomed.*, 3(54):173–181, 1997.

[108] K.G. Helmer, B.J. Dardzinski, and C.H. Sotak. The application of porous-media theory to the investigation of time-dependent diffusion in in vivo systems. *NMR in Biomedicine*, 8:297–306, 1995.

[109] M. Huang, C.J. Aine, S. Supek, E. Best, D. Ranken, and E.R. Flynn. Multi-start downhill simplex method for spatio-temporal source localization in MEG. *Electroenc. Clin. Neurophysiol.*, 108:32–44, 1998.

[110] G. Huiskamp, J. Maintz, G. Wieneke, M. Viergever, and A.C. van Huffelen. The influence of the use of realistic head geometry in the dipole localization of interictal spike activity in MTLE patients. *Biomedizinische Technik*, 42:84–87, 1997.

[111] G. Huiskamp, M. Vroeijenstijn, R. van Dijk, G. Wieneke, and A.C. van Huffelen. The need for correct realistic geometry in the inverse EEG problem. *IEEE Trans. Biomed. Eng.*, 46(11):1281–1287, 1999.

[112] S. Hütten. Über das asymptotische Verhalten von Simulated Annealing. Diplomarbeit in Mathematik, Institut für Statistik und Wirtschaftsmathematik, RWTH Aachen, 1993. http://www.stochastik.rwth-aachen.de/si/.

[113] B. Jähne. *Digitale Bildverarbeitung*. Springer-Verlag Berlin, 1991.

[114] L. Jantscher. *Distributionen*. W. de Gruyter, 1971.

[115] M. Jung and U. Langer. Applications of multilevel methods to practical problems. *Surv.Math.Ind.*, 1:217–257, 1991.

[116] J.P. Kaipio, P.A. Karjalainen, E. Somersalo, and M. Vauhkonen. State estimation in time-varying electrical impedance tomography. *Ann. NY Acad.Sci.*, 873:430–439, 1999.

[117] G. Karypis and V. Kumar. METIS – User's Guide, A software package for partitioning unstructured graphs, partitioning meshes, and computing fill-reducing orderings of sparse matrices, Version 4.0. University of Minnesota, http://www.cs.umn.edu/∼karypis, 1998.

[118] G. Karypis and V. Kumar. Multilevel k-way partitioning scheme for irregular graphs. *J. Par. Dist. Comp.*, 48(1):96–129, 1998.

[119] M. Kass and D. Witkin, A. amnd Terzopoulos. Snakes: Active contour models. *Int.J.Comput.Vis.*, 1(4):321–331, 1987.

[120] F. Kickinger. Algebraic multigrid for discrete elliptic second-order problems. In W. Hackbusch, editor, *Multigrid Methods V. Proceedings of the 5th European Multigrid conference*, pages 157–172. Berlin: Springer Lecture Notes Comput. Sci. Eng. 3, 1998.

[121] G. Knoll, H. Buchner, R. Beckmann, R. Schönen, and A. Rienäcker. Behandlung der Oberflächenintegrale und Ermittlung der Punktnormalen in FE Oberflächenstrukturen. Arbeitspapier zum Projekt Anatomische Abbildung elektrischer Aktivität des Zentralnervensystems, RWTH Aachen, November 1994.

[122] T.R. Knösche. *Solutions of the neuroelectromagnetic inverse problem.* PhD thesis, University of Twente, The Netherlands, 1997.

[123] T.R. Knösche, E.M. Berends, H.R.A. Jagers, and M.J. Peters. Determining the number of independent sources of the EEG. a simulation study on information criteria. *Brain Top.*, 11(2):111–124, 1998.

[124] T.R. Knösche, B. Maess, and A.D. Friederici. Processing of syntactic information monitored by brain surface current density mapping based on MEG. *Brain Top.*, 12(2):1–13, 1999.

[125] T.R. Knösche, B. Maess, A.D. Friederici, and D.Y. von Cramon. Localization of the sources of the ELAN from high resolution EEG data. In *Proc. of the 3rd Int.Conf. on Func. Map. of the Human Brain*, volume 5, page 539. NeuroImage, 1997.

[126] M. Koch. *Measurement of the Self-Diffusion Tensor of Water in the Human Brain.* PhD thesis, Univ. of Leipzig, Germany, 2000.

[127] R. Kories and H. Schmidt-Walter. *Taschenbuch der Elektrotechnik.* Verlag Harri Deutsch, Thun und Frankfurt a.M., 1993.

[128] A. Krechel and K. Stüben. Parallel algebraic multigrid based on subdomain blocking. *Parallel Comp.*, 27(8):1009 – 1031, 2001.

[129] F. Kruggel and G. Lohmann. Automatical adaption of the stereotactical coordinate system in brain MRI data sets. In J. Duncan, editor, *Int. Conf. on Information Processing in Medical Imaging*, Poultney, Vermont, USA, June 9–13, 1997. IPMI97.

[130] F. Kruggel and D.Y. von Cramon. Measuring the cortical thickness. In *IEEE Workshop on Mathematical Methods in Biomedical Image Analysis*, pages 154–161, Hilton Head Island, SC, June 11-12, Los Alamitos, CA, 2000. ISBN: 0-7695-0737-9.

[131] L.D. Landau and E.M. Lifshitz. *Electrodynamics of Continuous Media*. Pergamon Press, Oxford·New York·Toronto·Sydney·Paris·Frankfurt, 1985.

[132] LAPACK. *Linear Algebra PACKage User's Guide*. SIAM, 1992.

[133] L.L. Latour, K. Svoboda, P.P. Mitra, and C.H. Sotak. Time-dependent diffusion of water in a biological model system. *Proc.Natl.Acad.Sci.USA*, 91:1229–1233, 1994.

[134] P.C. Lauterbur. Image formation by induced local interactions: examples employing nuclear magnetic resonance. *Nature*, 242:469ff., 1974.

[135] S.K. Law. Thickness and resistivity variations over the upper surface of the human skull. *Brain Top.*, 2:99–109, 1993.

[136] C.L. Lawson and R.J. Hanson. *Solving Least Squares Problems*. Prentice-Hall, Englewood Cliffs, 1974.

[137] J.H. Lee, M. Garwood, R. Menon, G. Adriany, P. Anderson, C.L. Truwit, and K. Ugurbil. High contrast and fast 3D magnetic resonance imaging at high fields. *Magn.Reson.Med.*, 34:308–312, 1995.

[138] J.S. Lee. Digital image smoothing and the sigma filter. *Computer Vision, Graphics, and Image Processing*, 24:255–269, 1983.

[139] S. Lobregt and M.A. Viergever. A discrete dynamic contour model. *IEEE Trans. Med. Imag.*, 14(1):187–198, 1995.

[140] G. Lohmann. *Volumetric Image Analysis*. John Wiley & Sons, Chicester, 1998.

[141] G. Lohmann, K. Mueller, V. Bosch, H. Mentzel, S. Hessler, L. Chen, S. Zysset, and D.Y. von Cramon. Lipsia - a new software system for the evaluation of functional magnetic resonance images of the human brain. *Computerized Medical Imaging and Graphics*, 25(6):449–457, 2001.

[142] G. Lonsdale, R. Grebe, U. Hartmann, D.R. Hose, F. Kruggel, J.M.T. Penrose, and C.H. Wolters. Bio-numerical simulations with SimBio: project aims and objectives. In A. Makinouchi, S. Ebisuzaki, and R. Himeno, editors, *Symposium on Computational Biomechanics Simulation*, pages 187–196. RIKEN, May, 24-25, 2000.

[143] R. Lorente de No. Cerebral cortex: architecture, intracortical connections, motor projections. In J.F. Fulton, editor, *Physiology of the Nervous System*. Ch.15. University Press, Oxford, London, 1938.

[144] A. Louis and P. Maaß. A mollifier method for linear operator equations of the first kind. *Inverse problems*, 6:427–440, 1990.

[145] A.K. Louis. *Inverse und schlecht gestellte Probleme*. Teubner-Verlag, 1989.

[146] M. Lukaschewitsch, P. Maaß, and M. Pidcock. Tikhonov regularization for Electrical Impedance Tomography on unbounded domains. *Inverse Problems*, 2003. to appear.

[147] P. Maaß, S.V. Pereverzev, R. Ramlau, and S.G. Solodky. An adaptive discretization for Tikhonov-Phillips regularization with a posteriori parameter selection. *Numerische Mathematik*, 87(3):485–502, 2001.

[148] F. Maes, D. Vandermeulen, G. Marchal, and P. Suetens. Multimodality image registration by maximization of mutual information. *IEEE Trans. Med. Imag.*, 16(2):187–198, 1997.

[149] B. Maess, S. Koelsch, T.C. Gunter, and A.D. Friederici. Musical syntax is processed in broca's area: an MEG study. *Nature Neuroscience*, 4(5):540–545, 2001.

[150] R. Malladi, J.A. Sethian, and B.C. Vemuri. Shape modeling with front propagation: A level set approach. *IEEE Trans. Pattern Anal. and Machine Intelligence*, 17(2):158–169, 1995.

[151] G. Marin. *Utilisation de la méthode des éléments finis pour le calcul des champs électromagnétiques à l'aide d'un modèle réaliste de tête en MEG et EEG*. PhD thesis, Université de Paris-Sud, U.F.R. Scientifique d'Orsay, France, 1997.

[152] G. Marin, C. Guerin, S. Baillet, L. Garnero, and Meunier G. Influence of skull anisotropy for the forward and inverse problem in EEG: simulation studies using the FEM on realistic head models. *Human Brain Mapping*, 6:250–269, 1998.

[153] J. Mattiello, P.J. Basser, and D. Le Bihan. Analytical expressions for the b matrix in NMR diffusion imaging and spectroscopy. *J. Magn. Res. A*, 108:131–141, 1994.

[154] T. McInerney and D. Terzopoulos. Deformable models in medical image analysis: A survey. *Med.Imag.Anal.*, 1(2):91–108, 1996.

[155] E.R. McVeigh, M.J. Bronskill, and R.M. Henkelmann. Phase and sensitivity of receiver coils in MRI. *Med.Phys.*, 13:806–814, 1986.

[156] J.W.H Meijs, O.W. Weier, M.J. Peters, and A. van Oosterom. On the numerical accuracy of the boundary element method. *IEEE Trans. Biomed. Eng.*, 36:1038–1049, 1989.

[157] J.L. Melsa and D.L. Cohn. *Decision and Estimation Theory*. Mc-Graw-Hill Book Company, 1978.

[158] V. Menon, J.M. Ford, K.O. Lim, G.H. Glover, and A. Pfefferbaum. Combined event-related fMRI and EEG evidence for temporal-parietal cortex activation during target detection. *Neuro Report*, 8:3029–3037, 1997.

[159] N. Metropolis, A.W. Rosenbluth, M.N. Rosenbluth, A.H. Teller, and E. Teller. Equation of state calculations by fast computing machines. *J. of Chemical Physics*, 21:1087–1092, 1953.

[160] M. Meyer, A.D. Friederici, and D.Y. von Cramon. Neurocognition of auditory sentence comprehension: Event-related fMRI reveals sensitivity to syntactic violationsand task demands. *Cog.Brain Res.*, 9:19–33, 2000.

[161] J.C. Mosher, P.S. Lewis, and R.M. Leahy. Multiple dipole modeling and localization from spatio-temporal MEG data. *IEEE Trans. Biomed. Eng.*, 39(6):541–557, 1992.

[162] J.A. Nelder and R. Mead. A simplex method for function minimization. *Comp.J.*, 7:308–313, 1965.

[163] H.J. Neville, J. Nicol, A. Barss, K.I. Forster, and M.F. Garrett. Syntactically based sentence processing classes: Evidence from event-related brain potentials. *J.Cog.Neurosci.*, 3:151–165, 1991.

[164] C. Nicholson. Theoretical analysis of field potentials in anisotropic ensembles of neuronal elements. *IEEEBiomed*, 20:278–288, 1973.

[165] P.W. Nicholson. Specific impedance of cerebral white matter. *Exp.Neurol.*, 13:386–401, 1965.

[166] R. Nieuwenhuys, J. Voogd, and C. van Huijzen. *Das Zentralnervensystem des Menschen*. Springer-Verlag, 1991.

[167] W. Nolting. *Grundkurs: Theoretische Physik, Elektrodynamik*. Zimmermann-Neufang, Ulmen, 1992.

[168] D.G. Norris and P. Börnert. Coherence and interference in ultra-fast rare experiments. *J. Magn. Reson. A*, 105:123–127, 1993.

[169] H. Nowak, J. Haueisen, F. Giessler, and R. Huonker, editors. *BIOMAG2002, Proc. of the 13th Int. Conf. on Biomagnetism*. VDE Verlag GmbH, Berlin, Offenbach, 2002. http://biomag2002.uni-jena.de.

[170] P.L. Nunez. Localization of brain activity with electroencephalography. In *Sato, S. (ed.) Advances in Neurology, Magnetoencephalography*, volume 54, pages 39–65. Raven Press, New York, 1990.

[171] E. Odeblad and G. Lindström. Some preliminary observations of proton magnetic resonance in biological samples. *Acta Radiol.*, 43:469ff., 1955.

[172] Y. Okada. Neurogenesis of evoked magnetic fields. In S.N. Erné, H.D. Hahlbohm, and H. Lübbig, editors, *Biomagnetism*, pages 399–408. de Gruyter, Berlin, 1981.

[173] J. Ollikainen. *Modelling and Computational Aspects in EEG Inverse Problems*. PhD thesis, Kuopio University Publications C. Natural and Environmental Sciences 130, Kuopio, Finland, 2001.

[174] J. Ollikainen, M. Vauhkonen, P.A. Karjalainen, and J.P. Kaipio. Effects of local skull inhomogeneities on EEG source estimation. *Med.Eng.Phys.*, 21:143–154, 1999.

[175] B. Opitz, A. Mecklinger, D.Y. von Cramon, and F. Kruggel. Combining electrophysiological and hemodynamic measures of the auditory oddball. *Psychophysiology*, 36:142–147, 1999.

[176] B.U. Öztekin, G. Karypis, and V. Kumar. PMVIS – User's Guide, A program to visualize partitioned meshes, Version 1.06. University of Minnesota, http://www-users.cs.umn.edu/∼oztekin/pmvis/, 1998.

[177] R.D. Pascual-Marqui and C.M. Michel. Low resolution brain electromagnetic tomography (LORETA): New authentic 3D functional images of the brain. *ISBET Newsletter*, 5:4–8, 1994.

[178] C. Pastelak-Price. The international 10-20-system of electrode placement: Its rationale and a practical guide to measuring procedures and electrode placement. *EEG-Labor*, 5:49–72, 1983.

[179] B.A. Payne and A.W. Toga. Surface mapping brain function on 3D models. *IEEE Computer Graphics & Applications*, 10(5):33–41, 1990.

[180] M.J. Peters and J.C. de Munck. The influence of model parameters on the inverse solution based on MEGs and EEGs. *Acta Otolaryngol [Suppl] (Stockh)*, 491:61–69, 1991.

[181] D.L. Pham and J.L. Prince. An adaptive fuzzy C-means algorithm for image segmentation in the presence of intensity inhomogeneities. *Pat. Rec. Let.*, 20:57–68, 1999.

[182] W. Platzer, editor. *Pernkopf Anatomie*. Urban & Schwarzenberg, München, 1994.

[183] R. Plonsey and D. Heppner. Considerations on quasi-stationarity in electro-physiological systems. *Bull.math.Biophys.*, 29:657–664, 1967.

[184] R. Pohlmeier. Lokalisation elektrischer Gehirnaktivität durch inverse Analyse des Magnetoenzephalogramms (MEG) mit Finite-Elemente-Modellen des Kopfes. Diplomarbeit in Elektrotechnik, RWTH Aachen, 1996.

[185] R. Pohlmeier, H. Buchner, G. Knoll, A. Rienäcker, R. Beckmann, and J. Pesch. The influence of skull-conductivity misspecification on inverse source localization in realistically shaped finite element head models. *Brain Top.*, 9(3):157–162, 1997.

[186] E. Polak. *Computational Methods in Optimization*. New York Academic Press, 1971.

[187] W.H. Press, S.A. Teukolsky, W.T. Vetterling, and B.P. Flannery. *Numerical recipes*. Cambridge University Press, 2nd edition, 1992.

[188] E.M. Purcell, H.C. Torrey, and R.V. Pound. Resonance absorption by nuclear magnetic moments in a solid. *Phys.Rev.*, 69(37), 1946.

[189] S. Reitzinger. *Algebraic Multigrid Methods for Large Scale Finite Element Equations*. PhD thesis, Schriften der Johannes-Kepler-Universität Linz, Reihe C - Technik und Naturwissenschaften, No.36, 2001.

[190] A. Rienäcker, R. Beckmann, J. Pesch, G. Knoll, H. Buchner, and J. Silny. Dipolabbildung im FEM-Netz (III): Berücksichtigung höherer Dipolmomente. Arbeitspapier zum Projekt Anatomische Abbildung elektrischer Aktivität des Zentralnervensystems, RWTH Aachen, November 1994.

[191] A. Rienäcker, H. Buchner, and G. Knoll. Comparison of regularized inverse EEG analyses in finite element models of the individual anatomy. In *[253]*, pages 459–463, 1997.

[192] A. Rienäcker, D. Peters, G. Tokar, and B. Domes. Einsatz inverser Methoden zur Bestimmung der Rotorunwuchtverteilung eines Flugtriebwerks. BMW Rolls-Royce GmbH, EB-45 Gesamttriebwerksmechanik, Eschenweg 11, 15806 Dahlewitz, 1999.

[193] H. Rifai, I. Bloch, S. Hutchinson, J. Wiart, and L. Garnero. Segmentation of the skull in MRI volumes using deformable model and taking the partial volume effect into account. *Med.Imag.Anal.*, 4:219 – 233, 2000.

[194] B.J. Roth, M. Balish, A. Gorbach, and S. Sato. How well does a three-sphere model predict positions of dipoles in a realistically shaped head. *Electroenc. Clin. Neurophysiol.*, 87:175–184, 1993.

[195] B.J. Roth, D. Ko, I.R. von Albertini-Carletti, D. Scaffidi, and S. Sato. Dipole localization in patients with epilepsy using the realistically shaped head model. *Electroenc. Clin. Neurophysiol.*, 102:159–166, 1997.

[196] J.W. Ruge and K. Stüben. Algebraic multigrid (AMG). In S. McCormick, editor, *Multigrid Methods*, volume 5 of *Frontiers in Applied Mathematics*, pages 73–130. SIAM, Philadelphia, 1986.

[197] S. Rush and D.A. Driscoll. Current distribution in the brain from surface electrodes. *Anesthesia and analgetica*, 47(6):717–723, 1968.

[198] Y Saad. *Iterative methods for sparse linear systems*. PWS Publishing Company, 1996.

[199] J. Sarvas. Basic mathematical and electromagnetic concepts of the biomagnetic inverse problem. *Phys.Med.Biol.*, 32(1):11–22, 1987.

[200] M. Scherg and D. von Cramon. Two bilateral sources of the late AEP as identified by a spatio-temporal dipole model. *Electroenc. Clin. Neurophysiol.*, 62:32–44, 1985.

[201] P.H. Schimpf, C.R. Ramon, and J. Haueisen. Dipole models for the EEG and MEG. *IEEE Trans. Biomed. Eng.*, 49(5):409–418, 2002.

[202] U. Schmitt. *Effiziente Verfahren zur Regularisierung dynamischer inverser Probleme*. PhD thesis, Mathematisch-Naturwiss. Fakultät, Universität des Saarlandes, 2001.

[203] U. Schmitt and A.K. Louis. Efficient algorithms for the regularization of dynamic inverse problems: I.Theory. *Inverse Problems*, 18(3):645–658, 2002.

[204] U. Schmitt, A.K. Louis, C.H. Wolters, and M. Vauhkonen. Efficient algorithms for the regularization of dynamic inverse problems: II.Applications. *Inverse Problems*, 18(3):659–676, 2002.

[205] R. Schönen, A. Rienäcker, R. Beckmann, and G. Knoll. Dipolabbildung im FEM-Netz, Teil I. Arbeitspapier zum Projekt Anatomische Abbildung elektrischer Aktivität des Zentralnervensystems, RWTH Aachen, Juli 1994.

[206] H.R. Schwarz. *Methode der finiten Elemente*. PWS Publishing Company, 1996.

[207] P.N. Sen, C. Scala, and M.H. Cohen. A self-similar model for sedimentary rocks with application to the dielectric constant of fused glass beads. *Geophysics*, 46(5):781–795, 1981.

[208] A. Simmons, P.S. Tofts, G.J. Barker, and S.R. Arridge. Sources of intensity nonuniformity in spin echo images. *Magn.Reson.Med.*, 32:121–128, 1994.

[209] J.G. Sled and G.B. Pike. Understanding intensity non-uniformity in MRI. In W.M. Wells, A. Colchester, and S. Delp, editors, *Medical Image Computing and Computer Assisted Intervention: First International Conference*, pages 614–622. MICCAI98, Springer, 1998.

[210] C.P. Slichter. *Principles of magnetic resonance*. Springer-Verlag, Berlin, 3rd edition, 1990.

[211] W.R. Smythe. *Static and dynamic electricity*. Hemisphere Publishing, New York, 1989.

[212] E. Somersalo, M. Cheney, and D. Isaacson. Existence and uniqueness for electrode models for electric current computed tomography. *SIAM J.Appl.Math.*, 52:1023–1040, 1992.

[213] E. Somersalo, C. Johnson, and C. Wolters. Discussion about realistic modeling of white matter conductivity using EIT and DTI. "Computational Methods in Inverse Problems", http://www.sfb013.uni-linz.ac.at, 2002.

[214] L.H. Staib and X. Lei. Intermodality 3D medical image registration with global search. In *IEEE Workshop on Biomedical Image Analysis*. IEEE Computer Press, Los Alamitos, 1994.

[215] E.O. Stejskal. Use of spin echoes in a pulsed magnetic-field gradient to study anisotropic, restricted diffusion and flow. *J. Chem. Phys.*, 43:3597–3603, 1965.

[216] E.O. Stejskal and J.E. Tanner. Spin diffusion measurements: Spin echoes in the presence of time-dependent field gradients. *J. Chem. Phys.*, 42:288–292, 1965.

[217] J.A. Stratton. *Electromagnetic theory*. New York, McGraw-Hill Book Co., Inc., 1941.

[218] K. Stromswold, D. Caplan, N. Alpert, and S. Rauch. Localization of syntactic comprehension by positron emission tomography. *Brain Lang.*, 52:452–473, 1996.

[219] K. Stüben. A review of algebraic multigrid. Techn. Report 69, GMD, November 1999. http://www.gmd.de.

[220] C. Studholme, D.L.G. Hill, and D.J. Hawkes. Automated 3D registration of MR and CT images of the head. *Med.Imag.Anal.*, 1(2):163–175, 1997.

[221] W.W. Sutherling, P.H. Crandall, T.M. Darcey, D.P. Becker, M.F. Levesque, and D.S. Barth. The magnetic and electrical fields agree with intracranial localizations of somatosensory cortex. *Neurology*, 38:1705–1714, 1988.

[222] D. Terzopoulos and K. Fleischer. Deformable models. *The Visual Computer*, 4:306–331, 1988.

[223] D.S. Tuch, V.J. Wedeen, A.M. Dale, and J.W. Belliveau. Electrical conductivity tensor map of the human brain using NMR diffusion imaging: An effective medium approach. *ISMRM, 6th Scientific Meeting, Sydney*, 1998.

[224] D.S. Tuch, V.J. Wedeen, A.M. Dale, J.S. George, and J.W. Belliveau. Conductivity mapping of biological tissue using diffusion MRI. *Ann. NYAS*, 888:314–316, 1999.

[225] J.K. Udupa and S. Samarasekera. Fuzzy connectedness and object definition: Theory, algorithms and applications in image segmentation. *Graph. Models and Image Processing*, 58:246–261, 1996.

[226] G.M. Vainikko. The discrepancy principle for a class of regularization methods. *USSR Computational Mathematics and Mathematical Physics*, 22(3):1–19, 1982.

[227] S.P. van den Broek. *Volume Conduction Effects in EEG and MEG*. PhD thesis, Proefschrift Universiteit Twente Enschede, The Netherlands, 1997.

[228] S.P. van den Broek, F. Reinders, M. Donderwinkel, and M.J. Peters. Volume conduction effects in EEG and MEG. *Electroenc. Clin. Neurophysiol.*, 106:522–534, 1998.

[229] A. van Oosterom and J. Strackee. The solid angle of a plane triangle. *IEEE Trans. Biomed. Eng.*, 30(2):125–126, 1983.

[230] H.G. Vaughan, Jr. The analysis of scalp-recorded brain potentials. In R.F. Thompson and M.M. Patterson, editors, *Bioelectric Recording Techniques*, pages 158–207. Part B. Academic Press, New York, 1974.

[231] M. Vauhkonen. *Electrical Impedance Tomography and Prior Information*. PhD thesis, Department of Applied Physics, University of Kuopio, Finland, 1997.

[232] M. Vauhkonen. Electrical impedance tomography and prior information. *IEEE Trans. Biomed. Eng.*, 17(2):285–293, 1998.

[233] M. Vauhkonen, P.A. Karjalainen, and J.P. Kaipio. A Kalman filter approach to track fast impedance changes in electrical impedance tomography. *IEEE Trans. Biomed. Eng.*, 45(4):486–493, 1998.

[234] M. Vauhkonen, D. Vadász, P.A. Karjalainen, E. Somersalo, and J.P. Kaipio. Tikhonov regularization and prior information in electrical impedance tomography. *IEEE Trans. Biomed. Eng.*, 17(2):285–293, 1998.

[235] P.J. Vauhkonen, M. Vauhkonen, and J.P. Kaipio. Fixed lag smoothing and state estimation in dynamical electrical impedance tomography. *Int.J.Numer.Meth.Eng.*, 50:2195–2209, 2001.

[236] J. von Rango, H.A. Schlitt, H. Halling, and H.-W. Müller-Gärtner. Finite integration techniques for the MEG forward problem. In *[253]*, pages 336–338, 1997.

[237] T.D. Waberski, H. Buchner, K. Lehnertz, A. Hufnagel, M. Fuchs, R. Beckmann, and A. Rienäcker. The properties of source localization of epileptiform activity using advanced headmodelling and source reconstruction. *Brain Top.*, 10(4):283–290, 1998.

[238] C. Wagner. On the algebraic construction of multilevel transfer operators. *Computing*, 65:73–95, 2000.

[239] M. Wagner. *Rekonstruktion neuronaler Ströme aus bioelektrischen und biomagnetischen Messungen auf der aus MR-Bildern segmentierten Hirnrinde*. PhD thesis, Shaker-Verlag Aachen, ISBN 3-8265-4293-2, 1998.

[240] M. Wagner, M. Fuchs, M. Akhtari, A. Anwander, and C. Wolters. Discussion about anisotropic conductivity modeling for the three-layer skull. Biomag2002 and E-mail correspondance, 2002.

[241] M. Wagner, M. Fuchs, R. Drenckhahn, H.-A. Wischmann, Th. Köhler, and A. Theißen. Automatic generation of BEM and FEM meshes from 3D MR data. *Neuroimage*, 3:S168, 2000.

[242] M. Wagner, M. Fuchs, H.-A. Wischmann, R. Drenckhahn, and Th. Köhler. Current density reconstructions using the L1-norm. In *Proc. of the 10th Int.Conf.of Biomagnetism; Santa Fe*, pages 158–207. Biomag96, 1996.

[243] M. Wagner, M. Fuchs, H.-A. Wischmann, K. Ottenberg, and O. Dössel. Cortex segmentation from 3D MR images for MEG reconstructions. In *Biomagnetism: Fundamental Research and Clinical Applications, Amsterdam, The Netherlands.*, pages 93–101, 1995.

[244] G. Waldmann, H. Woldag, T.R. Knösche, and H. Hummelsheim. Movement related cortical magnetic fields in self induced wrist movement under a physiotherapeutic intervention. In *[169]*, pages 185–187, 2002.

[245] Y. Wang, D.R. Haynor, and Y. Kim. An investigation of the importance of myocardial anisotropy in finite-element modeling of the heart: Methodology and application to the estimation of defibrillation efficacy. *IEEE Trans. Biomed. Eng.*, 48(12), 2001.

[246] J.G. Webster. *Medical instrumentation: application and design*. John Wiley & Sons, Inc., New York, Chichester, Brisbane, Toronto, Singapore, 1995.

[247] D. Weinstein, L. Zhukov, and C. Johnson. Lead-field bases for electroencephalography source imaging. *Annals of Biomed.Eng.*, 28(9):1059–1066, 2000.

[248] W.M. Wells, W.E.L. Grimson, R. Kikinis, and F.A. Jolesz. Adaptive segmentation of MRI data. *IEEE Trans. Med. Imag.*, 15:429–442, 1996.

[249] W.M. Wells, P. Viola, H. Atsumi, S. Nakajima, and R. Kikinis. Multimodal volume registration by maximization of mutual information. *Medical Image Analysis*, 1(1):35 – 51, 1996.

[250] J. Werner. *Numerische Mathematik 1*. Vieweg, 1991.

[251] C. Wernicke. *Der aphasische Symtomenkomplex. Eine psychologische Studie auf anatomischer Basis.* Cohn und Weigert, Breslau, 1874.

[252] J.R. Wikswo, A. Gevins, and S.J. Williamson. The future of EEG and MEG. *Electroenc. Clin. Neurophysiol.*, 87:1–9, 1993.

[253] H. Witte, U. Zwiener, B. Schack, and A. Doering, editors. *Quantitative and Topological EEG and MEG Analysis*. Druckhaus Mayer Verlag GmbH Jena · Erlangen, 1997.

[254] C. Wolters. Direkte Methoden zur Berechnung dipolinduzierter elektrischer und magnetischer Felder und inverse Strategien zur Quellokalisation im Gehirn. Diplomarbeit in Mathematik mit Nebenfach Medizin, Institut für Geometrie und Praktische Mathematik, RWTH Aachen, 1997.

[255] C. Wolters, S. Reitzinger, A. Basermann, S. Burkhardt, U. Hartmann, F. Kruggel, and A. Anwander. Improved tissue modeling and fast solver methods for high resolution FE-modeling in EEG/MEG-source localization. In J. Nenonen, R.J. Ilmoniemi, and T. Katila, editors, *Proc. of the 12th Int. Conf. on Biomagnetism*, pages 655–658, Helsinki Univ. of Tech., Finland, Aug.13-17, http://biomag2000.hut.fi/papers_all.html, 2000.

[256] C. Wolters, A. Rienäcker, R. Beckmann, H. Jarausch, H. Buchner, R. Grebe, and A.K. Louis. Stable inverse current reconstruction in real anatomy using combinatorial optimization techniques combined with regularization methods. In *[253]*, pages 487–490, 1997.

[257] C.H. Wolters, A. Anwander, M. Dümpelmann, T. Knösche, and M. Koch. Influence of head tissue conductivity inhomogeneity and anisotropy on EEG and MEG based source localization in the human brain using high resolution FE modeling. in preparation, 2002.

[258] C.H. Wolters, A. Anwander, M. Koch, S. Reitzinger, M. Kuhn, and M. Svensén. Influence of head tissue conductivity anisotropy on human EEG and MEG using fast high resolution finite element modeling, based on a parallel algebraic multigrid solver. In T. Plesser and V. Macho, editors, *"Forschung und wissenschaftliches Rechnen", Contributions to the Heinz-Billing Award*, number 58, pages 111–157. Gesellschaft für wissenschaftliche Datenverarbeitung mbH Göttingen, 2001. ISSN: 0176-2516, http://www.billingpreis.mpg.de.

[259] C.H. Wolters, R.F. Beckmann, A. Rienäcker, and H. Buchner. Comparing regularized and non-regularized nonlinear dipole fit methods: A study in a simulated sulcus structure. *Brain Top.*, 12(1):3–18, 1999.

[260] C.H. Wolters, R.F. Beckmann, A. Rienäcker, and H. Buchner. A new regularization method for nonlinear and constrained dipole fit. *NeuroImage*, 9(6):S177, 1999.

[261] C.H. Wolters, U. Hartmann, M. Koch, F. Kruggel, S. Burkhardt, A. Basermann, D.S. Tuch, and J. Haueisen. New methods for improved and accelerated FE-volume conductor modeling in EEG/MEG-source reconsruction. In J. Middleton, M. Jones, N. Shrive, and G. Pande, editors, *4th Symposium on Computer Methods in Biomechanics and Biomed.Eng.*, pages 489–494, Lisboa, Okt.31-Nov.3, 1999. Gordon & Breach, ISBN: 9056993216.

[262] C.H. Wolters, M. Kuhn, A. Anwander, and S. Reitzinger. Fast anisotropic high resolution finite element head modeling in EEG/MEG-source localization. In *[169]*, pages 670–672, 2002.

[263] C.H. Wolters, M. Kuhn, A. Anwander, and S. Reitzinger. A parallel algebraic multigrid solver for finite element method based source localization in the human brain. *Comp.Vis.Sci.*, 5(3):165–177, 2002.

[264] C.C. Wood. Application of dipole localization methods to source identification of human evoked potentials. *Ann. New York Acad.Sci.*, 388:139–155, 1982.

[265] C. Xu, J. Pham, E. Rettmann, D.N. Yu, and J.L. Prince. Reconstruction of the human cerebral cortex from magnetic resonance image. *IEEE Transactions on Medical Imaging*, 18(6):467–480, 1998.

[266] M. Yedlin, H. Kwan, J.T. Murphy, H. Nguyen-Huu, and J.C. Wong. Electrical conductivity in cat cerebellar cortex. *Exp.Neurol.*, 43:555–569, 1974.

[267] B. Yvert, O. Bertrand, J.F. Echallier, and J. Pernier. Improved forward eeg calculations using local mesh refinement of realistic head geometries. *Electroenc. Clin. Neurophysiol.*, 95:381–392, 1995.

[268] B. Yvert, A. Crouzeix-Cheylus, and J. Pernier. Fast realistic modeling in bioelectromagnetism using lead-field interpolation. *Human Brain Mapping*, 14:48–63, 2001.

[269] F. Zanow and M.J. Peters. Individually shaped volume conductor models of the head in EEG source localisation. *Med. & Biol. Eng. & Comput.*, 7:151–161, 1995.

[270] E. Zeidler. *Nonlinear Functional Analysis and its Applications III: Variational Methods and Optimization.* Springer Verlag, New York·Berlin·Heidelberg·Tokyo, 1985.

[271] E. Zeidler, W. Hackbusch, and H.R. Schwarz. *Teubner-Taschenbuch der Mathematik.* B.G.Teubner, Stuttgart·Leipzig, 1996. ISBN 3-8154-2001-6.

[272] X. Zeng, L.H. Staib, R.T. Schultz, and J.S. Duncan. Segmentation and measurement of the cortex from 3D MR images using coupled-surfaces propagation. *IEEE Transactions on Medical Imaging*, 18(10):927–937, 1999.

[273] H. Zhou and A. van Oosterom. Computation of the potential distribution in a four-layer anisotropic concentric spherical volume conductor. *IEEE Trans. Biomed. Eng.*, 39(2):154–158, 1992.

Awards, projects, workshops, reviews and publications

Awards

1. Wolters, C.H., *Friedrich Springorum medal*, Rheinisch Westfälische Technische Hochschule Aachen, June 1998.

2. Anwander, A., Wolters, C.H., Dümpelmann, M. and Knösche, T.R. *Young Investigators Award for poster presentation*, 13th Int.Conf. on Biomagnetism, Jena, August 2002, http://biomag2002.uni-jena.de.

Projects

1. SimBio, A generic environment for bionumerical simulation, *European Commission, Information Society Technologies (IST) Programme, Framework V*, Project IST-1999-10378, http://www.simbio.de, Started on April 1st, 2000 lasting 3 years.

Workshops

1. Wolters, C.H., Accurate and fast methods for the treatment of head tissue anisotropy in EEG/MEG source localization. *Wolters, C.H. & Anwander, A. (org.): "Models to generate individual anisotropic conductivity maps of head tissues from multimodal MR and influence on EEG/MEG source localization"*, MPI of Cognitive Neuroscience Leipzig, Germany, November (2000).

2. Wolters, C.H., Influence of head tissue conductivities on EEG/MEG source localization. *European workshop on MEG (EUWOMEG)*, Erlangen, Germany, June (1999).

Reviews

1. Wolters, C.H., Reviewer for *"IEEE Transactions on Medical Imaging"* since November 2000.

Book chapters

1. Wolters, C.H., Anwander, A., Koch, M., Reitzinger, S., Kuhn, M. and Svensén, M., Influence of head tissue conductivity anisotropy on human EEG and MEG using fast high resolution finite element modeling, based on a parallel algebraic multigrid solver. In *T.Plesser & V.Macho (eds.):*

"Forschung und wissenschaftliches Rechnen" Contributions to the Heinz-Billing Award, Gesellschaft für wissenschaftliche Datenverarbeitung mbH Göttingen, http://www.billingpreis.mpg.de, ISSN: 0176-2516, **58**, pp. 111–157, (2001).

Papers and manuscripts

1. Wolters, C.H., Beckmann, R.F., Rienäcker, A. and Buchner, H., Comparing regularized and non-regularized nonlinear dipole fit methods: A study in a simulated sulcus structure. *Brain Topography* **12**(1), pp. 3–18 (1999).

2. Schmitt, U., Louis, A.K., Wolters, C.H. and Vauhkonen, M., Efficient algorithms for the regularization of dynamic inverse problems: II. Applications. *Inverse Problems* **18**(3), pp. 659–676 (2002).

3. Wolters, C.H., Kuhn, M., Anwander, A. and Reitzinger, S., A parallel algebraic multigrid solver for finite element method based source localization in the human brain. *Comp.Vis.Sci.* **5**(3), pp.165–177 (2002).

4. Fingberg, J., Berti, G., Hartmann, H., Basermann, A., Wolters, C., Anwander, A., McCarthy, A. and Woods, S., Bio-numerical simulations with SimBio, *NEC Research and Development* **44**(1), (2003).

5. Burkhardt, S., Wolters, C.H. and Saupe, D., Segmentation of human skull surfaces from bimodal MRI volumes, in preparation (2003).

6. Anwander, A., Haase, G., Reitzinger, S. and Wolters, C.H., High Performance Computations for Source Reconstruction in the Human Brain. in preparation (2003).

7. Wolters, C.H., Anwander, A., Dümpelmann, M., Knösche, T. and Koch, M., Influence of head tissue conductivity inhomogeneity and anisotropy on EEG and MEG based source localization in the human brain. in preparation (2003).

Proceedings

1. Wolters, C.H., Rienäcker, A., Beckmann, R., Jarausch, H., Buchner, H., Grebe, R. and Louis, A.K., Stable inverse current reconstruction in real anatomy using combinatorial optimization techniques combined with regularization methods. In *Witte, H., Zwiener, U., Schack, B. & Doering, A. (eds.): "Quantitative and Topological EEG and MEG Analysis"*, Druckhaus Mayer Verlag GmbH Jena-Erlangen, pp. 484–486 (1997).

2. Wolters, C.H., Hartmann, U., Koch, M., Kruggel, F., Burkhardt, S., Basermann, A., Tuch, D.S. and Haueisen, J., New methods for improved and accelerated FE-volume-conductor modelling in EEG/MEG-source reconstruction. In *Middleton, J., Jones, M., Shrive, N. & Pande, G. (eds.): "4th Symp. on Comp. Meth. in Biomech. and Biomed.Eng.", Lisboa, Portugal, Okt.31-Nov.3*, Gordon & Breach, ISBN: 9056993216, pp. 489–494 (1999).

3. Lonsdale, G., Grebe, R., Hartmann, U., Hose, D.R., Kruggel, F., Penrose, J.M.T. and Wolters, C.H., Bio-numerical simulations with SimBio: project aims and objectives. In *RIKEN, Symposium on Computational Biomechanics Simulation, May, 24-25*, pp. 187–196 (2000).

4. Wolters, C.H., Reitzinger, S., Basermann, A., Burkhardt, S., Hartmann, U., Kruggel, F. and Anwander, A., Improved tissue modeling and fast solver methods for high resolution FE-modeling in EEG/MEG-source localization. In *Nenonen, J., Ilmoniemi, R.J. & Katila, T. (eds.): Proc. of the 12th Int. Conf. on Biomagnetism, Helsinki Univ. of Tech., Espoo, Finland*, http://biomag2000.hut.fi, pp. 655–658 (2000).

5. Burkhardt, S., Kruggel, F., Saupe, D. and Wolters, C.H., Segmentierung des Knochens aus T1- und PD-gewichteten Kernspinbildern vom Kopf. In *Handels, H., Horsch, A., Lehmann, T. & Meinzer, H.-P. (eds.): "Bildverarbeitung für die Medizin"*, Springer-Verlag, Berlin, pp. 187–191 (2001).

6. Anwander, A., Wolters, C.H., Dümpelmann, M., and Knösche, T.R., Influence of realistic skull and white matter anisotropy on the inverse problem in EEG/MEG-source localization. In *Nowak, H., Haueisen, J., Giessler, F. and Huonker, R. (eds.): Proc. of the 13th Int. Conf. on Biomagnetism, University of Jena, Jena, Germany*, VDE Verlag GmbH, Berlin, Offenbach, http://biomag2002.uni-jena.de, pp. 679–681 (2002).

7. Wolters, C.H., Kuhn, M., Anwander, A. and Reitzinger, S., Fast anisotropic high resolution finite element head modeling in EEG/MEG-source localization. In *Nowak, H., Haueisen, J., Giessler, F. and Huonker, R. (eds.): Proc. of the 13th Int. Conf. on Biomagnetism, University of Jena, Jena, Germany*, VDE Verlag GmbH, Berlin, Offenbach, http://biomag2002.uni-jena.de, pp. 670–672 (2002).

8. Dümpelmann, M., Knösche, T.R., Anwander, A. and Wolters, C.H., Sensitivity of inverse source reconstruction results towards forward model inaccuracies: Application of a universal sensitivity analysis software framework on different tissue conductivity ratios. In *Nowak, H., Haueisen, J.,*

249

Giessler, F. and Huonker, R. (eds.): Proc. of the 13th Int. Conf. on Biomagnetism, University of Jena, Jena, Germany, VDE Verlag GmbH, Berlin, Offenbach, http://biomag2002.uni-jena.de, pp. 694–696 (2002).

Abstracts

1. Wolters, C.H., Beckmann, R.F., Rienäcker, A. and Buchner, H., New regularization method for nonlinear and constrained dipole fit. *NeuroImage* **9**(6), S177 (1999).

Invited talks

1. Wolters, C.H., Regularization methods for EEG/MEG source localization in the human brain. *P.Maaß (host), Institute of Mathematics, University of Potsdam, Potsdam, Germany*, (1999).

2. Wolters, C.H., Fast solver methods for FEM based EEG/MEG source localization in the human brain. *R.Schneider (host), Faculty for Mathematics, Technical University of Chemnitz, Chemnitz, Germany*, (1999).

3. Wolters, C.H., High resolution FE modeling of head tissue conductivity anisotropy by means of multi-modal MR imaging and applications to EEG-/MEG source localization in the human brain. *U.Langer (host), SFB F013 "Numerical and Symbolic Scientific Computing", University of Linz, Linz, Austria*, Nov. (2000).

4. Wolters, C.H., Influence of tissue conductivity inhomogeneity and anisotropy on EEG/MEG source localization in the human brain. *Engl, H.W. (org.): SFB-Conference on "Computational Methods for Inverse Problems", Strobl, Austria*, http://www.sfb013.uni-linz.ac.at, Aug. 25-31 (2002).

5. Wolters, C.H., Influence of tissue conductivity inhomogeneity and anisotropy on EEG/MEG source localization in the human brain. *Johnson, C. (host), Scientific Computing and Imaging Institute, University of Utah, Salt Lake City, USA*, July 10-11 (2003).

Talks

1. Wolters, C.H. Fast anisotropic high resolution finite element head modeling in EEG/MEG-source localization. *13th Int. Conf. on Biomagnetism, BIOMAG2002, University of Jena, Jena, Germany*, http://biomag2002.uni-jena.de (2002).

Curriculum Vitae

Carsten Hermann Wolters
born June 10, 1967 in Emsdetten (Westfalia)

School education

1973–1977	Primary school education at "Buckhoff-Grundschule", Emsdetten.
1977–07/1986	High school education at "Privates Arnold-Janssen Gymnasium", St.Arnold near Neuenkirchen, Westfalia.

Scientific education

10/1990–10/1997	M.Sc. in Mathematics, Minor in Medicine, RWTH Aachen (with distinction, 1.0), Masters thesis "Direkte Methoden zur Berechnung dipolinduzierter elektrischer und magnetischer Felder und inverse Strategien zur Quellokalisation im Gehirn", Institute for Geometry and Practical Mathematics and Institute of Physiology, RWTH Aachen.
09/1992–06/1993	DAAD scholarship for the INSA de Lyon and research work (with F. Perrin, O. Bertrand and J. Pernier), "La méthode des éléments de surface en utilisant une interpolation linéaire du potentiel afin de résoudre le problème direct.", INSERM-Unité 280, Lyon, France
02/1995–04/1995	Research work (with F. Frouin, H. Benali and R. di Paola), "Faktoranalysis einer Bildsequenz von enddiastolisch-endsystolischen Herzszintigraphiebildern", INSERM-Unité 494, Paris, France.
11/1997–07/2003	Scientific researcher and Ph.D. student at the MPI for Mathematics in the Sciences in cooperation with the MPI of Cognitive Neuroscience, Leipzig. Dissertation at the University of Leipzig (magna cum laude, 1.0).

from 07/2003   Scientific researcher and Post-doctoral associate at the MPI for Mathematics in the Sciences in cooperation with the MPI of Cognitive Neuroscience, Leipzig.

Professional education and experience

08/1986–08/1989   Education for "Mathematisch technischer Assistent", comparable to studies in Informatics (FH, Fach-Hochschule), Computer center, University of Münster, Examination at the Chamber of Industry and Commerce, Cologne.

02/1991–04/1991   Interface programming, Kolvenbach KG, electrofluid technology, Aachen, Germany.

08/1993–12/1993   Student assistant at the Institute of Physiology, RWTH Aachen.

08/1994–08/1996   Student lecturer in numerical analysis for students in Mathematics, Institute for Geometry and Applied Mathematics, RWTH Aachen

07/1996–12/1996   Coupling an Anaesthesia Work Station to the HP Viridia CMS, Patient Monitoring Division, Hewlett-Packard Medical Products Group, Böblingen, Germany.

Military service

10/1989–10/1990   Military service, Navy

Leipzig, 14th of July 2003